

University of South Wales



2060378

# ADAPTIVE SPLINE METHOD FOR THE ASSESSMENT OF CELL MOTILITY AND ITS APPLICATION TO LESIONS

ANDREAS HOPPE

A submission presented in partial fulfilment of the requirements of the  
University of Glamorgan  
for the degree of Doctor of Philosophy

This research programme was carried out in  
collaboration with the Department of Surgery,  
University of Wales College of Medicine

June 2001

## Abstract

Malignant disease is a major cause of morbidity and mortality in western Europe. Cancers which form distant metastasis are difficult to contain. Measures to stimulate or inhibit movement of cancer cells may play an important part in metastasis biology. The movement behaviour of individual cells within a cluster may give new clues about cell-to-cell interactions. However, the recognition and tracking of individual cells in clusters is difficult for a fully automated imaging system.

A principal aim of this study was to develop a semi-automatic image processing system to enable assessment of cell movement in clustered cancer cell colonies. The system would also be adapted and applied for the segmentation and analysis of macroscopic images of leg ulcers.

A piecewise cubic spline interpolation was used to describe cells by their boundary. The spline model was extended into the time domain with a deterministic relocation technique to facilitate tracking of cells, thus forming a new adaptive spline model.

The method was applied to investigate the movement behaviour of clustered human colon cancer cells *in vitro* associated with an added movement stimulant. The results demonstrated that stimulated cells show more movement activity and higher velocities than control cells. The system was also applied to assess morphology of neutrophils in brightfield microscopy and results were compared with a region-based segmentation technique. Furthermore the system was applied to assess cell morphology in relation to intracellular chemical changes in neutrophils.

On a macroscopic level, the spline technique was used to segment the wound boundary in leg ulcer images. The spline was used to generate a profile of the wound edge at the boundary of leg ulcers to extract new wound assessment parameters based on hue, saturation and intensity.

In summary, these adaptive spline methods enable the assessment of cell movement behaviour in clustered cells. Differences in behaviour between stimulated cells and control cells can be quantified. The system is also proving to be useful in segmenting macroscopic images such as leg ulcer images. Thus this system should be of value in macroscopic analysis of wound healing and microscopic analysis of cell movement and cell behaviour.

### **Meinen Eltern**

Heinz-Werner und Renate Hoppe

### **Acknowledgements**

I would like to thank my supervisors Prof R.J. Williams and Dr D.Wertheim for their support during my research work. Furthermore I would like to thank Dr W.G. Jiang and Dr M.C. Hallett from the University of Wales College of Medicine for their expertise and the use of their facilities. Many thanks also for Prof K. Harding and the support from the Wound Healing Research Unit.

## Table of Contents

<b>1.0 Introduction</b>	1
1.1 Background	2
1.2 Novel Tracking Technique	6
1.3 Aims and objectives	8
1.4 Contribution to original knowledge	10
<b>2.0 Background</b>	13
2.1 Image acquisition in the study of living cells in light microscopy	17
2.1.1 Image Acquisition	17
2.1.2 Light Microscopy	18
2.1.3 Fluorescence Microscopy	20
2.1.4 Phase Contrast and Interference Contrast Microscopy	21
2.1.5 Hoffman Modulation Contrast Microscopy	22
2.1.6 Phase Shifting Interference Microscopy	23
2.2 Image segmentation techniques for cell imaging	25
2.2.1 Region-based segmentation in digital imaging	26
2.2.2 Edge based segmentation	28
2.3 Model based approaches in image segmentation	30
2.3.1 Active contours	31
2.3.2 Geometrical deformable models (GDMs)	34
2.3.3 Active shape models	36
2.4 Tracking non-rigid objects	38
2.5 Description of cell morphology and cell motility	45
2.6 Example of systems for assessing cell motility	47
2.7 Conclusions	48
<b>3.0 Adaptive Spline Method</b>	49
3.0 Introduction	49
3.1 Cell Image Features	52
3.2 Adaptive Spline Contour	57
3.2.1 The spline contour	57
3.2.2 Spline deformation	61

3.3 Cell Tracking .....	63
3.3.1 Pixel flow property in point relocation .....	65
3.3.2 Gradient based property .....	68
3.3.3 Point relocation strategy .....	71
3.4 Cell shape parameters .....	72
3.5 Concluding remarks .....	75
 <b>4.0 Validation</b> .....	 76
4.0 Introduction.....	76
4.1 Segmentation of test object.....	77
4.2 Segmentation of real cell images .....	78
4.3 Repeatability of semi-automatic tracking .....	81
4.4 Automatic tracking .....	81
4.5 Conclusion .....	83
 <b>5.0 Cell Experiments</b> .....	 84
5.0 Introduction.....	84
5.1 Human colon cancer cells .....	86
5.1.1 Microscope setup and calibration .....	86
5.1.2 HT115 Series I .....	88
5.1.3 HT115 Series II, III and IV .....	91
5.2 HRT18 cells .....	99
5.3 Application of adaptive spline to neutrophils .....	101
5.4 Application of the spline to ratio imaging .....	104
 <b>6.0 Wound Experiments</b> .....	 109
6.0 Introduction.....	109
6.1 Colour variability .....	110
6.2 Clinicians assessment of digital wound images.....	112
6.3 Assessing the amount of slough.....	114
6.4 Wound profile assessment .....	116
6.5 Conclusions.....	118
 <b>7.0 Conclusion and Discussion</b> .....	 120

## **Appendix**

### **A References**

### **B Snapshots**

### **C Software**

- Class Diagram
- Class Description
- Source code examples

### **D Spline Calculations**

### **E Copy of Publications**

# Adaptive Spline Method for Assessment of Cell Motility and its Application to Lesions

## 1.0 Introduction

In western Europe at least one third of the population develops a malignant disease such as cancer [Lindblom and Liljegren, 2000]. The spreading of cancer and development of secondary tumours within the body are thought to be contributed by the ability of cells to move [Schiffmann, 1990].

Motility, a term describing movement behaviour, is a basic necessity for survival of all living organisms. This also applies on a microscopic level within each organism. From embryonic development to inflammatory processes, the ability of cells to divide and move is essential. For example, neutrophils are blood cells that are responsible for combating infection within the body. They move to a site of infection, engulf and kill the intruding micro-organisms. In wound healing the repair process of tissue involves both migration and proliferation of cells [Zahm *et al.*, 1997]. Epithelial cells were shown to migrate and reorganise, forming new tissue at the wound edge *in vitro*. Cell motility is a major factor in malignant diseases. For instance, the capability of cancer cells to move is thought to be crucial in the formation of distant metastases [Jiang *et al.*, 1994a]. The objective assessment of cell motility is therefore considered to be important for investigating these phenomena.

In this thesis, a new approach of assessing the motility of cells is described. In this method, a cell is described by a mathematical contour approximation of the boundary using splines. This *adaptive spline* method enables the semi-automatic segmentation of clustered cells and subsequent tracking in combination with a deterministic relocation technique. A cell tracking system was designed by developing software incorporating the adaptive spline method and other imaging techniques. The system was applied to quantify the movement behaviour of human colon cancer cells with and without added movement stimulators. The system was further adapted and

applied to segment macroscopic wound images in order to investigate the appearance of leg ulcers.

## 1.1 Background

The advent of light-microscopy in the early nineteenth century led to the discovery that all animal and plant tissues are aggregates of individual cells. In 1838, this was formally established as the *cell doctrine* by Schleiden and Swann [Alberts *et al.*, 1994]. In 1863 Virchow [1863] observed that there was movement of cells in tumours examined *ex vivo* after surgery. However, the ability to examine living cell cultures was limited until the first design of a suitable microscope technique in the early 1930s. Prior to the development of quantitative systems, the movement of cells was assessed by observing cell activity. For example, cell migration was assessed qualitatively by counting the number of cells that moved across a line. Other techniques used microscopic chamber assays allowing cells to migrate through micro pores. These include the Boyden chamber assay [Boyden *et al.*, 1962] and migration of cells from microcarrier beads onto flat plastic surface [Rosen *et al.*, 1990]. However, no quantitative assessment about individual cell velocities and cell shape changes could be made.

Later, photography was used to take single snapshots over a period of time and to evaluate cell movement by tracing the outline of cells manually and estimating their position [Hämmerli and Sträuli, 1981]. However, manual segmentation is time-consuming and may be prone to error. In order to assess the movement of freely moving cells more accurately, computer assisted image processing methods were applied. A number of image processing systems and methods have been established to assess the movement of single, detached cells [Thurston *et al.*, 1986; Tatsuka *et al.*, 1989; Hoffmann-Wellenhof *et al.*, 1994; Soll *et al.*, 1995; Zicha and Dunn, 1995].

Some systems for single cell analysis are based on a spatial segmentation of individual cells in an image sequence. This often requires a uniform background around the cell using brightfield or phase-contrast microscopy from which the cell

can be easily detected and described. An outline of the cell is generated in each image of the sequence without using temporal information from the previous or next frame. The location of the cell is calculated from its centre of area (centroid) and this can be used to calculate cell velocity.

In the case of single, detached cells, the segmentation of cell images is usually performed using low-level image processing algorithms, e.g. thresholding, edge detection and region growing to separate the background from the cell body. Applying morphological operators subsequently connects fragments of the boundary and creates a binary image with the cell body highlighted or just an outline of the cell as demonstrated by Tatsuka *et al.* [1989].

In some cases, however, the exact boundary location of an individual cell may be difficult to reconstruct by simply linking together fragments of the boundary. The contour of a cell or any object may be described more generally by providing additional information about the location and shape. Such a segmentation technique was suggested by Kass *et al.* [1987] and is known as an active contour model or *snake*. An initial contour is placed around or inside an object of interest and the contour is guided by internal and external forces to find a close fit to the object's contour. Leymarie and Levine [1993] developed and applied such an active contour model to delineate and track the boundary of single cells. An initial boundary was placed manually on the outside of the cell and the mathematical contour converged towards the cell boundary using a gravitational model based on the potential surface of the gradient. However, the snake method required clear gradient features to fit the boundary of the solitary cell. Their system performed on well defined edges on single cells but did not catch expanding cellular regions very well. Also, the lack of interactive measures meant that falsely segmented regions could not be corrected.

Another approach is to investigate differences between consecutive images as an indicator for cell movement activity [Hoffmann-Wellenhof *et al.*, 1994], facilitating so-called temporal information. These differences can be used to relocate and redefine the cell in consecutive frames. For example, Siegert *et al.* [1994] proposed a novel imaging method based on optical flow analysis to assess the movement of

cells. The movement and direction of movement of each pixel was assessed; this enabled movement analysis of whole cell colonies without the need to segment and identify each cell individually. An overall velocity of the cell colony was calculated. However, there was no distinction made between individual cells, rather, the movement of the whole colony was analysed.

The movement of single cells has been studied extensively, however, only a few studies have attempted to assess the movement of clustered cells, for example Siegert *et al.* [1994] by using optical flow analysis. Cells usually appear in clusters and there is a suggestion that cell-to-cell interactions may have an effect on their motility. Stoker and Gherardi [1991] suggest that cell adhesion molecules may restrict movement in clustered cell populations. The quantitative analysis of cell motility for clustered cells may hence be of value in determining the effect of those cell-to-cell adhesions which may ultimately be useful in providing information about preventing cancer cells from detaching and spreading.

The assessment of cell movement of clustered cells is very difficult if not impossible for a fully automated image processing system. Figure 1.1 shows an example of a clustered cell colony of HT115 human colon cancer cells. In the case of a tightly clustered environment where cells are close together or some cells even overlap, deciding which boundary segment belongs to which cell would be difficult for an automated vision system. Cells are no longer solitary and surrounded by a uniform background which can be segmented unambiguously. “Classical” imaging techniques such as thresholding and edge detection are unlikely to be sufficient to segment and track cells within clusters.

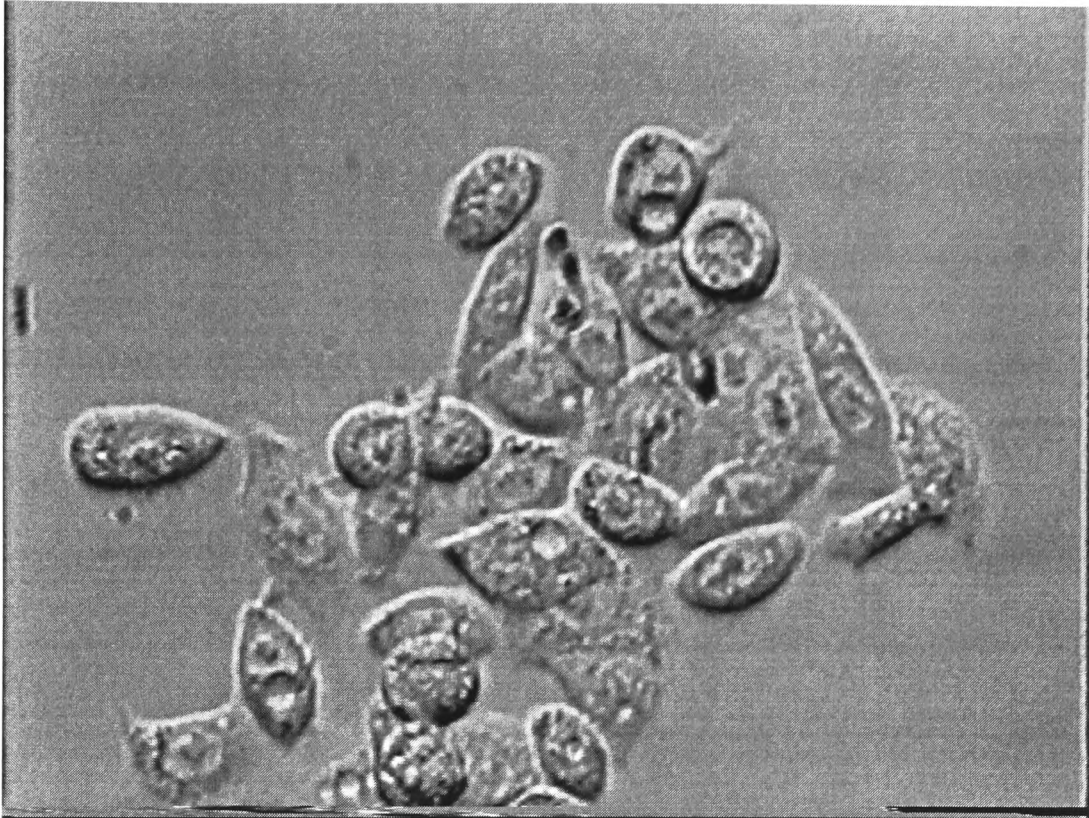


Figure 1.1: Example of a cluster of human colon cancer cells viewed by Hoffman modulation contrast microscopy at x320 magnification.

More importantly, since the segmentation is likely to be prone to error, the lack of user influence in this process makes it unsuitable for segmenting clustered cells.

The human observer considers many visual clues, e.g. intensity, gradient, uniformity, by which cells can be distinguished. Moreover, a human observer also applies his/her prior knowledge about cell structure and cell movement behaviour to facilitate the identification process. For example, an area of the cell boundary that changes rapidly between consecutive images may be identified as membrane ruffling. By linking spatial and temporal information together, a more accurate picture of moving cells in clusters may be generated.

Therefore, a method which could facilitate the segmentation and tracking of cells in clusters would be expected to have the following attributes:

- incorporates *a priori* knowledge about constraints of the cell boundary
- interactive for seamless user interaction, if necessary, to correct misinterpretation
- enables semi-automatic tracking of cells in consecutive frames
- using spatial and temporal information to guide image segmentation and tracking

## 1.2 Novel Cell Tracking Technique

A cell can be considered as a closed boundary (membrane) which can be described by a mathematical model of its boundary shape. A contour model suggested by Leymarie and Levine [1993] required clear gradient features to fit the boundary to a solitary cell. In a clustered environment, this is insufficient as cells can overlap or stick close together. To address these problems, a new adaptive spline model which forms the basis of a semi-automatic approach to cell tracking was developed. A deformable point model made of control vertices is combined with a cubic spline interpolation to render the cell boundary. In this technique, a cell is defined initially via an interactive boundary description facilitating *a priori* knowledge provided by an operator, placing only a few salient points on the cell boundary. The spline uses the information gathered from the initial placement to re-sample and relocate itself in consecutive images, hence allowing an interactive, dynamic tracking process. The

control points form an interactive interface between the user and the system. Spatial image information such as image gradient and temporal image information such as area matching form a deterministic spatio-temporal relocation process. In consecutive frames, the position of the spline boundary is used as an estimate and re-sampled and located accordingly. The devised system has enabled the analysis of attached cells in cancer cell colonies [Hoppe *et al.*, 1998a]. Also, the system was used to delineate the boundary of single neutrophils to enable the analysis of cell morphology and, in combination with ratio imaging, the measurement of localised intracellular chemical changes [Hoppe *et al.*, 2000a].

Cell motility is also of significance in inflammatory processes and during tissue regeneration. In wound healing, the repair process of tissue involves cell migration and proliferation [Zahm *et al.*, 1997]. Again, the effect of growth factors during *in vitro* wound healing have been studied [Schreier *et al.*, 1993]. However, studies at microscopic level may not be enough to study wound healing. Herbin *et al.* [1993] remarked that macroscopic assessment of wound healing may be more suitable for measuring healing kinetics and comparing new and traditional therapies. It has been suggested that changes of wound appearance, such as discolouration and the margin of the epithelium, may be useful in determining the healing progress in wounds [Cutting *et al.*, 1994]. For example, colour analysis using image processing has been used to describe and quantify the debridement and granulation in venous ulcers [Romanelli, 1997; Hoppe *et al.*, 2000b]. However, in order to compare digital images and their true colour representation and to produce consistent results, the question of colour consistency under clinical conditions has to be considered.

The author has investigated colour variations of images taken with a digital 3CCD camera under clinical conditions [Hoppe *et al.*, 1998c]. The Hue, Saturation and Intensity colour model was used which is considered to come close to a human interpretation of colour and provides a stable colour descriptor under varying lighting conditions [Gonzales and Woods, 1993]. However, it was concluded from this study that a colour reference is necessary in order to obtain reliable results for describing subtle changes in hue. If colour consistency between images cannot be obtained at a high degree, the appearance of the wound may also be assessed by comparing regions

within the wound itself. An intra-wound analysis method could therefore be more robust than an inter-wound analysis method. The adaptive spline method was adapted and applied to delineate the boundary of wounds. The spline contour was used to create a wound profile to help investigating the vicinity of the wound boundary [Hoppe *et al.*, 2000b].

In summary, the assessment of cell motility is thought to be important in understanding cancer metastasis. Several image processing methods have previously been developed to quantify and study the movement of single, detached cells. However, it is thought to be important to investigate the behaviour of single cells in clusters to enable studying treatments that effect cell-cell adhesions.

### **1.3 Aims and objectives**

The aim of this study was therefore to develop and apply a new method to facilitate the tracking of clustered and single cells. This method was thought to be of use also in segmenting wound images and assessing healing at the vicinity of the wound boundary and further work was aimed at this aspect. A number of objectives were therefore projected. They were

1. to review methods of assessment of cell motility

A number of computer-based systems were developed over the last fifteen years to monitor the movement of single cells. However, very few systems tried to address the problem of analysing cell movement in clusters. A literature review will be carried out describing current imaging methods of assessing cell motility. This includes the review of different light-microscopy techniques and appropriate image processing techniques to segment and track the movement of cells. The outcome of this review would be to identify possible techniques and avenues for segmentation and tracking clustered cells.

2. to develop an approach for segmenting cells in clusters

It is anticipated to develop a new method for segmenting cells in clusters. A fully

automated system identifying cells in a cluster automatically is considered unlikely to be successful and the proposed system will be of a semi-automatic nature with some degree of automation. The anticipated outcome of this work is to develop a semi-automatic segmentation technique which facilitates the description of cells in clusters. Furthermore, parameters to describe cell movement and behaviour will also be identified.

3. to combine the segmentation with a tracking mechanism

The intention is to combine the semi-automatic segmentation with a tracking mechanism to relocate the cell in consecutive images. A suitable tracking technique will be investigated and a new approach is developed which suits the problem of clustered cells. Cells are non-rigid objects expressing changes of shape and position simultaneously. Cell boundaries may also be weak in definition when membrane ruffling occurs or due to protrusion or retraction of cellular regions. The anticipated outcome is to enable the tracking of cells in clusters in combination with a semi-automatic segmentation and tracking technique. These will be incorporated into a newly developed software package for tracking cells.

4. to validate the new system

It is intended to validate the software against artificial and real images. A series of artificial test images will be created to validate measurement of size and position of objects. The system will then be applied to track single cells and cells in clusters. It is also intended to compare the performance of the system with a manual segmentation/tracking on real images. The outcome would be thorough analysis of the performance of the newly developed system.

5. to study the effect of HGF/SF motogen on Human Colon Cancer Cells *in vitro*

It is planned to study the effect of HGF/SF motogen on the movement behaviour of human colon cancer cells *in vitro*. With the new segmentation method it should be possible to assess the movement of cells within a cluster. This is especially useful in

order to quantify the 'scattering effect' of the motogen HGF/SF on cancer cells. Furthermore, it is anticipated to assess the effect of anti human E-cadherin antibody and motogen on the movement behaviour of human colon cancer cells.

6. to apply and extend the new method to ratio imaging for neutrophils

The system should be flexible enough to deal with other investigations in assessing morphological changes of cells. Furthermore, measuring intracellular chemical changes is considered to be important in understanding the mechanism of cell motility. It is intended to adapt the system to describe the morphology of expanding pseudopods in neutrophils while measuring the concentration of cytosolic free calcium. This may help to determine whether an inter-cellular chemical change can be associated with movement.

7. to apply the system to assess the appearance of ulcers in the vicinity of their wound boundaries

The system may further be used to delineate boundaries and to register image features of different types. It is envisaged to show its application to delineate the boundary of leg ulcers in order to assess the morphology of the boundary region. It is intended to create a means of describing the profile of boundaries based on colour.

8. to produce a comprehensive report and discussion on the results of the investigations.

#### **1.4 Contribution to original knowledge**

My original contribution to knowledge has been the development and application of a new semi-automatic, adaptive spline-based method to facilitate the assessment of cell motility in clustered cancer cells. Results were published in a full paper in Anticancer Research [Hoppe *et al.*,1998a]. The system was extended with a deterministic relocation algorithm based on image gradient which was applied to examine the

movement of cancer cells. A full paper was published in Medical & Biological Engineering & Computing [Hoppe *et al.*, 1999a]. The performance of the method was further enhanced by incorporating region matching techniques and a decision process with the spline. In a further development, the method was used together with ratio-imaging to measure changes in neutrophil cell morphology and intra-cellular chemical change [Hoppe *et al.*, 2000a].

On a macroscopic level, the colour distribution in wound images under clinical conditions has been investigated and the results of this study were presented at the European Tissue Repair Society meeting in Copenhagen and published in Wound Repair and Regeneration [Hoppe *et al.*, 1998b]. The adaptive spline method was used to semi-automatically segment wound boundaries in order to describe changes in the vicinity of the edge of leg ulcers [Hoppe *et al.*, 2000b].

The following list summarises key points of the method and results described in this thesis.

- Development of a new adaptive spline method to describe cell movement.  
The adaptive spline method is based on a geometrically deformable point model combined with a Hermite spline interpolation. Using a deterministic spatio-temporal relocation process for tracking cells, the system is capable to track clustered cells interactively.
- Using the above system we have been able to analyse the movement of clustered cancer cells and hence to compute cell area, cell velocity, relative movement (Centroid-Nucleus) and movement paths. As an indicator for cell shape the compactness or roundness was used. The method can also be applied to different types of cells, for example neutrophils.
- Analysis of movement behaviour of Human Colon Cancer cells (HT115) stimulated with HGF/SF.  
It was observed that the median cell velocity of stimulated HT115 cancer cells was greater than cells not treated with motogen. Median cell area variation was

greater with stimulated HT115 cancer cells than control cells. The movement path showed greater variation in stimulated cells in comparison with control cells. Some cells within a cluster did not seem to respond to the HGF/SF motogen.

- The method was combined with ratio-imaging to measure the concentration of cytosolic free calcium in neutrophils. Expanding and retracting pseudopods express greater changes in cytosolic free  $\text{Ca}^{2+}$  than the rest of the cell body.
- The method was also shown to be suitable for analysis of other medical and biological images, for example it has been adapted and applied to assess the appearance of leg ulcers. A system to capture wound images under clinical conditions has been developed and the analysis of the data collected showed the importance of using a colour patch chart for reference. The system was used to investigate the amount of slough in leg ulcers which was compared well with a clinicians assessment. An intra-wound analysis method based on the adaptive spline technique was used to generate a profile of the wound boundary edge which may be useful as a measure of wound appearance.

## 2 Review of Developments for the Assessment of Cell Movement in Light Microscopy and related Image Processing Techniques

### 2.0 Background

Cell motility is a wide ranging phenomenon describing biological processes, such as cytoplasmic streaming, and other forms of intracellular transport, as well as the movement behaviour of cells. Cell motility is studied at levels ranging from molecular and biochemical mechanisms to dynamic behaviour of single cells, whole tissues and organisms.

Cancer metastasis is a complex phenomenon that is thought to be based on the principle of motile cells [Schiffmann, 1990]. The motility of cancer cells is thought to be a principal cellular parameter, essentially required in the invasion and formation of distant metastasis in human cancer [Schiffmann, 1990, Jiang *et al.*, 1994a]. It involves primary proliferation of cells, their invasion through the basement membrane and extracellular matrix, which results in their appearance in the blood circulation system. It is followed by re-attachment and migration through the endothelial layer and finally the production of distant secondary tumours [Jiang *et al.*, 1994b]. Grimstad [1987] showed that cell locomotion contributes to the ability of cancer cells to invade new tissue.

Measures to stimulate or inhibit motility of cancer cells may play an important part in the understanding of metastasis biology in cancer. Special interest has been paid to the effect of factors which stimulate or inhibit motility. Stoker and Gheradi [1991] introduced a new term 'motogen' which describes any factors that promote cell motility. For example, cytokines can literally be described as 'cell movers' [Stoker and Gheradi, 1991]. HGF/SF<sup>1</sup>, a cytokine, is thought to be a trigger for cell spreading

---

<sup>1</sup> HGF/SF: Hepatocyte growth factor/scatter factor

[Rosen *et al.*, 1990, Bhargava *et al.*, 1993, Jiang *et al.*, 1997]. Thus the ability to quantify movement and spreading of cancer cells may be important for assessing the efficacy of new treatment strategies.

In immunology, the motility of neutrophils is crucial for combating infection within the body. Neutrophils move from the blood stream to a site of infection where they engulf (phagocytose) and kill the infecting micro-organism. These cells are capable of rapid and specific changes in cell shape. Immunological abnormalities such as the Chediak-Higashi syndrome may be detected by analysing the movement behaviour of neutrophils [Korzynska *et al.*, 1998]. However, it is as yet not fully understood which intracellular processes cause the cell to move. Several lines of evidence suggest that changes in calcium concentration may play a role in this response [Pettit and Hallett, 1998]. Despite the importance of this cellular activity, it has been surprisingly difficult to establish a link between an intracellular chemical change within a cell and an accompanying localised cell shape change. For example, the expansion of a cellular region in neutrophils is thought to be triggered by a sudden change in cytosolic free calcium [Pettit and Hallett, 1998]. A system for assessing localised cell shape changes and intracellular changes would be of great help to further observe this assumption.

Several systems and techniques have been developed to assess the movement of cells and this review is concerned with describing the principles and common techniques using digital image processing. Computer systems to study motility of cells typically comprise a microscope system fitted with a Charged-Coupled Device (CCD) camera connected to a computer or video system. Images are either recorded on a time-lapse video system or digitised directly with a computer equipped with an image capture board. The following Figure 2.1 visualises a typical system to study cell movement.

Typical systems found in the literature are operated such that data are analysed retrospectively. Hence, the first step involves image acquisition and storage, the second step concerns image segmentation and image interpretation while the final step is used to analyse and interpret the acquired data. In contrast, Thurston *et al.* [1986] introduced a system based on a moving microscope stage that enabled the

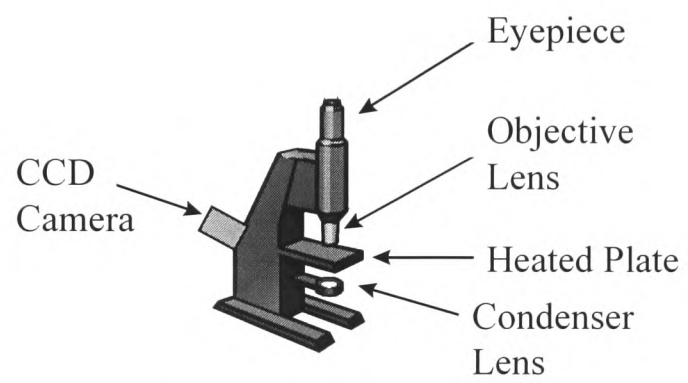


Figure 2.1: Configuration of a microscope system to acquire live cell images

movement analysis of single cells in real time. The authors system would be based on retrospective analysis of video images.

Tracking of cells expands the image segmentation approach into the time domain. Segmentation of video images may be considered separately or an inter-frame approach, such as differences between frames, may be used as the basis for tracking and relocating objects.

This literature review includes light microscopy systems and common image processing techniques and their application to segment cell images and facilitate the tracking of cells. The following aspects were reviewed:

- *Principles of light microscopy and image acquisition.* This part focused on techniques in light microscopy; it included bright-field, phase-contrast, differential interference contrast, Hoffman modulation contrast and finally phase-shifting interference contrast microscopy. It was anticipated to get an understanding of light microscopy and suitable techniques for studying living cells (Section 2.1).
- *Image segmentation techniques* were discussed and examples given when used in specific systems for segmenting cell images. The success of image segmentation may be increased by facilitating prior information about the objects to be segmented. Therefore, attention was paid to model based segmentation approaches using *a priori* knowledge, such as Active Contour Models and Geometrically Deformable Models (GDMs). It was anticipated to explore possible segmentation techniques which may form the basis for a new segmentation technique for cells in clusters (Section 2.2 and 2.3).
- *Tracking techniques* were reviewed and different types of motion were discussed in respect to cell movement. The principles of motion in digital imaging were described. This was to explore possible techniques which, in combination with a new segmentation technique, may facilitate the tracking of clustered cells (Section 2.4).

- *Parameters to describe cell movement* and cell shape were identified. Once cells were segmented, suitable parameters to describe their movement behaviour need to be identified. It was intended to describe the most common descriptors of cell motility (Section 2.5).
- *Image processing systems* to study cell motility were described. Two research systems which are used to assess the movement of cells were described (Section 2.6).
- The last part of the literature survey summarises previous methods and possible new avenues to explore are discussed (Section 2.7).

## 2.1 Image Acquisition in the study of living Cells in Light Microscopy

Optical Systems are the key to the discovery of the cell structure and cell behaviour. However, cells are typically 10µm to 20µm in diameter, and thus invisible to the naked eye. The development of light microscope technology in 1674 by van Leeuwenhoek provided a technological breakthrough for studying small specimen. This led to the discovery of cellular composition by Schleiden and Schwann in 1838. However, it was not until the second half of the nineteenth century that the internal structure of cells could be examined [Alberts *et al.*, 1994].

The process from the microscope cell image to the digital image requires several stages of conversions which have an effect on the quality and appearance of the acquired image. The microscope configuration, video camera and digitising equipment determine the formation process of digital images. For example, in brightfield microscope setup, contrast is generated by differences in light absorption in cells. In phase-contrast microscopy, phase shifts due to the different refractive index of areas within the cell are translated into image intensity. It is also important to consider artefacts introduced by different microscopy techniques, e.g. a halo around cells in phase-contrast or gradient directionality in Hoffman modulation contrast.

### 2.1.1 Image Acquisition

In order to obtain a digital image from a microscope, a video camera is mounted on the optical axis of the microscope. Video cameras incorporate a CCD array and may be divided into two groups [Van Vliet *et al.*, 1998]:

- Video Rate Cameras
- Integrating Digital Cameras (scientific cameras)

Both types consist of an array of photosensitive elements (CCD) but differ in the mode of operation. The spatial resolution of a scientific CCD camera equals that of its photosensitive array. The photoelectrons are accumulated over a specific time interval (integration time) at each pixel and during the readout period a shutter blocks

new photons from reaching the array (black-out period). The electrical potential at each pixel is digitised by an analogue to digital (A/D) converter, usually with 12 bit resolution, and thus the full image is available in digital format.

In contrast, video rate cameras do not allow for a black-out periods but rather enable a simultaneous integration and readout time. After integration, the potential in each pixel is transferred to a non-photosensitive pixel which is read out during the next integration cycle. Integration time is determined by the video format (20ms for PAL<sup>2</sup>) and the potential along a line of pixels is converted into a video signal.

Video cameras enable convenient storage of image data using a standard video recording system and subsequent digitisation with an image frame grabber board. Furthermore, a time-lapse video system enables storage of long recordings, such as overnight recordings. However, since there is no longer a one-to-one relationship between CCD pixel and image pixel, the digitised video image is subject to artefacts and hence the quality is inferior to that of a scientific CCD camera. The choice of camera system depends on the purpose of the analysis. Long recording cell behaviour studies result in an enormous amount of digital data and may therefore be better stored on conventional video recording equipment. The advent of optical storage disks, such as CD-RW and DVD-RAM will undoubtedly lead to more digital recording.

### 2.1.2 Light Microscopy

The visibility of details in cellular structure depends on availability of enough contrast. However, the light absorbance of cells is not enough to create sufficient contrast which led to the development of techniques that take advantage of phase shifts and interference between light rays [Wilkinson, 1998]. In its most basic configuration, a light microscope consists of a condenser lens and an objective lens. A beam of light rays is focused onto each point of the specimen by the condenser lens. The objective lens collects these light rays and constructs an image which is

---

<sup>2</sup> Video standard in the United Kingdom and central Europe

visible through the eyepiece or projected onto a CCD array. This principle is illustrated in the Figure 2.2.

In this configuration, contrast is achieved by differences in light absorbance of different cellular regions and between the cell and its surrounding background. The light rays that are focused onto each point of the specimen are of the same amplitude and phase. The specimen has the ability to modify light such that it changes the amplitude by absorbing light and phase shifts are caused by different refractive indices. Bright field illumination is the most common form of illumination in microscopes, and its components are illustrated in Figure 2.2. The image intensity is a function of the light absorption of objects within the bright field. Hence, these are called *amplitude objects*, i.e. objects which change the amplitude of light rays passing through them [Wilkinson, 1998]. The image intensity  $I(x,y)$  is a function of light extinction coefficient  $\varepsilon$  at each point  $(x,y,z)$  as described by Wilkinson *et al.*, [1998].

$$I(x,y) = I_0 e^{-\tau(x,y)} \text{ with } \tau(x,y) = \int_0^{\tau_{\max}} \varepsilon(x,y,z) dz \quad (2.0)$$

The resolution of a light microscope is limited to the wavelength of visible light - 400nm (violet) to 800nm (red) [Alberts *et al.*, 1994]. However, due to interference between light waves the possible resolution is further decreased. These optical diffraction effects limit the resolution which also depends on the numerical aperture (NA) of the lens system. For example, a small point will be displayed as a circular spot, hence two points close to each other can be blurred into one. The resolution limit  $r_0$  is expressed by the *Rayleigh criterion*

$$r_0 = \frac{0.61\lambda}{NA} \quad (2.1)$$

where  $\lambda$  is the wavelength of light and NA the numerical aperture (NA < 1 in air, NA < 1.3 in water) [Wilkinson, 1998]. The resolution achieved in light microscopy is 0.2  $\mu\text{m}$  with a wavelength of 400nm [Brocksch, 1994].

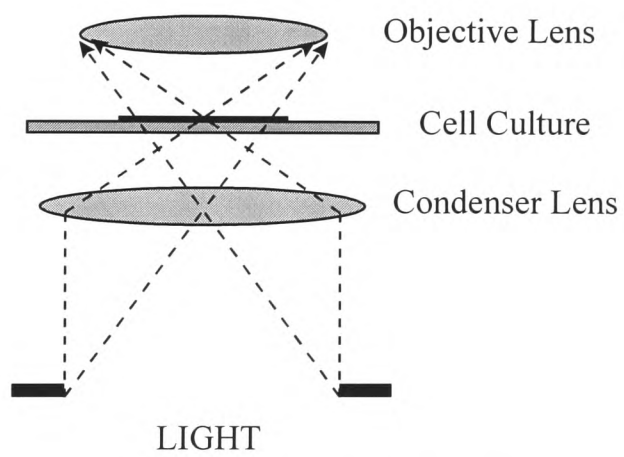


Figure 2.2: Principal components of a bright-field microscope.

However, there is little in the contents of cells (which are 70% water by weight) to impede the passage of light rays and thus they are almost invisible through an ordinary light microscope [Alberts *et al.*, 1994]. One possibility is to increase the light extinction coefficient by staining cells with a coloured dye to make cells visible. Another approach is exploit the phase shifts caused by different refractive indices. Both techniques are described in the next two sections.

### 2.1.3 Fluorescence Microscopy

In fluorescent microscopy, fluorescent molecules are bound to antibody molecules which move and attach to particular regions within the cell. These molecules absorb light at one wavelength and emit it at a longer wavelength [Alberts *et al.*, 1994]. This enables, for instance, the targeting of a specific area within the cell body. If a fluorescent molecule is illuminated and then viewed through a filter that allows only light of the emitted wavelength to pass through, only the fluorescent molecules are clearly visible. These images are then easy to segment. A cell can be stained with different fluorescent molecules allowing several regions to be stained differently at the same time. Furthermore, fluorescent molecules can be used as tags or indicators of proteins and or small ions, such as  $\text{Ca}^{2+}$  or  $\text{H}^+$  [Whitaker, 1994]. This is an important technique since the intracellular ionic composition is thought to be related to cellular activity [Slavik, 1998].

A disadvantage of many traditional dyes for fluorescent microscopy is that they can be toxic to cells at useful concentrations [Wilkinson, 1998]. Studying living cells requires a very low concentration of dyes since they may have an effect on the life cycle and behaviour of cells. This may be overcome by using image intensifiers to enhance the brightness of low concentration dyes.

Although fluorescently labelled antibodies have been used for locating proteins in living cells, they are usually used with dead cells. Measuring the changing concentrations of ions in living cells, however, is important in understanding the biochemical processes and cellular activity [Slavik, 1998]. Ratio-imaging can be used to obtain quantitative information about the concentrations of ions, for instance  $\text{Ca}^{2+}$

using lower concentrations of sensing agents. Taking the ratio of two images at two different wavelengths (ratio-imaging) produces the data to calculate the ion concentration [Slavik, 1998]. For example, ratio-imaging has been used to measure the concentration of free  $\text{Ca}^{2+}$  in living cells [Hallett *et al.*, 1996].

#### 2.1.4 Phase-Contrast and Interference Contrast Microscopy

The cellular structure can only be partially made visible through staining. In order to view unstained, living cells the phase-contrast microscopy technique was developed by Zernicke in 1932 [Alberts *et al.*, 1994]. In phase-contrast, changes in phase delays between light rays are translated into differences in image intensity. The phase of the light passing through a cell is changed according to the cell's refractive index [Alberts *et al.*, 1994]. Phase-contrast greatly increases the apparent contrast between cell organelles as small phase differences can be made visible by exploiting interference effects. For instance, the light passing through a thick part of the cell, such as the nucleus, is more deflected and diffracted than the phase of light that passes through the thinner region next to it. An annular phase plate is mounted above the objective lens (see Figure 2.2) which attenuates and advances the phase of the undeflected light rays by 90 degrees [Brocksch, 1994]. The diffracted (and deflected) light is now approximately 180 degrees out of phase and due to interference, reduce each other significantly, leading to darker areas. Thus, the thicker nucleus appears darker than the thinner surrounding cellular region. The following image in Figure 2.3 shows a single cell viewed by phase-contrast microscopy.

To further enhance contrast from phase delays, Normanski [1955] developed a differential interference contrast (DIC) method using polarised light. The light wave is split up into parallel rays at right angles to each other. These are then displaced in the order of micrometers above the resolution limit of the microscope. These two light rays enter the specimen in phase and become out of phase if passing through an area with different refractive indices. Finally, the displacement between the two rays is compensated and both rays are recombined passing through a second polariser, the so called analyser [Brocksch, 1994]. Since the light wave is no longer polarised but

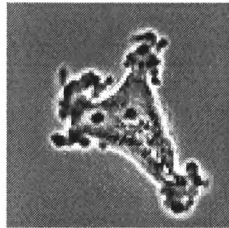


Figure 2.3: Example of a single cell viewed through a phase-contrast microscope

its constituent parts are out of phase, interference causes its amplitude (and hence brightness) to alter according to the phase difference.

Phase contrast and DIC rely on the interference between light waves, which may lead to interference fringes and halos around objects [Wilkinson, 1998]. DIC has extended resolution and contrast of previous light microscopy techniques and thus allows cell structure to be highly resolved [Foskett, 1993]. In order to avoid some of the artefacts introduced by interference, Hoffman [1977] created a system whereby phase gradients are transformed into intensity changes without relying solely on the interference principle.

### 2.1.5 Hoffman Modulation Contrast Microscopy

The Hoffman modulation contrast (HMC) principle was designed by Hoffman in 1975. The modulation contrast microscope enables unstained, living cells to be viewed with high contrast [Hoffman, 1977]. This system exploits phase gradients rather than phase differences between light waves and converts them into intensity changes. A specimen with varying thickness also expresses continuously changing optical gradients. Different gradients cause different angles of light refraction. Light from the specimen is passed onto a modulator, which can be described as a graded filter. Refracted light passes through the modulator at a different location and is thus transformed into different intensities [Wilkinson, 1998]. The image intensity of opposite gradients are opposite, hence one gradient is dark while the opposite gradient is bright in the image. This leads to a three-dimensional appearance of the cells within the image. In fact, as light intensities vary above and below an average value - the light is said to be modulated, hence the term modulation contrast [Hoffman, 1977]. The following Figure 2.4 shows a single cell viewed by Hoffman Modulation contrast microscopy. The opposite gradients at the edge of the cell image are clearly visible.

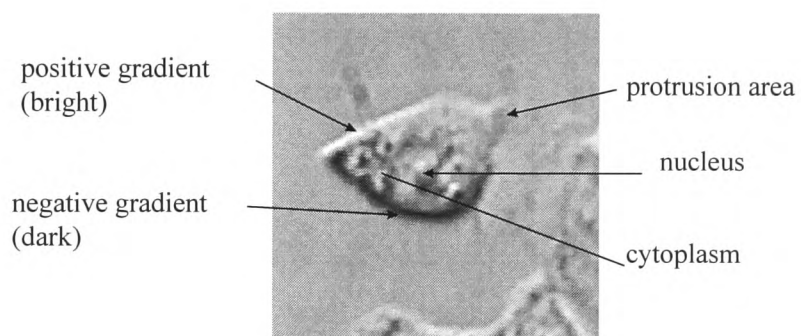


Figure 2.4: Directional optical gradients in Hoffman Modulation Contrast demonstrated on a single human colon cancer cell.

DIC and HMC use relative differences in phase shifts and optical gradients to translate into image intensity. Although structural features are expressed well in both DIC and HMC, there is no linear relationship between the optical gradient and density of the specimen. One way of achieving this has been demonstrated by Bereiter-Hahn [1985] using a phase shifted interference technique.

### 2.1.6 Phase Shifting Interference Microscopy

The phase shifted interference principle (PSI) [Bereiter-Hahn, 1985] makes use of the interference between phase delays of two separate light beams. Dunn and Zicha [1995] developed an image processing system which allows the phase difference to be accurately related to the distribution of dry mass inside cells (DRIMPAS system - digitally recorded interference microscopy with automatic phase-shifting). In their microscope configuration (Horn microscope), one light beam passes through the specimen while the second beam passes through a dummy chamber. This was combined with a computer system to calculate the true phase difference by solving a set of interference equations and thus the accurate density of dry mass in cells. Moreover, the system can also be adjusted such that cellular regions are brighter than the surrounding background, hence the segmentation process is less complex. Unfortunately, the Horn microscope is no longer available but work is under way to construct a new, less expensive version of the double-beam Horn microscope with integrated digital image processing functions to allow the accurate calculation of dry mass distribution [Dunn, 1998].

### Summary

Light microscopy enables the study of cell structures but it was not until the development of the phase-contrast microscope that detailed studies of living cells and their behaviour was made possible. The fact that light rays passing through a specimen are delayed led to the development of microscopy techniques based on exploiting phase changes rather than differences in light absorption. Techniques such as phase-contrast, DIC and HMC greatly improve the contrast between cellular

structure and background and enable the study of cell morphology. Fluorescent techniques and ratio imaging are primarily used to study intracellular biochemical changes.

There is a trend to combine these two avenues to study intracellular functionality in combination with changes in cell morphology. For example, Foskett [1993] described a system which enabled simultaneous DIC imaging with quantitative fluorescence imaging.

Any technique to distinguish cells within a cluster relies on enough contrast between cellular structures. The author intends to use Hoffman modulation contrast microscopy due to the enhanced bright and dark regions at the boundary of cells. Opposite gradients at the cell boundary may help to separate touching cells or even overlapping cells.

## 2.2 Image Segmentation Techniques for Cell Imaging

Image segmentation in the context of cell imaging is concerned with the description of cells in microscope cell images. Tracking movement adds a further dimension to the segmentation. In the next two sections (section 2.2 and 2.3), techniques for segmenting static images are reviewed while in section 2.5 motion and tracking techniques are described.

Image segmentation is a process in which regions or features sharing similar characteristics are identified and grouped together. For example, a uniform background may be distinguishable from a non-uniform cell body. Image segmentation may use thresholding, edge detection, region detection, texture descriptors or any combination of these techniques. The segmentation is followed by an image interpretation, whereby the extracted features from the segmentation process are combined to describe real-world objects. For example, boundaries from an edge-detection process may be linked to form a closed boundary describing the outline of a cell body. The image interpretation applies high-level knowledge about the object to describe an image or objects appearing in an image. However, this high-level knowledge may also be applied during the segmentation stage which may enhance the success of the segmentation and thus the overall image interpretation.

Medical images may thus be segmented in two different approaches.

- a) Low-level features such as uniform regions or discontinuities are extracted and grouped together. High-level knowledge is then applied to use these features to form a meaningful interpretation of the image, for example, to identify cells. Image segmentation may use thresholding, edge detection, region detection, or any combination of these techniques (Section 2.3).
- b) In a second approach *a priori* high-level knowledge about objects to be identified is used to guide the segmentation process. This so-called *model-based* approach depends on a shape model that contains information about the expected objects in

the image, such as anatomical structure. Such information may be used to decide, for example, whether an edge is part of a structure or artefact (Section 2.4).

### 2.2.1 Region-based Segmentation in Digital Cell Imaging

All segmentation techniques are concerned with being able to distinguish the cell body from the surrounding background. A simple question has to be asked: ‘Does a particular pixel belong to the cell body?’ The result of the region-based segmentation process should lead to a description of the cell by its body mass. Region-based segmentation methods attempt to partition or group regions according to common image properties. These image properties may consist of

- Intensity values
- Textures or patterns that are unique to each type of region
- Spectral profiles in the frequency domain.

Thresholding is the simplest way to perform segmentation, and it is used extensively in many image processing applications. In its simplest form, threshold selection is done on a pixel by pixel basis, by comparing the grey level of each pixel  $f(x, y)$  with some predetermined value  $T$ . If the grey level is below the threshold, the pixel  $f(x, y)$  is assigned ‘1’, otherwise ‘0’, hence creating a binary image. A number of sophisticated thresholding techniques have been introduced which automatically define an optimal threshold value  $T$  or even multiple threshold values  $T_1..T_n$ . Threshold values may even differ within regions of an image creating a dynamic, regional based thresholding algorithm [Lee *et al.* 1990, Sahoo *et al.* 1988]. The following Figure 2.5 shows a single human colon cancer cell viewed by Hoffman modulation contrast microscopy. Two global thresholds have been applied at  $\pm 5\%$  of median intensity, filtering out the non-modulated background in HMC.

Thresholding is often used when sufficient contrast between the cell body and background is present. Thurston *et al.* [1986] developed an automated microscope system to measure motility of single cells based on a global thresholding principle in brightfield microscopy. Tatsuka *et al.* [1989] created an image processing system

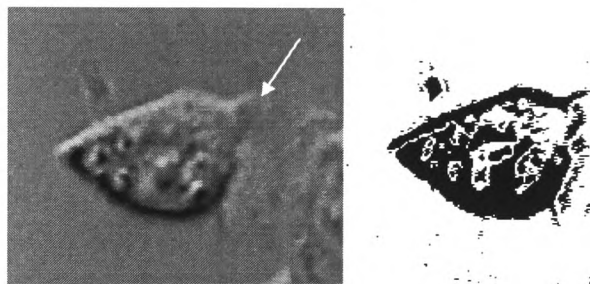


Figure 2.5: Example of global thresholding using two global thresholds at  $\pm 5\%$  of median intensity. Left image shows a single human colon cancer cell (HT115) and the right image the area above and below the two thresholds. Pseudopod marked by white arrow.

which used an adaptive thresholding algorithm for detecting cell outlines in phase-contrast microscopy. It is assumed that the cell is distinguishable from the background by its intensity values. However, as seen in Figure 2.5, pixel values close the background intensities can occur in protruding or retracting areas (Pseudopods). These problems are caused by non-homogeneous optical properties of the cell [Gauthier *et al.*, 1997]. Phase shifted interference microscopy has been shown to create an image whereby cell images have different intensity values to the background [Brown and Dunn, 1989, Zicha and Dunn 1995]. However, it is important to note that such global region-based segmentation techniques are sensitive to a non-uniform lighting distribution and any distortion must be corrected.

Regions may also be identified through structure and appearance. In this context, the analysis of texture may be used as a means of differentiating regions. One common definition for texture is that it is composed of basic patterns that are repeated in a periodic manner [Wechsler, 1980]. This is most applicable in describing deterministic types of texture, such as in tiling. These basic patterns, or textons, are homogenous with respect to defined rules [Julesz, 1981]. Other types of texture are more random (stochastic) in nature, having no basic pattern or dominant repetition frequency present. Yet, there may be a relationship between pixels in a region that is detectable by the human vision system. The probabilities of occurrences of pixel combinations has been shown to be important in the human analysis of texture [Pratt *et al.*, 1978]. Texture has been used extensively to segment macroscopic images for example in aerial surveillance. On the microscopic level, texture values can be re-mapped to intensity values and previously described image segmentation methods may be used for further analysis. Korzynska *et al.*, [1998] used texture to segment neutrophil images. However, working with texture implies the loss of resolution since texture is described as a function of its neighbourhood. Thus resolution is compromised and the visualisation of small structures may be eliminated.

### 2.2.2 Edge based Segmentation

Edge based segmentation methods are often used to look for explicit or implicit boundaries between regions. A cell, or indeed any object, can also be described by its boundary rather than the mass of its body. Segmentation methods on the basis of edge detection are very common. In fact, the human vision system is thought to recognise shapes in an image mostly by discontinuities, such as boundaries and peaks [Hubel and Wiesel, 1977].

The image gradient can be computed by simply applying the gradient operator to the entire image function  $f(x,y)$ . The two-dimensional gradient-operator  $\nabla f$  is generally defined as [Gonzales and Woods, 1993],

$$\nabla f = \begin{bmatrix} \frac{\partial f}{\partial x} \\ \frac{\partial f}{\partial y} \end{bmatrix}. \quad (2.2)$$

The gradient is represented by a vector with a direction and magnitude. The direction of the gradient may be useful in estimating the orthogonal vector of a boundary. In general, the magnitude of the gradient vector is what is usually referred to as the gradient. The magnitude of the gradient requires the partial derivatives  $\partial f / \partial x$  and  $\partial f / \partial y$  of each pixel to be calculated which in its explicit form is quite time-consuming. Several discrete approximations have been developed based on spatial operator masks, for example Robinson [1965], Prewitt [1970] and Sobel [Gonzales and Woods, 1993].

The exact location of an edge can be calculated with the second-order derivative of the image function [Gonzales and Woods, 1993]. The zero crossings indicate the crossover between a rising and a falling part of an edge. A common technique for this operation is the magnitude of the two-dimensional Laplacian function applied to the image. However, the second order derivative is unacceptably sensitive to noise and Marr and Hildreth [1980] combined the Laplacian operator with Gaussian smoothing

to overcome the problem. The so-called *Laplacian-of-Gaussian* (LoG)  $\nabla^2 G$  filter is based on the second derivative of the Gaussian function  $G(x, y, \sigma)$

$$\nabla^2 G = G_{xx} + G_{yy} \quad \text{and} \quad G(x, y, \sigma) = \frac{1}{2\pi\sigma^2} \cdot e^{-\frac{x^2+y^2}{2\sigma^2}} \quad (2.3)$$

with

$$G_{xx}(x, y) = \frac{\partial^2 G(x, y)}{\partial^2 x} \quad \text{and} \quad G_{yy}(x, y) = \frac{\partial^2 G(x, y)}{\partial^2 y} \quad (2.4)$$

Figure 2.6 shows a human red blood cell viewed by brightfield microscopy and applied with a 3x3 Prewitt as well as 3x3 Laplacian of Gaussian spatial operator mask.

The image of a red blood cell in Figure 2.6a shows a strong inner gradient and a weaker outer gradient of the boundary. These double edges occur at the rising and falling edge by using the first derivative. As mentioned earlier, the second derivative may be used for edge location and image 2.6c shows the same blood cell segmented with second derivative filter LoG operator. In the case of a simple structure like the blood cell, the boundary may be located easily. However, in more complex cellular structures, the boundary is often fragmented due to expanding regions as can be seen in Figure 2.7. In the right hand image, the boundary is visible as well as inner cellular structures such as the nucleus. The gradient may enable the detection of boundaries. Interpreting and forming a closed curvature from such images, however, is a more complex task.

Due to the limitations of brightfield technology some regions of the cell may have poor contrast and thus express no gradient at the boundary. However, modulation interference microscopy emphasises ‘optical gradient’ as shown in figure 2.7b. Soll *et al.* [1995] concludes that although gradient methods appear to be the most versatile approach, they also generate more complex images since gradient methods find all edges, including those inside the cell perimeter. Additional methods such as edge linking, thresholding and binary morphology may be necessary to obtain a cell

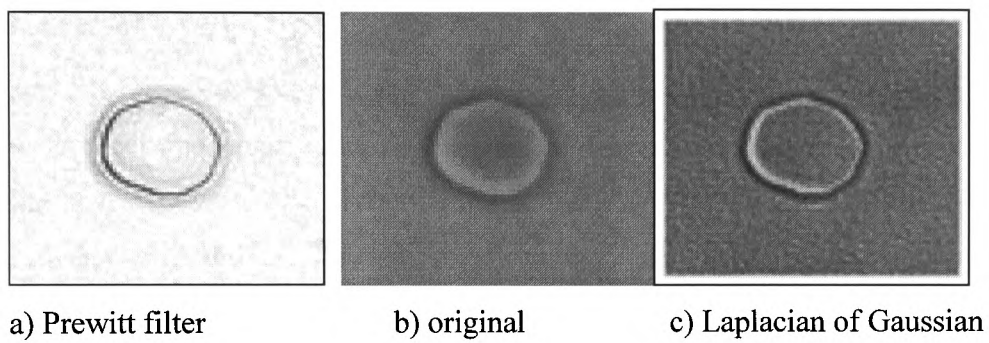


Figure 2.6: Double edge in picture a , while dark boundary represents the zero-crossing and hence the location of the edge of the blood cell in c.

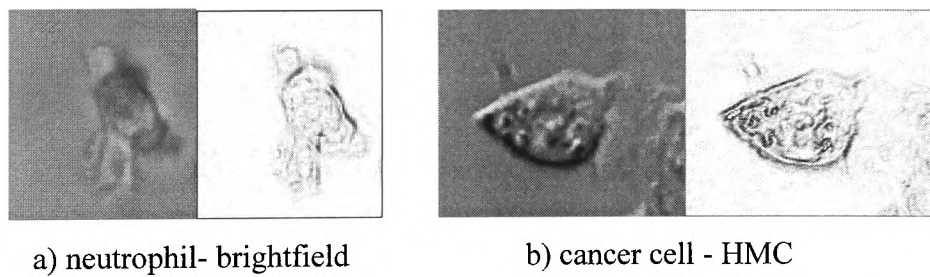


Figure 2.7: Gradient (first derivative) of neutrophil (a) and HT115 cancer cell (b) using a 3x3 Prewitt operator.

outline. Soll *et al.* [1995] describes the principal application of binary morphology for gap-filling in a fragmented boundary. Tatsuka *et al.* [1989] used a combination of dynamic thresholding, gap-filling and edge detection to generate the outline of single cells viewed by phase-contrast. However, this technique does not use information about the object to be segmented and may hence produce unreliable results.

An advantage of edge detection over thresholding is that it depends on local differences and hence is mostly independent from global effects such as non-uniform lighting. As with many systems, a combination of different methods can yield a satisfactory solution. For example, Kittler *et al.* [1985] proposed an automatic threshold algorithm based on intensity and gradient information.

Thresholding may only be used when dealing with single, detached cells. Since cells with the same optical properties cannot be distinguishable when attached. Clustered cells may be distinguishable by the orientation of their gradient. However, it is difficult to determine which fragment of the boundary belongs to which cell without any *a priori* knowledge. Moreover, the cell membrane may not always be homogeneous and noise as well as intracellular organelles may lead to misinterpretations.

## 2.3 Model based approaches in Image Segmentation

The shape of an object is commonly described by its outline, hence the detection of the cell contour is of great importance. It is possible to describe a contour with a mathematical model. Parameters of that model are determined by *a priori* knowledge, such as anatomical features, and from imaging features detected by low-level techniques. These so-called 'Active Contour Models' are flexible descriptions of contours which can be manipulated to fit an image contour. One of the first models used for describing contours is the 'Snake' devised by Kass *et al.* [1987]. Active contour models are popular in segmenting and tracking anatomical structures because of the availability of *a priori* knowledge of these structures and their spatial relationship. Many techniques have been developed such as Active Contour Models

(*Snakes*) [Kass *et al.*, 1987], Geometrically Deformable Models (*GDMs*) [Miller, 1990], and Active Shape Models [Cootes *et al.*, 1992]. Some of these techniques have been adapted to tracking objects. Recently, Peterfreund [1999] developed a *Snake* for tracking non-rigid objects which is based on motion estimation.

Contour models describe a boundary with a mathematically defined curvature  $Q$  as a function of its arc length  $u$ . In the case of a two-dimensional space the curvature is formed parametrically as

$$Q(u) = (X(u), Y(u)) \quad (2.5)$$

Since the shape of boundaries is usually a complex formation it is unlikely that a single function would satisfy the description. A boundary is therefore split up into several segments, each between two control points. The continuous representation of a curvature is approximated with a finite number of points. Kass *et al.* [1987] used finite differences to approximate the curvature. Another very common choice is to use higher order polynomials which reduce the number of control points needed, and forming a *piecewise polynomial* curvature as shown in Figure 2.8. This contour representation can be combined with low-level image processing techniques to form an active model that attracts the contour towards edges and peaks. In this review the original idea of an active contour by Kass is described while references to further developments are made.

### 2.3.1 Active Contours

Kass *et al.* [1987] proposed the concept of an energy minimising spline guided by external constraint forces and influenced by image forces (*Snakes*). Each force generates energy which has an influence of the total energy  $E_{\text{total}}$  of the spline. *Snakes* are active because they actively alter their shape and position while seeking an optimal position based on energy minimisation. A two-dimensional dynamic contour called  $v$  can be defined in terms of its  $x$  and  $y$  coordinates, which in turn are parameterised by the linear parameter  $s$ , and the time parameter  $t$ ,

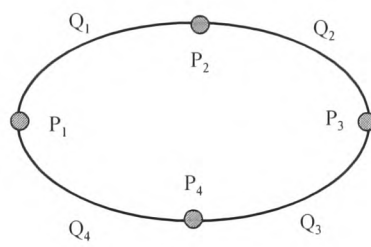


Figure 2.8: A closed curvature made of four segments.

$$v(s, t) = (x(s, t), y(s, t)). \quad (2.6)$$

The parameter  $s \in [0...1]$  and parameter  $t \in [0...∞]$ . Each time step would bring the snake closer to an energy minimum until an equilibrium of all forces is reached. Kass defined that the total energy of his model was made of three energy terms.

$$E_{total} = \int_Q [E_{internal} + E_{image} + E_{external}] \quad (2.7)$$

The internal energy  $E_{internal}$  describes the bending and stretching of the curvature.  $E_{image}$  is the image energy and depends on the image intensity and gradient values along the path of the contour.  $E_{external}$  is created by artificial energy fields imposed by the user or other high-level features. Other energy terms have been proposed, such as optical flow for the velocity snake [Peterfreund, 1999].

The internal energy is defined as

$$E_{internal} = \frac{1}{2} \alpha \left| \frac{\partial v}{\partial s} \right|^2 + \frac{1}{2} \beta \left| \frac{\partial^2 v}{\partial s^2} \right|^2, \quad (2.8)$$

where  $\alpha$  controls the amount of stretching of the snake and  $\beta$  controls the amount of bending along the boundary. Large values of  $\alpha$  will increase the internal energy of the snake as it stretches more, whereas small values of  $\alpha$  will make the total energy less sensitive to the amount of stretching. Similarly, large values of  $\beta$  will increase the internal energy of the snake as it develops more curves and vice versa.

The image energy of the snake is defined as

$$E_{image} = \omega_1 f(x, y) + \omega_2 \left| \nabla f(x, y) \right|^2. \quad (2.9)$$

Large values of  $\omega_1$  make the snake align itself with bright regions in the image. Similarly, large values of  $\omega_2$  tend to make the snake align itself with large image

gradients in the image whereas large negative values of  $\omega_2$  make the snake avoid these gradients. Small absolute values of  $\omega_2$  make the snake indifferent to edges in the image. Kass also introduced a line energy term which uses the Laplacian of Gaussian to align the snake to zero-crossings in the image.

The external energy is defined as a negative energy field where spline points cannot move. So-called spring forces were introduced which pushed snake points towards a location while volcano forces push points away from a location. Springs and volcanoes provide indirect user interference to guide the snake indirectly to a correct position if necessary.

The minimisation of the energy function yields an optimal solution for the position of each snake point on the contour in respect to internal forces, image forces and external forces. Kass used variational calculus to find the minimum of the snake energy. First and second order derivatives are approximated by finite differences and at each time step the position of control points is changed in that direction which yields a lower energy. However, the calculated solution may only express a local minimum of the global energy solution and thus not the correct boundary location. Therefore, other techniques to enhance the minimisation process have been proposed.

Amini *et al.* [1990] suggested the use of dynamic programming for the optimisation of the discrete sum of independent energy terms. Another discrete optimisation technique has been proposed by Williams and Shah [1992]. Their so-called *greedy* optimisation examines the neighbourhood of each control point and searches for a energy minimum locally.

Quite often contour models are used for both segmentation and tracking of structures simultaneously. After initial placement, the snake searches for an energy minimum in the first frame and uses the found position as an initialisation for the next frame. Applications for snakes include the segmentation and tracking of echocardiographic sequences by Mikic *et al.* [1993] and tracking the aorta in 2D Magnetic Resonance (MR) images [Rueckert *et al.*, 1997].

On a microscopic level, Leymarie and Levine [1993] adapted and further developed an active contour model to track single, detached cells in brightfield microscopy. The snake is attracted to the gradient of the boundary at different scales. This coarse to fine fitting facilitates a scale-space approach using a Gaussian spatial operator to decrease the scale and then a Sobel operator mask to produce a gradient image.

As concluded by Leymarie and Levine [1993], this approach only works well with good contrast boundaries. Thin, expanding regions of the cell, such as pseudopods, were not included in the final boundary description. The lack of interaction between user and snake optimisation meant that wrong interpretations could not be corrected interactively. The calculated position of the snake boundary at equilibrium does not necessarily represent a valid solution. Image features may have been taken into the calculation of a solution which were not part of an object. There is no higher-level decision making process involved to decide which image features are valid or invalid.

### 2.3.2 Geometrical Deformable Models (GDMs)

The previously described contour models are physical based implicit models which are influenced by external forces, such as user intervention and image features and internal smoothness constraints. Miller *et al.* [1991] introduced an explicit model based on a vertex model that is able to adapt and resample itself according to the complexity of the shape it describes. This ability is performed in a two step approach:

- *Deformation:* In this step the vertices are pushed towards image features such as boundaries or intensity values. The shape is solely determined by the number of vertices, hence any information between points is not taken into account. In Miller's model, each vertex  $v_i$  can move along the normal vector  $n_i$  to a new position. A global cost function  $C$  is used as an assessment of how well the vertex model fits the boundary and topology of the object.

$$C = \sum_n C_i \quad (2.10)$$

According to Miller, the cost function for a two-dimensional GDM is made of the following components:

$$C_i(x, y) = a_0 D(x, y) + a_1 I(x, y) + a_2 T_i \quad (2.11)$$

where  $C_i(x, y)$  is the cost of a particular vertex at position  $(x, y)$  which is made of the weighted sum of  $D(x, y)$ , a potential field that pushes the vertex towards the boundary,  $I(x, y)$  an image term that identifies image features and  $T_i$ , a measure of smoothness of the current vertex position in context with its neighbours.

- *Resampling*: Miller introduced a scheme whereby vertices are added and deleted according to the distance between neighbours. If the distance is greater than a threshold  $T_1$ , a new vertex is added and if it falls below a threshold  $T_2$  a vertex is deleted. This enables the model to control its resolution and ensures smoothness.

Fitting of the vertex contour is achieved by minimising the cost function (2.11). Points are moved to a new position along the normal vector such that the cost of each point staying at the new position is lower than the previous position, otherwise it will remain in that position.

The vertex model has been combined with a spline interpolation and an energy minimising approach similar to snakes [Rueckert *et al.*, 1997]. It has been used successfully to track the aorta in cardiovascular magnetic resonance (MR) images with a high degree of *a priori* knowledge available.

### 2.3.3 Active Shape Models

The amount of *a priori* knowledge may be used further to restrict the number of possible shapes the contour can develop. For example, if the shape of an object is known and the variations of the shape can be described statistically from a training set of shapes. This information is used to limit the movement possibilities for the active contour and hence a higher degree of successful fitting may be achieved. Cootes and Taylor [1992, 1995] described variations in shape of an object by a point distribution model (PDM) as following

$$x = \bar{x} + Pb \quad (2.12)$$

where  $x$  represents all landmark points describing the boundary of the object,  $\bar{x}$  is the mean position of those points,  $P$  is a matrix containing the modes of variation and  $b$  is a vector of weights for each mode. Instead of using all modes of variation, limiting the number of variations can still be sufficient to describe a large proportion of the shape variations.

An instance of the shape of the object may be created by varying the weights for each mode of variation  $b$ . According to Cootes *et al.* [1995], an instance  $X$  of the shape can then be described by adding translation  $X_c$ , and shape changes  $M$  (orientation  $\theta$  and scale  $s$ )

$$X = M(s, \theta)[x] + X_c \quad (2.13)$$

Active shape models use an instance of the shape as a first approximation of the contour. For each landmark point, a displacement is calculated according to image features, for example the maximum edge strength along the normal vector. Using the current shape parameters, a best possible fit is tried by translating, rotating and scaling the current shape defined in equation 2.13. In a final step, adjustments to the original weights  $b$  are made to optimise further a closer fit. The most interesting feature of active shape models is their ability to learn shapes from a training set which enables a more successful fit. However, a large set of shapes is required for

training to capture the variability and the training process may be time-consuming. Only objects with a limited and known variability can be segmented with the help of such a model. In medical imaging, objects with known anatomical features can be segmented successfully with Active Shape models. On the other hand, cells do not express a limited number of shape variations and hence may not be suitable to be segmented by a shape model.

## Summary

In summary, snakes are a model-driven approach for solving many image understanding problems that are difficult, if not impossible, to tackle using classical approaches. Just like human vision, snakes start with an *a priori* model of initial shape of an object. By using the smoothness constraints, they are able to fill in for missing and noisy boundary information. As a result, they are more robust than non-model based methods, which make little use of knowledge about image structure. Active contour models are used to represent physical contours in medical images with a high degree of *a priori* knowledge from, for example, anatomical features, e.g. Rueckert *et al.*, [1997]. However, these techniques have been implemented mostly in research based systems. In cell imaging, however, there is a lesser degree of *a priori* knowledge since cells can develop an arbitrary number of shapes. Therefore, active shape models based on modelling shape variations would not be appropriate to describe cell shapes.

Contour models are often adopted to detect or follow boundaries as part of a tracking algorithm. However, the degree of user intervention in the segmentation and tracking process is often limited. In the original snake model, Kass provided for indirect user inter-action by defining positive and negative external forces which influence indirectly the fitting process of the snake. The global optimisation process of many contour models often leads to overlooking subtle features such as, for example, expanding pseudopods in cells. The calculated position at equilibrium may not always represent a viable image segmentation solution as seen in the case of cell image segmentation by Leymarie and Levine [1993].

## 2.4 Tracking non-rigid Objects

The ultimate aim of this project is to be able to track the movement of non-rigid objects in a noisy environment. Some tracking techniques are based on an accurate segmentation of the object outline in each frame without any temporal information as described in the previous sections. An outline of an object is generated from a single frame without using any information from the previous or consecutive frames. Another approach is to investigate directly the motion of an object. Many early motion estimation techniques simplified the process of the quantitative assessment of movement by assuming rigid motion of objects. However, with cells and indeed with most objects in real world, non-rigid motion is the norm. Huang *et al.* [1990] classified motion as shown in Figure 2.9.

Articulated motion occurs where parts of an object express rigid movement but move independently from each other. However, the overall motion of the object is non-rigid. Often articulated motion is referred to as piecewise rigid motion.

Elastic motion can be described as motion with certain constraints. Aggarwal *et al.* [1994] used the example of a bending metal sheet as an example of elastic motion whereby the bending is constrained by physical parameters. Another example of elastic motion is the bending and flexing of muscles. In these examples a high degree of *a priori* knowledge exists in terms of shape and motion and is often used to simplify the motion analysis. However, fluid motion is free of any constraints and may even include turbulent deformations [Aggarwal *et al.*, 1994].

### 2.4.1 Assessment of Motion

Many attempts have been made to understand how motion is perceived in biological visual systems in order to model the methodology with a computer system. The assessment of visual motion can be categorised in low-level techniques, based on pixel analysis and high-level techniques using *a priori* knowledge. High-level

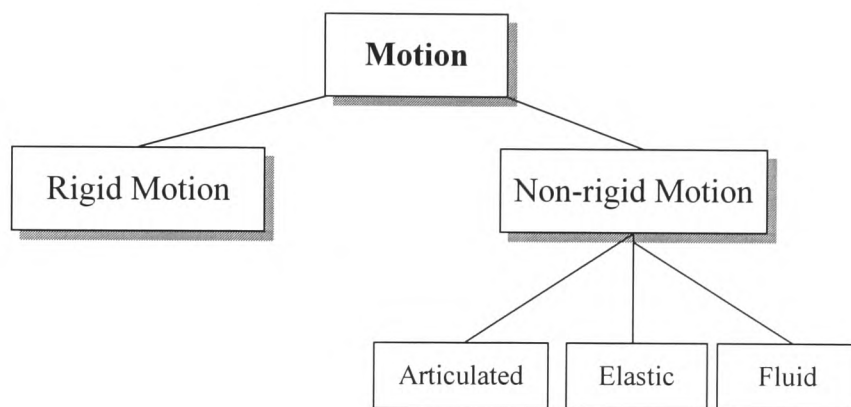


Figure 2.9: Classification of motion according to Huang *et al.* [1990]

techniques are a combination of low-level motion features and information about the movement, such as smoothness, shape or movement constraints.

### Low-level flow estimation

In an early review, Thomson and Barnard [1981] distinguish between three basic approaches for low-level motion estimation: differencing techniques, temporal-spatial gradient analysis and matching techniques.

- a) *Differencing techniques* determine changes in image intensity at each point  $f(x,y)$  in time. Consecutive frames are subtracted and values over a threshold indicate movement while those underneath the threshold  $T$  may be interpreted as noise. A difference image  $d(x,y)$  can be described as shown by Gonzalez and Woods, [1993]

$$d(x,y) = \begin{cases} 1 & \text{if } |f(x,y,t_1) - f(x,y,t_2)| > T \\ 0 & \text{otherwise} \end{cases} \quad (2.14)$$

Miyata *et al.* [1988] used the differences between three frames at different intervals to detect and quantify cell membrane ruffling (small, rapid changes at cell membrane).

- b) *Temporal-spatial gradient techniques* use changes in image intensity locally at an image point over both time and space to estimate the translation of that point. The velocity information is most reliably available near the intensity discontinuities, such as edges and peaks since the effect of noise is less distorting on these areas. Although the velocity of each point is calculated individually, the movement of the neighbourhood area is taken into account too. In its simplest form, the spatial variability is represented by a gradient vector  $\vec{g}$ . A small area within the image may shift by the amount  $d\vec{s}$  and causes the intensity change  $di$ . This yields the following relationship [Thomson and Barnard, 1981].

$$di = -\vec{g} \cdot d\vec{s} = -(g_x ds_x + g_y ds_y) \quad (2.15)$$

If there is only a single rigid object moving within an image, one can determine a set of linear equations from  $n$  observation points.

$$[G]d\vec{s} = \vec{d} \quad (2.16)$$

with

$$[G] = \begin{bmatrix} g_{x1} & g_{y1} \\ & : \\ g_{xn} & g_{yn} \end{bmatrix}, \quad d\vec{s} = \begin{bmatrix} ds_x \\ ds_y \end{bmatrix}, \quad \vec{d} = \begin{bmatrix} -di_1 \\ : \\ -di_n \end{bmatrix} \quad (2.17)$$

Due to the problem with noise when analysing the movement of individual pixels, a more generalised approach has been developed by Horn and Schunck [1981]. Their approach is based on the movement of brightness patterns rather than a single object, the so-called optical flow. The brightness at point  $(x,y)$  in an image  $f(x,y)$  at time  $t$  is denoted as  $E(x,y,t)$ . The brightness of a particular point is considered to be constant, hence  $dE / dt = 0$ . This yields

$$\frac{\partial E}{\partial x} \frac{dx}{dt} + \frac{\partial E}{\partial y} \frac{dy}{dt} + \frac{\partial E}{\partial t} = 0. \quad (2.18)$$

This can be rewritten as a single linear equation with two unknown  $u$  and  $v$  as

$$E_x u + E_y v + E_t = 0, \quad \text{with } u = \frac{dx}{dt}, v = \frac{dy}{dt}. \quad (2.19)$$

This equation is widely known as the *motion constraint equation*. However, this equation is not sufficient to determine uniquely the two components of a movement vector. Hence, Horn and Schunck [1981] introduced an additional smoothness constraint assuming that the velocity of a brightness pattern varies smoothly over the image plane. The partial derivatives of the image brightness  $E_x$ ,  $E_y$  and  $E_t$  are estimated by finite differences while the smoothness is described by the Laplacian of the  $x$  and  $y$  component of the flow. With many independently moving objects, the smoothness constraint of the flow field cannot be guaranteed.

Also, the estimation of the gradient by finite differences is sensitive to noise and may thus lead to false readings.

To overcome this problem, optical flow based on a field theory approach has been proposed by Numura and Miike [1991]. Instead of describing the movement of brightness pattern it measures the outflow and inflow of '*image current*' within a small area. Their approach is based on the continuity equation from hydrodynamics which is described as

$$\frac{\partial \mathcal{G}}{\partial t} + \text{div } \mathbf{i} = s_m \quad (2.20)$$

where  $\mathcal{G}$  is the density of fluid and  $\mathbf{i}$  is the current density of the flow while  $s_m$  is the rate of material formation. On the assumption that no new material is formed ( $s_m=0$ ) and  $\mathbf{i}$  corresponds to the '*image current density*', Nomura and Miike rewrote the above equation as

$$\frac{\partial g}{\partial t} + \text{grad}(g) \cdot \mathbf{v} = 0, \quad (2.21)$$

where  $g$  describes the image intensity at a specific pixel location in time  $g(x,y,t)$ . Grad is the image gradient at position  $(x,y)$  and time  $t$  while  $\mathbf{v}$  represents the  $x$  and  $y$  component of the flow vector. Considering the same point in two consecutive frames yields two equations which can be written in matrix form as

$$\begin{bmatrix} \frac{\partial g_1}{\partial x} & \frac{\partial g_1}{\partial y} \\ \frac{\partial g_2}{\partial x} & \frac{\partial g_2}{\partial y} \end{bmatrix} \cdot \begin{bmatrix} v_x \\ v_y \end{bmatrix} = \begin{bmatrix} -\frac{\partial g_1}{\partial t} \\ -\frac{\partial g_2}{\partial t} \end{bmatrix}. \quad (2.22)$$

The two components of the flow vector  $\mathbf{v}$  can be determined by matrix inversion as long as the determinant of the coefficient matrix is non-zero. Nomura and Miike further introduced a temporal optimisation scheme using all available frames  $n$  with a least square minimisation to solve the  $n$  equations. Siegert *et al.*

[1994] used this approach for optical flow to describe the movement of single cells as well as the movement of clustered cells. However, cells were not distinguished within a cluster, rather the overall velocities of the whole cluster were evaluated.

Brown and Dunn [1989] analysed the movement of dry mass in fibroblasts. Their method is based on the field theory equation (2.20) where the divergence of dry mass current  $\rho v$  is equal to the rate of decrease in dry mass density  $\partial \rho / \partial t$ .

$$\text{div } \rho v = -\frac{\partial \rho}{\partial t} \quad (2.23)$$

c) *Matching techniques* were the first to be used in motion estimation. It is possible to match a small region in one image frame to a region of the same size in its neighbourhood in a consecutive frame. In its simplest form, a region is selected and an organised search for a corresponding area is performed using some optimisation criteria. Two measures of similarity are commonly used, the sum of squared differences (SSD):

$$SSD(x, y) = \sum_{(x, y)} (I(x, y, t_1) - I(x + \partial x, y + \partial y, t_2))^2 \quad (2.24)$$

The above equation calculates the sum of square differences in intensity  $I$  of a small area centred at point  $p(x, y)$  at time  $t_1$  and several other locations  $(x+dx, y+dy)$  in the neighbourhood of  $p(x, y)$  at time  $t_2$ . The position of the minimum of the SSD indicates the best fit and hence determines the position the area has moved to.

The second measure of similarity is the cross-correlation between a small area at time  $t_1$  and several other locations  $(x+dx, y+dy)$  at time  $t_2$  can be described as:

$$COR(x, y) = \sum_{(x, y)} I(x, y, t_1) \cdot I(x + \partial x, y + \partial y, t_2). \quad (2.25)$$

Englert and Sheng [1990] used a normalised cross-correlation algorithm to determine the flow of particles. As pointed out by Thomson and Barnard [1981] regions with high information content are chosen preferably which are likely to provide good auto-correlation. This so-called '*feature point matching*' uses low-level image segmentation techniques, for example peak detection, prior to the area matching. These features are then traced using the above correlation technique. Interestingly, features points may also be determined from objects to be monitored. *A priori* knowledge about the shape of objects may help finding suitable feature points and hence enhancing the success of the matching techniques.

## Summary

Optical flow techniques have been used successfully to track the movement of rigid objects and on non-rigid objects. These techniques do not incorporate any information about the image structure and objects. Having information about the moving objects in an image may be of great advantage. For example, the movement of a human may be seen as articulated motion, piecewise rigid motion of the limbs and body. Due to the anatomical structure of the skeleton and muscles, a limited number of movements is possible which may be described in a model. The tracking of a person's movement may be simplified significantly by applying the model as a signature of walking patterns. Such a model is described as a parametric model where objects have a finite number of shapes or the deformation can be modelled mathematically Aggarwal *et al.* [1994].

However, the motion of cells can be described as being elastic or with respect to a small area  $dA$  as being articulated. Parametric models are inadequate for this type of motion.

It is important to note that optical flow has been used to track single cells or the whole cluster, but in case of clustered cells there was no distinction made between individual cells within the cluster [Siegert *et al.*, 1994].

Active contour models have been used to track objects but without the use of spatio-temporal information such as optical flow. Only recently has motion analysis been combined with an active contour model [Hoch and Litwinowicz, 1996] and the so-called velocity snake [Peterfreund, 1999]. Both use motion estimation to place the snake closer to the boundary in situations of motion.

## 2.5 Description of Cell Morphology and Cell Motility

This thesis is concerned with the assessment of cell movement behaviour and the term motility is used for describing morphological changes and translocative movement. Once objects have been identified, parameters such as position, size and shape may be used to describe the objects, e.g. cells. The centroid  $P(x_c, y_c)$  of the area occupied by the cell is often used as the position of the cell [Soll, 1995]. This is used as a basis to calculate cell velocity.

$$x_c = \frac{1}{A} \int_{(A)} x dA \quad y_c = \frac{1}{A} \int_{(A)} y dA \quad (2.26)$$

Cell motility describes changes in shape and location over time of cells. Haemmerli, [1978] described two different types of motility of cells.

- *Stationary motility* describes the appearance and disappearance of pseudopods without changing the position of the cell.
- *Translocative motility* describes directional movement when the cell is polarised. This is often accomplished by cytoplasmic extensions of the cell front.

Translocative velocity is the distance between two positions over time. However, it is somewhat controversial what the ‘optimal’ time-interval should be. Soll [1995] remarks that it is important to choose the same time-interval if velocities are to be compared.

Shape changes are usually accompanied when cells are moving, however, stationary motility may also express changes in cell shape due to pseudopod expansion. The shape of cells has been described by higher-order moments [Dunn and Brown, 1990] or as circular maps [Killich *et al.*, 1993]. A common size-independent descriptor for shapes is the roundness, defined as [Schnorrenberg *et al.*, 1997]

$$roundness = \frac{perimeter^2}{4\pi \cdot area}. \quad (2.27)$$

This may be used as a descriptor for stationary motility.

## 2.6 Example of Systems for Assessing Cell Motility

This section gives an overview of two systems, which demonstrate the computer-assisted assessment of the movement of several single or clustered cells.

### DRIMAPS System (Dunn and Zicha, 1995)

Phase-shifted interference images represent the distribution of dry mass inside cells. The phase shifted interference principle (PSI) [Bereiter-Hahn, 1985] makes use of the interference between phase delays of two separate light beams. In the Horn microscope configuration used, one light beam passes through the specimen while the second beam passes through a dummy chamber. This was combined with a computer system to calculate the true phase difference by solving a set of interference equations and thus the accurate density of dry mass in cells. Cells were masked out using a Sobel edge detector with the boundaries diluted. The remaining background image was used to determine a polynomial transformation to compensate for the inherent fluctuations in background intensities. The system can also be adjusted such that cellular regions are brighter than the surrounding background, hence the segmentation process is less complex. The system calculates area and velocity and higher order moments for cell shape assessment from the dry mass distribution.

### A gradient method for the quantitative assessment of cell movement and tissue flow (Siegert *et al.*, 1994)

The system addresses the problem of describing the movement of multicellular cultures. Instead of identifying each cell individually within a colony, Siegert's approach is based on the analysis of pixel flow in all regions of a frame. In analogy to the flow measurement of particles in fluids [Numura *et al.*, 1991], Siegert calculates the average velocity vector for every pixel from 25 vectors in a 5x5 region and thus the movement of a small region. Images were digitised at a five-second interval. To reduce noise, the average velocity vector was calculated. However, no distinction was made between individual cells.

## 2.7 Conclusions

The assessment of cell motility may be described as an image segmentation problem and a motion detection problem. Many techniques have been developed to segment single, detached cells using a variety of microscope techniques. Low-level image segmentation techniques have been used successfully in cases where single cells had different intensity values from the image background. Such techniques are tailor made to the image properties from images using a specific light microscopy methods. For example, objects in the image plane in phase-contrast microscopy develop a halo around their boundary which has been used to facilitate cell boundary detection. A number of automated systems have been used to describe the movement of single, detached cells. Most systems are based on a combination of low-level image segmentation techniques such as thresholding and edge detection. One system used an active contour model to segment a single cell in consecutive frames.

The segmentation of individual cells in clusters is challenging. Siegert *et al.*, [1994] used optical flow analysis to measure the movement of all cells within a clustered region. Since there is a clear interest in measuring the behaviour of cells in clusters, the analysis of cell movement of individual cells in clusters would be of great advantage. Since segmentation of clustered cells without high-level knowledge is very difficult, an interactive adaptive contour model is proposed to segment and track individual cells in an interactive fashion.

Such a model should have the following properties:

- semi-automatic contour initialisation
- semi-automatic fitting to cell shape to reduce user bias
- relocation of contour in consecutive frames
- allow easy user interaction to correct relocation if necessary

## 3 Adaptive Spline Method

### 3.0 Introduction

The tracking of non-rigid objects such as cells is a complex task. In this chapter a novel approach of describing cells and assessing their motility is presented. This approach allows the tracking of individual cells in clusters which is considered to be important in the study of cell behaviour. One of the difficulties of segmenting cells is that their boundary is not consistent around the cell body. Cells constantly change their appearance due to protrusion and retraction of the cell margin. The boundary may be very weak and does not express a predominant gradient. The ruffling of the cell membrane may lead to a blurred boundary which could be difficult to detect in a fully automated system.

In this new approach, a cell is described by a piecewise cubic spline interpolation facilitating *a priori* knowledge about the boundary of cells. The cell boundary is approximated by a spline-based contour model describing the shape of the cell membrane. A semi-automatic, interactive tracking approach has been adopted which requires the positioning of control points<sup>1</sup> onto or close to the cell boundary at the start of the monitoring process. This is combined with an adaptive relocation approach using image features in the vicinity of the cell boundary.

The essence of the method is to use image features in the near neighbourhood of the salient control points that can be relocated in consecutive frames using gradient and pixel flow properties. In Figure 3.1 the four corner stones of the adaptive spline method are shown. The method is designed to allow interaction between the cell segmentation and tracking process as well as user influence on the final result of the segmentation process. This semi-automatic approach allows the operator to intervene in the automatic tracking process to ensure correct interpretation of the cell boundary in clustered cells.

---

<sup>1</sup> In the literature the term vertex is often used instead of control point

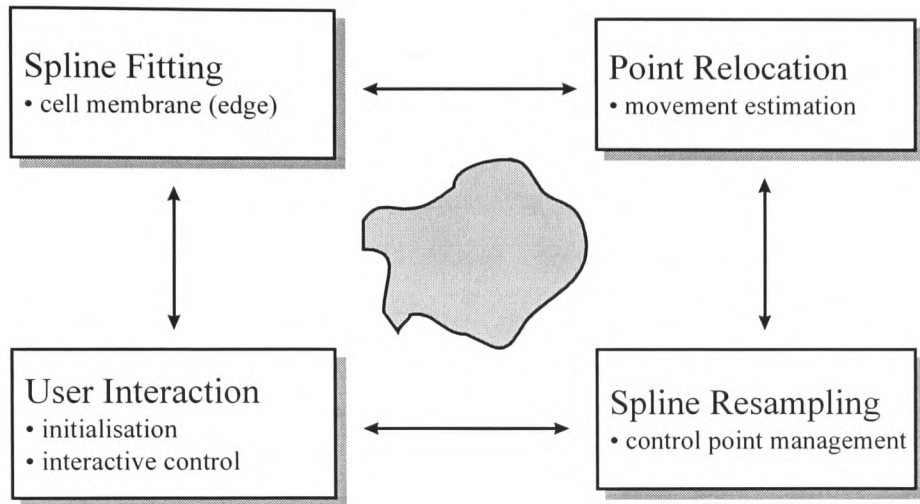


Figure 3.1: Overview of four main components of adaptive spline technique

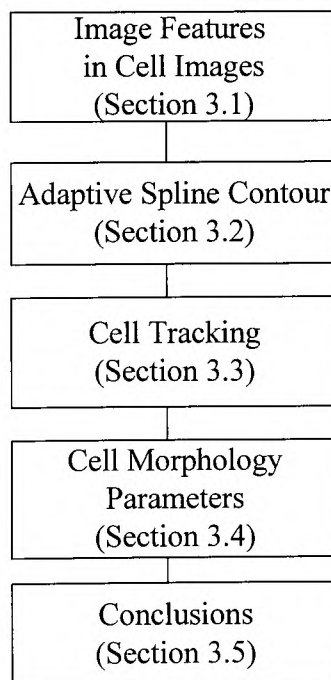


Figure 3.2: Schematic overview of method section

- The ***user interaction*** mechanism is through the salient control points on which the spline boundary is interpolated. Moving single points changes the shape of the rendered boundary, also points may be added or deleted. However, this so called ***re-sampling*** process may also be performed more automated whereby control points are added and deleted according to a the length of spline segments.
- The ***spline fitting*** process moves control points closer to the boundary if a sufficient gradient is apparent.
- The ***point relocation*** process is based on a spatial-temporal area matching technique to approximate the piecewise rigid movement of each control point. This movement information is combined with gradient information in a decision making process to determine the new position of each control point in consecutive frames.

The arrows between those four blocks symbolise the dependency between those components. The functionality of each block is described in this chapter.

In summary, the proposed spline-based contour model has the following properties:

- semi-automatic, initial control point selection
- automatic fitting to cell shape to reduce user bias (where unambiguous)
- cell tracking in consecutive frames
- allows easy user interaction
- limited search space (neighbourhood processing) due to clustered cells
- tracking of centroid

Figure 3.2 outlines the way in which the method section of the thesis is organised.

The adaptive spline method was used to investigate the movement of cancer cells as described in chapter 5.

It is also shown that the spline technique may be used in other areas of image segmentation, such as the delineation of the wound edge in ulcers. The adaptive spline model was further used to approximate the position of the boundary of leg

ulcers and to derive features from the boundary. An orthogonal profile was created from the spline which was used to describe new wound assessment parameters. The application of the spline to wound imaging will be discussed in chapter 6.

The adaptive spline method was developed preliminarily in the Java language (Sun Microsystems Inc.). Image enhancement techniques were developed preliminarily in Matlab (The Mathworks Inc.) environment using the Image Processing Toolbox.

Finally, a stand-alone software package was designed in C++ using Borland C++ (Borland Inc.) on Microsoft Windows95. The software contains image capture software and the implementation of the adaptive spline technique together with tracking and image enhancement features. The software was developed in an object-orientated fashion. A class diagram is attached in the appendix C. Parts of source code describing the adaptive spline class are also shown in appendix C. The software was written in ANSI C++ and it is anticipated to port the application to the Linux environment. Snapshots of the software in action are attached in appendix B.

### 3.1 Cell Image Features

Cells are usually between 10 $\mu$ m and 30 $\mu$ m in diameter and consist of a nucleus surrounded by cytoplasm. A literal description of the cell is given as follows [Alberts *et al.*, 1994]:

Any one of the minute protoplasmic masses that make up organised tissue, consisting of a nucleus which is surrounded by cytoplasm enclosed in the cell membrane.

Viewed by an ordinary brightfield microscope, cell features are almost invisible due to the low light extinction coefficient of cells. As discussed in chapter 2, techniques such as phase contrast, DIC and Hoffman modulation contrast (HMC) microscopy are used to view unstained, living cells and their structure. In HMC, optical gradients due to phase shifts are highlighted and objects have a three-dimensional appearance due to the directionality of the optical gradient. The image in Figure 3.3 shows a single cancer cell viewed by HMC.

The opposite gradients are clearly marked by bright and dark areas on the cell membrane as seen in Figure 3.3. The protruding area appears to be ‘thinner’ and hence expresses a lesser gradient. Structural features such as the nucleus and nucleolus may also be identified as spots within the cytoplasm thanks to the three-dimensional appearance. The directionality of the gradient may be used to distinguish two neighbouring cells as seen in Figure 3.4. The areas of interest are marked by a white arrow in Figure 3.4.

The positive and negative gradient between touching cells makes HMC suitable for assessing clustered cells. It is important to note that the cell margin may be very thin in expanding regions of the cell and hence would be very difficult to detect from the weak gradient alone. However, a human observer may still be able to distinguish these expanding regions when viewed as an image sequence. Subtle changes in image

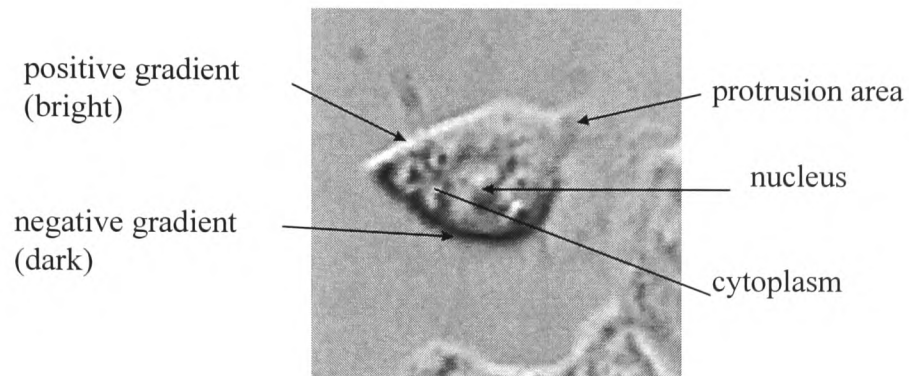


Figure 3.3: Single human colon cancer cell as viewed by HMC microscopy



(a) touching cells      (b) overlapping cells

Figure 3.4: Applications of HMC to visually distinguish touching or even overlapping cells.

intensity over time are recognised and the human high-level vision system appears to form a segmented cell out of the spatio-temporal information.

This is the reason why changes between video frames (temporal information) is combined with spatial information such as image intensity and image gradient, to form a spatial-temporal technique of describing and tracking cells. This is combined on a higher level with a spline-based mathematical contour to finally describe the shape of cells. As in the human vision system, edges are the first and most important clue to the position and shape of an object. In general, the location of a boundary is determined by the zero crossings of the second derivative of the image function [Gonzalez and Woods, 1993]. Figure 3.5 shows this principle applied to a basic test image. The outline of the test image in Figure 3.5 denotes the zero-crossings of the Laplacian filter. However, in a real world imaging situation objects are not as well defined as the test image in Figure 3.5.

The location of an edge in Hoffman Modulation Contrast images is more complex due to the fact that the HMC image already represents a gradient image. Furthermore, this so called ‘optical gradient’ in HMC is directional dependent [Hoffman, 1977]. A possible location technique for an edge in HMC on a test image and on a real image of a single cell is demonstrated. The same procedure is applied to detect the boundary of clustered cells. It is important to note that the boundary may not be detected fully due to weak boundary definition at retracting and protruding cell areas.

The test image in Figure 3.6 is a simple approximation of the effect of modulation contrast. The image was created by applying a horizontal first derivative filter mask. It is important to mention that this approximation introduces a systematic error to the image. The artificial object ‘increases in size’ by one pixel each on the positive as well as negative slope of the edge. This is not the case in modulation contrast. The bright and dark areas introduced by the optical gradient are part of the object. This can be explained with the following equations.

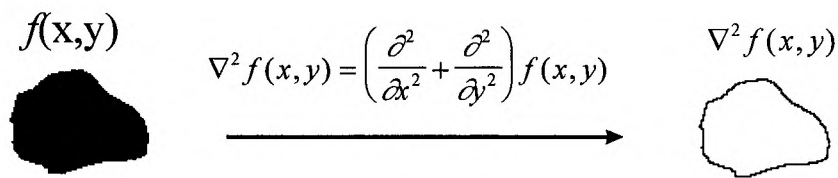


Figure 3.5: Locating a boundary with zero crossings using a Laplacian filter  $\nabla^2 f(x,y)$

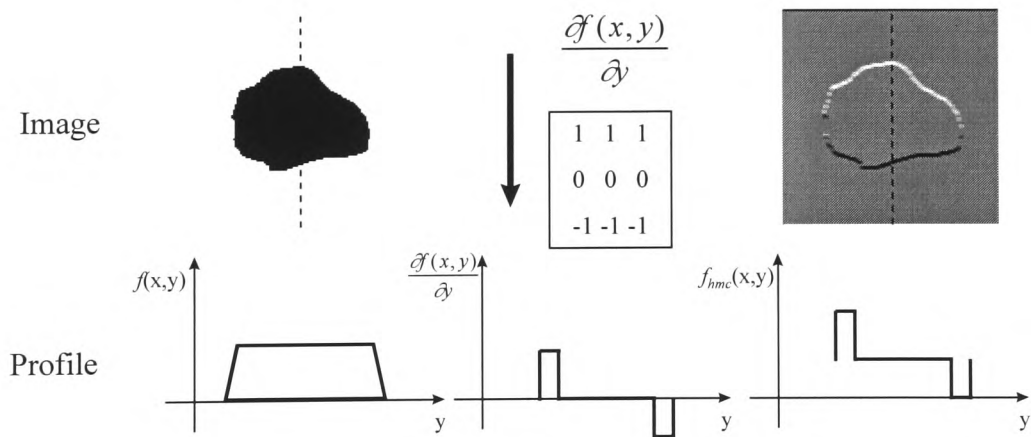


Figure 3.6: Simple test object ‘Hoffman modulated’. A cell shape (left image) viewed by HMC (right image) simulated by a horizontal edge detector mask.

$$\text{discrete: } \nabla f(x, y) = \frac{\Delta f(x, y)}{\Delta x} \quad \text{continuous: } \nabla f(x, y) = \lim_{\Delta x \rightarrow 0} \frac{\Delta f(x, y)}{\Delta x} = \frac{\partial f(x, y)}{\partial x}. \quad (3.0)$$

The steps of the optical gradient are infinitesimally small  $\Delta x \rightarrow 0$  while the steps of the gradient in the test image are one pixel width ( $\Delta x = 1$ ). The size of the test object has increased but due to the fact that bright and dark areas are part of the object in HMC, this will then become the new test image. The created image expressed a grey background where no optical gradient is apparent while one side of the object is dark and the opposite side is bright. Purely vertical edges are not expressed in HMC but any edge with a horizontal component expressed a gradient as on the artificial test image seen in Figure 3.6.

Since the HMC image already represents the (directional) first derivative, a natural progression would be to derive the image  $f(x, y)$  a second time. In order to investigate a valid method to determine the *location* of the cell boundary from the gradient, the method was first applied on an artificial HMC test image and was later applied to a real cell image. Figure 3.7 shows the artificial HMC test image and the appropriate derivative. A standard 3x3 Prewitt filter mask was used for the horizontal and vertical component. As shown in the equation in Figure 3.7, the two components were simply added together. This resulted in positive and negative gradients at the inner and outer boundary to create a high contrast. This process is explained in Figure 3.8. A profile of an artificial object is shown and the position of the edges are marked as a dotted line in the profile graph. The intensity plot shows the profile of the same object viewer under HMC. Typical features are the bright and dark edges of the object giving it a three dimensional appearance. The derivative plot shows the positive and negative gradient values which occur at the boundary of an HMC image. In the image next to the derivative plot, high gradients are expressed as dark values, hence the dark outline in that image represents the true location of the boundary.

The same procedure is now applied to a real cell image viewed by Hoffman modulation contrast microscopy. Figure 3.9 shows a single cell image with two profiles marked by a white line in the image. The corresponding profile plots are

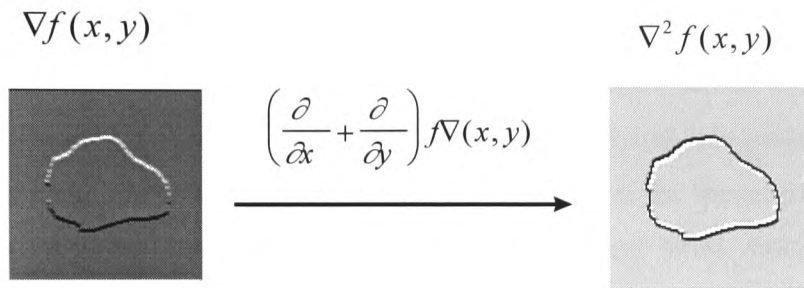


Figure 3.7: Simple test object 'Hoffman modulated' with first derivative Prewitt operator applied. The resulting image was overlaid with the true position of the edge (black outline).

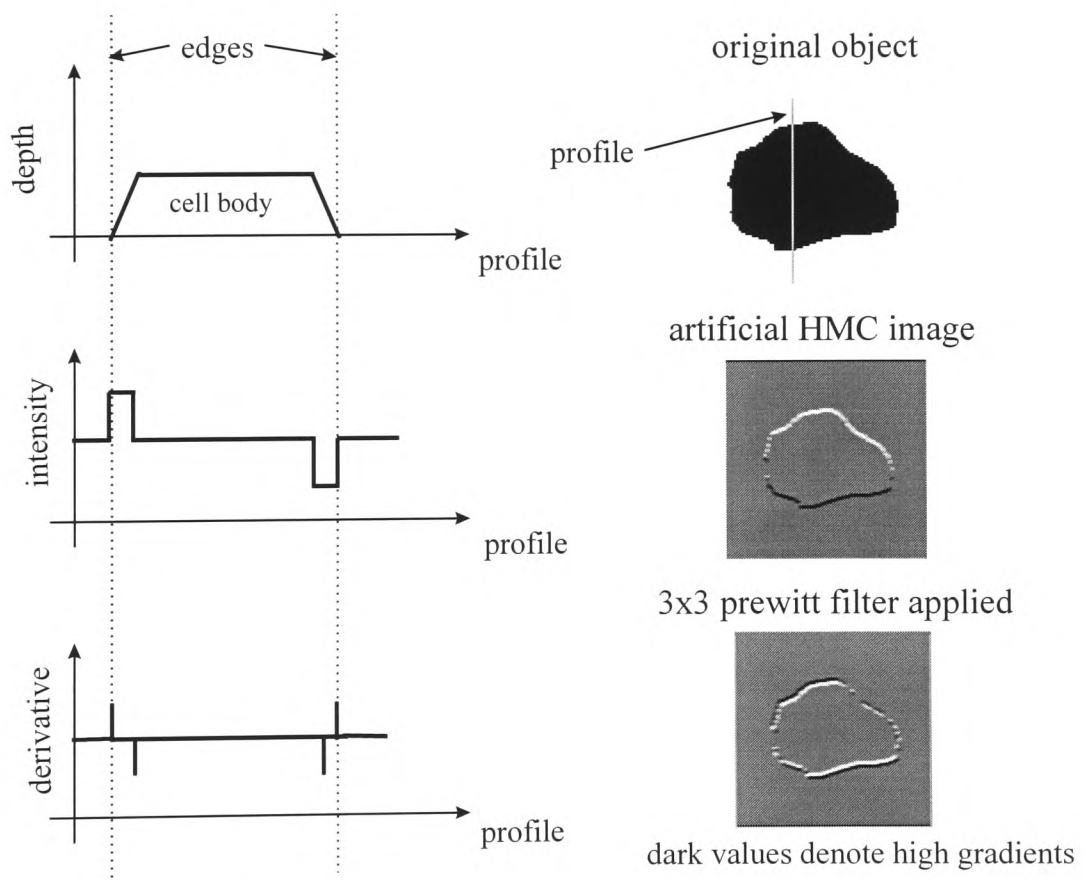


Figure 3.8: Edge location in artificial HMC image using a 3x3 Prewitt filter

situated on right to the image. The perceived boundary position is marked on the profile plots by a dotted line.

The location of the boundary in Figure 3.9 can be determined at the rise and fall of the optical gradient values which are represented by high and low intensity values. This is very clear when investigating horizontal edges as in the image in Figure 3.9. Since HMC images already represent an optical gradient (first order) a natural progression would be to use the second derivative as an indicator for the location of an edge. This coincides with the perception of the position of the boundary at the rising edge of the optical gradient as shown in Figure 3.9. The position of the edge in Figure 3.9 is indicated by two dotted lines in the profile graphs.

This proposition is further investigated in Figure 3.10 where a profile is generated from a cross-section of a cell image. The spatial resolution of the Prewitt filter mask was extended to a size 5x5 due to improve the definition of the boundaries. The horizontal and vertical component of the filter mask are shown below.

1	1	1	1	1
0.5	0.5	0.5	0.5	0.5
0	0	0	0	0
-0.5	-0.5	-0.5	-0.5	-0.5
-1	-1	-1	-1	-1

horizontal

1	0.5	0	-0.5	-1
1	0.5	0	-0.5	-1
1	0.5	0	-0.5	-1
1	0.5	0	-0.5	-1
1	0.5	0	-0.5	-1

vertical

(3.1)

The two vertical and horizontal components are added together. The resulting image expressed positive and negative gradients which are then normalised to the range [0..1, or 0..255 if mapped into grey level range]. This provides dark regions at the cell boundary and bright regions on the inner side of the cell boundary. Figure 3.10 shows a cross-section through a single cell viewed by HMC. The profile is marked on both the HMC image and the gradient image with a dotted line. The location of the boundary is determined at the position of the lowest gradient (dark region).

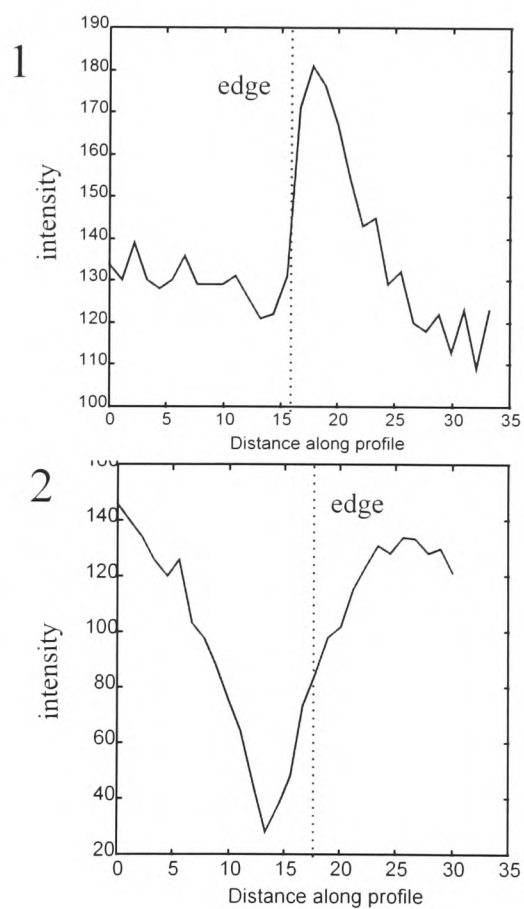
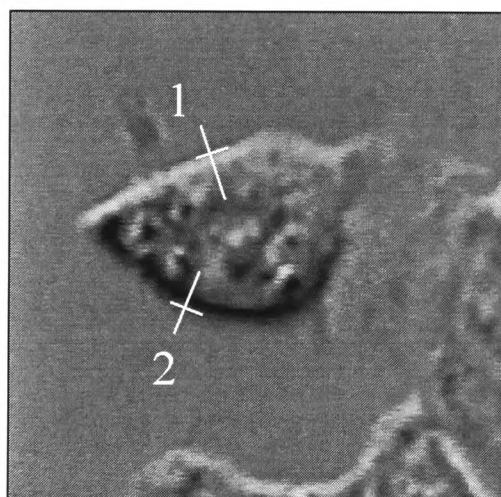
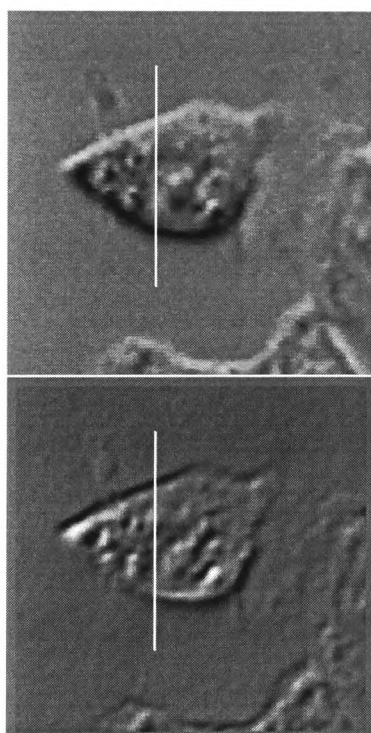


Figure 3.9: Profile of line (1) and (2) over the positive and negative edge of an human colon cancer cell viewed by Hoffman modulation contrast.



gauss smooth, 5x5 prewitt

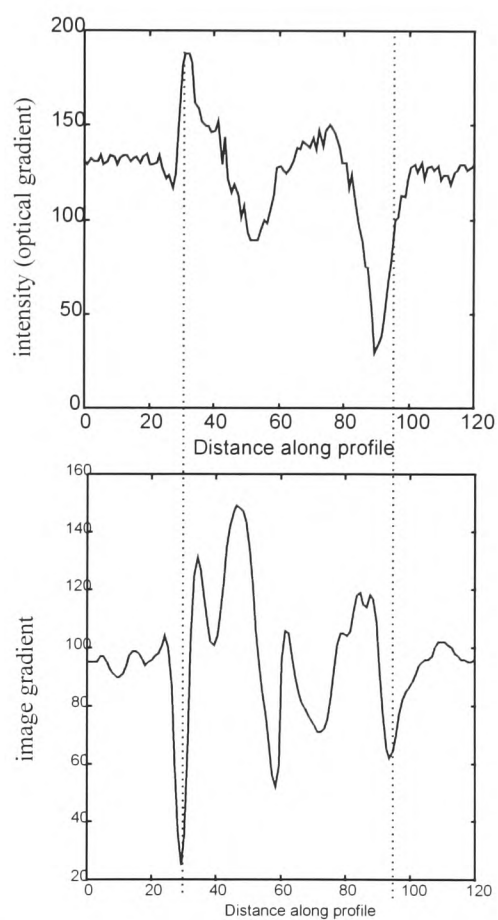
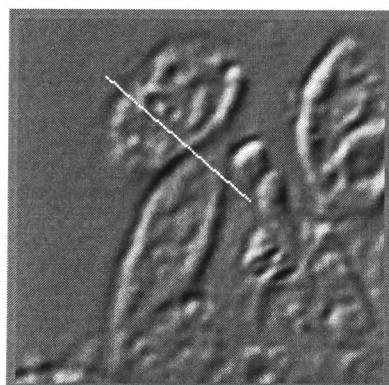
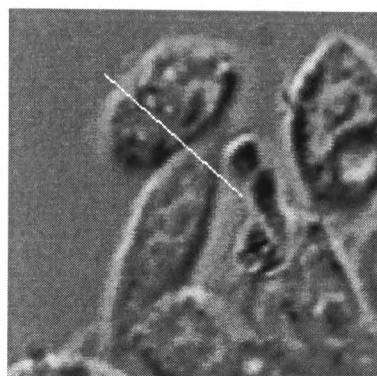


Figure 3.10: Vertical profile through single cell viewed by HMC. The first derivative is used as indicator of boundary location. The position of the edge is marked by two vertical dotted lines in the profile graphs.

An absolute vertical edge of a cell would not show up in HMC. Fortunately, edges are never really straight and cells usually develop a curved or jagged boundary with horizontal and vertical components.

The boundary of clustered cells can also be detected using the Prewitt filter mask (3.1). Figure 3.11 shows two cells touching and a cross-section through both cells as indicated by a white line. The boundary between the two cells is located by the lowest gradient in the region of the boundary. The boundaries may be distinguished further by using the intensity of the optical gradient. The top left cell in the image in Figure 3.11 shows a lower intensity at the boundary between the two cells while the boundary of the adjacent cell expresses a higher intensity.



gauss smooth, 5x5 prewitt

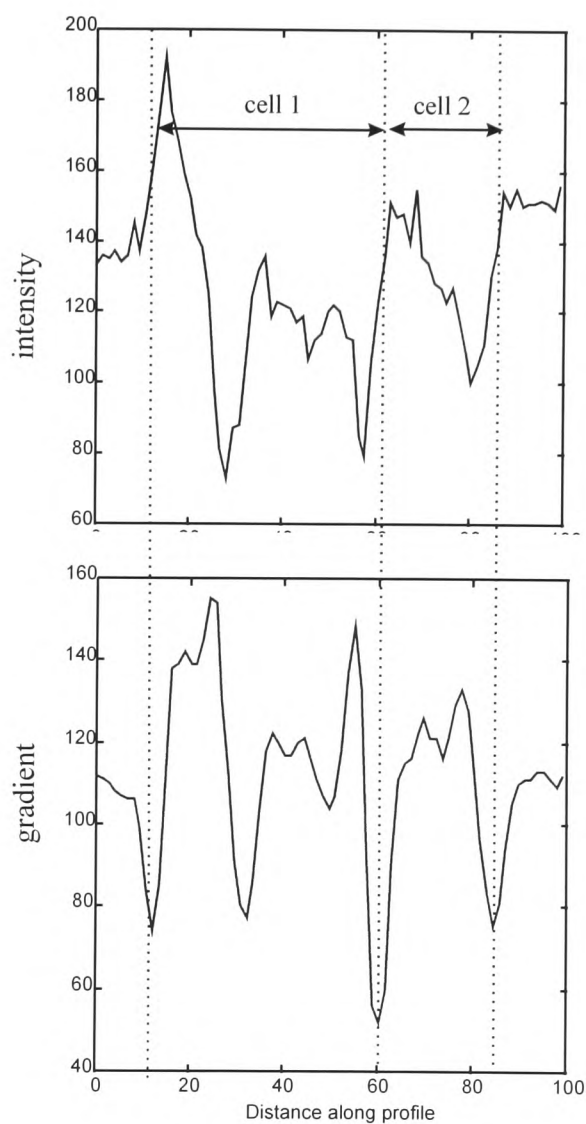


Figure 3.11: Profile through two clustered cells viewed by HMC. The first derivative is used as indicator of boundary location. The position of the edges is marked by three vertical dotted lines in the profile graphs. The boundary between the two touching cells is clearly visible.

### 3.2 Adaptive Spline Contour

This section is concerned with the definition of splines and their application to description of cell like shapes. The mathematics of the spline model are derived and suitable parameters to describe the morphology of cell shapes are described. The accuracy of delineating artificial and real cell shapes is discussed in chapter 4.

#### 3.2.1 The Spline Contour

The cell boundary is described by two-dimensional rendering of the cell membrane, using splines. To describe a cell shape, a sequence of control points is specified on the boundary, which will in some way describe how the curvature is formed. The function of the control points is twofold:

1. They determine the contour formation. The contour is required to pass through these points, hence the type of spline to be chosen is interpolating. Other types, e.g. Bezier splines approximate the location of their control points and run close to these points.
2. They form an interface between user interaction and contour formation.

In general, any object contour  $Q$  can be described by a piecewise formation of individual curve segments  $Q = \{Q_1, \dots, Q_n\}$ . The smoothness of the contour is determined by the type of curve segment, e.g, linear or polynomial. A two-dimensional contour  $Q$  can be defined in terms of its x and y co-ordinates which form a parameterised curve with the linear parameter  $u$ ,

$$Q(u) = (X(u), Y(u)) \quad u_{\min} \leq u \leq u_{\max} \quad (3.2)$$

The range of the parameter  $u$  is usually defined in the closed interval  $[0,1]$ .

Splines can be categorised as described by Bartels *et al.* [ 1987], in to:

- Approximating/Interpolating: A spline that passes through a set of control points interpolates while a spline that passes close to the control points approximates its path to the location of those points.
- Global/Local control of splines: The parameters of one spline segments depend on the location of all control points forming the contour. Locally controlled splines calculate the parameters of one segment depending on the neighbouring segments only.
- Control point spacing: Many splines assume an equidistant spacing between control points. This leads to a uniform range of the parameter  $u$ , e.g.  $0 < u < 1$ . Non-uniform parameterisation may perform better in some cases.
- Continuity: The continuity describes the transition between two neighbouring spline segments. For example, a  $C^2$  continuity describes spline segments with equal first and second derivatives at the transition point.

The aim is to render the membrane of a cell with a suitable curvature. This is used as an approximate shape descriptor from which other parameters, such as position and compactness can be calculated. The curvature  $\mathbf{Q}(u)$  is formed by a number of segments that are defined by control points  $\mathbf{P}_i (x_i, y_i)$  at the beginning and the end of each segment  $\mathbf{Q}_i(u)$ . Another requirement for the curvature is to pass through the specified control points, interpolating the shape with a smooth curvature in between. Figure 3.12 shows a closed curvature, interpolating between four control points  $P_1..P_3$ .

The most commonly used type of polynomial are of the 3<sup>rd</sup> order, so-called cubic splines. For example, a single two-dimensional curve segment  $\mathbf{Q}_i(u)$  can be described by the following pair of cubic equations for each dimension.

$$\mathbf{Q}_i(u) = (X_i(u), Y_i(u)) \quad \text{with} \quad Q_i(u) = a_i u^3 + b_i u^2 + c_i u + d_i \quad (3.3)$$

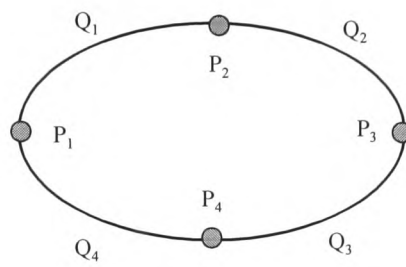


Figure 3.12: A contour made of four spline segments

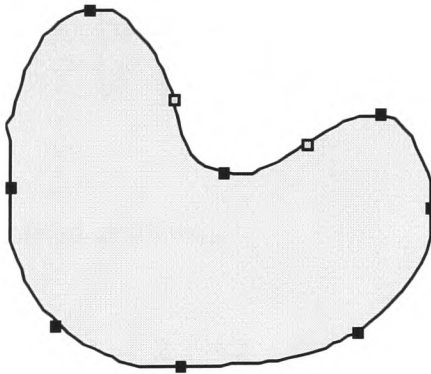


Figure 3.13: An example shape with control points placed as a first approximation (black) and a further refinement (grey).

This leaves four coefficients which need to be determined individually for each segment. Also, the coefficients have to be determined for the x and y coordinate separately.

The following four equations can be established for the y-coordinate. The same conditions apply for the x-coordinate. For convenience, one writes  $a_i$  instead of  $a_{yi}$ :

$$y_i = a_i u^3 + b_i u^2 + c_i u + d_i \quad \text{with } 0 \leq u \leq 1$$

$$\begin{aligned} 1) & y_i(0) = d_i \\ 2) & y_i(1) = y_{i+1}(0) = a_i + b_i + c_i + d_i \\ 3) & y_i'(0) = c_i \\ 4) & y_i'(1) = y_{i+1}'(0) = 3a_i + 2b_i + c_i \end{aligned} \quad (3.4)$$

These equations can be written in matrix form and the matrix can be solved by matrix inversion.

$$\begin{pmatrix} 0 & 0 & 0 & 1 \\ 1 & 1 & 1 & 1 \\ 0 & 0 & 1 & 0 \\ 3 & 2 & 1 & 0 \end{pmatrix} \begin{pmatrix} a_i \\ b_i \\ c_i \\ d_i \end{pmatrix} = \begin{pmatrix} y_i \\ y_{i+1} \\ y_i' \\ y_{i+1}' \end{pmatrix} \quad (3.5)$$

The inverse matrix is calculated as follows

$$\begin{pmatrix} a_i \\ b_i \\ c_i \\ d_i \end{pmatrix} = \begin{pmatrix} 2 & -2 & 1 & 1 \\ -3 & 3 & -2 & -1 \\ 0 & 0 & 1 & 0 \\ 1 & 0 & 0 & 0 \end{pmatrix} \begin{pmatrix} y_i \\ y_{i+1} \\ y_i' \\ y_{i+1}' \end{pmatrix} \quad (3.6)$$

The suggested solution requires the derivatives between two segments at a control point to be known. This may be overcome by estimating the derivatives at the control points using finite differences,

$$y'_i \approx \frac{y_{i+1} - y_{i-1}}{2} \quad \text{and} \quad y'_{i+1} \approx \frac{y_{i+2} - y_i}{2} \quad (3.7)$$

however, a better solution is at hand using knowledge about the cell shape. The cell membrane expresses a continuous boundary as shown in the example cell image in Figure 3.3. If one has to describe such a curvature with a few points, one tends to place points at local maxima and minima of the curvature. The following Figure 3.13 shows an example shape with points marked by a user as a means of approximating the shape.

The spline has to be designed such that it is intuitive to place control points on the boundary that will closely render the boundary. Following the example shape in Figure 3.13, all points set as a first approximation have in common a smooth second order transition. Therefore, we introduce a new condition, such that the second derivatives at the end of one segment equal those at the beginning of the following segment. This form of spline is called a ‘Natural Cubic Spline’, a special case of a Hermite spline interpolation [Bartels *et al.*, 1987].

$$\begin{aligned} y''_{i-1}(1) &= y''_i(0) \\ 6a_{i-1} + 2b_{i-1} &= 2b_i \end{aligned} \quad (3.8)$$

The first derivative can be calculated and hence the parameters  $a_i, b_i, c_i, d_i$  by substituting the equations of (3.6) into the above equation (3.8).

$$y'_{i+1} + 4y'_i + y'_{i-1} = 3(y_{i+1} - y_{i-1}) \quad (3.9)$$

It is important to note that the cell boundary is a closed curvature, hence the last segment is connected to the first segment. Lets assume our contour is made out of  $m+1$  control points  $P_0 \dots P_m$ . For each control point we need to calculate the first derivative, hence one has to solve  $m+1$  equations of 3.9. This shows that each derivative depends on the derivatives of its neighbours and so forth, hence the change

of one control point has an effect of all the other points. This makes the spline globally controlled.

The  $m+1$  equations in matrix form are

$$\begin{pmatrix} 4 & 1 & 0 & 1 \\ 1 & 4 & 1 & 0 \\ & & \ddots & \\ 1 & 0 & 1 & 4 \end{pmatrix} \begin{pmatrix} y'_0 \\ \cdot \\ \cdot \\ y'_m \end{pmatrix} = \begin{pmatrix} 3(y_1 - y_m) \\ \cdot \\ \cdot \\ 3(y_0 - y_{m-1}) \end{pmatrix}. \quad (3.10)$$

The first derivatives can hence be calculated and with the help of equation 3.6 the four spline coefficients  $a_i$ ,  $b_i$ ,  $c_i$  and  $d_i$  can be determined. This way, the spline is fully described mathematically. The following image in Figure 3.14 shows an example of a cell described by the developed spline method. The boundary is marked with control points (squares) and its interpolation between segments (dotted line).

### 3.2.2 Spline Deformation

Cells are non-rigid objects that change shape and location at any given moment in time. The spline model is able to adapt to these changes and ensure a close fit description of the cell boundary. Rigid deformations such as translation and rotation are almost certain to be found in combination with non-rigid deformation of the cell shape. These deformations are well served with the spline based model. Figure 3.15 shows possible deformations of the spline model. The freedom of movement and ability to describe complex shapes is guaranteed by the fact that control points can be moved individually and the number of control points is variable. The position of a control point is either changed manually or according to the location of image features.

After each deformation process the re-sampling process can be performed where control points are added or deleted. The number of control points is variable and hence determine the resolution of the model. Complex shapes need a greater number of control points than simpler shapes.

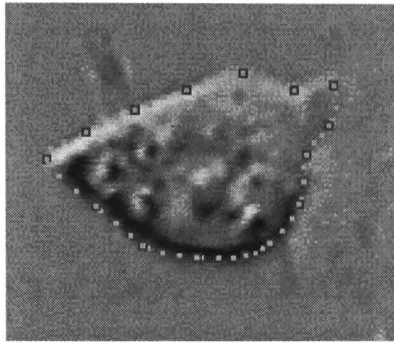


Figure 3.14: Single cell viewed by HMC and delineated with the spline model. The boundary is marked with control points (red squares) and its interpolation between segments (green dots).

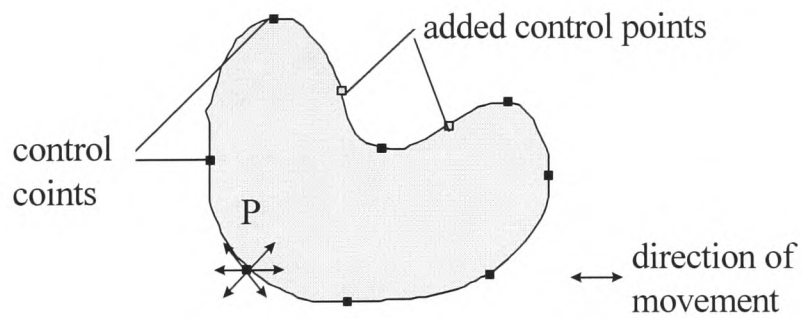


Figure 3.15: Control point P of spline contour can move in eight directions independent of all the other control points. Control points can also be added or deleted to adjust the resolution of the spline model.

Control points are added if the length of a segment between two control points is greater than a set threshold  $T_{\max}$ . Control points are deleted if two points are close to each other and the segment length is below a set threshold  $T_{\min}$ . The two thresholds depend on the image resolution and the size of cells.

Deformation and re-sampling is performed at a control point level. The control points are connected by a cubic spline to form a smooth curvature. Segments are formed such that the overall length of the contour reaches a minimum. The implementation of the sorting algorithm can be found in appendix C. The following Figure 3.16 illustrates this problem. If a crossover were to occur in the spline boundary in Figure 3.16 between the two control points in the thin region, the overall length of the boundary would be larger than the displayed optimal solution. Whenever the position of a control point changes, the process of finding the minimum length of the contour is performed and the segment coefficients are calculated accordingly.

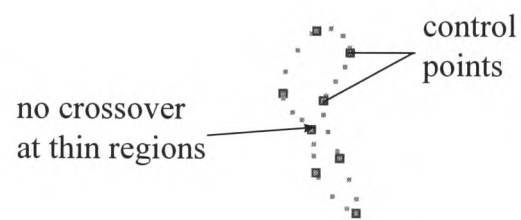


Figure 3.16: Shape described by spline model with a thin region

### 3.3 Cell Tracking

The spline has been designed such that it can approximate the shape of objects, or cells. A cell is described by the location of its boundary. The manual positioning of salient control points from which the boundary is formed is used as a first approximation of the boundary location. This method, however, is user dependent and one would like to reduce user-bias further. The adaptive spline method combines fitting and tracking of cells in a new contour model. The aim of the tracking process is to relocate the cell boundary in consecutive frames. There are two major approaches to tracking objects.

- The first approach is based on locating objects in each frame individually. This process is repeated for each frame and objects with similar size and position are identified in consecutive frames as being one and the same object. This method does not require a high frame rate and considerable changes between frames are possible.
- The second approach does not identify objects in frames, it rather finds similarities - or differences - between frames. In an ideal situation the movement of each pixel can be traced and thus pixels belonging to an object are identified in consecutive frames. One disadvantage of this approach is that it allows only few changes between frames and thus a much higher frame rate is needed.

Motion analysis methods are generally more sensitive to noise while the first approach is more robust.

The following Figure 3.17 shows an example of an early technique to identify motion in consecutive frames by creating a difference image. The images in Figure 3.17 show a simple subtraction of two consecutive images. Areas of many changes between frames are bright while few changes are represented by dark areas. The bottom half of the cell in Figure 3.17 moved upwards, hence the bright area.

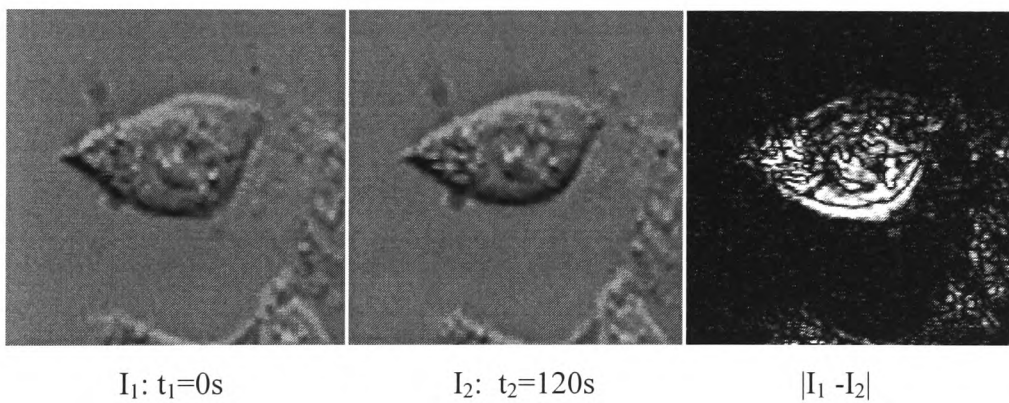


Figure 3.17: A single HT115 colon cancer cell shown at  $t_1=0s$  and  $t_2=120s$ . The third image shows the absolute difference between the two image frames.

However, the differences between image frames should only be an indicator of movement and may be used to quantify the motion of isolated objects. Cells express changes at the boundary as well as within the cytoplasm and the difference technique would thus not be sufficient to describe their movement.

The tracking technique developed for the adaptive spline method combines the two approaches described in the section above. Spatial information is used to fit the spline boundary according to the gradient while temporal information from the movement of small regions is gathered to approximate the cells motion. In this method, the movement of a cell is described by the movement of its boundary. Since the boundary constitutes several control points, the movement of the cell is determined by the relocation of each control point. This forms a new spline based *spatio-temporal* approach to tracking objects. Alternatively, the control points may also be moved manually by an operator if necessary.

In summary, the motion of control points on the boundary is approximated using an area matching technique. A confidence parameter  $C_{\text{flow}}$  [0..1] (pixel flow) is calculated according to how well the found position compares to the position in the previous frame.

In a second step, the location of each control point will also be determined by moving the points to high gradients which are expressed by the cell boundary. However, the spline will only adjust its points towards an edge if there is sufficient evidence of an edge. A confidence parameter  $C_{\text{gradient}}$  [0..1] is calculated for each control point which gives an indication of whether an edge has been located in the neighbourhood of the control point and how well it is able to fit to this boundary. This uses *a priori* knowledge about the cell boundary (e.g. closed, continuous curvature). The edge fitting can be guided by the result of the pixel flow estimation. One novel aspect is that the final location of a control point is determined by a decision making process based on the newly introduced *confidence parameters*.

The control points also form an interface between the user and the spline model. This enables an interactive process and final control over the delineated contour by the operator. The following schematic in Figure 3.18 shows this concept of the control point relocation.

Image features are detected by using low-level imaging functions such as edge detection and motion analysis. Unlike snakes, image features do not directly determine the position of the contour. The image information gathered from low-level imaging techniques in the vicinity of control point is passed to a decision making process which ultimately relocates the position of each point. The constituent parts of the image features used are shown in the Figure 3.19.

The proposed discrete spatial-temporal model is based on this decision making process for all control points using the image features described above. The following sections describe the calculation of pixel flow features (section 3.3.1) and the gradient features (section 3.3.2). Section 3.3.4 describes the decision making process used in the point relocation strategy.

### 3.3.1 Pixel Flow Property in Point Relocation

The control points which the spline boundary is made of, need to be relocated in order to track the movement of the cell membrane. The aim of the pixel flow analysis is to provide an approximation of the movement of individual control points. In this section a technique is developed based on region matching which approximates the movement of a control point close to the cell boundary.

As described in the literature review, motion in images can be determined by a number of methods, including spatial-temporal techniques and cross-correlation techniques.

An analogy to fluid analysis has been made by Horn *et al.* [1985] where the ‘flow’ of pixels is assessed and described as ‘optical flow’. However, this approach relies on

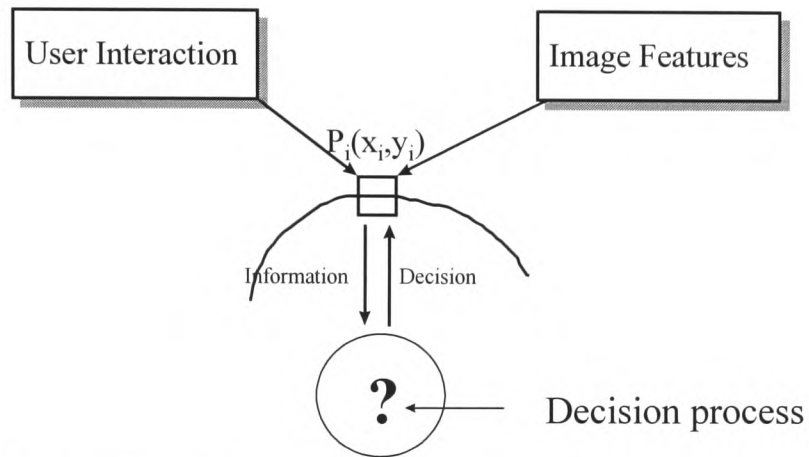


Figure 3.18: Schematic model of point relocation of spline boundary

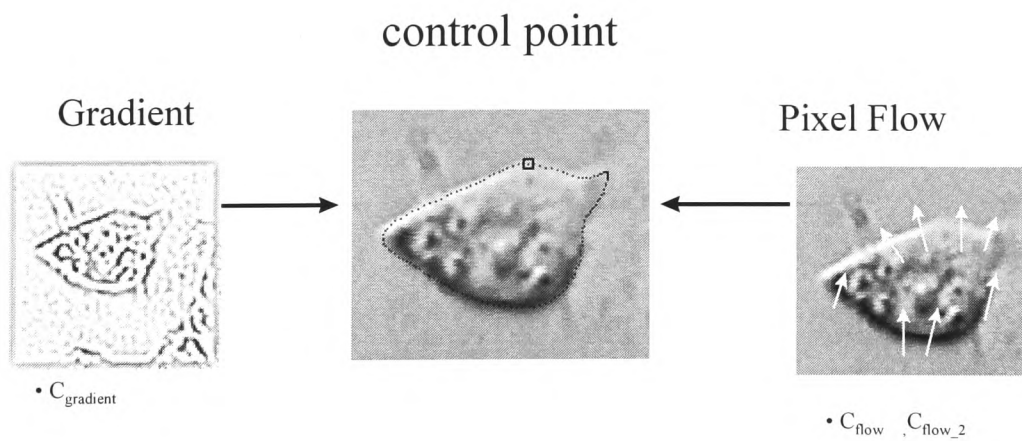


Figure 3.19: Image features used to determine the repositioning of individual control points. Gradient features are used to fit the spline to edges while the pixel flow is used as an approximation of control point motion as indicated by white arrows in the image.

intensity gradient. The flow parameter is anticipated to be independent of the image gradient since the gradient is used separately for relocation purposes. In this instance, the movement of the neighbourhood area  $A_{jk}$  around a control point will be estimated using the sum of squared differences between the area  $A_{jk}$  and any possible location in a specified search space  $A_{mn}$  between consecutive frames as illustrated in Figure 3.20.

The sum of squared differences in area can be calculated as following:

$$D_{flow} \approx \min \sum_{m,n} (A_{jk} - A_{mn})^2 \quad (3.11)$$

In its simplest form, each control point is relocated to the position with a best fit, or the least difference  $D_{flow}$ . In an ideal situation,  $D_{flow}$  equals zero. The range of values for  $D_{flow}$  is [0..25] in a 5x5 region. As with any decision making process, it is important to know how reliable the information provided is. In this case, it is anticipated to describe the *confidence* of the flow parameter  $D_{flow}$ .

The confidence parameter of pixel flow  $C_{flow}$  will be defined as following.

$$C_{flow} = \begin{cases} 1 - D_{flow} & \text{if } D_{flow} \leq 1 \\ 0 & \text{if } D_{flow} > 1 \end{cases} \quad (3.12)$$

Areas that match well express little difference ( $D_{flow} \leq 1$ ) and hence will express a high confidence parameter  $C_{flow}$ . Areas with larger differences are not taken into account ( $C_{flow} = 0$ ). Thus, the confidence parameter has the range [0..1]. The pixel flow is calculated at the exact location of each control point.

However, misfits can occur due to noise and hence it would not be sufficient to rely on a single fit. To overcome the problem, the flow confidence  $C_{flow}$  for every pixel ( $C_{flow_i}$ ) within a small region around the control point is calculated. The influence of a possible misfit is minimised by using the weighted sum of the possible movement

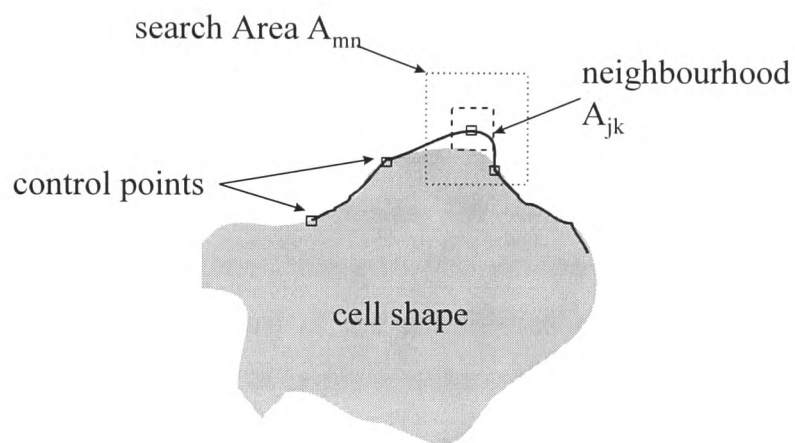


Figure 3.20: Relocation with region matching: The sum of squared differences between the neighbourhood region  $A_{jk}$  in frame  $F_1$  and regions of the same size within the search space area  $A_{mn}$  in frame  $F_2$  are calculated.

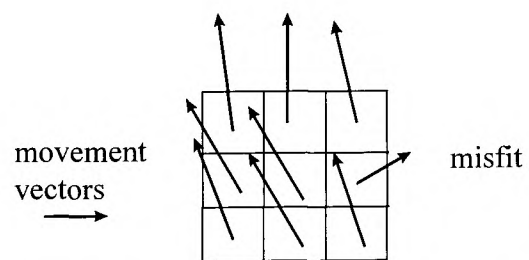


Figure 3.21: Movement vectors around a small 3x3 region with one misfit.

vectors within that small region as shown in the illustration in Figure 3.21. The influence of each movement vector is weighted according to its pixel flow confidence  $C_{flow_i}$ . The total new confidence parameter is now calculated as

$$C_{flow} = \frac{1}{n} \sum_i C_{flow_i} \quad (3.13)$$

where  $n$  is the number of pixels in the region around the control point and  $C_{flow_i}$  is the confidence parameter of each pixel in that area.

Choosing the right size for the search area  $A_{mn}$  can be quite difficult. If the search space is too small, the correct location may be outside this area while an area too large increases the possibilities of misfits. The search area ( $A_{mn}$ ) size of 9x9 was found to be sufficient combined with a neighbourhood area ( $A_{jk}$ ) size of 5x5. In some cases, however, the movement of the cell superseded the search space area. To overcome this problem without having to increase the search area, the method of area matching is performed at two different scales. A second confidence parameter  $C_{flow\_2}$  and its movement vector is introduced which describes the pixel flow at a coarser scale. The same tracking is performed at full and half the original scale and a decision is made on the basis of the higher confidence value.

Figure 3.22 shows the occurrence of confidence values  $C_{flow}$  during the tracking of a single cell for 2 ½ minutes. The tracking was performed for seven consecutive frames with  $\Delta t = 20s$ . The majority of confidence values was observed between 90 % and 100 %.

Fast moving cells may move outside the search space at the original scale which results in a poor  $C_{flow}$ . In this case, a better result may be achieved by relying on the pixel flow estimation at half the original scale if  $C_{flow\_2}$  expresses a sufficient high confidence. Figure 3.23 shows the occurrence of confidence parameters at half the resolution. There are fewer confidence values at the lower end of the scale, however, tracking at half the scale introduces an inherent error of one pixel displacement. A

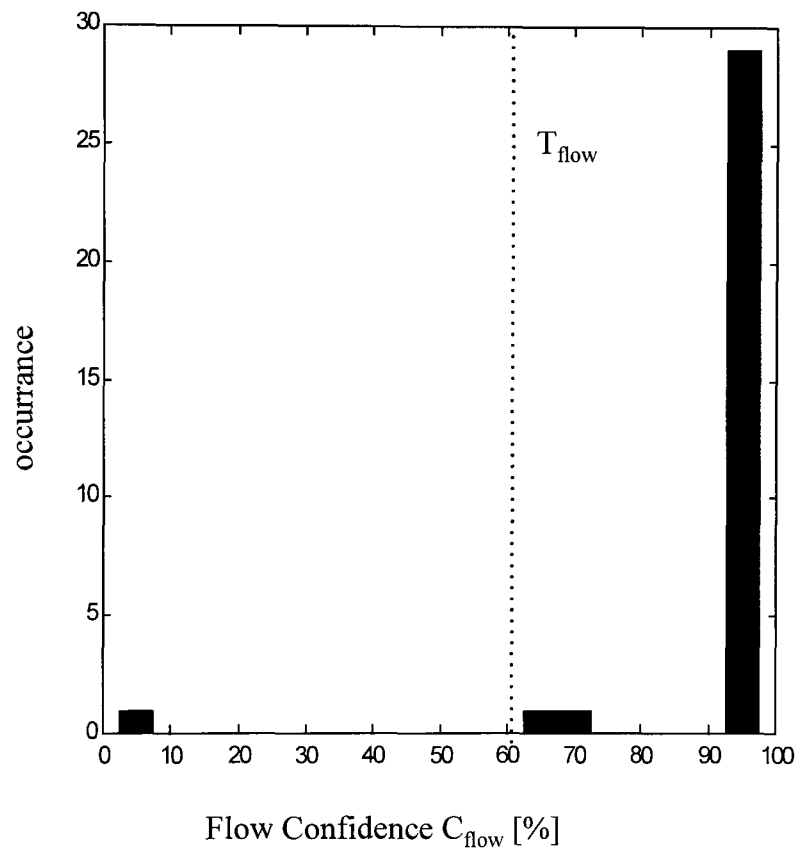


Figure 3.22: Distribution of flow confidence values during a single tracking procedure for 16 control points for five image frames. The tracking was performed at full resolution. The neighbourhood area was 5x5 using a 9x9 search space. The dotted line shows the suggested threshold value of  $T_{\text{flow}} = 60$ .

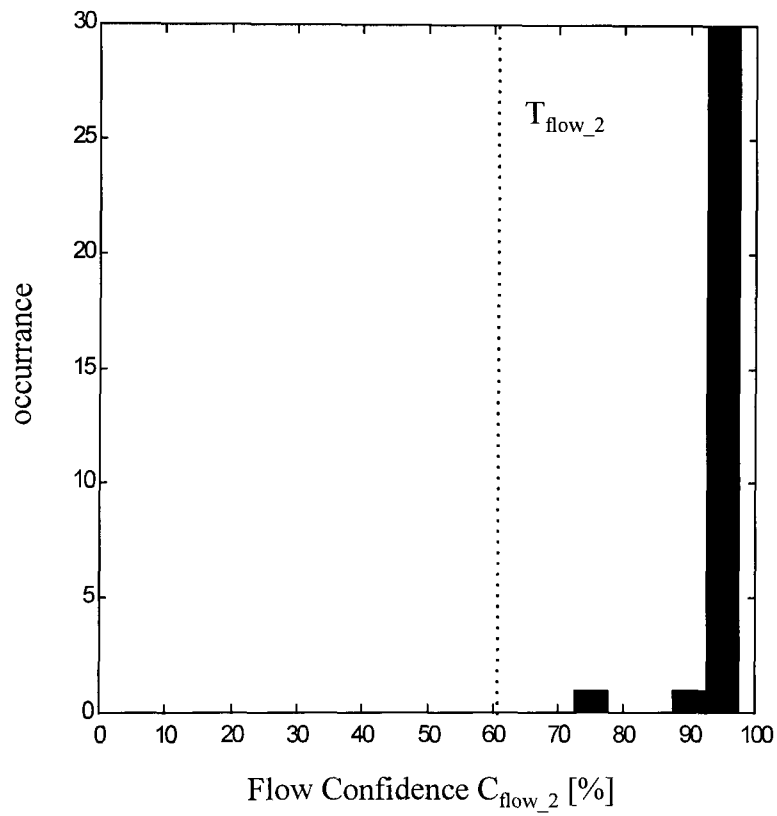


Figure 3.23: Distribution of flow confidence values during a single tracking procedure for 16 control points for five image frames. The tracking was performed at half full resolution. The neighbourhood area was 5x5 using a 7x7 search space. The dotted line shows the suggested threshold value of  $T_{\text{flow}_2} = 60$ .

threshold parameter  $T_{\text{flow}}$  (and  $T_{\text{flow}_2}$ ) was defined which decides whether a pixel position suggested from the area matching technique is considered a valid estimation. A threshold value of 60% was found to be appropriate.

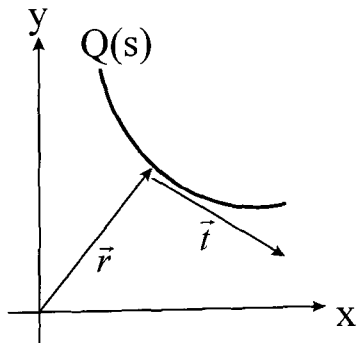
### 3.3.2 Gradient Based Property

The fitting and relocation of the cell boundary happens at the control points only. The area around the neighbourhood of the control points is searched for a closer fit of the spline segment.

Several strategies to locate a boundary are possible

- maximum gradient along orthogonal profile
- maximum gradient along normal profile
- maximum gradient in area

In each of these cases, the spline is placed initially close to the cell boundary or partly on the boundary. For example, the image in Figure 3.24 shows the gradient of an elliptical shape with the initial placement of the spline boundary. In this simple example, the boundary can be located by searching along the orthogonal profile for the highest gradient along the normal profile of each control point. From each position along the spline boundary, the tangential vector  $\vec{t}$  can be calculated. The vector  $\vec{r}$  describing a point on a curvature  $Q(s)$  is denoted as



$$\vec{r} = \begin{pmatrix} X(s) \\ Y(s) \end{pmatrix}$$

$$\vec{t} = \frac{\vec{r}(s + \Delta s) - \vec{r}}{\Delta s}$$

(3.12)

The normal vector, defined at  $\Delta s \rightarrow 0$ , yields [Papular, 1991]

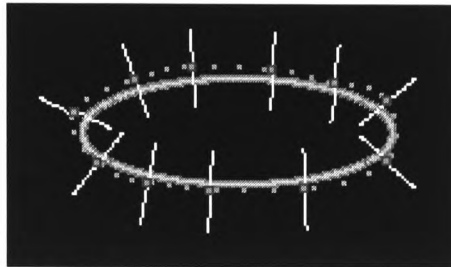


Figure 3.24: Gradient image of simple shape with spline approximation and gradient profiles (white) prior to the fitting process.

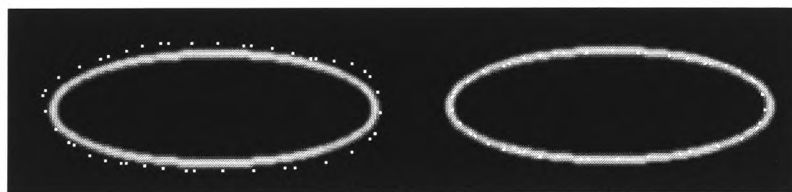


Figure 3.25: Simple cell shape before (left) and after spline fitting process (right).

$$\lim_{\Delta s \rightarrow 0} \frac{\vec{r}(s + \Delta s) - \vec{r}}{\Delta s} = \begin{pmatrix} X'(s) \\ Y'(s) \end{pmatrix}. \quad (3.13)$$

The tangential vector is therefore calculated from the derivatives of each component of the parameters describing the curvature. Applied to the spline curvature  $Q(X(u), Y(u))$ , the normal vector  $\vec{n}(u)$  can be calculated as

$$\vec{n}(u) = \begin{pmatrix} -Y'(u) \\ X'(u) \end{pmatrix}, \text{ hence } \vec{n}(u) = \begin{pmatrix} \frac{-y'(u)}{\sqrt{x'(u)^2 + y'(u)^2}} \\ \frac{x'(u)}{\sqrt{x'(u)^2 + y'(u)^2}} \end{pmatrix} \quad (3.14)$$

By calculating the orthogonal profile for each control point, in this instance, the highest gradient along the profile denotes the new position of the control point. Each control point is moved according to this criterion. Figure 3.25 shows the spline before and after this fitting procedure in the simple test image.

Usually, the gradient image is not as clear as in this simple example. Noise and other artefacts may provide high gradient values not only on the boundary but also inside the cell and on the outside of the cell. It is therefore not sufficient to rely on a single high gradient along the orthogonal gradient. A boundary is found whenever there are a number of gradient values along the spline segment in the neighbourhood of each control point. This condition is used as a criterion for the location of a boundary segment. Figure 3.26 shows the principle of the new criterion. The sum of the gradient along the short spline segment (marked a) is calculated. The boundary is located according to the maximum negative gradient (Prewitt filter template) which is accumulated over  $\pm 3$  positions on both sides of the control point. The search space is a vector along the normal vector. The minimum sum of the gradient is taken to be the best fit of the spline to the boundary. This forms the basis for the gradient confidence parameter.

$$C_{\text{gradient}} = 1 - \frac{1}{n} \sum_n f(x, y) \quad (3.15)$$

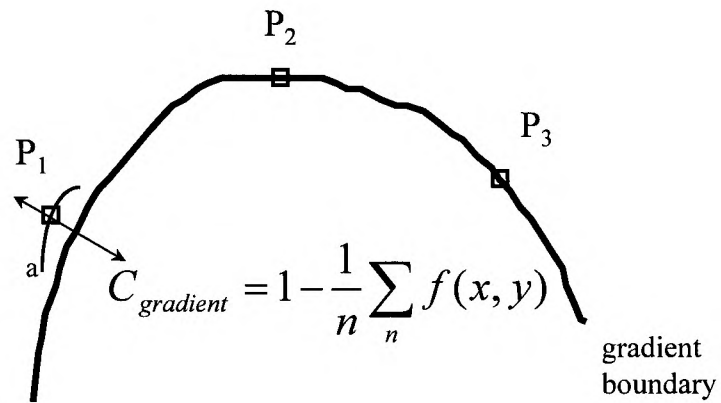


Figure 3.26: The confidence parameter of a spline fit to the boundary is calculated as the sum along the spline segment  $a$  in the neighbourhood of each control point over  $n$  pixels.

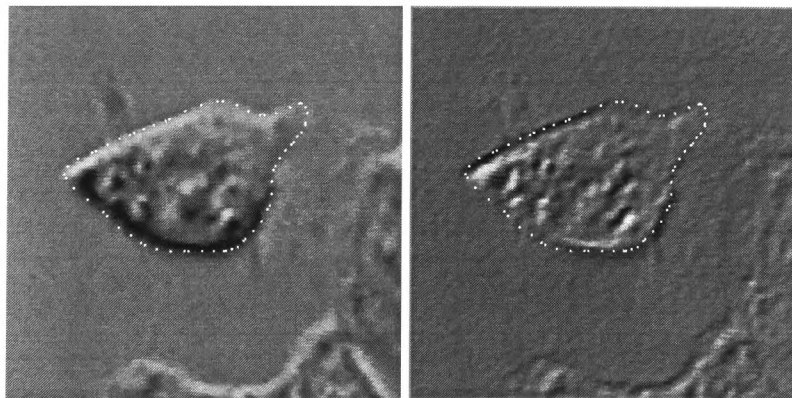


Figure 3.27: Example of spline fitting using the maximum negative gradient using a 5x5 Prewitt filter mask along the spline profile.

The confidence parameter of the gradient provides a high reading if there is a sufficient gradient (low intensities in gradient image) along the boundary. Figure 3.28 shows the distribution of gradient confidence values during the tracking procedure of a single cell through 7 frames. The majority of confidence values appeared to be above 60% which then became the threshold for a sufficient gradient  $T_{\text{gradient}}$ .

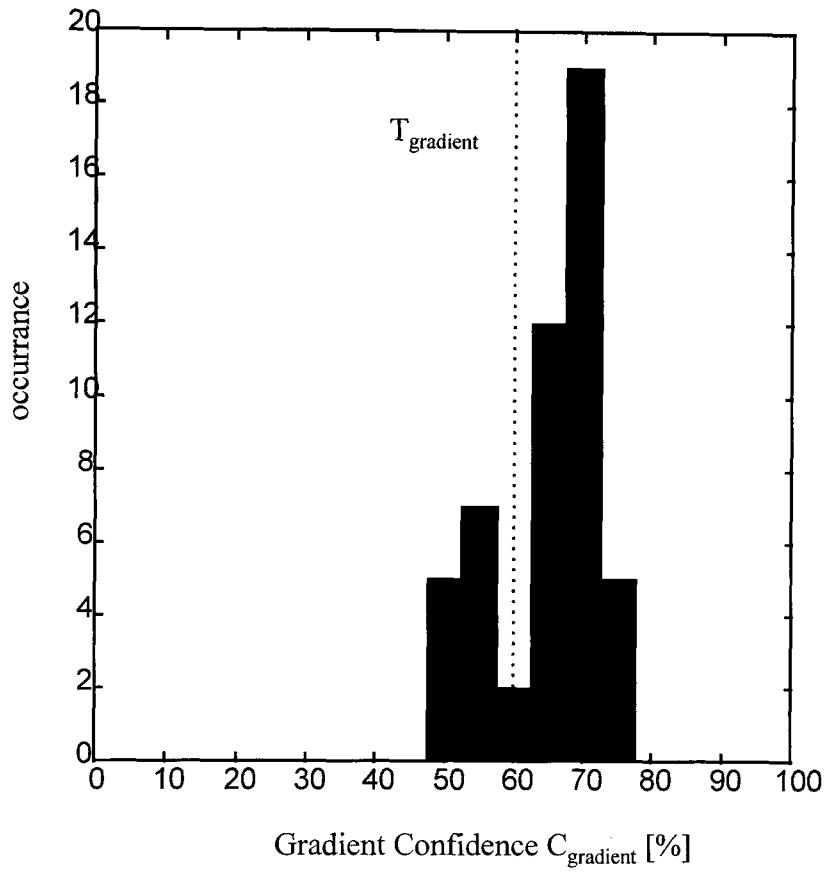


Figure 3.28: Distribution of gradient confidence values during a single tracking procedure for 16 control points for five image frames. The neighbourhood area was 3-3 along the normal profile using a 7-7 search space. The dotted line shows the suggested threshold value of  $T_{\text{gradient}} = 60$ .

### 3.3.3 Point Relocation Strategy

The point relocation mechanism is illustrated in Figure 3.29. The spline consists of a piecewise cubic interpolation between salient control points. These control points are placed initially on the cell boundary at the beginning of the tracking process and subsequently relocated on the basis of a decision making process on gradient and pixel flow information.

The **boundary rendering** describes the calculation of the spline coefficients from the position of the salient control points. Furthermore the re-sampling of the spline points is also part of the boundary rendering.

The **relocation process** is performed individually for each control point based on the image information (Figure 3.30) and confidence parameters  $C_{\text{flow}}$ ,  $C_{\text{flow}_2}$  and  $C_{\text{gradient}}$ . These parameters are calculated from the image data as shown in Figure 3.31 and described in the previous sections. The flow property is used as an initial approximation of the point movement. The flow is estimated at two different scales, full and half scale, which results in the calculation of two confidence parameters  $C_{\text{flow}}$  and  $C_{\text{flow}_2}$ . A decision is made as to which estimation to use on the basis of the higher confidence value.

Both pixel flow and gradient parameters are an average of several individual values. A threshold is introduced to ensure enough evidence of good confidence in both types of confidence values. Only if  $C_{\text{flow}}$  or  $C_{\text{flow}_2}$  are above a threshold  $T_{\text{flow}}$  or  $T_{\text{flow}_2}$  respectively, is then the flow estimation used to move the control point to a new approximate position. Gradient information is used in a subsequent boundary-fitting step, if the gradient confidence  $C_{\text{gradient}}$  is above a threshold  $T_{\text{gradient}}$ . If no sufficient confidence in either flow or gradient is available, the control point remains in the previous position. Figure 3.32 shows a flow diagram of the decision-making process for each control point. The technique can be described as a flow guided gradient fitting process based on confidence parameters used in a deterministic decision making process.

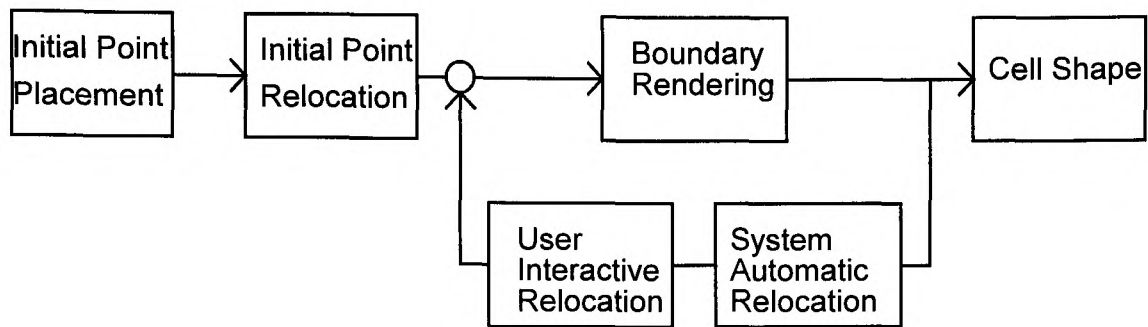


Figure 3.29: Schematic of point relocation process.

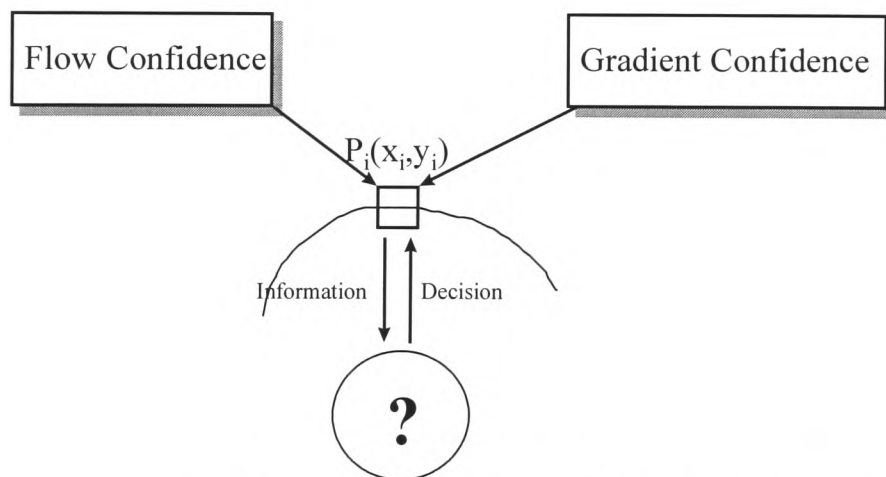


Figure 3.30: Schematic of relocation process for an individual control point.

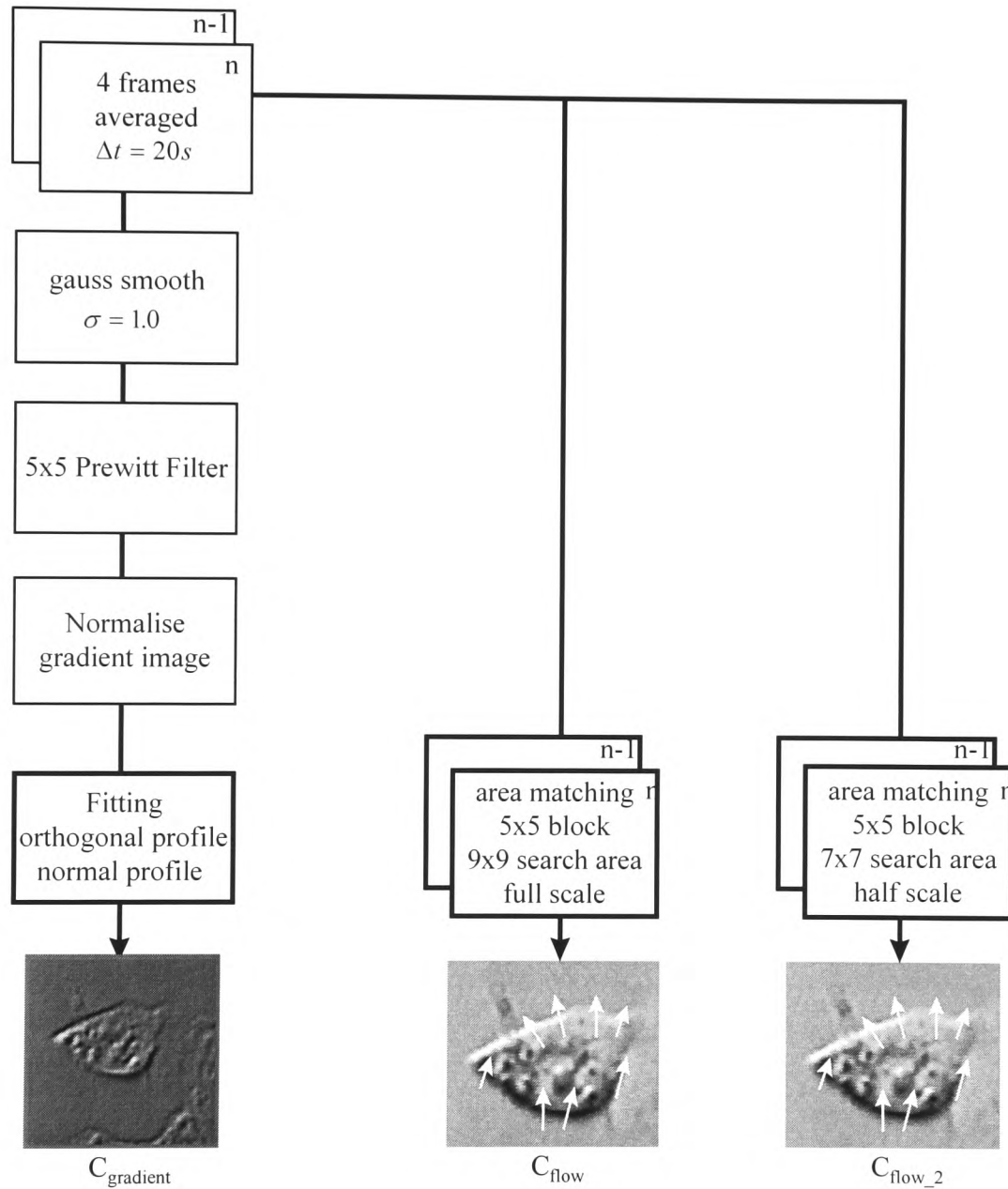


Figure 3.31: Schematic of image processing techniques used for image segmentation and tracking. These three components are used for the point relocation. For each component, a confidence parameter is calculated.

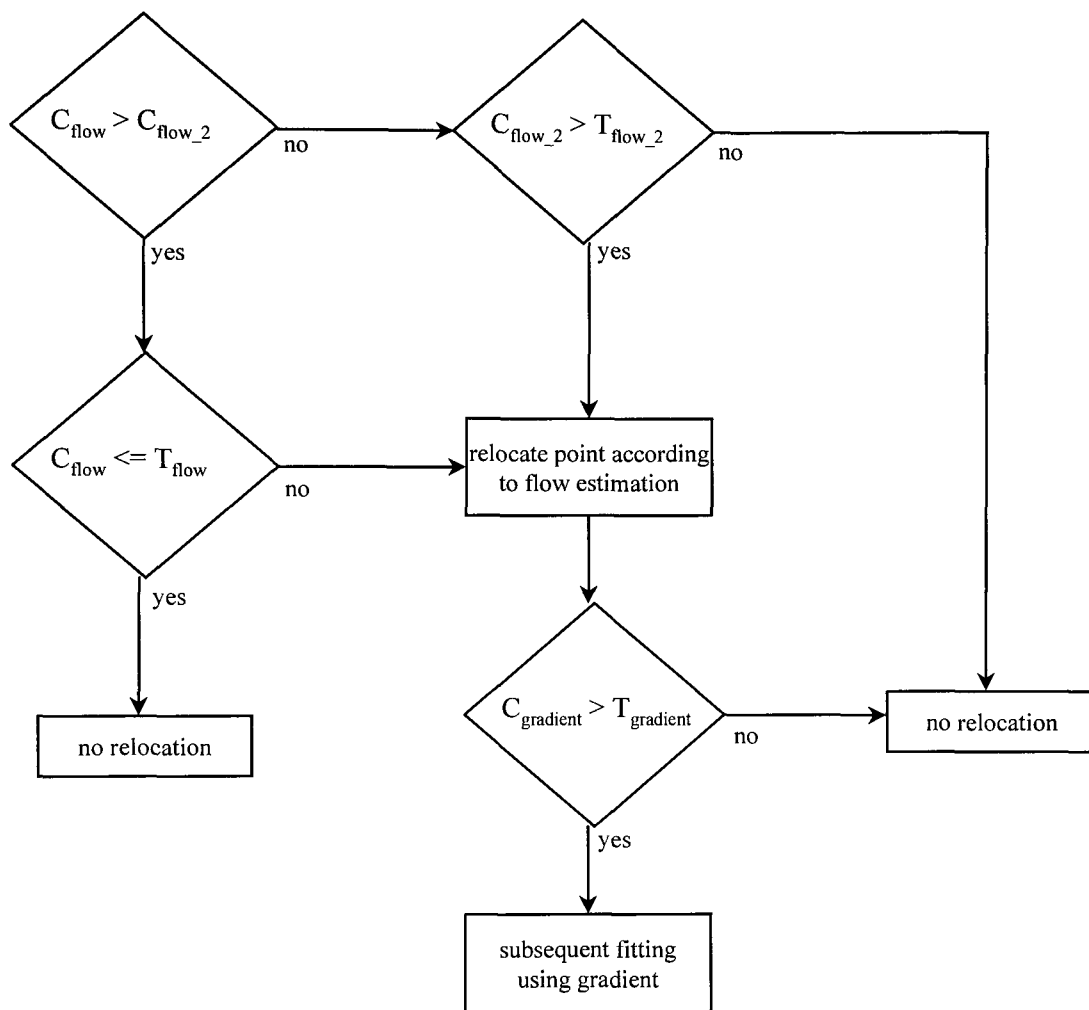


Figure 3.32: Flow diagram of point relocation process based on a decision tree and confidence parameters.

### 3.4 Cell Shape Parameters

#### Cell Area

Once the shape of the boundary has been defined mathematically, the area  $A_i$  under each spline segment  $Q_i(u)$  can be calculated as

$$A_i = \int_{(A)} Q_i(u) du . \quad (3.16)$$

All boundary segments are described mathematically and thus the centre of area (centroid) can be determined mathematically from the cubic spline equation. The total area is calculated as the sum of the area underneath  $n$  segments.

$$A = \sum_n A_i \quad (3.17)$$

Depending on the orientation, areas may be positive or negative. The area  $A_i$  for a segment  $Q_i$  can be calculated as

$$A_i = \int_0^1 Y_i(u) \frac{\partial X_i(u)}{\partial u} du . \quad (3.18)$$

#### Cell Centroid

The centre of area  $P(x_c, y_c)$  is calculated as [Papula 1991]

$$x_c = \frac{1}{A} \int_{(A)} x dA \quad y_c = \frac{1}{A} \int_{(A)} y dA \quad (3.19)$$

Again, the centroid is calculated for each segment first and the total overall position of the cell is calculated from the individual position and area of each segment as shown in equation 3.14.

$$x_i = \frac{1}{A_i} \int_0^1 Y_i(u) X_i(u) \frac{\partial X_i(u)}{\partial u} du \quad y_i = \frac{1}{2 A_i} \int_0^1 Y_i^2(u) \frac{\partial X_i(u)}{\partial u} du \quad (3.20)$$

The equations 3.18 and 3.20 are explained further in appendix D.

The centroid of the cell ( $X_c$ ,  $Y_c$ ) is then calculated from the centroid and area of each segment such

$$x_c = \frac{1}{\sum A_i} \sum x_i A_i \quad y_c = \frac{1}{\sum A_i} \sum y_i A_i . \quad (3.21)$$

The area and centroid are calculated only from the mathematical model. This is different from pervious methods that use pixel counting as a means of determining the centroid and area.

### Perimeter Length

The total perimeter length is calculated as the sum of the length of each segment

$$L = \sum_n L_i , \quad (3.22)$$

while the length of each segment can be calculated as

$$L_i = \int_0^1 \sqrt{[X_i'(u)]^2 + [Y_i'(u)]^2} du \quad (3.23)$$

### Shape parameter

As a shape descriptor, a parameter independent of size is needed. A common choice is the roundness of an object as defined [Schnorrenberg *et al.*, 1997]

$$roundness = \frac{perimeter^2}{4\pi \cdot area}. \quad (3.24)$$

This shape parameter, which is of no dimension, expresses a value of 1 if the shape is a perfect circle and increases in value the more complex the shape of an object gets.

### **3.5 Concluding Remarks**

In this chapter the development of a novel adaptive spline method was described. The method uses control points placed on the boundary to form a piecewise cubic interpolation of the cell membrane. Control points can be moved manually and adjusted, added or deleted. A cell can be easily manually segmented with this method.

The spline model was developed into an adaptive spline that is enabled to track and adapt itself to non-rigid deformations of the cell boundary. Tracking is facilitated by combining gradient and flow information in the neighbourhood of control points using a novel decision making process to minimise false identifications in a clustered environment. The interactive nature of the method and the ease of use make it suitable for tracking clustered cells where a fully automated system may fail to operate. The time involved in monitoring cells interactively can also be used for observations about their behaviour.

## 4 Validation

### 4.0 Introduction

Validation of the new method involved the definition of an objective method to compare the results achieved with a well established method. Cell images can be segmented in many different ways and it was potentially difficult to find a ‘best’ segmentation method to compare with. The adaptive spline method was therefore validated against artificial objects with known area and shape and against manually segmented cell images. The comparison of two segmentation methods may be performed in many ways. Wilkinson [1998] suggested two methods by which systems can be compared with a ‘gold standard’.

- Results generated by two methods are compared
- Parameters describing the results are compared

For example, a cell segmented by two different systems may express the same area but still have differences in shape. Overlaying the two segmented cell areas would yield the ‘true’ difference between these two methods. However, it may be difficult to find a ‘gold standard’ to compare with. In the case of cells, the exact location of the boundary can be slightly ambiguous. Therefore, the segmented area was compared (overlaid) with an artificial test image. Cell images, however, were compared by measured parameters, such as area, position and roundness.

The adaptive spline method was first validated against the area and shape of a know artificial test object (Section 4.1). In section 4.2 the variability of the spline method due to different operators was analysed. The spline may be initialised differently and the variability introduced is an important factor. Section 4.3 assesses the repeatability of the semi-automatic tracking of a clustered cell. Finally, section 4.4 describes the influence of gradient and flow properties on the accuracy of the tracking of single and clustered cells.

### 4.1 Segmentation of test object

The aim of this test was to investigate the accuracy of the adaptive spline method by applying it to an artificial test object of a known size and shape. Two test objects were created, a circle with a diameter of  $20\mu\text{m}$  and a single cell cut out of a cluster and placed on a uniform background.

#### Circle

The circle was of similar size to HT115 cells viewed at x320 magnification. It had a diameter of  $21\mu\text{m}$  (79 pixels), an area of  $357\mu\text{m}^2$  (4901 pixels), a perimeter length of  $66\mu\text{m}$  (248 pixels) and a roundness of 1.0.

The circle was defined six times by manually placing salient control points onto the boundary. No automatic fitting procedure was applied and the circle was defined using 4, 6 and 8 control points.

The six definitions were compared against the known area and shape of the circle. The error in area was calculated on the basis of the differences (XOR) between the circle image and the spline image. Perimeter length, roundness and position were compared against the calculated values from the circle dimensions. From six consecutive definitions, the maximum error was calculated as displayed in Table 4.1.

Control points:	4	6	8
<b>area</b>			
max error [%]	4.55	6.9	7.49
<b>perimeter</b>			
max error [%]	1.61	2.02	2.02
<b>roundness</b>			
max error [%]	0.93	1.07	2.85
<b>position</b>			
max displacement [ $\mu\text{m}$ ]	0.27	0.27	0.27

Table 4.1: Maximum error in describing a circle with the adaptive spline method.

The circle was defined six times using 4, 6 and 8 control points.

The maximum error in area was 7.5% while the maximum error in perimeter length was just over 2%. There was a tendency of placing control points onto the outer boundary of the circle, increasing the size and hence the error in area. The maximum

error in roundness was 2.85%. The position of the circle, which was determined by calculating the centroid from the spline coefficients, was in good agreement with the actual position. There was a maximum displacement of 1 pixel ( $0.27\mu\text{m}$ ) observed in all three cases.

### Cell

An image of a single cell was cut out of a cluster and placed on a uniform white background. A 3x3 median filter was applied to smooth the transition between cell boundary and white background. The cell was defined ten times with eight salient control points placed on the cell boundary. Figure 4.1 shows the test image to which the spline boundary was applied. Figure 4.2 plots the calculated area from the spline over ten trials in comparison to the actual area determined through pixel counting.

The actual area to which it was compared to was obtained by pixel-counting. The area was  $348\mu\text{m}^2$  and is represented by a horizontal line in the graph in Figure 4.2. It was observed that the actual area is slightly larger than the calculated area from the spline with a maximum error of 10%. This may be explained by the fact that the median filtering enlarged the cell boundary slightly. The median area was  $322\mu\text{m}^2$  while the range was from  $313\mu\text{m}^2$  to  $345\mu\text{m}^2$ .

## 4.2 Segmentation of real cell images

The aim of this test was to investigate the inter-observer and intra-observer variability in defining the cell boundary using the adaptive spline method. An image of a single cell viewed by HMC was defined six times by three independent observers. Also, an image of a clustered cell viewed by HMC was defined six times by the same independent observers. Cell boundaries were defined by placing salient points on the cell boundary while the computer formed a closed boundary each time a control point was added. The two cells are shown in Figure 4.3. The results from the segmentation was tested as to whether the definition of the cell boundary by the individuals was consistent with a normal distribution. Figure 4.4 shows the result of the Ryan-Joiner test of normality [Altman, 1991] for cell area in 18 cell definitions by three individuals.

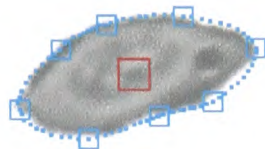


Figure 4.1: Test image with delineated spline boundary (blue)

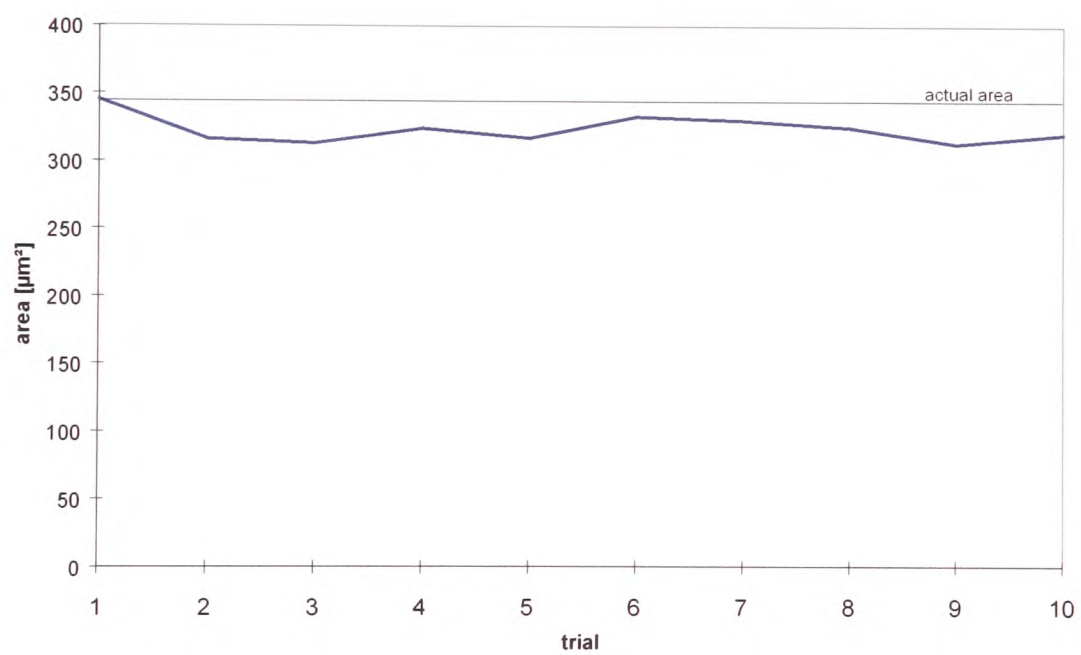


Figure 4.2: Area of test object in ten trials.

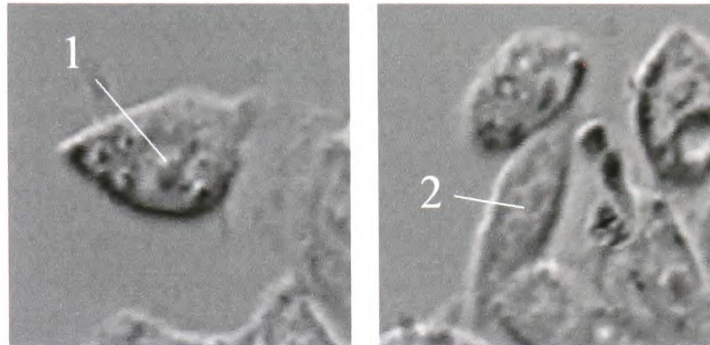


Figure 4.3: Two test cells which were defined six times each by three independent observers. A total of 18 cell definitions were acquired per image.

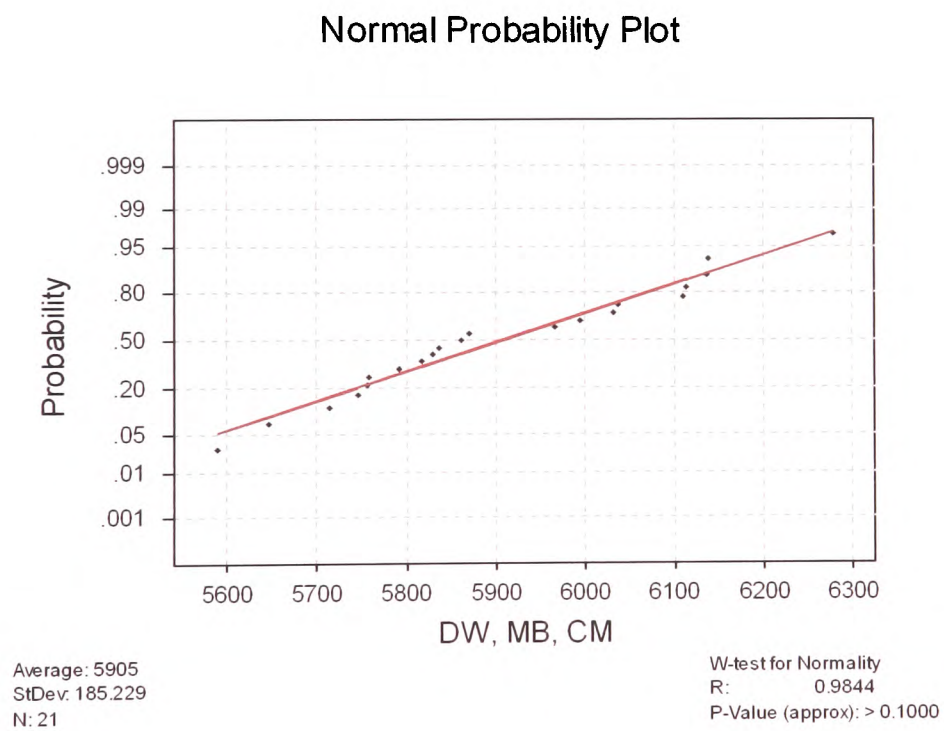


Figure 4.4: Ryan-Joiner test of normality from the 18 cell definitions

The analysis suggested that the definition of the cell boundary was consistent with being normally distributed. The mean value over 18 definitions was then used as the control area.

<b>Trial Single</b>	<b>1</b>	<b>2</b>	<b>3</b>	<b>Control</b>
Area [pix <sup>2</sup> ]				
median	<b>5745</b>	<b>5994</b>	<b>6031</b>	<b>5905</b>
min	5589	5755	5816	5589
max	5835	6113	6278	6278
max error	<b>3%</b>	<b>4%</b>	<b>4%</b>	<b>6%</b>

Table 4.2: Results of the six trials of a single cell by three observers (1-3). The control column shows the actual (mean) cell area and the lowest and highest value in the three trials.

The individuals were consistent within each others definition of the cell boundary. There was a maximum error of 4% over the three observers. However, there was a difference between observer 1 and 2&3 in what was to be perceived as the cell boundary. Comparing the minimum and maximum area in all three observers to the average area of 18 definitions, the maximum error resulted to 6%.

<b>Trial Cluster</b>	<b>1</b>	<b>2</b>	<b>3</b>	<b>Control</b>
Area [pix <sup>2</sup> ]				
median	<b>3528</b>	<b>3398</b>	<b>3889</b>	<b>3594</b>
min	3343	3310	3670	3310
max	3607	3524	4057	4057
max error	<b>5%</b>	<b>4%</b>	<b>6%</b>	<b>13%</b>

Table 4.3: Results of the six trials of a clustered cell by three observers (1-3). The control column shows the actual (mean) cell area and the lowest and highest value in the three trials.

In the case of a clustered cell, the observers were less consisted within each others definition of the cell boundary than in the case of the single cell. There was a maximum error of 6% over the three observers. Again, there was a difference between observers 1, 2 and 3 in what was to be perceived as the cell boundary. Comparing the minimum and maximum area to the average area of 18 definitions, the maximum error increased to 13%.

To increase the consistency of cell definition, a fitting procedure was applied after the cell had been defined. This procedure moved each individual control point to the maximum negative gradient (5x5 Prewitt filter ) occurring in a  $\pm 7$  pixel area along the orthogonal profile. The fitting process is described in chapter 3.3.2 and is part of the relocation process.

<b>Trial Single</b>	<b>1</b>	<b>2</b>	<b>3</b>	<b>Control</b>
Area [pix <sup>2</sup> ]				
median	5982	6036	5999	6011
min	5886	5867	5864	5864
max	6065	6263	6347	6347
max error	2%	4%	6%	6%

Table 4.4: Results of the six trials of a single cell by three observers (1-3). The cell boundary was dynamically fitted according to the maximum negative gradient at the boundary. The control column shows the actual (mean) cell area and the lowest and highest value in the three trials.

The consistency between the three individual trials was improved. The median area across observers in Table 4.4 is more consistent than those in Table 4.2. However, the fitting process did not always seem to improve the observers definition of the cell boundary. The overall maximum error remained at 6%.

<b>Trial Cluster</b>	<b>1</b>	<b>2</b>	<b>3</b>	<b>Control</b>
Area [pix <sup>2</sup> ]				
median	3967	3917	4251	4045
min	3622	3882	4116	3622
max	4260	4063	4302	4302
max error	9%	4%	3%	10%

Table 4.5: Result of the six trials of a clustered cell by three observers (1-3). The cell boundary was dynamically fitted according to the maximum negative gradient. The control column shows the actual (mean) cell area and the lowest and highest value in the three trials.

The consistency of cell definition between the median area of the three trials was improved. The median area across observers in Table 4.5 is more consistent than those in Table 4.3. Comparing the minimum and maximum area to the actual cell

area calculated as the mean value of 18 definitions, the maximum error decreased to 10%.

### 4.3 Repeatability of semi-automatic tracking

The aim of this test was to investigate the repeatability in tracking cells using the adaptive spline method. A clustered human colon cancer cell was tracked semi-automatically over a period of 30 minutes in three trials. The velocity was calculated at a five minute interval. The cell was relocated using gradient information and the interactive user input whenever control points were not relocated properly from visual inspection. As shown in section 4.1, there was a displacement of one pixel in defining the cell boundary. An expected error in velocity was therefore calculated on the basis that there was an inherent error due to point displacement of one pixel (diagonal  $\sqrt{2}$  pixels). This resulted in an absolute error of  $\pm 5 \mu\text{m/h}$  measured in a 5 minutes interval as indicated by error bars in Figure 4.5. The cell was analysed three times and the result of the velocity calculations are shown in Figure 4.5. The median velocity of the three trials was used as the true velocity of the cell.

The results suggest a good repeatability within the limits of the expected error. On two occasions did the calculated velocity supersede the expected error of  $\pm 5 \mu\text{m/h}$ . A maximum error in velocity of  $7.5 \mu\text{m/h}$  was observed.

### 4.4 Automatic tracking

The aim of this test was to evaluate the performance of the automatic point relocation technique. For a short period of time (2 ½ minutes) a single cell and a clustered cell were tracked automatically without any interactive user involvement. Salient control points were placed on the cell boundary at the beginning of the tracking process and control points were relocated using flow and gradient information.

The automatic tracking was performed three times using different methods. Tracking was performed (1) using pixel flow estimation, (2) using pixel flow estimation at half

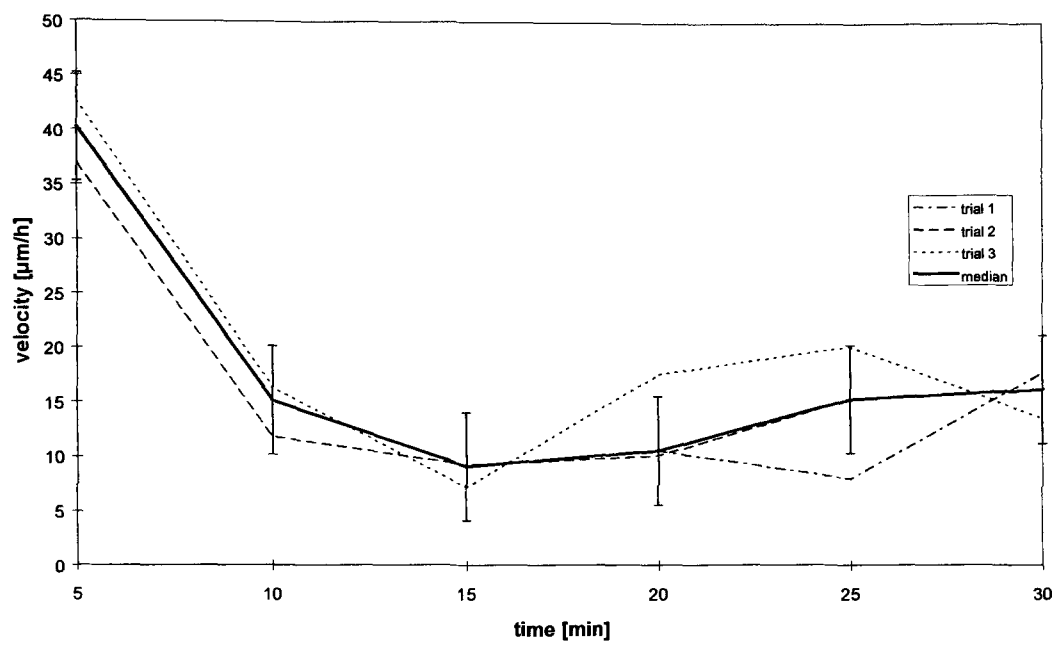


Figure 4.5: Velocity validation of a single cell where the velocity was calculated in three trials.

scale and (3) using gradient and flow in a decision making process described in chapter 3.3.3. The threshold values were set as following:  $T_{\text{flow}} = 60\%$ ,  $T_{\text{flow2}} = 60\%$ ,  $T_{\text{gradient}} = 60\%$ . The neighbourhood area size was 5x5 for both flow parameters. The size of the search space was 7x7 for flow/2 and 9x9 for flow. The gradient search region was  $\pm 7$  along the normal vector.

Figure 4.6 shows a single human colon cancer cell before and after the tracking has finished. The spline boundary was marked by a white contour, control points are not shown. The area values were compared with a manual segmentation of the cell boundary. Figure 4.7 shows the error in area using different tracking techniques. Tracking at a lower scale created a greater error (max. 15%) than tracking at the original scale (max. 8%). The gradient fitting combined with the flow estimation seems to produce the best results with a maximum error of 3% in area. There was a similar behaviour when assessing the perimeter length of the same cell. Figure 4.8 shows the error in percent in perimeter length during the tracking of a single cell. In one instance, however, the error was increased by the gradient fitting technique, perhaps due to misinterpretation of the gradient along the cell boundary.

The same test was performed on a clustered cell shown in Figure 4.9. The area values were compared with a manual segmentation of the cell boundary. Figure 4.10 shows the error in area using different tracking techniques. Tracking at a lower scale created a greater error (max. 13%) than tracking at the original scale (max. 11%). The gradient fitting combined with the flow estimation seems to produce the best results with a maximum error of 8% in area. Interestingly, the error in flow seemed to be larger than the flow estimation at half scale. This may be due to the fact that faster moving parts of the cell boundary are better followed at a lower scale. This was also observed when assessing the perimeter length of the same cell. Figure 4.11 shows the error in percent in perimeter length during the tracking of a clustered cell. The maximum error in perimeter length was 6% while the maximum error using the gradient and flow technique was reduced to 3.5%. In one instance, however, the error was increased by the gradient fitting technique, perhaps due to misinterpretation of the gradient along the cell boundary.

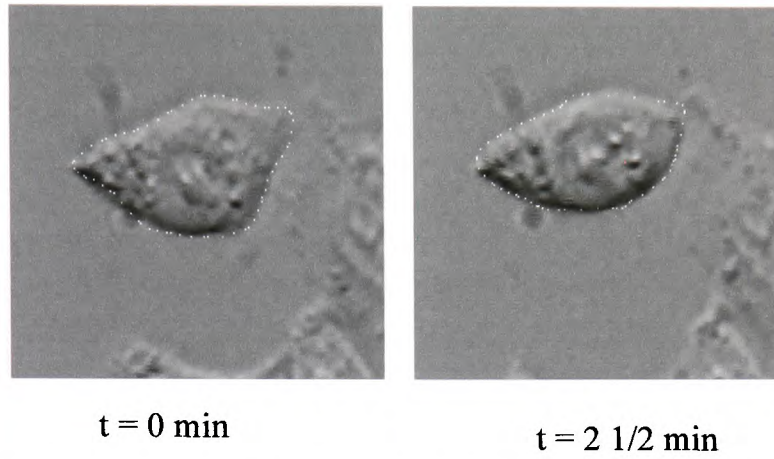


Figure 4.6: Example of tracking a single cell. Cell shown with delineated boundary at  $t=0\text{min}$  and  $t=2\frac{1}{2}\text{min}$ .

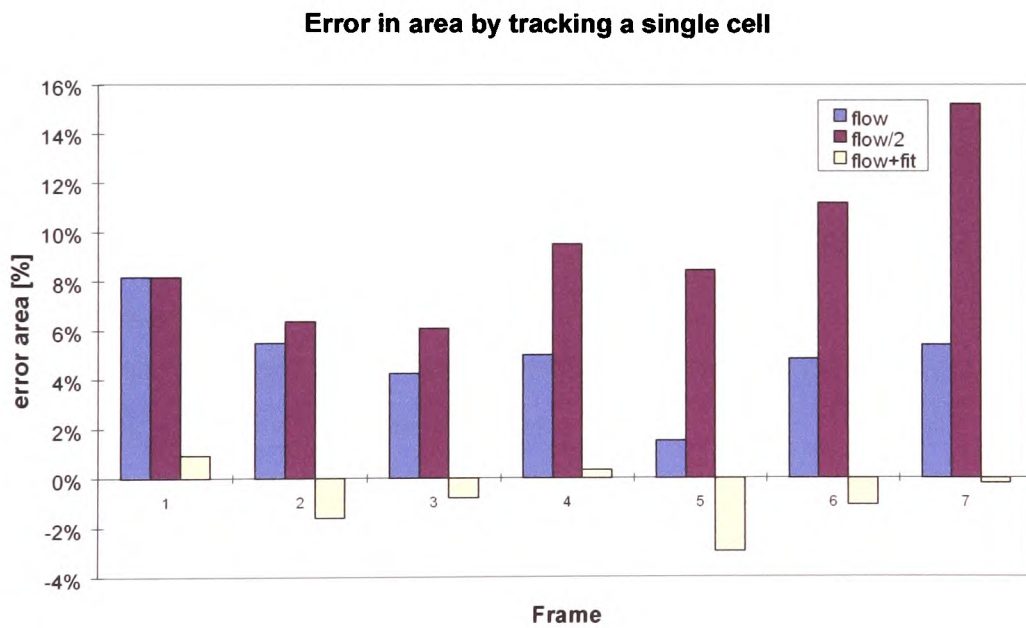


Figure 4.7: Error in percent in area during the tracking of a single cell in seven frames with a 20 second difference between frames. The blue and red bar show the error using the pixel flow property while the yellow bar shows the error when using gradient and flow for point relocation.

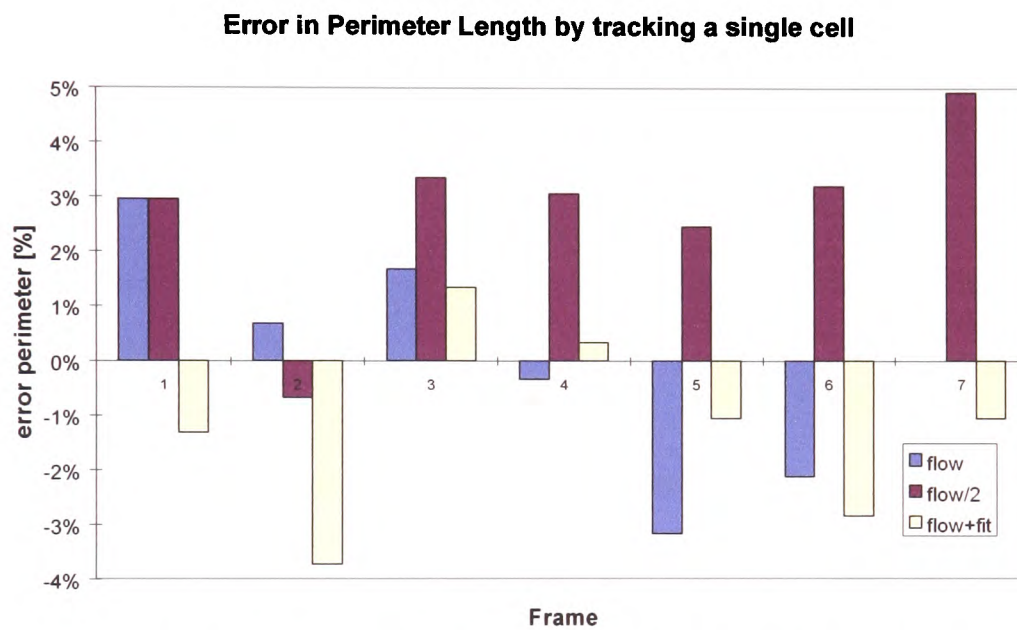


Figure 4.8: Error in percent in perimeter length during the tracking of a single cell in seven frames with a 20 second difference between frames. The blue and red bar show the error using the pixel flow property while the yellow bar shows the error when using gradient and flow for point relocation.

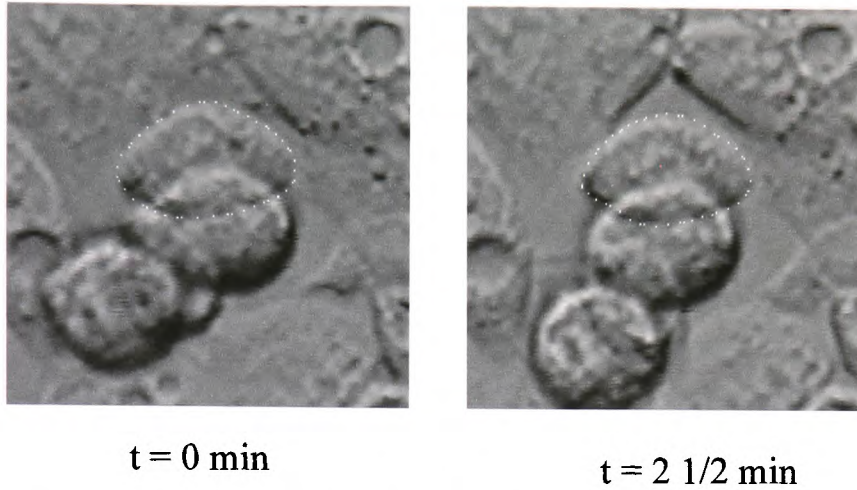


Figure 4.9: Example of tracking a clustered cell. Cell shown with delineated boundary at  $t=0\text{min}$  and  $t=2 \frac{1}{2} \text{ min}$ .

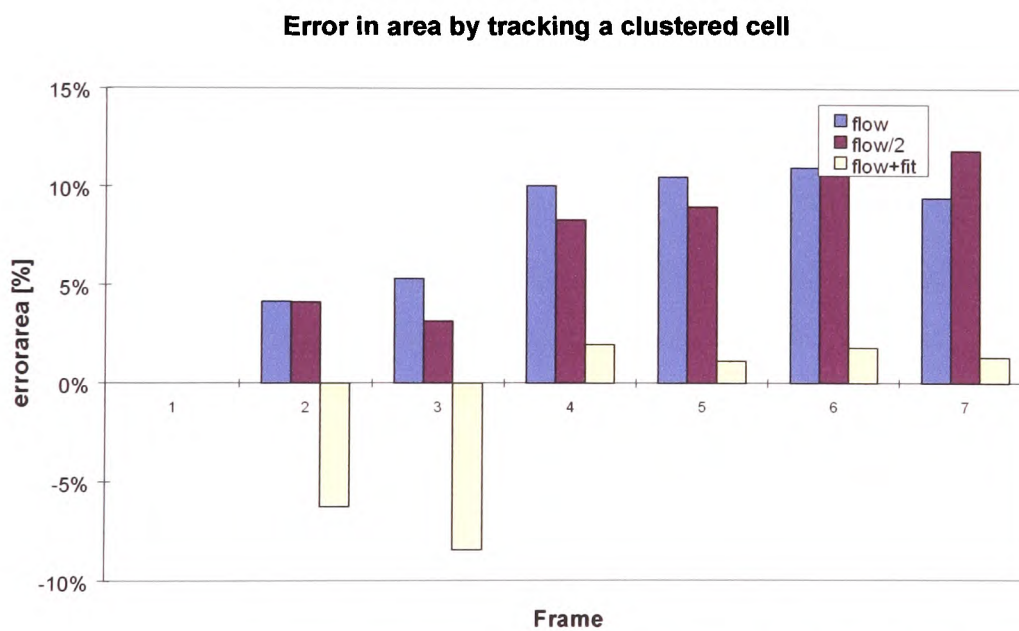


Figure 4.10: Error in percent in area during the tracking of a clustered cell in seven frames with 20 seconds difference between frames. The blue and red bar show the error using the pixel flow property while the yellow bar shows the error when using gradient and flow for point relocation.

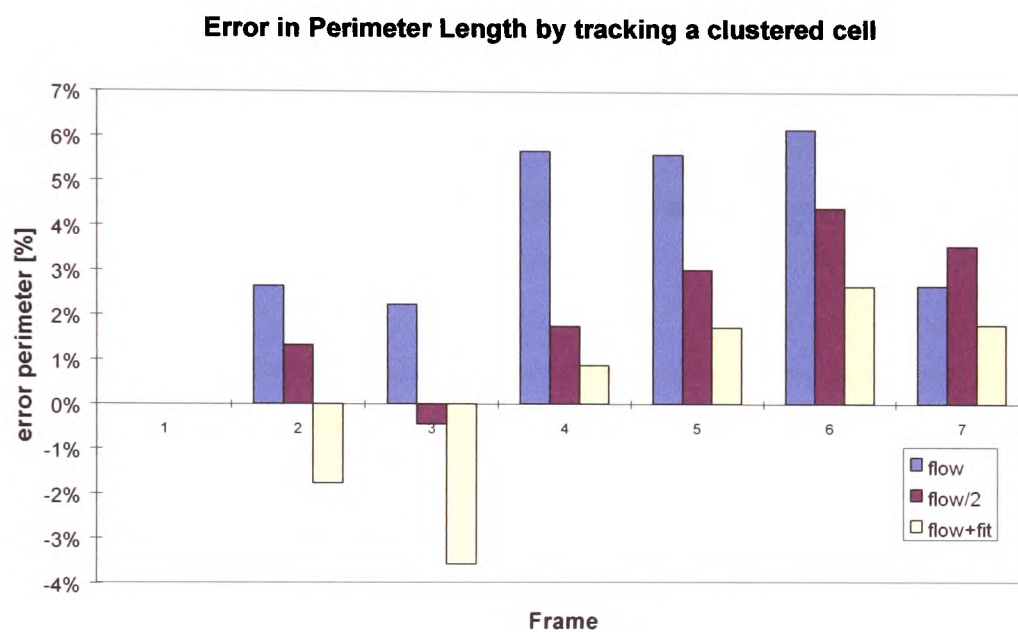


Figure 4.11: Error in percent in perimeter length during the tracking of a clustered cell in seven frames with a 20 second difference. The blue and red bar show the error using the pixel flow property while the yellow bar shows the error when using gradient and flow for point relocation.

## 4.5 Conclusion

The adaptive spline method was validated by analysing artificially generated objects and real cell images. A simple circle was used to test area and shape measurements with the spline method. A maximum error of 7.5% in area and 2% in perimeter length was determined. Roundness was used as a shape descriptor which expressed a maximum error of 2.85%. On a single cell shape, the maximum error in area was 10%.

In order to test inter- and intra-observer variability, the application of the spline to real cell images by three independent observers showed at maximum error of 6% in area while the error in definition of a clustered cell increased to 13%. This may be explained by the fact that the boundary definition can be more ambiguous in clustered cells. However, the gradient based fitting process seemed to reduce inter-observer variability and the maximum error in area of clustered cells was reduced to 10%.

The semi-automatic tracking of cells seem to provide good repeatability. An estimated error  $\pm 5\mu\text{m/h}$  was calculated. A maximum error in velocity of  $7.5\mu\text{m/h}$  based on the centroid calculation was observed during the repeatability trial.

The gradient and pixel flow based relocation performed well. Using only the flow estimation, a maximum error of 15% in area was observed. This could be further reduced to 8% by combining flow estimation with gradient fitting. However, it is important to note that some control points may not satisfactorily follow the cell boundary throughout the monitoring process. Hence, there is always the ability to adjust the position of single control points as part of an interactive relocation process.

## 5 Cell Experiments

### 5.0 Introduction

The movement of cancer cells is thought to be important in forming distant metastasis [Grimstad, 1987]. The movement behaviour of single cells as well as cells in clusters may provide a measure of assessing treatment strategies. A number of systems have been developed which investigate the movement of single, detached cells. However, cells usually appear in colonies and the ability for cells to detach from a colony and migrate is considered to be necessary in the formation of metastasis [Jiang *et al.*, 1994a].

In this chapter, the effects of HGF/SF<sup>1</sup> motogen on the movement behaviour of human colon cancer cells in clusters were studied. Changes in area and cell velocity were assessed as an indicator of cell behaviour. Two forms of cell motility were investigated: Stationary motility as described by changes in cell area and cell shape, and translocative motility as described by cell velocity and movement path.

The newly developed semi-automatic adaptive spline method has been used for cell segmentation and tracking. Four series of HT115 cells with added motogen were analysed and their movement was compared with control cells. Section 5.1 describes the method and results of the analysis of HT115 human colon cancer cells with and without added motogen. In a second step, a different cell line of human colon cancer cells (HRT18) was analysed to study the effects of added HGF/SF motogen and HECD-1<sup>2</sup> antibody. The results were compared with a set of control cells as described in section 5.2.

In section 5.3 it is demonstrated that the adaptive spline method can also be used in brightfield microscopy by segmenting neutrophils. The results from the spline-based segmentation technique were compared with a region based segmentation system based on texture [Korzynska *et al.*, 1998].

---

<sup>1</sup> HGF/SF Hepatocyte growth and scatter factor motogen

<sup>2</sup> HECD-1 Human E-cadherin-1, monoclonal antibody

Finally, it is demonstrated that the developed system can also be used in ratio-imaging, measuring the calcium concentration in living cells. A cell outline is created from a ratio image using the adaptive spline method. This enables to compare cell shape changes with intra-cellular chemical changes in order to analyse changes of  $\text{Ca}^{2+}$  in comparison with changes in cell morphology (Section 5.4). The last section summarises the findings of the experiments.

## 5.1 Human Colon Cancer Cells

The movement of single cells has been studied extensively. However, most cells appear in clusters and the ability of cancer cells to detach from a colony, known as disassociation, is widely accepted as a pre-condition for cancer metastasis [Jiang *et al.*, 1994b]. In order to assess this behaviour *in vitro*, a cluster of human colon cancer cells (HT115) was observed. Cells were lightly clustered and the movement behaviour of individual cells within the cluster was analysed. To enhance their ability to move, HT115 cells were stimulated with the motogen known as Hepatocyte Growth Factor / Scatter Factor (HGF/SF). This motogen is expected to increase the cells desire to move [Rosen *et al.*, 1990]. However, cell-to-cell adhesions are not affected by the motogen.

The effect of HGF/SF motogen on HT115 human colon cancer cells was studied in four experiments; three at 50ng/ml concentration and one at 40ng/ml concentration. Four sets of control cells were analysed to compare cell behaviour with non-stimulated cells.

In a further experiment, cell-to-cell adhesions were impaired by HECD-1 antibody. Three series of HRT18 human colon cancer cells were analysed, one with added HECD-1 antibody at 0.6µg/ml, one with added HGF/SF motogen at 100ng/ml and one control series.

### 5.1.1 Microscope Setup and Calibration

A Leica microscope (Leica DM IRB, Germany) was fitted with a Hoffman Modulation Contrast Condenser HMC 20 (Hoffman, Greenvale, N.Y.,USA) to enhance the structural features of the cells. A cell colony with up to 10 cells was chosen at random from the culture and monitored for up to three hours on a time-lapsed video system either in real time or time lapse mode. A colour video camera (Panasonic WV-CL350, Japan) was connected to the microscope. After each recording, a calibration square was captured at x100 magnification showing a 250µm square and at x320 magnification three parallel lines separated by 25µm. This has

been used for calibration at different magnifications. The following Figure 5.1 shows two calibration images at x100 and x320 magnification on the Leica microscope.

Video frames were digitised as a series of true-colour images at a resolution of 768 by 576 pixels using a DT3153 frame grabber board (Data Translation, Marlboro, MA, USA). To reduce the amount of disk space needed and to further speed up the image processing, images were converted into 8 bit grey scale. The spatial resolution was the same for all experiments. The calibration image at x100 magnification was used to check the horizontal and vertical resolution which were found to be in agreement. Table 5.1 shows the result of this calibration. The horizontal and vertical distance was measured six times and a mean value was calculated. The mean vertical distance was 292.5 pixels while the mean horizontal distance was 293.5 pixels.

The three parallel stripes were used for calibration at the higher x320 magnification. Again, the distance between those stripes was taken six times and a mean value was calculated.

Number	vertical pixel	horizontal pixel
1	291	291
2	293	291
3	293	291
4	293	292
5	293	292
6	292	292
Mean	<b>292.5</b>	<b>291.5</b>
Std	0.84	0.55

Table 5.1: Results of image calibration at x100 magnification where vertical and horizontal denote the equivalent distance along the square.

The spatial resolution was calculated by measuring the distance between two parallel stripes at x320 magnification six times and then calculating the average distance. In this example, the resolution was calculated to be  $0.2683\mu\text{m}$  per pixel length which corresponded well with the resolution calculated at x100 magnification ( $0.2675\mu\text{m}$  per pixel).



magnification x100



magnification x320

Figure 5.1: Calibration image at x100 and x320 of Leica microscope.

### 5.1.2 HT115 Series I (control and 40ng/ml HGF/SF)

A cluster of 10 cells was chosen at random and six cells in each cluster were analysed. One series from which six cells were chosen was used as a control series while in a second series, 40 ng/ml motogen (HGF/SF) was added to the cell colony. The cells were monitored for three hours on a time-lapse video system. Images were captured from the video tape at an equivalent of a 5 minute interval in real time. The position of cells was defined by calculating the centre of area (centroid) from the spline interpolation.

In this initial analysis, six cells were analysed using the semi-automatic spline method without enabling the automatic relocation process. The outline of a previous frame was copied onto the next consecutive frame and slightly adjusted if necessary. This does not require a high frame rate since no flow information is used for the relocation process.

From the cell boundary the area of the cell can be measured and from its position the velocity and movement can be calculated. The velocity was calculated over a 5 minute interval. This was chosen as the movement of stimulated cells was found to be sufficient enough between two frames to be above the expected error in cell position. The assessment of error in movement has been covered in the validation section (chapter 4). Changes in area, velocity and movement path of six single cells within a cell colony were analysed.

### **Materials**

Human colon cancer cells HT115 (obtained from the European Collection for Animal Cell Culture, Salisbury, England) were used throughout the HT115 experiments. Cells were cultured in DMEM medium supplemented with 10% fetal calf serum, Penicillin and Streptomycin. The medium was HEPES buffered to provide a stable pH during long period recording in open atmosphere.

Two sets of HT115 human colon cancer cells of the same cell line were analysed, one of which had added motogen. The motogen used was a recombinant human

hepatocyte growth factor (HGF/SF) from DNA-transfected CHO cells [Jiang *et al.*, 1995, Jiang *et al.*, 1999].

Cells were prepared and cultivated on Petri dishes (Nunc, Denmark) and kept in an incubator at a temperature of ( 37°C and 5% CO<sub>2</sub>) for cells to adhere to the surface. The cell culture was placed under a Leica DM IRB microscope (Leica, Germany) with a heat control and an attached colour CCD camera. The dish was kept at a constant temperature of 37.2 °C.

## Results

The median area of the six control cells within one cell cluster at the start of the recording was 259  $\mu\text{m}^2$ . The maximum area of such cells was 428  $\mu\text{m}^2$  while the minimum was 169  $\mu\text{m}^2$ . The median area of six control cells and six cells with added HGF/SF motogen is shown in Figure 5.2. There were only small variations in area of the control cells. In contrast, there were greater changes in area in the cells treated with HGF/SF. The median area of six clustered cells with added motogen was observed to rise from 289  $\mu\text{m}^2$  to its maximum of 401  $\mu\text{m}^2$  during the first 35 minutes. It then showed a periodic pattern of changing its area.

The median velocity of six control cells belonging to the same cluster was 55  $\mu\text{m}/\text{h}$  at the start of the recording; it was observed that the velocity changed over time in both, Control and HGF/SF induced cells. The median velocity of HGF/SF induced cells is approximately twice as high as that of control cells as shown in Figure 5.3. Moreover, there was also a greater variability observed in the HGF/SF cells. The range of the velocity was 20  $\mu\text{m}/\text{h}$  to 190  $\mu\text{m}/\text{h}$ , while the range of the control cells was 0  $\mu\text{m}/\text{h}$  to 90  $\mu\text{m}/\text{h}$ . An overall decrease in velocity during the first 20 minutes was observed before the velocity changes appeared to show a periodic pattern.

Cells treated with added HGF/SF motogen showed more variation in velocity and overall higher values in velocity. Figure 5.4 shows the median velocity of six cells with added HGF/SF motogen.

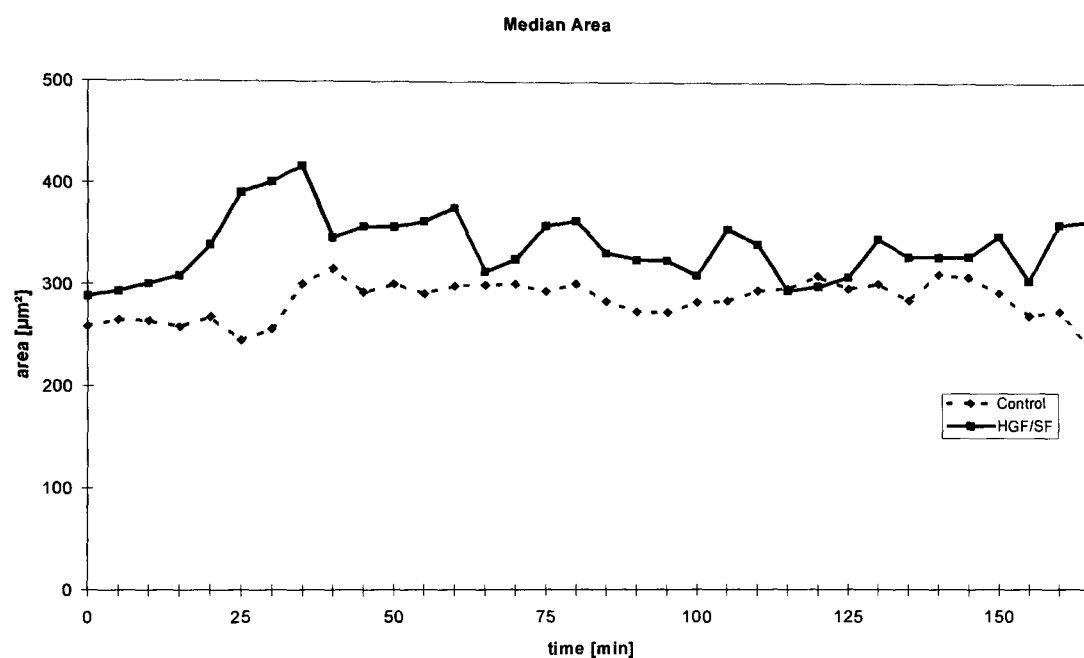


Figure 5.2: Median area of six Control and six HGF/SF (40ng/ml) cells

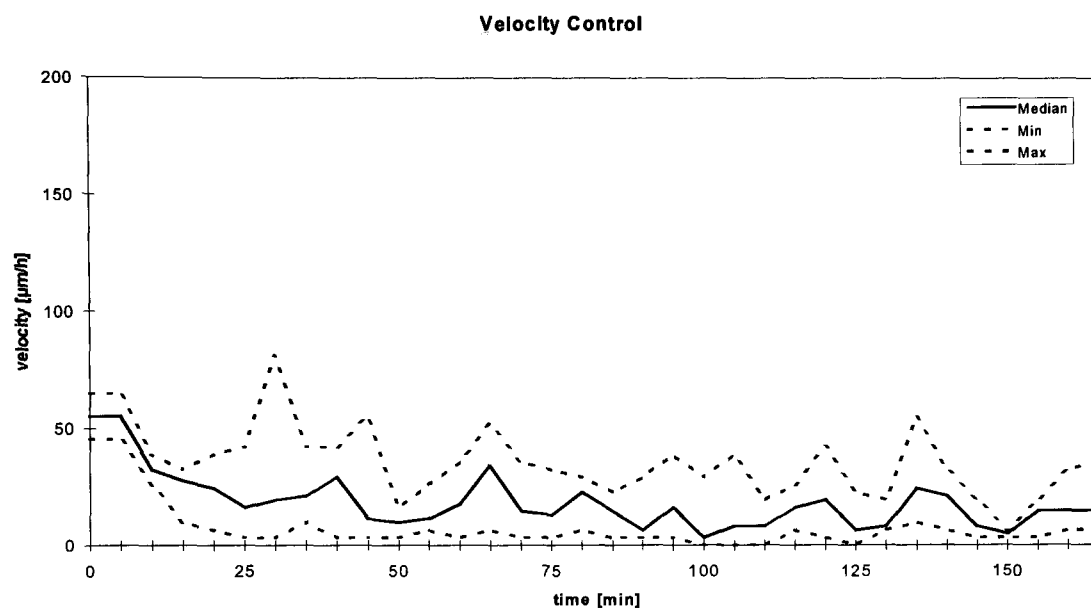


Figure 5.3: Median and range velocity of six HT115 control cells

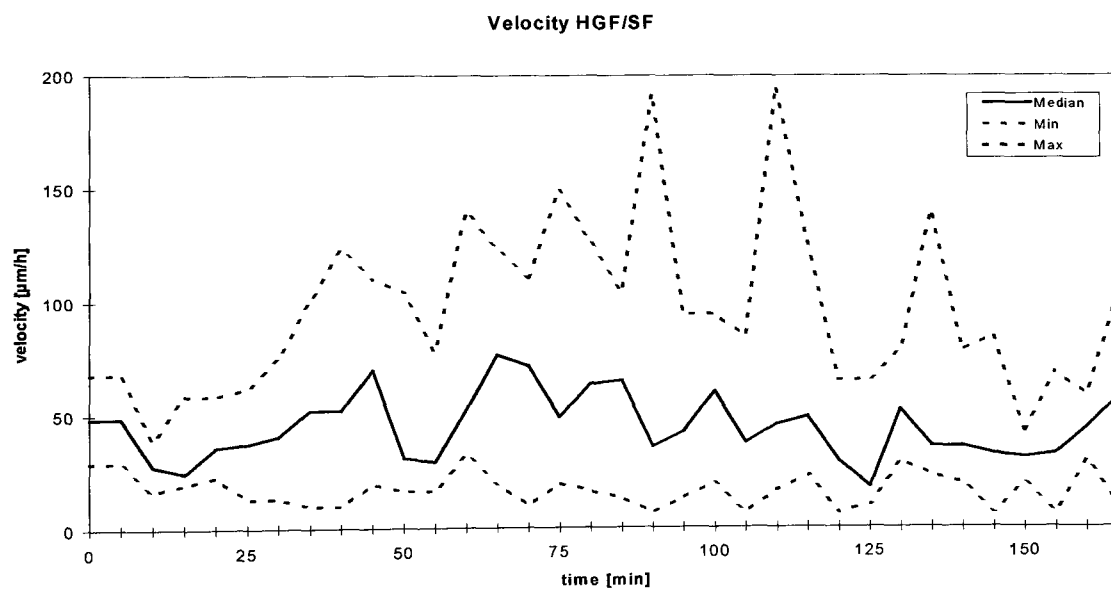


Figure 5.4: Median and range velocity of six HT115 cells with added 40ng/ml HGF/SF motogen

The control cells showed less movement, slower movement and there appeared to be only small changes in area and velocity. In contrast, cells treated with HGF/SF seemed to move more vigorously in a variety of directions and the cell colony scattered. Figure 5.5 shows the path of a single Control and a single HGF/SF stimulated cell within a cell colony in area of 30 micrometers square. Cells with added motogen expressed greater movement and more erratic movement as shown in the example of movement paths of two cells.

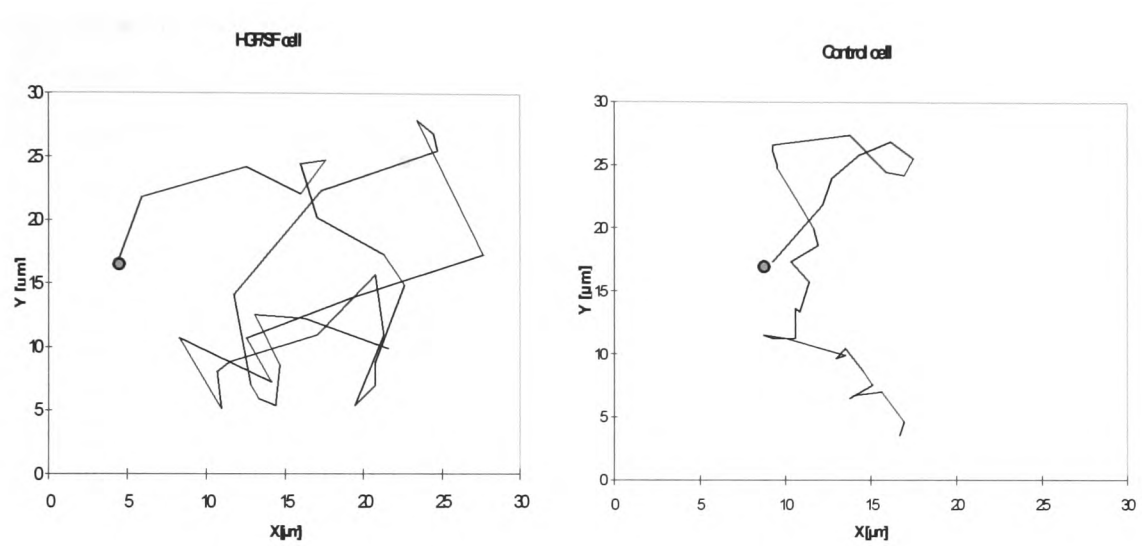


Figure 5.5: Example of movement paths of two HT115 cells (left with added motogen, right control)

### 5.1.3 HT115 Series II, III and IV (control and 50ng/ml HGF/SF)

A cluster of 10 cells was chosen at random and six cells in each cluster were analysed. One series consisted of six control cells while in a second series, 50 ng/ml motogen (HGF/SF) was added to the cell colony. The cells were monitored for two hours in Hoffman Modulation Contrast (HMC) microscopy and videotaped in real time. Images were captured from the video tape at a 5 second interval at 768 by 576 resolution. To reduce noise, four frames were averaged. In order to enhance contrast, the grey-level distribution was stretched by a third prior to the averaging process. The series of images had thus a higher contrast, noise was reduced and the interval size was increased to 20 seconds.

The position of cells was calculated from the adaptive spline method. The semi-automatic relocation was enabled using pixel flow and gradient information as described in chapter 3. The system operated in a semi-automatic mode whereby spline control points were placed on the boundary initially and pixel flow and gradient information was used to adapt to changes at the cell boundary in consecutive frames. The spline control points were relocated according to the pixel flow around the each control point in five consecutive frames. The spline is then displayed and changes can be made interactively by moving single control points before the next series of five frames is analysed.

In order to compare these results with previous analysis, the velocity was calculated from 5 minutes intervals (15 frames) and the area was calculated from a 1.33 minute interval (five frames). From the spline boundary the area of the cell was calculated and from its position the velocity and movement can be calculated. Thus changes in area, velocity and movement of single cells within a cell colony were analysed. The roundness was used as a shape descriptor.

## Materials

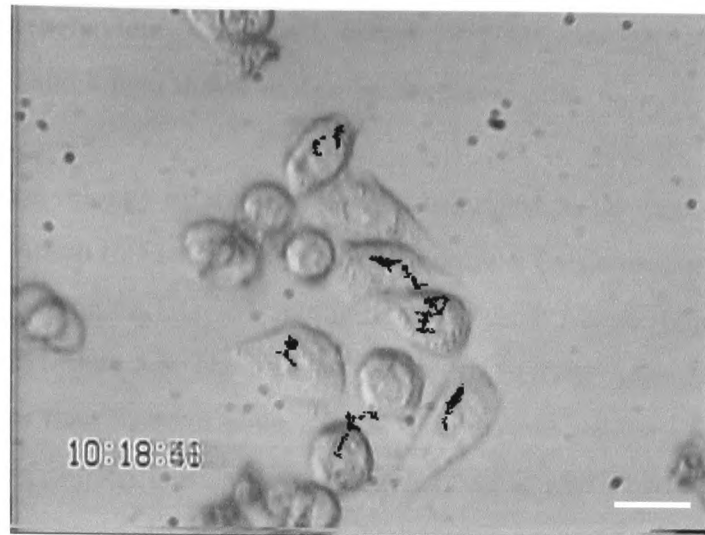
Human colon cancer cells HT115 (obtained from the European Collection for Animal Cell Culture, Salisbury, England) were used throughout the HT115 experiments. Cells were cultured in DMEM medium supplemented with 10% fetal calf serum, Penicillin and Streptomycin. A light oil ball was placed on top of the medium to provide stable pH during the recording period [Jiang *et al.*, 1999].

Two sets of HT115 human colon cancer cells of the same cell line were analysed, one of which had added motogen. The motogen used was a recombinant human hepatocyte growth factor (HGF/SF) from DNA-transfected CHO cells [Jiang *et al.*, 1995]. Cells were prepared and cultivated on Petri dishes (Nunc, Denmark) and kept in an incubator at a temperature of ( 37°C and 5% CO<sub>2</sub>). The cell culture was placed under a Leica DM IRB microscope (Leica, UK) with a heat control and an attached colour CCD camera. The dish was kept at a constant temperature of 37.2 °C.

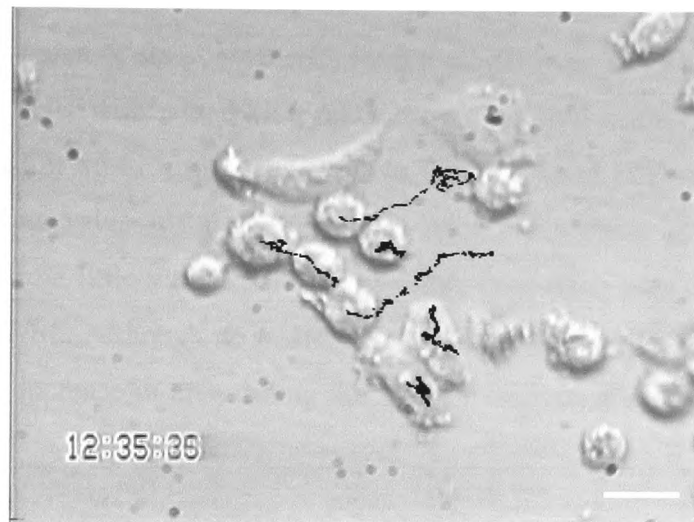
## Results Series I

Six cells were chosen at random from a cluster of approximately 10 control cells and 10 cells with added HGF/SF motogen as shown in Figure 5.6. The position of each cell during the monitoring period, marked by a black dot, was overlaid onto the cell image at the beginning of the monitoring process as shown in Figure 5.6. The distribution of black dots within a cell shows their centroid positions over the monitoring period. Most control cells seemed to remain stationary as the highest distribution of positions is within the boundary of the original location of the cell. In this experiment, only one out of six control cells seem to have moved further than its original border. Cells with added HGF/SF motogen seem to express two different behaviours. Some cells expressed hardly any movement similar to those of control cells while in this series three stimulated cells showed to be very motile which is expressed by a long movement path in the bottom image in Figure 5.6.

Neither control cells nor stimulated cells seem to have moved to a preferred direction, however, highly motile cells appeared to show a more directional



HT115 control



HT115 50ng/ml HGF/SF

Figure 5.6: A cluster of HT115 control cells (top) and HT15 cells with added 50ng/ml HGF/SF (bottom). The movement track (black) is overlaid, white bar 25 $\mu$ m.

movement behaviour. Cells with added HGF/SF motogen seem to express more movement and longer movement paths as control cells.

The median velocity of six control cells belonging to the same cluster was  $15\mu\text{m/h}$  (range:  $0.5\mu\text{m/h}$  to  $53\mu\text{m/h}$ ) as shown in Figure 5.7. The median velocity of six cells with added  $50\text{ng/ml}$  HGF/SF motogen was  $19\mu\text{m/h}$  (range:  $1\mu\text{m/h}$  to  $127\mu\text{m/h}$ ) and is shown in Figure 5.8. The median velocity of HGF/SF induced cells was just about 25% higher than those of control cells. This may be explained by the fact that only half of the chosen cells expressed higher velocities. However, cells with added motogen appeared to show more variation in velocity and a greater range in velocities.

The median area of six control cells from a cluster was  $444\mu\text{m}^2$  (range:  $275\mu\text{m}^2$  to  $720\mu\text{m}^2$ ). Cells with added HGF/SF motogen showed a median area of  $329\mu\text{m}^2$  (range:  $179\mu\text{m}^2$  to  $613\mu\text{m}^2$ ). The graph in Figure 5.9 and 5.10 shows the median and range of area values of six HT115 cells with and without added motogen. There appeared to be little variation in median area in control cells as well as cells with added HGF/SF. Although no tendency in area could be observed, there appeared to be a slight increase in area during the first 25 minutes after the motogen had been added.

Changes in area may be used as an indicator of stationary motility, however, a size independent parameter would be desirable. Roundness has been used as a size independent shape descriptor. A circle has a roundness of 1.0 while more complex shapes develop a higher roundness values as the ratio perimeter length to area increases. Cells with added HGF/SF motogen expressed on average an approx. 25% higher median roundness during the first hour of the monitoring process as shown in Figure 5.11. In the latter half of the observation period, the roundness of stimulated cells seemed to be similar to those expressed by control cells.

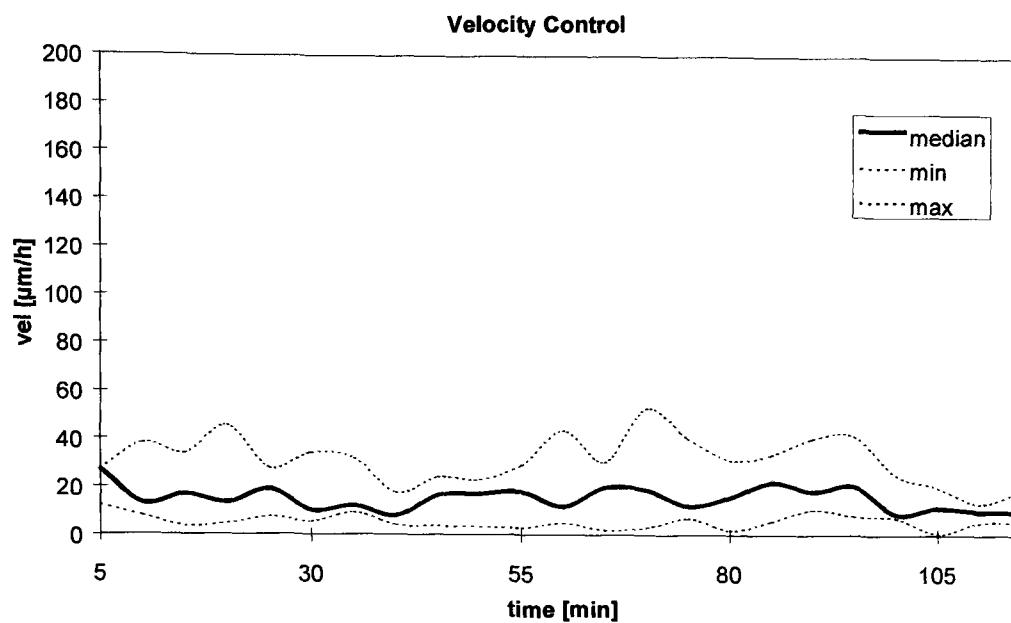


Figure 5.7: Median and range of velocity of six HT115 cells.

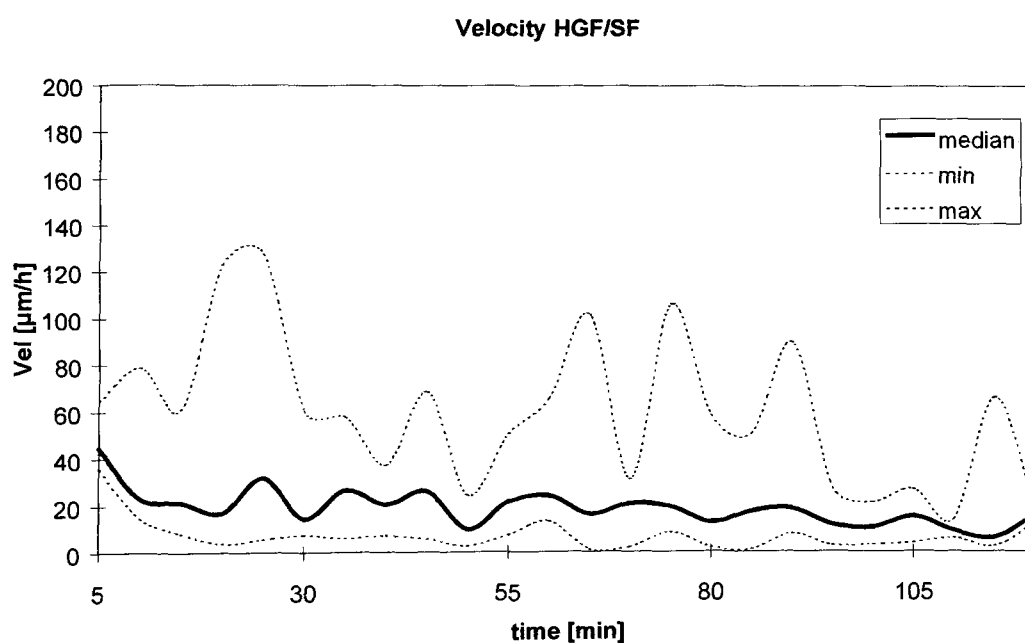


Figure 5.8: Median and range of velocity of six HT115 cells with added 50ng/ml HGF/SF motogen.

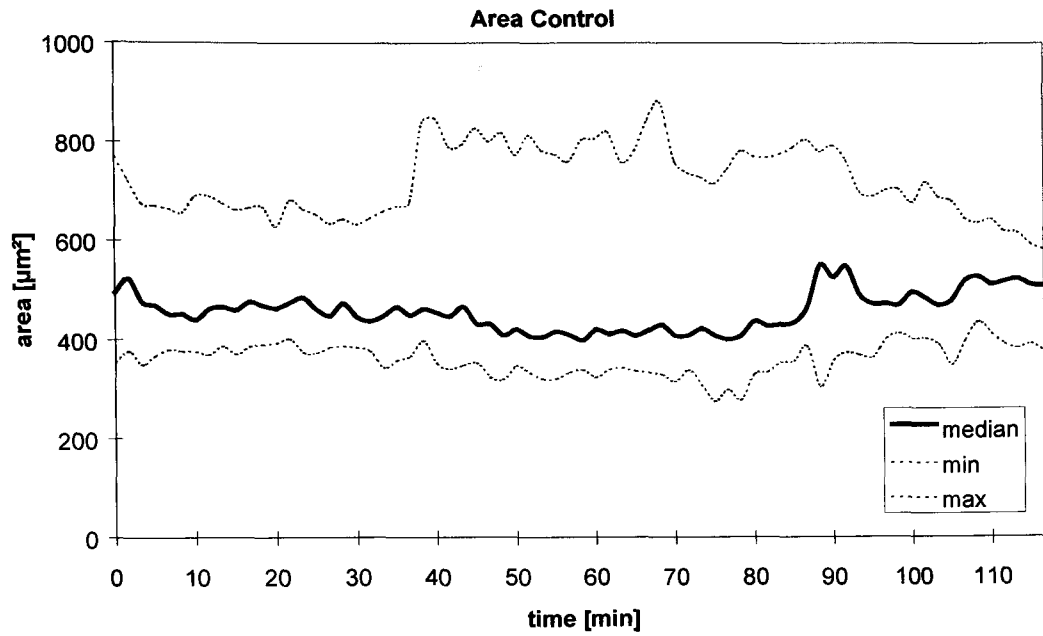


Figure 5.9: Median and range of area of six HT115 cells.

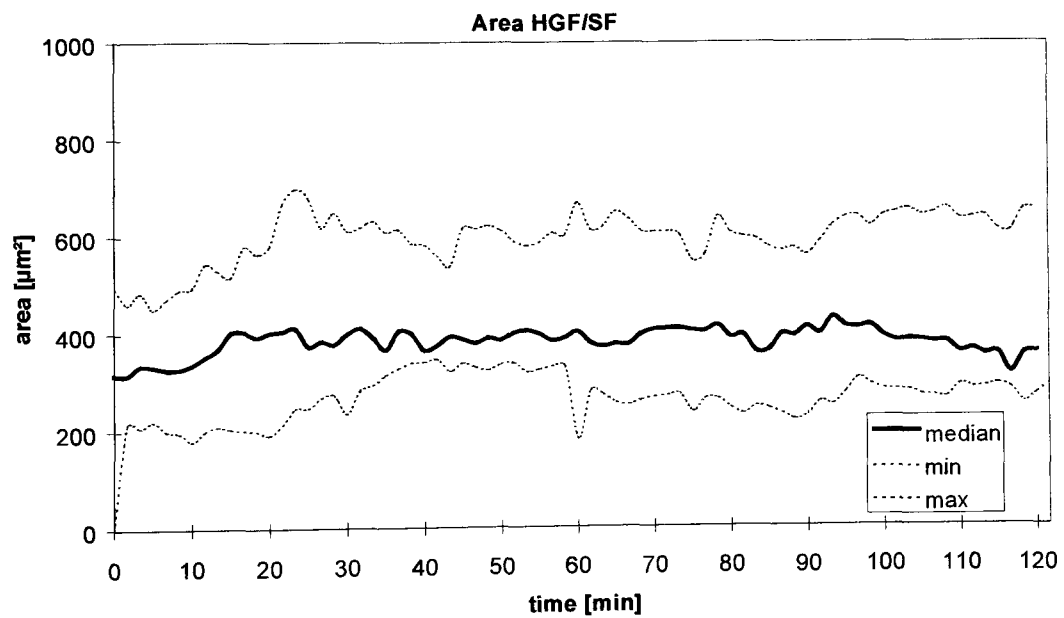


Figure 5.10: Median and range in area of six HT115 cells with added 50 ng/ml HGF/SF motogen.

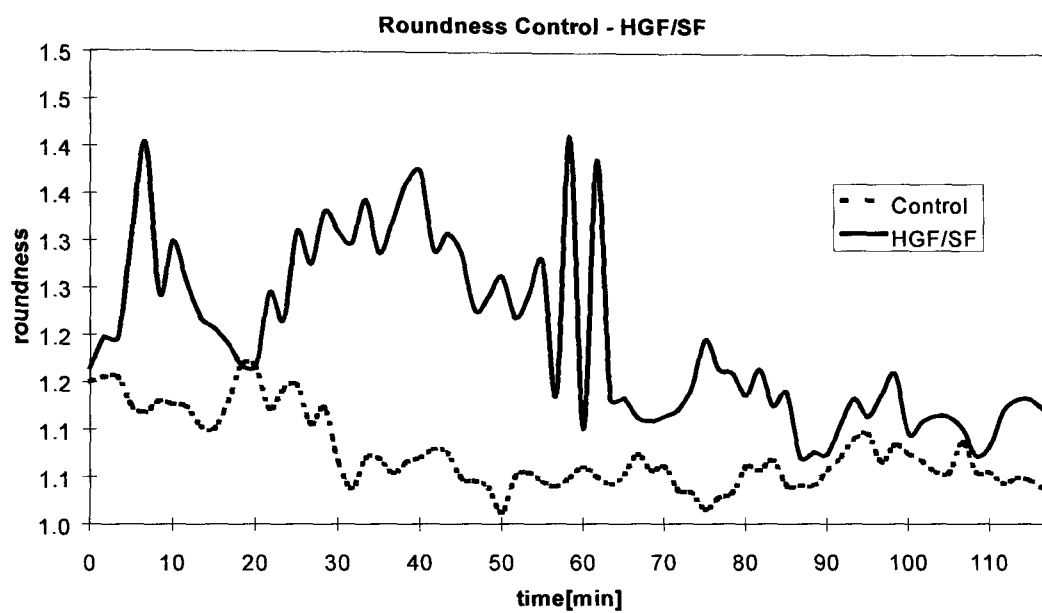


Figure 5.11: Median roundness of six HT115 control cells and six HT115 cells with added 50ng/ml HGF/SF motogen.

## Results Series 2

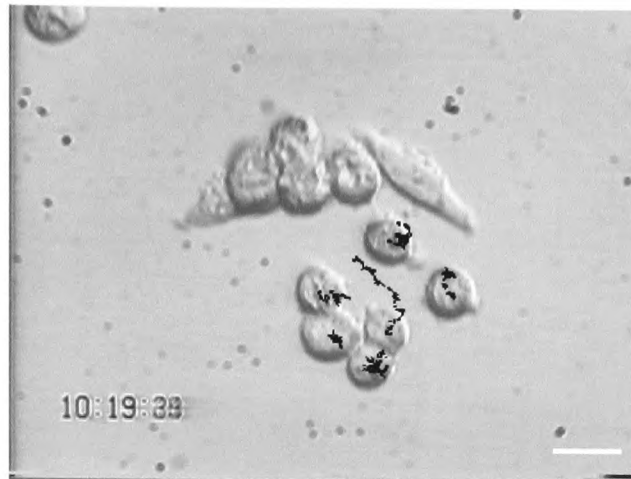
In a second series, six cells were chosen at random from a cluster of approximately 10 control cells and 10 cells with added HGF/SF motogen as shown in Figure 5.12. The position of each cell during the monitoring period was overlaid onto the cell image at the beginning of the monitoring process as shown in Figure 5.12. Cells with added HGF/SF motogen seem to express longer movement paths as control cells.

All but one control cell showed little movement with a high density of positions close to the original position at the start of the observation. In this series, stimulated cells expressed significantly more movement than control cells. Two cells moved apart from each other only to reunite later, forming a new cluster with two other cells.

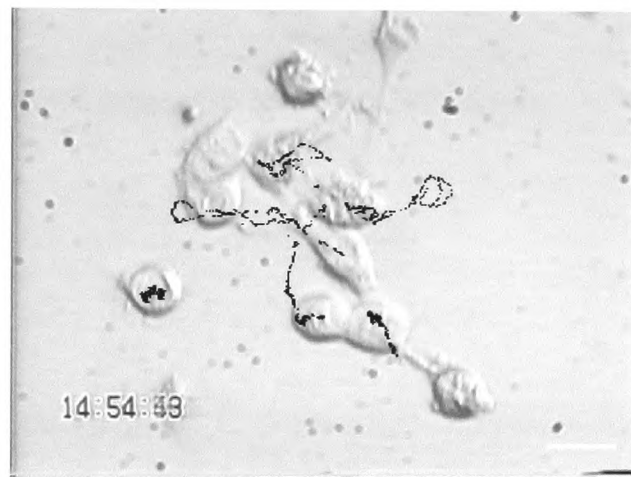
The movement behaviour is reflected in the higher median velocity of stimulated cells. Figure 5.13 and 5.14 show the median velocity of six control cells and six cells with added 50 ng/ml HGF/SF motogen. However, two stimulated cells did not show any increased movement behaviour. The median velocity of six control cells belonging to the same cluster was  $16\mu\text{m/h}$  (range:  $1.6\mu\text{m/h}$  to  $84\mu\text{m/h}$ ) as shown in Figure 5.13. The median velocity of six cells with added 50ng/ml HGF/SF motogen was  $25\mu\text{m/h}$  (range:  $1\mu\text{m/h}$  to  $265\mu\text{m/h}$ ) as shown in Figure 5.14. The median velocity of HGF/SF induced cells in this second series was about 50% higher than those of non-stimulated control cells. However, cells with added motogen appeared to show more variation in velocity and a far greater range in velocities.

The median area of six control cells from a cluster was  $272\mu\text{m}^2$  (range:  $32\mu\text{m}^2$  to  $408\mu\text{m}^2$ ). Cells with added HGF/SF motogen showed a median area of  $376\mu\text{m}^2$  (range:  $206\mu\text{m}^2$  to  $639\mu\text{m}^2$ ). The graph in Figure 5.15 and 5.16 shows the median and range of area values of six HT115 cells with and without added motogen.

In this series, there appeared to be little variation in area in control cells. Cells with added HGF/SF motogen appeared to show increased changes in the range of cell area during the first 50 minutes in the monitoring period.



HT115 control



HT115 50ng/ml HGF/SF

Figure 5.12: A cluster of HT115 control cells (left) and HT15 cells with added 50ng/ml HGF/SF (right). The movement track (black) is overlaid, white bar 25 $\mu$ m.

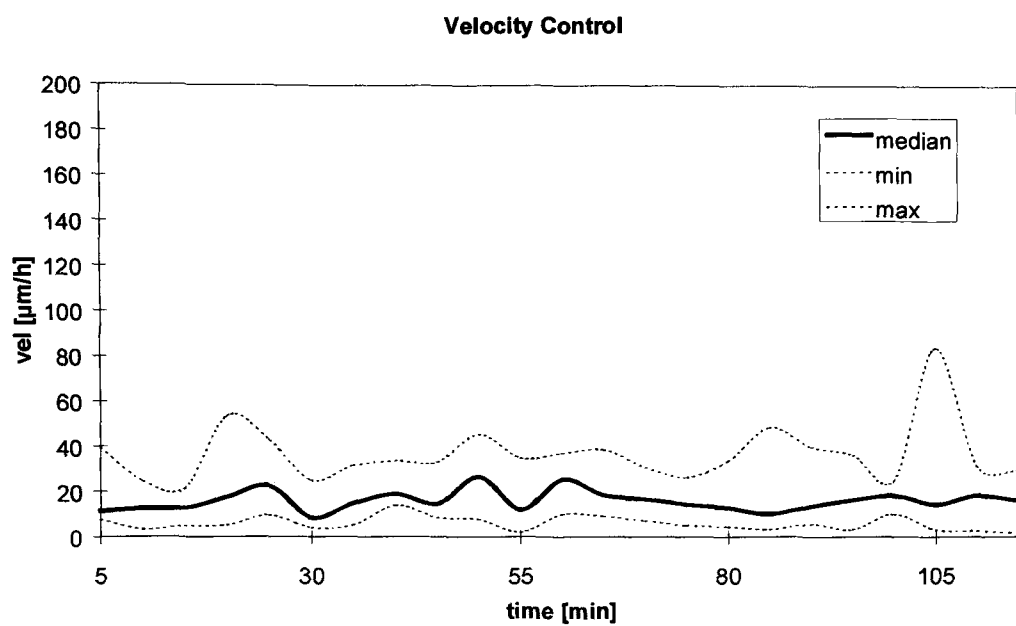


Figure 5.13: Median and range of velocity of six HT115 cells.

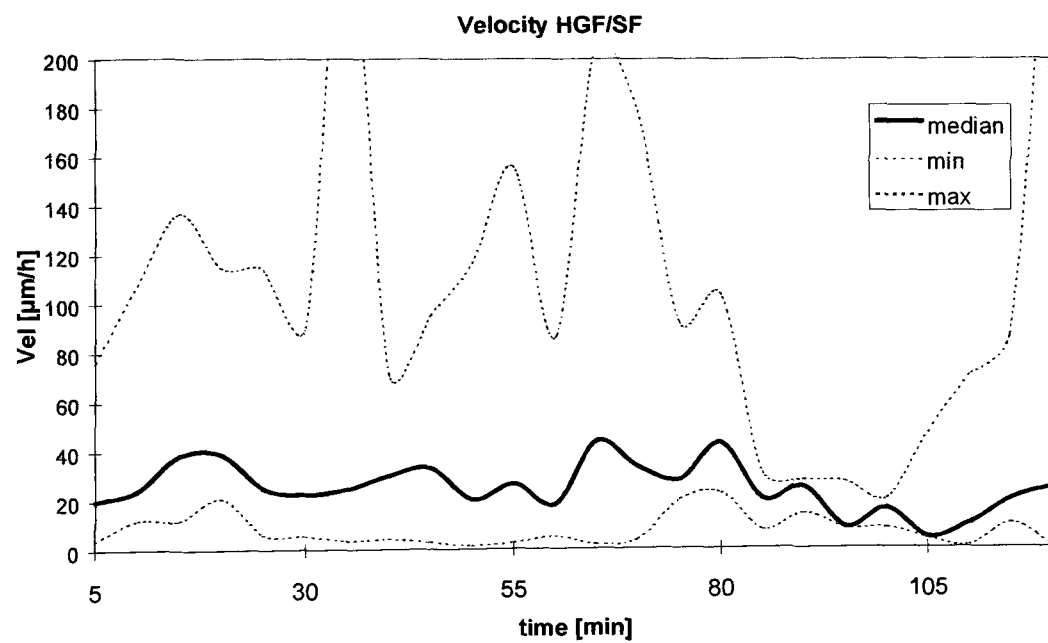


Figure 5.14: Median and range of velocity of six HT115 cells with added 50ng/ml HGF/SF motogen.

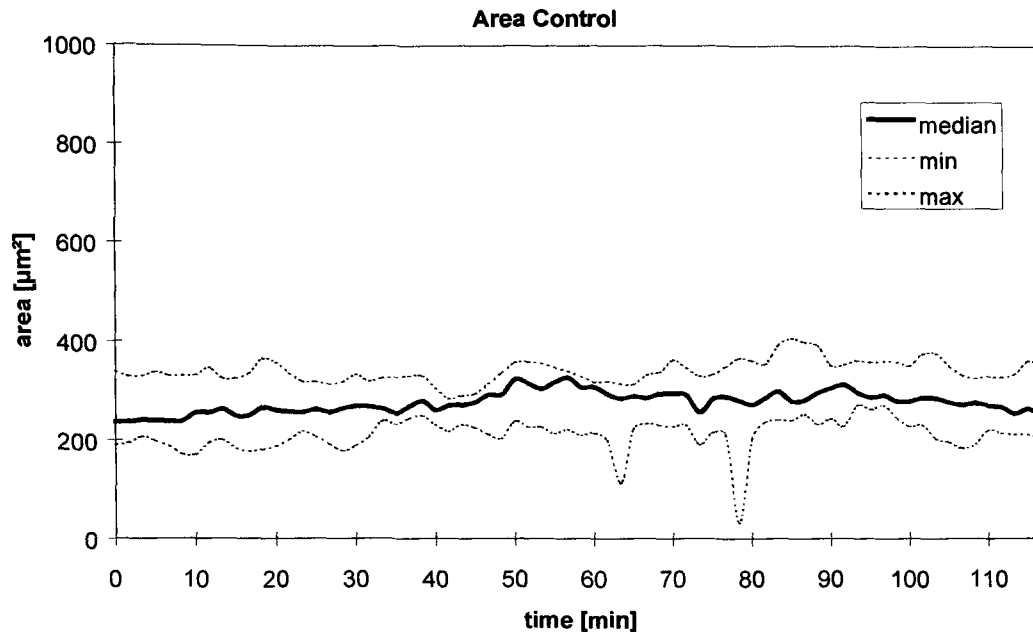


Figure 5.15: Median and range of area of six HT115 cells.

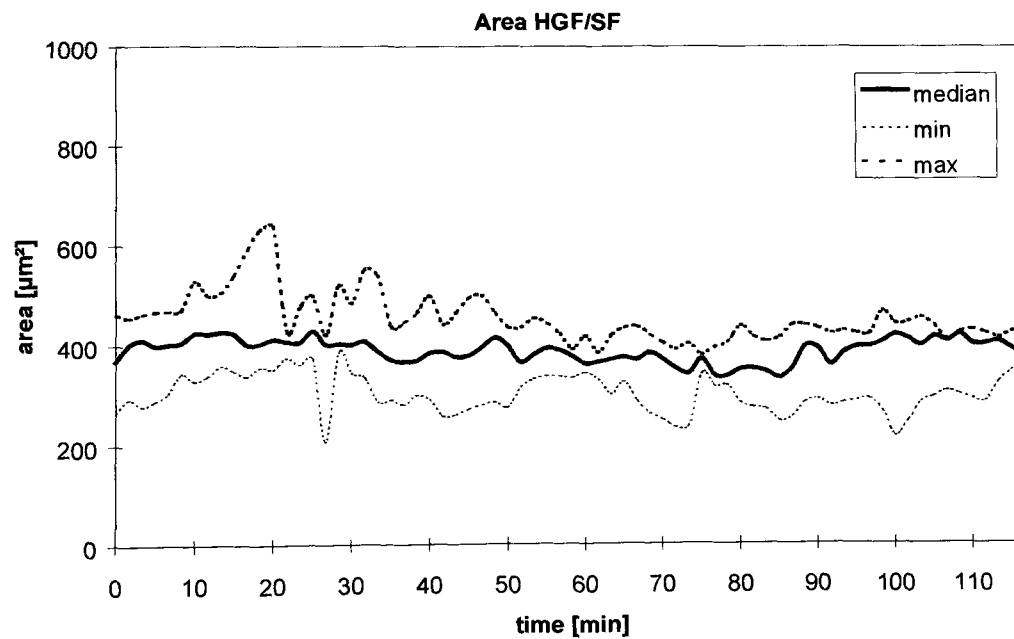


Figure 5.16: Median and range in area of six HT115 cells with added 50 ng/ml HGF/SF motogen.

The roundness was used as a descriptor of cell shape. Any circle has a roundness of 1.0 while more complex shapes develop a higher roundness values as the ratio perimeter length to area increases. Figure 5.17 shows the median roundness of six control and six stimulated cells. In this series, cells with added HGF/SF motogen expressed only marginally higher roundness values compared to control cells. Higher roundness values occurred during the first 30 minutes of the monitoring period as well as around 60, 90 and 120 minutes into the experiment.

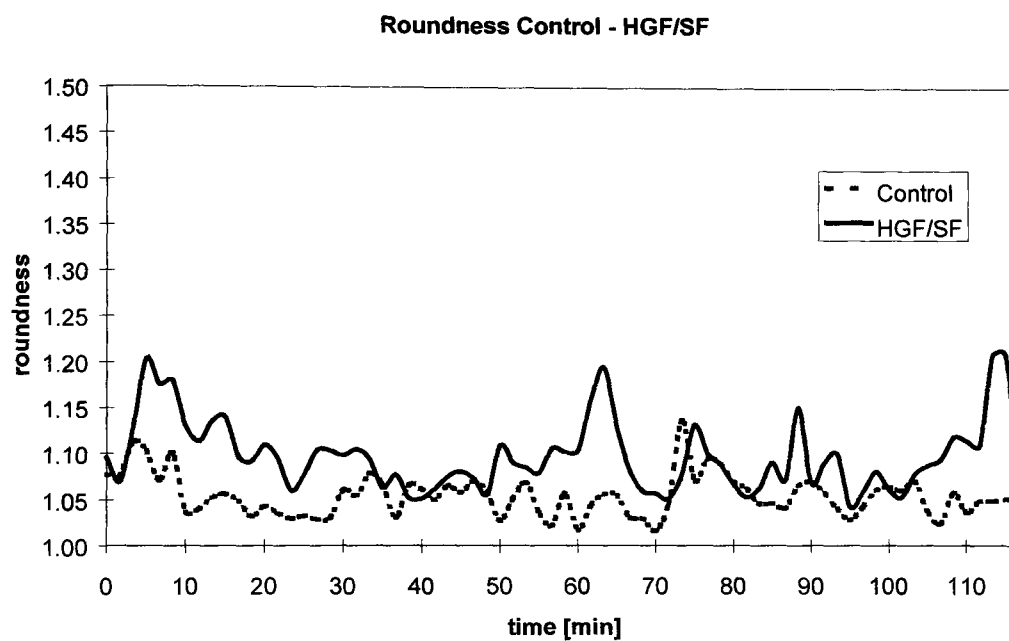


Figure 5.17: Median roundness of six HT115 control cells and six HT115 cells with added 50ng/ml HGF/SF motogen.

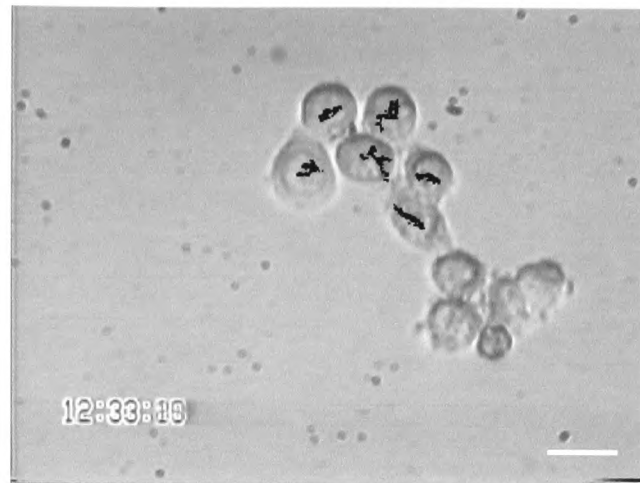
### Results Series III

In a third series, six cells were chosen at random from a cluster of approximately 10 control cells and 10 cells with added 50 ng/ml HGF/SF motogen as shown in Figure 5.18. The position of each cell during the monitoring period was overlaid onto the cell image at the beginning of the monitoring process as shown in figure 5.18. In this series, two cells of the stimulated cluster divided after 23 minutes and 67 minutes after the experiment started. Again, control cells expressed little movement as shown in the upper image in Figure 5.18. Cells with added HGF/SF motogen appeared to have a more directional movement and longer movement path.

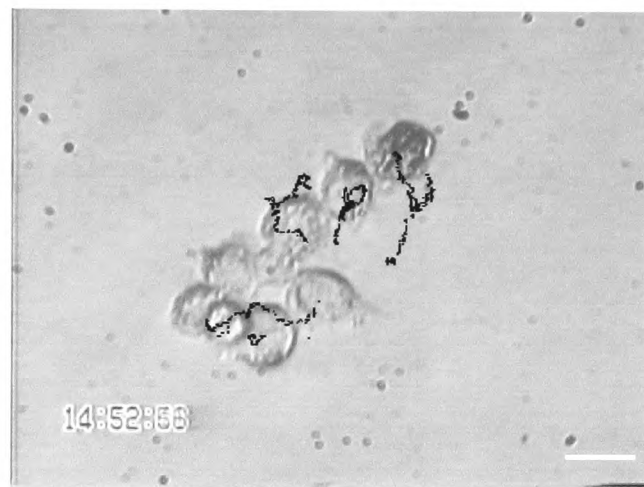
The median velocity of six control cells belonging to the same cluster was  $14\mu\text{m/h}$  (range:  $1\mu\text{m/h}$  to  $53\mu\text{m/h}$ ) as shown in Figure 5.19. The median velocity of six cells with added 50ng/ml HGF/SF motogen was  $24\mu\text{m/h}$  (range:  $1.4\mu\text{m/h}$  to  $92\mu\text{m/h}$ ). The median velocity of HGF/SF induced cells was about 60% higher than those of non-stimulated control cells. However, cells with added motogen appeared to show more variation in velocity and a far higher range in velocities as shown in Figure 5.20. The highest velocities occurred during the first 30 minutes of the monitoring period and at about 60 minutes as well.

The median area of six control cells from a cluster was  $330\mu\text{m}^2$  (range:  $234\mu\text{m}^2$  to  $566\mu\text{m}^2$ ). Cells with added HGF/SF motogen showed a median area of  $445\mu\text{m}^2$  (range:  $341\mu\text{m}^2$  to  $574\mu\text{m}^2$ ). The graph in Figure 5.21 and 5.22 shows the median and range of area values of six HT115 cells with and without added motogen. There appeared to be little variation in area in control cells. However, stimulated cells showed a greater variation in area.

In this series, cells with added HGF/SF motogen expressed a similar median roundness compared to control cells. In the latter half of the observation period, the roundness of stimulated cells seemed to be similar to those expressed by control cells, see Figure 5.23.



HT115 control



HT115 50ng/ml HGF/SF

Figure 5.18: A cluster of HT115 control cells (left) and HT115 cells with added 50ng/ml HGF/SF (right). The movement track (black) is overlaid, white bar 25 $\mu$ m.

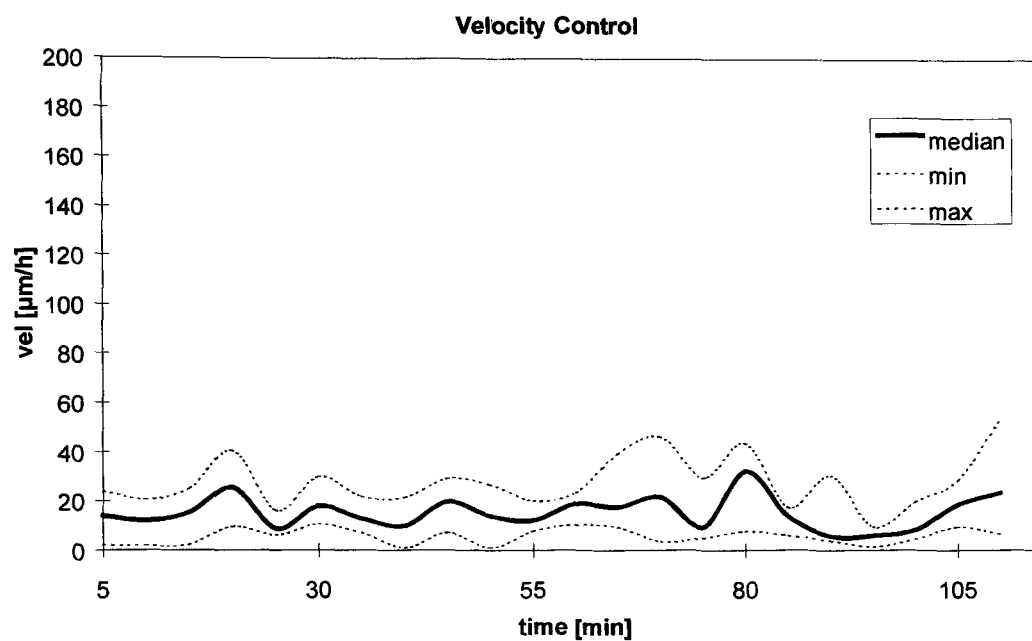


Figure 5.19: Median and range of velocity of six HT115 cells.

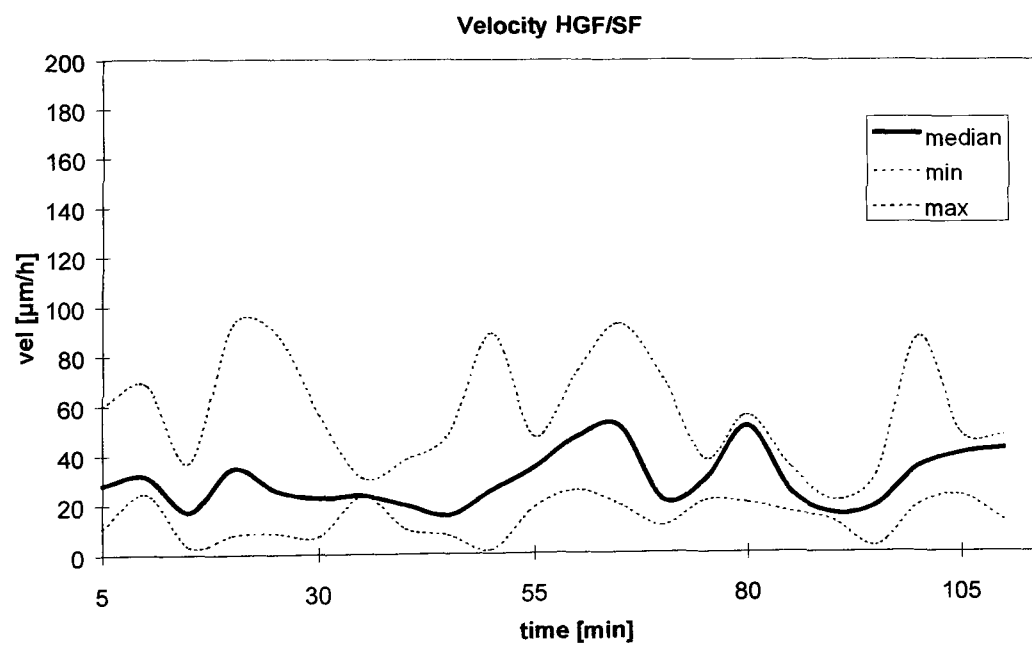


Figure 5.20: Median and range of velocity of six HT115 cells with added 50ng/ml HGF/SF motogen.

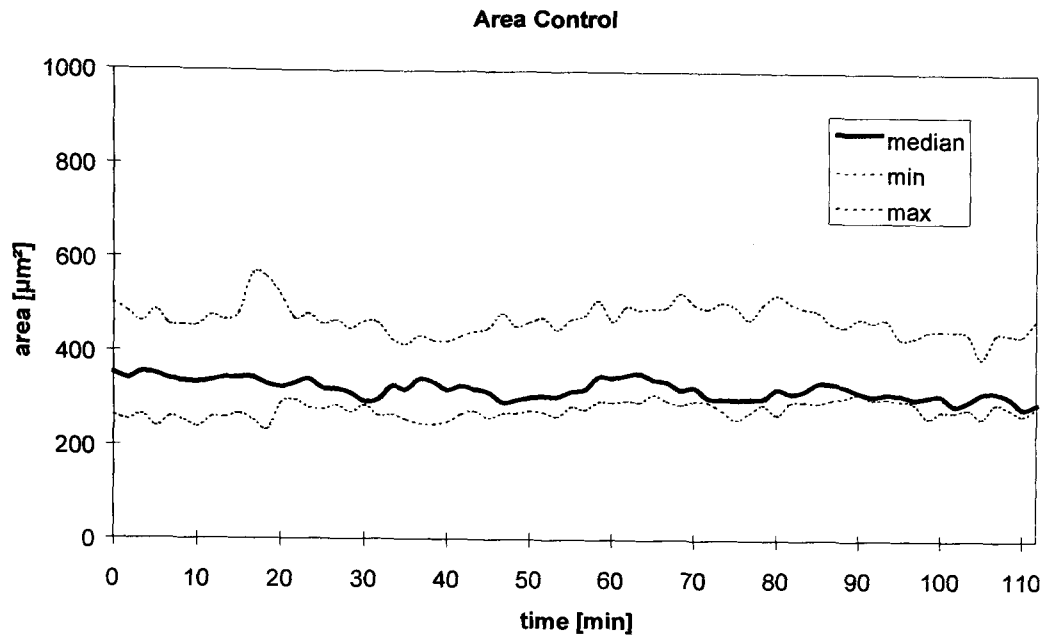


Figure 5.21: Median and range of area of six HT115 cells.

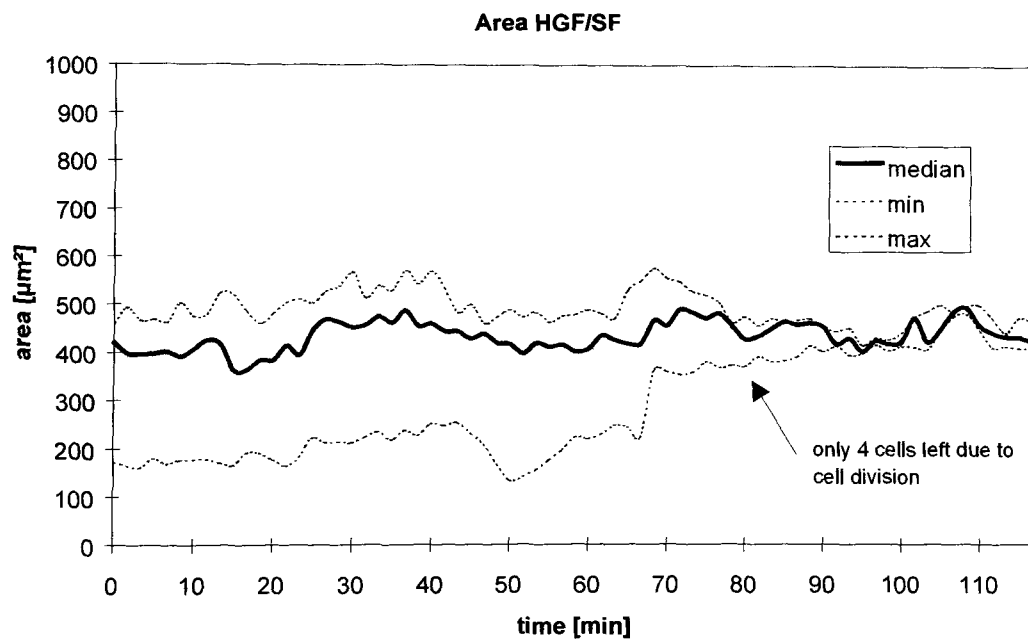


Figure 5.22: Median and range in area of six HT115 cells with added 50 ng/ml HGF/SF motogen.

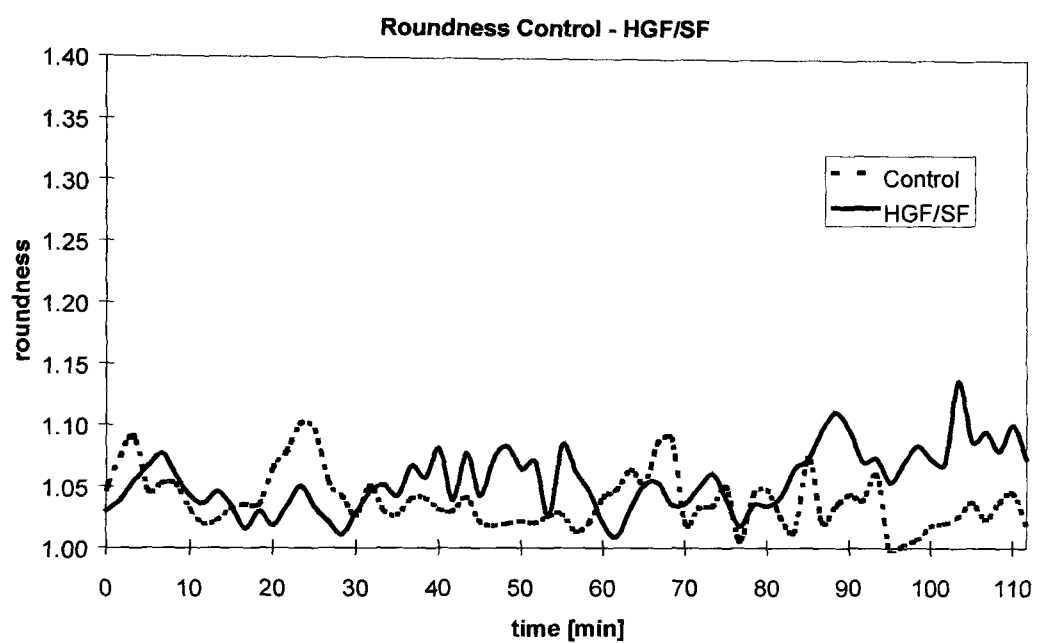


Figure 5.23: Median roundness of six HT115 control cells and six HT115 cells with added 50ng/ml HGF/SF motogen.

## Discussion

In this study the adaptive spline method was applied to describe and track single cells in clusters. This system enabled analysis of cell behaviour within a clustered colony by calculation of the cell centroid and calculating cell area. As a size independent shape parameter, the roundness has been used.

The effect of HGF/SF motogen on human colon cancer cells (HT115) during at least two hours of monitoring was assessed. Six cells out of a cluster of 10 cells were chosen and changes in area, velocity and shape were analysed.

In all experiments, cells with added HGF/SF motogen showed more movement activity expressed by longer movement paths and higher velocities. Non-stimulated cells moved in random directions while stimulated cells seem to move partially more directional.

Cells with added HGF/SF motogen at 50ng/ml concentration expressed an overall higher median velocity than control cells, which is in accordance with previous studies [Bhargava *et al.*, 1993]. The median velocity varied from experiment to experiment. Cells with added motogen expressed an 25% increase in median velocity up to 100% increase in median velocity. This may be explained by the fact that not all cells seem to respond to the added HGF/SF motogen equally. Although HT115 cells are derived from the same tumour, there is a possibility that the cells may exist as heterogenous populations. It has indeed been demonstrated by previous studies that in a cluster some cells exhibit higher level of HGF/SF receptors (c-met) than others [Jiang *et al.*, 1993, Hiscox *et al.*, 1999]. The variation in behaviour of cells in this study may be at least partly the result of various levels of HGF/SF receptors and their response to the motogen.

In series I, only half of the cells showed an increased movement activity while the other half had no increased movement at all. This resulted in an overall lower median velocity. In Series II and III of the HGF/SF experiments, a larger number of cells had increased translocative motility which lead to an overall higher median velocity of

more than a 50% increase. However, it was also observed that cell velocity varies in time and these results suggest that this variation is greater in cells with added motogen.

Stationary motility was measured by changes in area and shape. The size independent roundness is used as a measure of shape complexity in irregularity. In series I, all cells expressed higher roundness values compared to control cells indicating the development of more complex cell shapes. Moreover, there was a greater variation in roundness in stimulated cells.

An increased roundness value may perhaps be due to pseudopodial expansions and membrane ruffling. In two experiments (I,II) there was an increased roundness especially during the first 30 to 40 minutes of the monitoring process. Ruffling normally appears from 5 minutes and reaches a maximum in 30 minutes after the motogen has been added [Jiang *et al.*, 1995]. This is perhaps one factor that contributes to the increase of roundness seen in this study.

Cell area was found to be similar in cells with and without motogen, however, there was greater variation in area with time in those cells treated with motogen and in three instances the median cell area increased during the first hour after the motogen has been applied.

In summary, HGF/SF leads to more movement activity in HT115 cells. Stimulated cells expressed higher movement velocities and a greater variability in movement compared to control cells. However, some cells seemed not to respond to the added HGF/SF motogen. Cells with added HGF/SF motogen seem to move greater distances and also were found to detach more easily from the cell cluster.

## 5.2 HRT18 Cells ( control, antibody and motogen)

The aim of this experiment was to study the effect of HECD-1 antibody and HGF/SF motogen on HRT18 cells. HRT18, colorectal cancer cells, share the same histological origin with HT115, i.e. colon epithelium. One of the most striking characteristics of HRT18 cells is that they express strong cell-to-cell adhesion mechanisms, manifested by its high level of E-cadherin [Jiang *et al.*, 1995], the most important cell-to-cell adhesion molecule in this tumour type. The aim of this study was to quantify differences in movement behaviour and response to HGF/SF motogen and by manipulating the function of E-cadherin.

A cluster of 10 cells was chosen at random and three cells in each cluster were analysed. Three series of HRT18 cells were monitored for three hours using a Leica microscope (Leica DM IRB, Germany) fitted with a Hoffman modulation contrast condenser (Hoffman, Greenvale, N.Y.,USA) connected to a time-lapse video recording system. Recordings were made at  $\frac{1}{4}$  of the normal speed and frames were digitised at a 10 second interval real time at 768x576 spatial resolution. Two frames were averaged to reduce noise and subsequently converted into 8 bit grey scale images.

One series of cells was treated with 100ng/ml HGF/SF and one other series with 1.5 $\mu$ g/ml HECD-1 antibody. A third series was used as a control reference. Each series consisted of three cells. Cells were segmented using the adaptive spline method. Cell area and cell velocity was calculated from change of position of its centroid. In order to compare these results with previous analysis, the velocity was calculated over the distance between 5 minutes of movement.

### Results

All three series of cells appeared to show little translocative motility. The median velocity of three control cells was 5.6 $\mu$ m/h [0 $\mu$ m/h to 32 $\mu$ m/h]. Cells with added motogen (100ng/ml) expressed a median velocity of 7.7 $\mu$ m/h [0 $\mu$ m/h to 44.8 $\mu$ m/h] while cells with added HECD-1 antibody expressed the highest median velocity

9.7 $\mu$ m/h [0 $\mu$ m/h to 53.1 $\mu$ m/h]. Figure 5.24 shows the median velocity of three HRT18 control cells (c), three HRT18 cells with added 100ng/ml HGF/SF motogen (m) and three HRT18 cells with added HECD-1 antibody (a).

Cells with added antibody seem to express greater translocative motility than control cells and cells with added HGF/SF motogen. The median velocity of cells with added HECD-1 antibody was almost twice as high as that of control cells. The median velocity of cells with added motogen was in between that of control cells and cells with added antibody.

Stationary motility was assessed by investigating the changes in area. Figure 5.25 shows the median area of three cells: control, 100ng/ml HGF/SF and 0.6  $\mu$ g/ml antibody. Control cells expressed very little changes in area and hence stationary motility. The highest changes in area occurred in cells with added HGF/SF motogen. There appeared to be an increase in cell area during the first hour of the monitoring period in cells with added HGF/SF motogen.

Interestingly, according to Figure 5.25, cells with added motogen expressed slightly more changes in area than cells with added antibody despite the fact that they showed less translocational movement.

## Discussion

In this study HRT18 cells with added HGF/SF motogen expressed higher median velocities than control cells. Added HECD-1 antibody impairs cell-to-cell adhesions which then may enable those cells to move more freely leading to an increased velocity of HRT18 cells.

Interestingly, stationary motility is higher in cells with added HGF/SF motogen. This may be explained by the fact that HGF/SF motogen increases the desire of cells to move. This increased ability of movement is reflected by increased changes in area and cell shape as cells are trying to explore new territory.

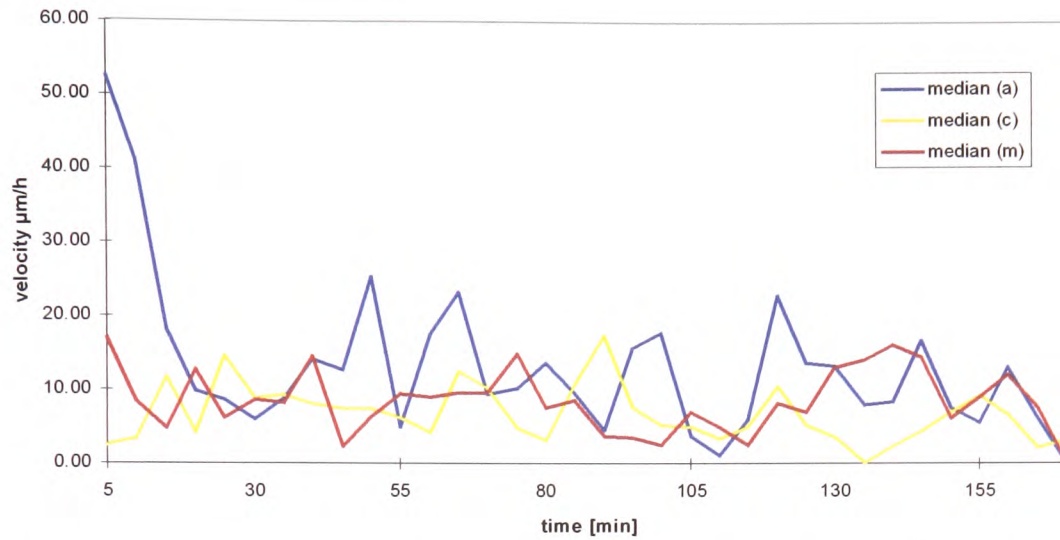


Figure 5.24: Median velocity of three control, with HGF/SF and with HECD-1 HRT18 cells

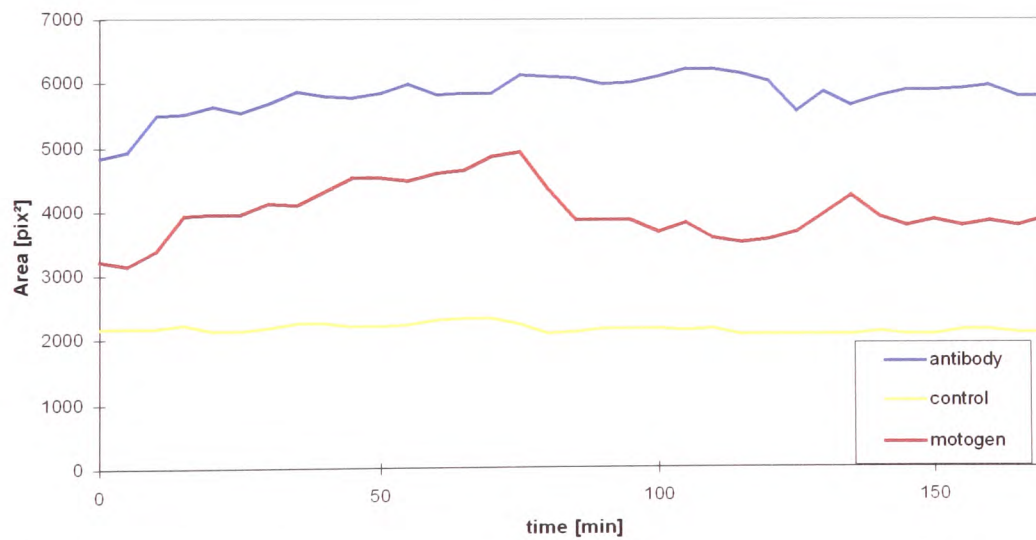


Figure 5.25: Median area of three control, HGF/SF and HECD-1 cells of HRT18.

### **5.3 Application of the Adaptive Spline method to assess the Movement of Neutrophils**

The aim of this study was to adapt and apply the semi-automatic spline method to segment neutrophils in brightfield microscopy. The cell boundary is described with the adaptive spline technique. The results of area measurements are compared with a system devised by Korzynska [1998]. Their system provides functionality for a semi-automatic segmentation of neutrophils using a region-based texture segmentation technique Korzynska [1998]. The neutrophil images were provided by Korzynska.

#### **Materials**

Two series of microscopic neutrophil images were digitised at a 2 second interval, one other series was digitised at 25 frames per second for 2 seconds. Each image contained a single or two separated neutrophils. Neutrophils were obtained from fresh finger blood coming from healthy, grown-up donors. Cells were isolated using the Harris method based on their adhesion to glass [Harris, 1973].

Images were acquired using a OPTIPHOT-2 (Nikon) microscope fitted with a LWD condenser connected to a 1/2" CCD camera (J COHU). The frame grabber used was the SVIST (WIKOM) and images were digitised as 8-bit 512x512 grey level images and subsequently analysed.

#### **Method**

Images were segmented using the adaptive spline method. The original cell image expressed low contrast within the cell body and pseudopodial expansions. Figure 5.26 shows a single neutrophil viewed in brightfield microscopy.

There are three areas in the neutrophil in Figure 5.26 that need to be distinguished in order to obtain a successful segmentation. Region (1) is the cell body, region (2) are expanding cell pseudopods and finally the peripheral area which is halo (3) and is not part of the neutrophil. Although the main cell body (2) has different intensity values from the background and halo, expanding and retracting pseudopods often contain a

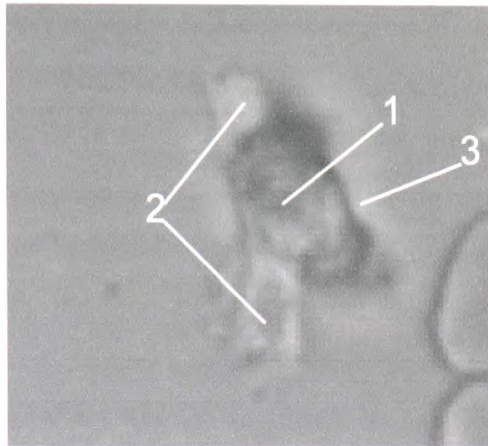


Figure 5.26: Single neutrophil with cell body (1) , expanding pseudopods (2) and halo (3) around the cell.

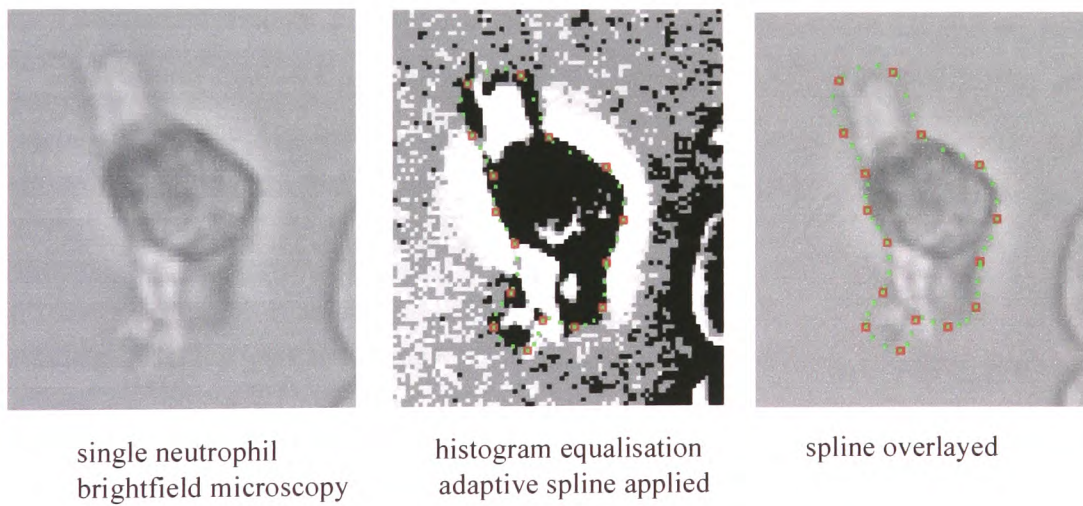


Figure 5.27: Application of the adaptive spline technique to delineate the cell boundary of a neutrophil.

similar range of intensities found in the halo (3) or background. This makes an image like that in Figure 5.26 difficult to segment by a region-based segmentation method.

To overcome the problem, the adaptive spline method was applied to describe the neutrophil by its outline rather than occupied area. However, it was difficult to locate control points in the original brightfield image shown in Figure 5.27. Fortunately, expanding pseudopods seem to express a higher density and hence slightly lower intensity at the very edge of expansion. Due to the lack of contrast between those cellular regions, a histogram equalisation [Gonzales and Woods, 1993] was performed to greatly enhance the contrast between cell body, pseudopods and halo. The second image in Figure 5.27 shows the histogram equalised cell image. The boundary of pseudopods, although fragment, is clearly distinguishable from the halo and background. The spline interpolation is used to link those fragments with the main cell body to form a smooth representation of the neutrophil boundary.

The spline control points are located at the outer edge of the cell body and pseudopod fragments. Figure 5.27 shows the adaptive spline contour describing a single neutrophil facilitation histogram equalisation. Pseudopodial regions can be engulfed in the spline contour regardless of bright image regions within their area. When surrounded by a halo, after histogram equalisation, there appeared to be better contrast between cell boundary and background.

The tracking was performed semi-automatically by defining the cell outline at the beginning of the monitoring process. Control points were relocated at the outside of dark cellular regions after histogram equalisation (see Figure 5.27). This was used as an estimate of the position in consecutive image frames. Single control points were moved manually if the suggested position did not accord with the operators perception of the cell boundary location.

## Results

A single series of neutrophils was analysed independently with the two segmentation methods. Each frame was segmented using a regional textured based method

[Korzynska, 1998] and the adaptive spline method. A total of 25 image frames were analysed. Figure 5.28 shows the difference in area comparing the two segmentation methods using Altman-Bland analysis [Bland and Altman, 1986].

The absolute maximum difference between the two measurement methods was 25% in area while the mean difference between the two systems was calculated as 7.5%. As seen from the Figure 5.28, none of the systems is biased towards bigger or smaller area values. However, the majority of larger errors occur where the measurement by the regional texture segmentation shows a larger reading in area than the spline method. The large differences in area in some cases may perhaps be explained by the fact that the adaptive spline technique interpolates over regions that are not included in the texture based segmentation.

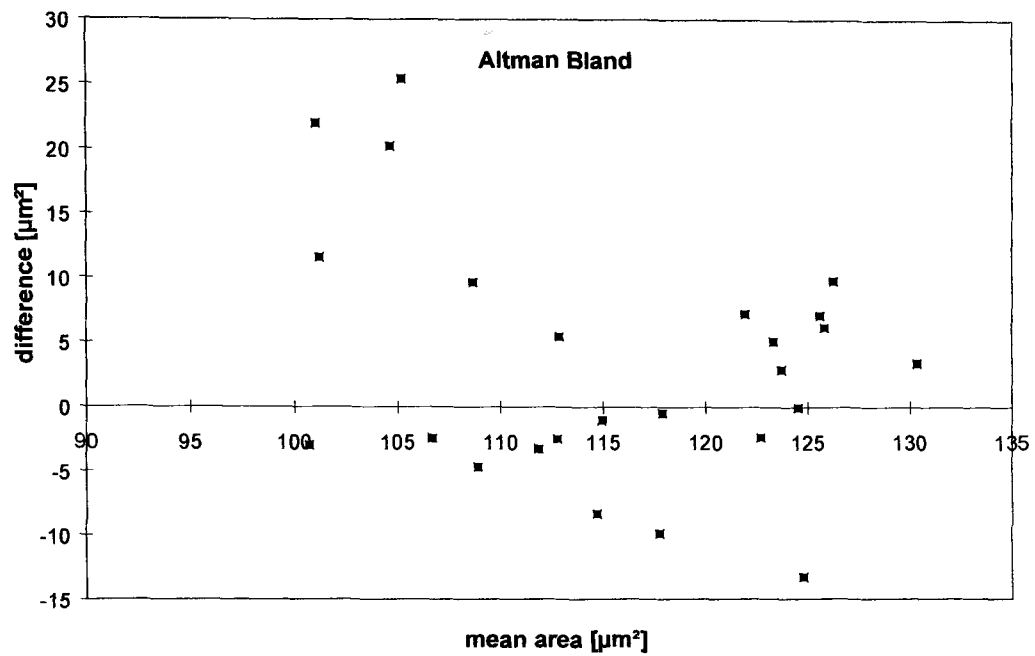


Figure 5.28: Altman-Bland analysis of area values acquired by using the two segmentation methods (texture region-based and spline boundary based).

## 5.4 Application of Spline to Assess the Morphology and Intracellular chemical changes in Neutrophils

The aim of this study was to adapt and apply the adaptive spline method to segment neutrophils which are viewed by ratio-imaging. Using  $\text{Ca}^{2+}$  imaging techniques, it is possible to acquire images which contain information of both cytosolic free  $\text{Ca}^{2+}$  concentration and cell shape. However, the inability to extract  $\text{Ca}^{2+}$  data from a dynamic region defined in relationship to a localised cell shape change remains a major problem. In static cells, a region of interest is usually defined within which cytosolic free  $\text{Ca}^{2+}$  concentration is extracted. With neutrophils, this approach extracts data from regions of differing cell activity at different times as the cell moves relative to the region of interest. In this section the spline-based semi-automatic cell segmentation method is adapted to enable interactive segmentation of cellular regions in neutrophils in ratio-imaging.

### Materials

Neutrophils were isolated from heparinized blood of healthy volunteers as described previously [Davies and Hallett, 1995]. Following dextran sedimentation, centrifugation through Ficoll-Paque (Pharmacia) and hypotonic lysis of red cells, neutrophils were washed and resuspended in Krebs buffer (120 mM NaCl, 4.8 mM KCl, 1.2 mM  $\text{KH}_2\text{PO}_4$ , 1.2 mM  $\text{MgSO}_4$ , 1.3 mM  $\text{CaCl}_2$ , 25 mM HEPES and 0.1% bovine serum albumin, adjusted to pH 7.4 with NaOH).

### Method

Neutrophils were loaded with fura-2 from its acetoxy-methyl ester as previously described [Davies and Hallett, 1995]. This fluorescent indicator of cytosolic free  $\text{Ca}^{2+}$  concentration provides quantitative information of when the ratio of two excitation signals is calculated [Hallett *et al.*, 1996]. Excitation at 340nm and 380nm was achieved by using a rapid access monochromator changer (Delta-RAM) with a transfer time between wavelengths of 2 msec and emission images (> 490nm) two

wavelengths were acquired using an intensified IC-200 CCD camera (Photon Technology International, Surbiton, UK) coupled to an inverted Nikon microscope. Ratios of the images were calculated using ImageMaster (PTI). Acquisition of ratio images was performed after averaging 16 frames, and using only a thresholding algorithm (no masking applied) which produced a cell image of equal size to that viewed by phase contrast. This enabled both cytosolic free  $\text{Ca}^{2+}$  concentration and cell shape to be measured simultaneously and calculated from the same image data set. The cytosolic free  $\text{Ca}^{2+}$  concentration was calculated as the mean pixel value within cell area which excluded the actual cell edge as this was often contaminated with artefactual ratiometric values resulting from the low fura2 intensity in this region [Hallett *et al.*, 1991]. The edge of the neutrophil in the ratio image appeared jagged and a 3x3 median filter was applied to smooth the boundary and to reduce noise.

A neutrophil was segmented in the first image frame by placing manually a few salient points (about 10 points) close to the cell boundary. The spline boundary was subsequently re-sampled increasing the number of control points up to 25 points. The fitting of the spline to the boundary is performed along the normal vector  $n(u)$  at each control point.

$$n(u) = \left( \frac{-y'(u)}{\sqrt{x'(u)^2 + y'(u)^2}}, \frac{x'(u)}{\sqrt{x'(u)^2 + y'(u)^2}} \right) \quad (5.1)$$

The edge is located within a  $\pm 10$  pixel profile orthogonal to each control point. The edge is relocated wherever two values, which are not the background, appear in the profile towards the cell. In consecutive frames, control points of the previous frame are copied onto the next one and adjusted using the same procedure. The flow property has not been used since the boundary was clearly visible in most cases and changes in image intensity may not be associated with movement. Figure 5.29 demonstrates the fitting process of the adaptive spline to a neutrophil boundary.

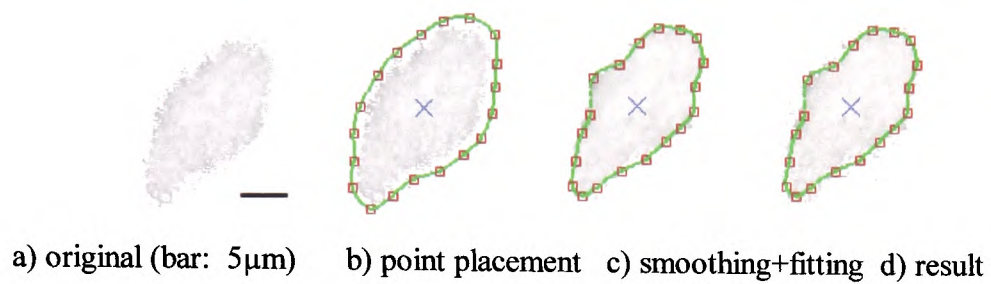


Figure 5.29. Example of boundary fitting to a single, stained neutrophil (centroid X, control points  $\square$ )



Figure 5.30: Example of a single neutrophil with highlighted pseudopod region before and after retraction (bar: 5 $\mu$ m)

The cubic spline description produces a smoothed boundary. This is of great advantage since a slightly jagged boundary may give inappropriately high readings of perimeter length. As a shape descriptor, the roundness was calculated as:

$$roundness = \frac{perimeter^2}{4\pi \cdot area} \quad (5.2)$$

### **Pseudopods**

One of the objectives was to monitor calcium changes in expanding and retracting pseudopods. Since there are no landmarks within the cell image apart from the cell boundary, a method was devised that relates the definition of pseudopods to the overall shape of the boundary. A cell is defined by the same spline method as defined above, however, a small sub-region can be formed by highlighting several control points on the spline. Figure 5.30 shows a single neutrophil with a highlighted pseudopodial sub-region. The calcium concentration was only calculated in that sub-region. As the pseudopod shrinks, the area gets smaller and the number of control points decreases as they move closely together.

### **Results**

The adaptive spline method was applied to track six neutrophils in two series (phag\_3 and phag\_5) with three cells each. Area, length of perimeter and roundness were calculated from the spline description. The median area of six cells was  $62 \mu m^2$  (range:  $41 \mu m^2$  -  $169 \mu m^2$ ) and the median perimeter length was  $32 \mu m$  (range:  $27 \mu m$  -  $49 \mu m$ ).

The roundness was used as a descriptor for cell shape changes. Figure 5.31 and Figure 5.32 show the roundness of three cells per series. A roundness of 1.0 describes a circular shape, higher values express more complex shapes. By visual inspection, neutrophils in the phag\_5 series appeared to show greater phagocytosis and more changes in cell shape than cells in the phag\_3 series; this is supported by greater variation in roundness in the phag\_5 series compared to the phag\_3 series. However,

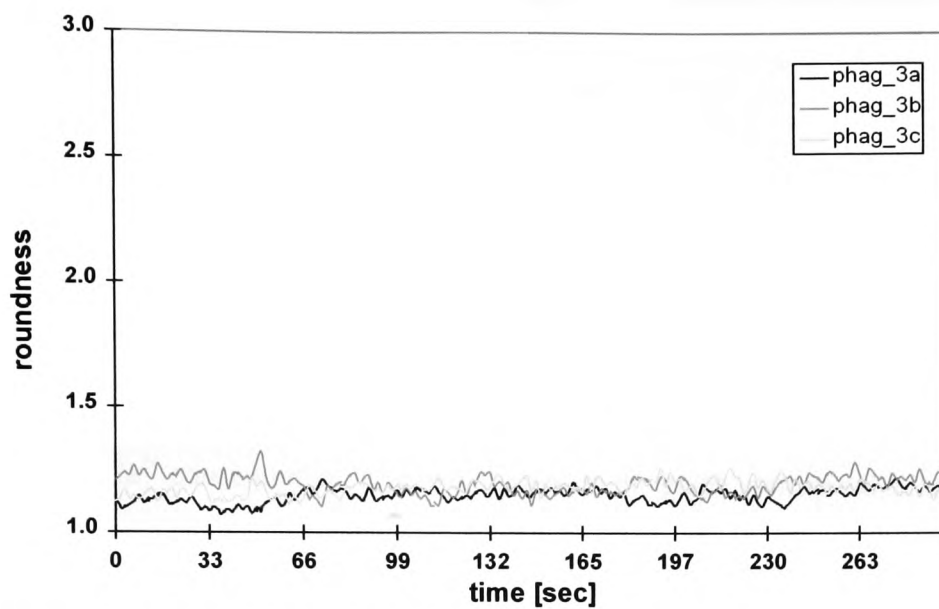


Figure 5.31: Roundness of three cells in phag\_3 series

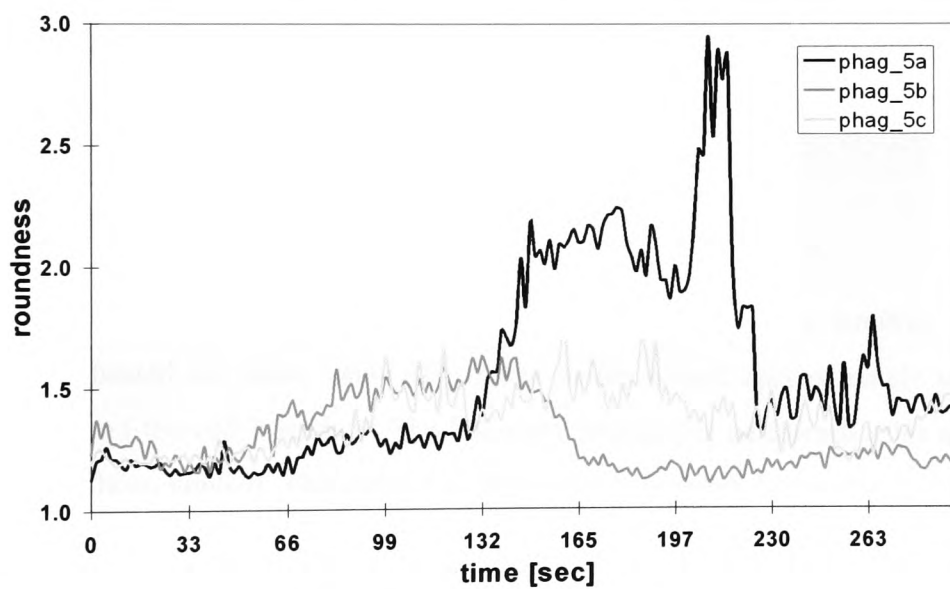


Figure 5.32: Roundness of three cells in phag\_5 series

it was anticipated to measure changes in shape with localised changes in calcium concentration.

As an example, the calcium concentration in the neutrophil shown in Figure 5.30 was calculated using ImageMaster (PTI). The concentration of cytosolic free  $\text{Ca}^{2+}$  was calculated in the whole cell body as well as in the sub-region marked in Figure 5.30. The graph in Figure 5.33 shows the calculated calcium concentration and roundness of that neutrophil. The roundness of the cell body is also plotted as a comparison to the  $\text{Ca}^{2+}$  concentration. The two markers in the graph correspond to regions in the left (1) and right (2) image in Figure 5.30. In this example, a greater calcium concentration was observed in the region of the pseudopod compared to the overall concentration within the neutrophil. The graph suggests that there may be a relationship between the morphology of the neutrophil and the calcium concentration of the pseudopod. In this example, a sudden decrease in  $\text{Ca}^{2+}$  in the pseudopod region (marker 2 in Figure 5.33) may be associated with the retraction of the pseudopod as indicated by a drop in roundness.

### **Validation**

To validate the spline boundary description, the same neutrophil image was delineated six times using 10 control points placed approximately equally spaced around the cell boundary. The boundary fitting was performed after a median filter had been applied. The spline boundary was compared with a description based on a linear interpolation using 50 points placed on the cell boundary.

A maximum error of 3% in area was observed. The maximum difference in perimeter length between the linear interpolation of 50 points and the 10 point cubic spline interpolation was 10%. However, the spline perimeter was smaller in all six cases, confirming a smoother cell boundary.

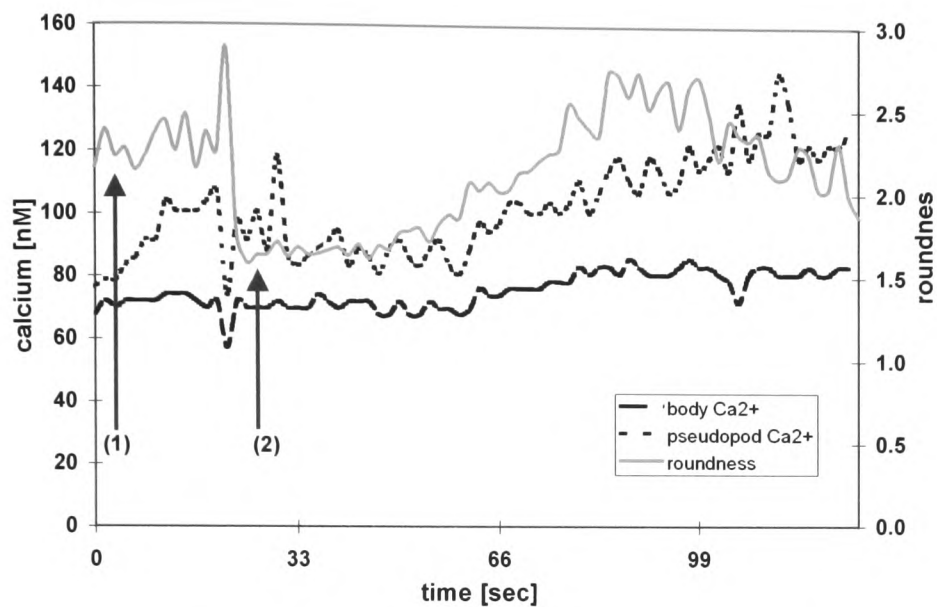


Figure 5.33: Example of Calcium  $\text{Ca}^{2+}$  concentration in the cell body (-) and a pseudopod (--) of the same cell. The two positions in the graph correspond to the cell before and after pseudopod retraction in Figure 5.30

## **Discussion**

In this study the semi-automatic adaptive spline method was used to track single neutrophils. The method is based on the adaptive spline interpolation of the boundary combined with a relocation mechanism for the control points. There is a clear definition of the boundary due to the ratio-imaging, however, concentration values inside the cell may drop below the set threshold and thus 'holes' may appear within the cell. Therefore, the boundary-based segmentation was found to be a suitable approach for cell definition and semi-automatic tracking.

The definition of pseudopod regions was successfully performed by forming a sub-region of the adaptive spline contour. This enabled the assessment of localised changes in calcium concentration in pseudopods while monitoring morphological changes at the same time. The semi-automatic nature of the spline technique enables manual intervention if, for example, two cells are attached. Thus, this system may help in investigating the role of calcium concentration in neutrophil motility.

## 6 Wound Experiments

### 6.0 Introduction

Leg ulcers are often painful and debilitating and about 1.8 per 1000 population develop such a condition [Baker *et al.*, 1991]. Long healing periods cause major costs in treatment of care for the National Health Service in England and Wales.

Objective assessment of healing progress is vital, however, at present it is difficult to predict how well wounds are healing. It has been suggested that analysis of wound colour may be of clinical value [Romanelli, 1997; Boardmann *et al.*, 1994; Mekkes *et al.*, 1995; Herbin *et al.*, 1993]. However, these studies were only of small number of wounds and either looked at the entire wound or a small section and did not necessarily use colour patches for reference. Some systems were operated under a special experimental setup which may prove impractical in a day to day clinical routine.

This chapter describes the application of the semi-automatic spline method to wound imaging. The spline was used to delineate the wound boundary and a case will be made for assessing the image in the vicinity of the wound boundary. Prior to the application of the spline, an analysis of colour variability will be performed. The aim of this aspect was to assess colour variability between images taken under clinical conditions with a digital video system. (section 6.1).

The accuracy of colour assessment was compared with a clinical trial whereby clinicians assessed the amount of slough (necrotic tissue) from digital images (section 6.2). Furthermore, the clinicians perception of wound infection from digital images was also assessed (section 6.3).

During the healing progress, wounds were observed to show a more blurred and convoluted boundary [Herbin *et al.*, 1993]. However, non responding wounds or indeed, infected wounds, may stagnate or increase in size [Cutting *et al.*, 1994]. The

state of the tissue in the boundary region may thus be of value in describing new healing characteristics. In this study, in order to achieve more objective measures of wound appearance, digital image acquisition is used. This is combined with the adaptive spline technique and image analysis to assess the profile of the wound boundary (section 6.3).

## 6.1 Colour Variability

The aim of this study was to assess colour variability in images taken with a digital video system. Images were taken under clinical conditions and the aim was to assess the variation in colour under not fully controllable lighting conditions. A new 3CCD digital camera was used to capture wound images forming a novel approach in the use of digital image processing in wound healing.

Images of leg ulcers on 10 patients were obtained using a digital video camera (Panasonic NVDX100 B, Matsushita Electric Industrial Co. Ltd., Japan). This camera incorporates three separate CCD arrays, one each for the red, green and blue colour plane. This provides good colour reproduction and reduces interference between neighbouring pixels [Sangwine, 2000].

A 10W video light was mounted on the video camera and used to improve lighting conditions. The camera was operated in still picture mode and images were acquired in true-colour and subsequently downloaded digitally to a PC workstation. A graduated scale with additional colour patches (FUJI Colour Scale) was held close to the wound in order to provide a means of colour reference as seen in Figure 6.1. This was used to compare the variability of colour values between different images.

All ten images of leg ulcers were taken under clinical conditions, hence the lighting conditions could not be fully controlled. For example, some rooms of the clinic had daylight from windows while other rooms relied on fluorescent lighting. Images taken from the camera were described by its Red, Green and Blue (RGB) components. In this colour model, however, the value of each component strongly depends on the light intensity which is influenced by the different lighting conditions

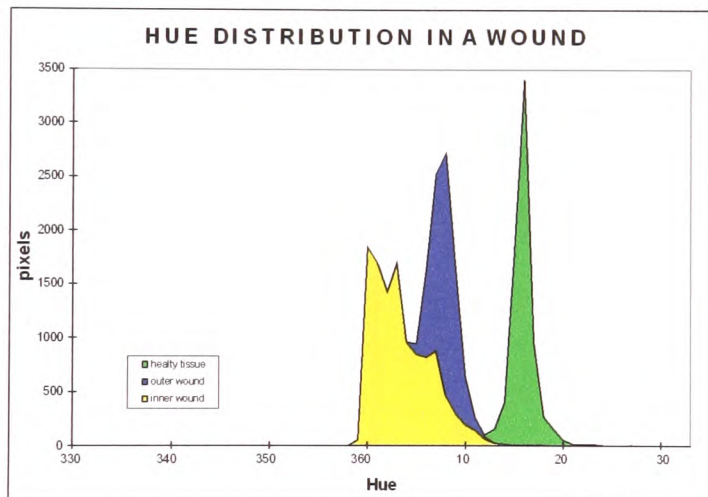


Figure 6.1: Distribution of hue values in different regions of a wound image

Gonzalez *et al.* [1993]. As suggested previously [Boardman *et al.*, 1994; Herbin *et al.*, 1993], the HSI (Hue, Saturation, Intensity) colour model was used in this study. In this model, the intensity is separated from the other two components. Hue is the measure of wavelength of the main colour and represented by an angle  $[0^\circ..360^\circ]$ , saturation is related to the amount of white light included, while the intensity is a measure of brightness [Gonzalez and Woods, 1993].

The variation of hue, saturation and intensity values in red colour patches of ten wound images was analysed. The red hue region in the HSI colour model ranges from  $330^\circ$  to  $30^\circ$ . For example, the graph in Figure 6.1 shows the distribution of hue values over three marked regions in the wound image above.

Analysing hue as a non-continuous value causes problems numerically and hence the HSI colour model was modified by shifting the hue range to allow a continuous range of red hue values ( $120^\circ$  -  $180^\circ$ ) as seen in Table 6.1.

colour	hue range $^\circ$	shifted hue $^\circ$
red	330-30	120-180
yellow	30-90	180-240
green	90-150	240-300
turquoise	150-210	300-360
blue	210-270	0-60
violet	270-330	60-120

Table 6.1: HSI colour conversion table

## Results

The range in hue values for the red colour patch held close to 10 wounds was analysed. The range of values occurring in the red colour patch was compared the range of hue values occurring within each wound region. Hue values were mapped (Hue  $\rightarrow$  Hue') according to Table 6.1. Figure 6.2 shows the comparison of red hue ranges in colour patches and the wound area. The colour patch was of uniform hue and a six degree variation in hue was observed. The total range of hue values

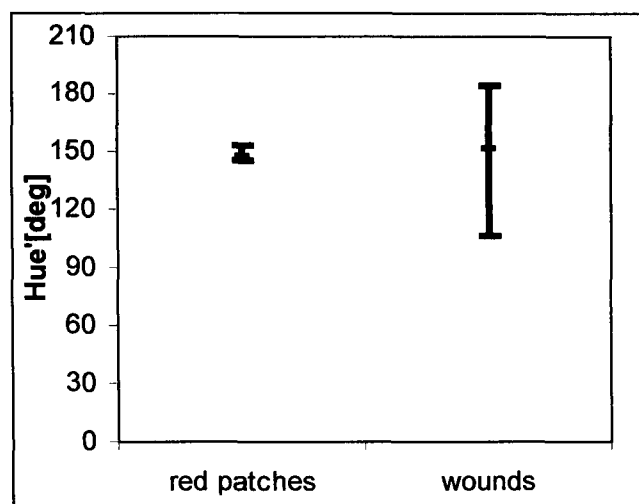


Figure 6.2: Comparison of median and range of red hue values in the 10 images of the red colour patch and 10 wounds

observed over the 10 wounds was 110°-190° and extended over the whole range of red into yellow.

	min	Median max	% of range
Red Hue	144	150	10
Saturation	69	99	30
Intensity	168	240	28

Table 6.2: Range of median values in 10 images of the red colour patch

In Table 6.2, the variations in red hue, saturation and intensity in the 10 images of the red colour patch are shown. The range of scale for the red hue was 60 degrees, the range of saturation was 100% and the range of intensity was 255. The hue components showed the least variation with 10% over its range. Saturation and intensity expressed a much higher variation of up to 30% between images of the same colour patch.

## 6.2 Clinicians assessment of digital wound images

This study was conducted to assess the clinicians perception of colour in wound images using a digital video camera system. Twelve wound images were take with a 3CCD camera (Panasonic NVDX100 B, Matsushita Electric Industrial Co. Ltd., Japan) and printed out onto standard white paper. Two experienced clinicians were asked to rate each image according to whether the wound depicted in the image appeared infected.

The following four grades were defined:

- appears infected
- possibly infected
- probably not infected
- appears not infected

## Results

The two clinicians were asked to grade each wound according to their perception of the wound image and the result is shown in Table 6.3.

wound	appears infected	possibly infected	probably not infected	appears not infected
1			XO	
2	O	X		
3			X	O
4	X	O		
5		O	X	
6			XO	
7			O	X
8				XO
9			X	O
10		X	O	
11				XO
12		X		O

Table 6.3: Assessment of wounds from digital images by two clinicians (X and O)

As seen from Table 6.3, there seems to be little agreement between two clinicians of whether a wound appears infected. There was full agreement in only 4 cases out of 12 (33%) and light agreement (one grade out) in a further 7 cases (58%).

The agreement was also assessed using kappa analysis [Altman, 1991]. Using four classification grades, the kappa value for assessment of agreement was 0.06 while using only two classification grades, the kappa value was calculated as 0.4.

### 6.3 Assessing the amount of slough

This study was conducted to assess the feasibility of using a digital video camera system to assess the colour appearance of wound images. More specifically, the image processing system was used to quantify the amount of slough in leg ulcers.

Thirty leg ulcer images were acquired using a digital video camera (Panasonic NVDX100 B, Matsushita Electric Industrial Co. Ltd., Japan). A 10W video light was mounted on the video camera and used to improve lighting conditions. The camera was operated in still picture mode and images were acquired in true-colour and subsequently downloaded digitally to a PC workstation.

#### Clinicians Assessment

The images were shown in random order to three experienced clinicians who graded images according to amount of slough they perceived. Five images were shown twice in order to test intra-observer variability.

Grading was performed according to the Table 6.4 below.

Grade	Rating
1	clean wound, no slough
2	minimal slough
3	moderate slough
4	moderate to heavy slough
5	heavy slough

Table 6.4: Clinicians grading table for assessment of slough in wound images

#### Wound Imaging

The wound was delineated using the adaptive spline technique by placing a few salient points onto the wound boundary. Points could be adjusted by moving them to a new location such that the boundary was described closely. The area within the spline was used as a region of interest and within that region the amount of slough was calculated in relation to the overall size of the region.

The amount of slough was calculated from the hue values between two thresholds  $T_1=180^\circ$  and  $T_2=240^\circ$  of the shifted hue scale in Table 6.1. These threshold values were determined after consulting the clinicians' perception of slough. Figure 6.3 shows the two thresholds on the shifted hue colour scale. Pixel values with an excessive intensity ( $I > 0.9$ ), indicating specula reflection, were excluded. Also, dark regions were excluded ( $I < 0.1$ ). The following two images in Figure 6.4 show an example of expressing different amounts of slough.

The percentage values obtained from the image analysis were mapped in a linear fashion onto a grading system with grades 1-5 to be compatible with the clinicians' assessment.

## Results

Thirty images were assessed and classified into five categories by three experienced clinicians. In five cases there was full agreement (16.6%) between the three clinicians while in a further 19 cases (63.3%) there was a difference of only one grade where the two other clinicians agreed. Six cases did not experience any agreement (20%).

The result of the (19+5) wound images from the clinicians' assessment, where at least two clinicians agreed, was compared against the results from the image analysis. In 12 cases (50%), the image colour analysis expressed the same grade as the clinicians assessment while in a further six cases (25%) the result suggested by the image analysis was only one grade different from the clinicians assessment. In six cases (25%), however, the image processing technique and the clinicians disagreed.

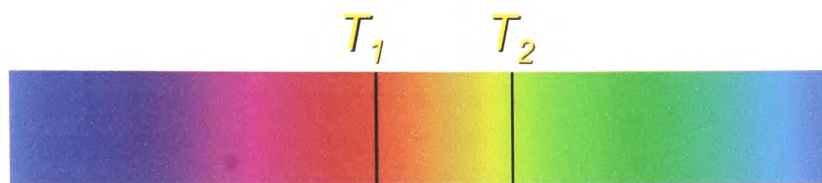
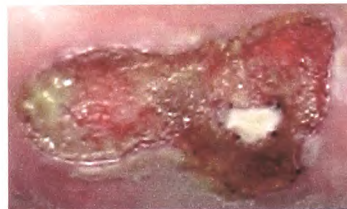
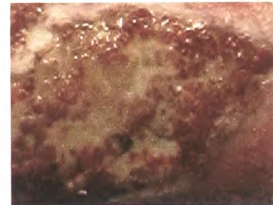


Figure 6.3: The hue values within the two thresholds  $T_1$  and  $T_2$  are classified as slough



*21 % Slough*



*75 % Slough*

Figure 6.4: Example of two images with different amount of slough.

## 6.4 Wound Profile Assessment

The objective for the descriptor of the boundary was to provide a flexible and easy method to define and refine the approximate location of the wound boundary in an image. To describe a wound shape, a sequence of control points is specified on the boundary; the control points help to describe the curvature. The contour model used to delineate the wound boundary is based on the adaptive spline described in chapter 3. Figure 6.5 shows an example wound image delineated by the spline model.

Once the boundary  $Q(x(u), y(u))$  has been described mathematically, the normal vector  $n(u)$  at any given position of the spline  $u$  can be calculated as

$$n(u) = \left( \frac{-\dot{y}(u)}{\sqrt{\dot{x}(u)^2 + \dot{y}(u)^2}}, \frac{\dot{x}(u)}{\sqrt{\dot{x}(u)^2 + \dot{y}(u)^2}} \right) \quad (6.1)$$

The profile, which was set to 31 pixels in width, is centred over the boundary location and divided into three regions: Outer boundary, centre region and inner boundary as seen in Figure 6.6. The width of the outer and the inner section is 10 pixels while the boundary section has a width of 11 pixels.

Each wound was described by eight spline segments and in this study, two profiles per segment were taken. However, the number of profiles per spline segment can be set to a different number. The mean and standard deviation of hue, saturation and intensity values occurring in those three regions of 16 profiles per wound was analysed. Figure 6.7 shows a single wound image with 16 profiles along the spline boundary.

## Results

The mean and standard deviation of values occurring in the outer (o), boundary (b) and inner (i) region of the profile of 10 wound images was analysed. The analysis was performed on hue, saturation and intensity values.

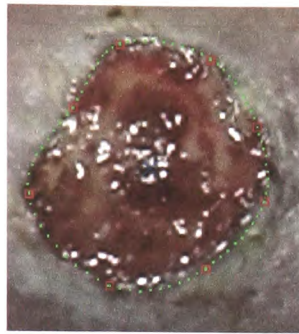


Figure 6.5: Wound image with delineated spline boundary

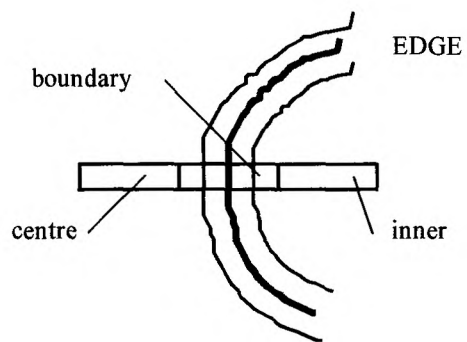


Figure 6.6: Wound profile generated from the spline boundary description. The profile is divided into outer, boundary and inner region.

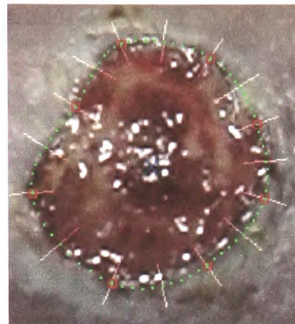


Figure 6.7: Wound image with profiles along the spline boundary

WOUND	HUE' [°] (mean)			HUE' [°] (stdev)		
	o	b	l	o	b	l
1	141	149	154	6	7	5
<b>2</b>	<b>169</b>	<b>167</b>	<b>154</b>	<b>8</b>	<b>7</b>	<b>3</b>
3	170	160	153	9	11	6
4	149	150	150	4	3	3
5	151	153	156	9	9	10
6	146	144	147	6	5	6
7	141	143	142	3	3	1
<b>8</b>	<b>156</b>	<b>153</b>	<b>153</b>	<b>2</b>	<b>2</b>	<b>2</b>
9	141	143	145	3	3	2
<b>10</b>	<b>155</b>	<b>154</b>	<b>152</b>	<b>3</b>	<b>3</b>	<b>2</b>

Table 6.5: Mean hue and standard deviation in 10 wound images. Wounds in bold were considered to be infected by visual inspection from an experienced clinician.

As seen in Table 6.5, most wounds expressed little differences in mean hue values between the three regions of the wound profile despite its different appearance. There was no obvious trend by which the mean hue values increased/decreased from the outer towards the inner wound region. Those wounds considered to be infected did not show any significant differences in hue values at the boundary.

WOUND	SAT (mean)			SAT(stdev)		
	o	b	l	o	b	l
1	21	31	38	9	13	11
<b>2</b>	<b>57</b>	<b>54</b>	<b>49</b>	<b>15</b>	<b>10</b>	<b>5</b>
3	19	32	44	5	12	13
4	49	65	75	12	17	14
5	41	52	58	9	16	17
6	34	51	59	15	20	21
7	39	52	58	9	10	6
<b>8</b>	<b>60</b>	<b>83</b>	<b>91</b>	<b>11</b>	<b>14</b>	<b>8</b>
9	40	62	88	15	23	13
<b>10</b>	<b>47</b>	<b>53</b>	<b>61</b>	<b>8</b>	<b>10</b>	<b>6</b>

Table 6.6: Mean saturation and standard deviation in 10 wound images. Wounds in bold were considered to be infected by visual inspection from an experienced clinician.

As seen in Table 6.6, there seems to be a common pattern between the three regions of the profile for the mean saturation. All except one wound appeared to show an increase in saturation from the outer to the inner region of the wound boundary. The mean saturation of wound 2 decreased from the outer to inner region unlike the data

from the other wound images. Two of three wounds that were considered to be infected seemed to be more saturated on the outer boundary.

WOUND	INT(mean)			INT(stdev)		
	o	b	l	o	b	l
1	160	143	144	35	37	26
2	<b>153</b>	<b>170</b>	<b>184</b>	<b>36</b>	<b>27</b>	<b>19</b>
3	125	99	105	26	29	41
4	182	147	125	46	49	43
5	156	141	137	32	36	36
6	158	140	135	30	32	39
7	129	111	110	22	26	16
8	<b>166</b>	<b>120</b>	<b>108</b>	<b>29</b>	<b>30</b>	<b>24</b>
9	220	191	161	25	36	25
10	<b>121</b>	<b>98</b>	<b>86</b>	<b>25</b>	<b>28</b>	<b>20</b>

Table 6.7: Mean intensity and standard deviation in 10 wound images. Wounds in bold were considered to be infected by visual inspection from an experienced clinician

As seen in Table 6.7, the mean intensity values appear to decrease from the outer towards the inner boundary profile. Again, the profile of the likely infected wound 2 behaved differently. However, this behaviour was not observed in wound 8 and 10, which were also considered to be infected by visual inspection of a clinician.

## 6.5 Conclusion and Discussion

The results suggest that recording images digitally on a 3 CCD chip camera is a feasible way of determining wound colours under clinical condition. Despite the influence of daylight and/or fluorescent light, there was a maximum shift of six degrees (10%) in hue in the red colour patches. Intensity and saturation expressed a greater variation of up to 30%. Hue appears to be the most stable component of the HSI colour model for colour analysis which is in accordance with previous observations [Boardman *et al.*, 1994]. However, it also shows that calibration is necessary to obtain reliable results in order to be able to describe subtle changes in hue.

The assessment of wound appearance from digital images alone seemed not to be sufficient enough for experienced clinicians to determine whether a wound is infected. There was full agreement of only 33% between two experienced clinicians in determining wound infection visually from digital images. Clinicians take many other factors into account, such as the patients history, odour, pain, size and surrounding tissue [Cutting *et al.*, 1994]. Image processing may provide a tool to assess objectively colour appearance of wound images. The developed system was used to quantify the amount of slough in leg ulcers with a 75% agreement between clinicians' assessment and computer analysis.

The adaptive spline technique was implemented to provide a new measure of assessing the wound boundary and surrounding tissue. It was used successfully to delineate the boundary of leg ulcers and to describe variations of colour in the vicinity of the wound boundary. Intensity and saturation expressed a clear trend from the inner to the outer wound boundary. Two images out of 10, however, did not follow this trend and one of which was considered to be infected. The wound boundary profile may be useful in a quantitative assessment of changes at the wound boundary, especially the wound edge convolution during progress in the wound healing process.

## 7.0 Conclusion and Discussion

In this project, a new semi-automatic technique was devised that enabled the analysis of movement of clustered cells. Some computerised systems have been developed previously to analyse the movement of single cells *in vitro*. However, the segmentation of clustered cells by a fully automated image processing system is likely to be unreliable. Therefore, a new semi-automatic image processing system which facilitates the segmentation and tracking of cells in a clustered cell colony was developed. The following aims and objective were set out to be accomplished:

### *1. to review current methods of assessment of cell motility*

The literature review covered many aspects of light microscopy relevant for monitoring living cell cultures. Image processing techniques to segment microscopic images were discussed. A number of systems to access cell motility were described and some their techniques highlighted. However, most systems were designed to monitor single cells or multiple detached cells. In one instance, a system enabled the analysis of the whole cell cluster without distinguishing between individual cells. The problem is recognising and segmenting cells automatically with an image vision system. Model based approaches have been used to enhance the segmentation success in difficult situations by using *a priori* knowledge about the objects occurring in an image. For example, a contour model was applied to segment and track single cells, however, this method did not perform well on pseudopodial regions. A model-based, semi-automatic system was thought to be more appropriate, enabling interactive segmentation and tracking of clustered cells.

### *2. to develop an approach for segmenting cells in clusters*

In order to enable the segmentation of cells in clusters, a semi-automatic technique based on two-dimensional rendering of the cell boundary was developed. The boundary is interpolated between control points placed initially on the cell boundary, forming a piecewise cubic spline boundary. The number of control points can be

changed manually or an automated re-sampling technique can be used. The first and second derivative of the boundary at control points is continuous enabling a smoothed representation of the cell boundary. The initial definition of the cell by an observer overcomes the problems an automated image vision system may have in locating cells. This way, expanding and protruding cellular regions can be described with the spline representation as long as they are recognisable.

After the initial placement of control points, in order to reduce inter-observer variability, a fitting process is applied. Control points are moved towards high image gradients whenever a high image gradient along a short section of the boundary is detected. A confidence parameter is introduced which estimates the degree of a good fit of each control point. This minimises the effect of control points moving to false locations due to gradient peaks in the image which is a great advantage over traditional segmentation techniques.

Image fitting has been localised and does not rely on a global fitting constraint such as global energy minimisation in snakes. This takes into account that some cellular regions can express a high image gradient while others no clear image gradient. If a control point is located falsely, the operator has full control over the position of each control point and hence may move a point manually to ensure a proper representation of the cell boundary.

### *3. to combine the segmentation with a tracking mechanism*

It was anticipated to develop a technique to facilitate the tracking of cells in clusters. The spline based segmentation process was therefore combined with a spatio-temporal tracking technique to relocate cells in consecutive frames. Image features from image gradient and intensity are used in a subsequent tracking process to relocate each control point from which a new boundary representation is rendered. This spatio-temporal approach enables the tracking of regions that do not express a predominant image gradient such as expanding pseudopodial regions. Tracking is performed by approximating the movement of each control point using an area matching technique based on image intensity. Another confidence parameter is

calculated describing the likelihood of a good movement estimation from the area matching which is used for the final assessment of movement of individual control points. However, control points are only moved to a new location if there is sufficient confidence of a good fit. At the same time, the image gradient in the near neighbourhood is analysed and a gradient confidence parameter is calculated as well. The position of each control point is relocated individually based on a decision making process using the confidence parameters of image gradient and area matching. This forms a new spatio-temporal technique for tracking objects.

The advantage is that control points are relocated individually and can be moved interactively to a more suitable position if the automatic relocation technique does not suggest an appropriate solution. Areas where no predominant gradient is expressed may still be able to be tracked after an initial placement of control points.

#### *4. to validate the new system*

It was anticipated to validate the system by describing objects with a known size. The system was validated by segmenting artificially generated test images and agreement within 10% of area was found. The adaptive spline technique was also validated by delineating the cell boundary in real cell images viewed by Hoffman Modulation Contrast microscopy. In this test, three independent operators placed points onto the cell boundary from which the cell boundary was rendered. There was a maximum error of 6% in area with single cells and a maximum error of 13% with clustered cells. Inter-observer variability could be reduced further by applying a gradient based fitting process.

The system was found to be well suited for the description of movement of single cells in a clustered environment. The gradient and flow based relocation method appeared to work well on clearly definable cells within a cluster. However, the system did not accurately reflect movements of the cell boundary when heavy membrane ruffling occurred. In such cases, the fully interactive nature of the method can be used by simply adjusting single control points manually to ensure a close fit.

### *5. to study the effect of HGF/SF motogen on Human Colon Cancer Cells in vitro*

The method has been used in a series of experiments to assess the effects of HGF/SF motogen on the movement of HT115 human colon cancer cells. Four series of HT115 cells were analysed with six clustered cells each. In each series, one set of cells was stimulated with HGF/SF motogen while the other set was used as a control reference. Changes in cell area, movement and cell shape were analysed. Translocative motility was assessed using cell velocity while changes in cell area and shape were used as an indicator of stationary motility. The results showed that cells with added HGF/SF motogen expressed a velocity of 25% to 100% higher than those without any added motogen. However, it was also observed that cell velocity varies in time and our results suggest that this variation is greater in cells treated with motogen.

Cells with added motogen expressed more movement and longer movement paths than cells without added motogen. This is in accordance with a previous study [Goldberg and Rosen, 1993]. There were also more changes in area and cell shape with stimulated cells indicating more morphological activity. Cell area was found to be similar in cells with and without motogen, however, there was greater variation in area with time in those cells treated with motogen. Some stimulated cells did not seem to respond to the motogen resulting in a similar movement behaviour to control cells. This may be explained by the fact that some cells do not have enough receptors for the HGF/SF to take effect.

In a further experiment, HRT18 cells were used to compare the effects of HECD-1 human E-cadherin antibody and HGF/SF motogen on their movement behaviour. Changes in area and velocity were analysed. Although the number of cells analysed was low, cells with added antibody expressed more variation in velocity and higher median velocities than cells with added HGF/SF motogen. HRT18 cells with added antibody showed increased ability to move more freely resulting in higher translocative motility compared to cells with added HGF/SF motogen. As suggested by Hiscox and Jiang [1999], this may be explained by impairing cell-to-cell adhesions by the antibody which gives the tumour cell a possibility to escape from

the cluster. Interestingly, cells with added HGF/SF motogen seem to express higher stationary motility as indicated by a higher range and more frequent changes in cell area. HGF/SF stimulates the desire of cells to move [Schiffman 1990] but the cell-to-cell adhesions may still restrain their translocative movement.

The system is also applicable for assessing the movement of single cells. The system was compared with a region-based segmentation system for analysing the movement of single neutrophils [Korzynska, 1998]. The area measurements of three cells were compared and a maximum difference in area of 25% was observed in one case while a mean difference between the two measurement systems was 7.5% in area.

#### *6. to apply and extend the new method to ratio imaging for neutrophils*

Another aspect of studying cell motility is to assess whether an intracellular chemical change is responsible for changes in cell morphology and the mechanisms of cell movement. The system was adapted for measuring cytosolic free calcium in neutrophils using ratio imaging. The level of cytosolic free calcium is thought to be a factor in the neutrophils ability to protrude [Pettit and Hallett, 1998]. Special interest was paid to calcium changes in expanding and retracting pseudopodial regions. The adaptive spline was used as a description of the neutrophil boundary while a dynamic sub-region could be defined in which the calcium concentration was assessed. The results suggest that in retracting pseudopods the level of cytosolic free calcium is higher than in the rest of the cell body.

The advantage of using a boundary based segmentation method instead of a region based segmentation technique lies in the fact that regions that fall below a calcium threshold are still included in the area calculations. Furthermore, the boundary representation is smoothed which avoids false readings when using the perimeter length as part of a shape descriptor.

*7. to apply the system to assess the appearance of ulcers in the vicinity of the wound boundary*

The system for segmenting cell images was also applied to macroscopic wound images. In wound imaging, the appearance of the wound boundary may be an indicator of wound healing.

Some previous studies have looked at changes in wound colour or texture on a global level, though not taking into account any specific regions. Also, in some studies, wound images were taken under a special experimental set-up to minimise variations in lighting. However, in order to be practical, a system to assess wound healing should be able to work under normal clinical conditions which tend to have slightly varying ambient lighting conditions.

A system was developed comprising of a 3CCD array digital camera to acquire wound images and image processing software, which has been shown to be a feasible way of determining wound colours under clinical condition. The RGB colour values were converted into a slightly modified HSI colour model for colour separation. Despite the influence of daylight and/or fluorescent light, there was a maximum shift of 6 degrees (10%) in hue of the red colour scale. However, it also shows that colour reference is necessary to obtain reliable colour values in order to be able to describe subtle changes in hue.

The system was tested by analysing the amount of slough in wounds in comparison with clinicians' assessment. The results suggest that the computer colour analysis using a 3CCD camera under clinical conditions compares well with the assessment of three experienced clinicians.

Wound appearance alone as a measure of wound infection was not found to be reliable. In another study, two clinicians assessed wound images and there was little agreement between their assessment. Wound appearance may thus not be enough in, for example, assessing whether a wound is infected. Indeed, a number of other criteria has been suggested such as pain, odour and friable granulation tissue [Cutting

*et al.*, 1994]. However, computerised colour analysis provides a more objective assessment of wound colour even when used under clinical conditions.

Objective assessment of certain areas of the wound by visual inspection may also be difficult for a clinician. The adaptive spline technique was used successfully to delineate the boundary of leg ulcers in a semi-automatic approach. The region on both sides of the boundary was used for further analysis. A profile of the wound boundary was created from the spline location and changes in colour and intensity were analysed. Most wound images followed a clear trend in changes of colour from the inner wound region to the outer boundary region. Some wound images did not follow this trend of which one was considered to be infected by experienced clinicians. Such an intra-wound assessment technique may be used to avoid inconsistencies in colour representation under clinical conditions.

#### *Further Studies*

The system was shown to be useful in assessing the motility of cells in clusters. It is intended to use the system to study the effects anti metastatic drugs on cell movement. The assessment of clustered cells may also provide a way of quantifying the breaking up of cell-to-cell adhesions. It is also anticipated to use the system in a broader study to assess the level of cytosolic free calcium in pseudopodial regions of neutrophils undergoing motion.

#### *Summary Conclusion*

The developed system was shown to be useful in objectively describing the movement of cancer cells in clusters. The semi-automatic nature of the technique enables segmentation of cells which otherwise would be difficult to describe. The tracking of clustered cells was performed on eight series of HT115 cells and on three series of HRT18 cells. The system was also used in assessing motility and morphological changes of neutrophils and in measuring changes in calcium concentration in ratio-imaging.

Thus, the devised system provides a tool for assessing motility in clustered cells. Cell motility plays an important role in the establishment of cancer metastasis. This may lead to a further understanding in cancer metastasis.

The system was also shown to be valuable for segmenting macroscopic wound images. The 3CCD digital camera system was used to acquire wound images digitally for processing. Colour representation using the HSI colour model produced a stable red hue component with a maximum of 6 degrees variation under clinical conditions. The adaptive spline technique was able to generate a wound profile which was used to analyse changes in the vicinity of the wound boundary.

Thus, the system developed should help to further understanding in wound healing and cell motility analysis.

# Appendix

## A References

## B Snapshots

## C Software

- Class Diagram

- Class Description

- Source code examples

## D Spline Calculations

## E Published Work

## Appendix A - References

- Aggarwal JK, Cai Q, Liao W, Sabata B . Articulated and elastic non-rigid motion: A review. Proc of IEEE Workshop on Motion of non-rigid and articulated objects, Austin, TX, pp 16-22, 1994
- Alberts B, Brag D, Lewis J, Rolf M, Roberts K, Watson JD. Molecular Biology of The Cell. Third Edition, Garland Publishing Inc., 1994
- Alpha S, Manley SW. Thyrotrin inhibits the instrinsic locomility of tyroid cells organized as follicles in primary culture. Exp Cell Res: 214, 408-417, 1994
- Altman DG. Practical statistics for medical research. Chapman and Hall, London, 1991
- Amini AA, Curwen RW, Gore JC. Snakes and Splines for Tracking Non-Rigid Heart motion. Computer Vision: ECCV'96, 251-261, 1996
- Azzara A, Chimenti M, Azzarelli L, Fantini E, Carulli G. An image processing workstation for automatic evaluation of human granulocyte motility. J of Immunological Methods: 148, 29-40, 1992
- Baker SR, Stacey MC, Jopp-McKay AG, Hoskin SE, Thompson PJ. Epideriology of venous ulcers. British J Surg. 78: 864-867, 1991
- Belmont MR, Hotchkiss AJ. Generalized Cross-Correlation Functions for Engineering. Journal of Applied Mechanics: 64, 321-326, 1997
- Bereiter-Hahn J. Computer assisted microscope interferometry by image analysis of living cells. Advances in Microscopy. Progress in Clinical and Biological Research (ed. Cowden R, Harrison FW), 196, pp. 27-44, Alan R. Liss Publ., 1985
- Bhargava MM, Li Y, Joseph A, Jin L, Rosen EM, Goldberg ID. Hepatocyte Growth and Scatter Factor (HGF/SF) and the c-met Receptor, ed. Goldberg ID and Rosen EM. Birkhäuser Verlag Basel/Switzerland, 341-349, 1993
- Blake A, Yuille A. Active Vision. MIT Press, 1993
- Bland JM, Altman DG. Statistical methods for agreement between two methods of clinical measurement. Lancet 1 (8476): 307-310, 1986
- Boardmann M, Melhuish J, Palmer K, Harding KG. Hue Saturation and Intensity in the healing wound image. J of Wound Care, 3, 314-319, 1994

- Boyden SV. The chemotactic effect of mixtures of antibody and antigen on polymorphonuclear leucocytes, *J Exp. Med.* 115, 453ff, 1962
- Brocksch D. Phase-contrast, Normanski contrast and Dark-Field Microscopy. *Cell Biology: A laboratory handbook*, (ed. Celis JE), pp. 5-14, Academic Press, 1994
- Brown AF, Dunn GA. Microinterferometry of the movement of dry matter in fibroblasts. *J Cell Science* 92: 379-389, 1989
- Coates TD. Behavioral aspects of neutrophil motility. *Curr Opin Hematol*: 3, 41-47, 1996
- Cootes TF, Taylor CJ, Cooper DH, Graham J. Active Shape Models - their training and applications. *Computer Vision Image Understanding* 61, 38-59, 1995
- Cootes TF, Taylor CJ. Active shape models - smart snakes. *British Machine Vision Conference*: pp 276-285, 1992
- Cotton S, Claridge E. Noninvasive monitoring skin imaging. *Inf. Proc. in Med. Imag.* 1230, 501-507, 1997
- Curwen R, Blake A. Dynamic Contours: Real time active splines. *Active Vision*: pp 39-58, MIT Press, 1996
- Cutting KF, Harding KG. Criteria for identifying wound infection. *J Wound Care*, 3, 198-201, 1994
- Davis L, Johns S, Aggarwal JK. Texture Analysis using generalized co-occurrence matrices. *IEEE Trans Pattern Recognition and Machine Intelligence*: 1, 3, 251-259, 1979
- Davies, EV and Hallett MB. A novel pathway for  $\text{Ca}^{2+}$  signalling in neutrophils by immune complexes, *Immunology* 85, 538-543, 1995
- Delanges P, Benois J, Barba D. Active Contours Approach to object tracking in image sequences with complex background. *Pattern Recognition Letters*: 16,2,171-178, 1995
- Dunn GA, Zicha D. Using interference microscopy to study cell behaviour. *Cell Biology: A laboratory Handbook* (eds. Celis JE) pp. 25-33, Academic Press, 1994
- Dunn GA. Transmitted-light Interference Microscopy: a technique born before its time. *Proceedings RMS*, 33, 189-195, 1998
- Engelbert SE, Sheng Z. The evaluation of a cross-correlation pattern recognition technique for flow visualisation. *Pattern Recognition*: 23, 237-243, 1990

Foskett JK. Simultaneous differential interference contrast and quantitative low-light fluorescence video imaging of cell function. Optical Microscopy, pp 237-261, Academic Press, 1993

Fram JR, Deutsch ES. On the quantitative evaluation of edge detection schemes and their comparison with human performance. IEEE Trans Computers, C-24, 6, 616-628, 1975

Gey GO. Some aspects of constitution and behavior of normal and malignant cells maintained in continuous culture. The Harey Lectures, Series L: 154-229, 1954

Gonzalez RC, Woods RE. Digital Image Processing. Addison Wesley Publishing Company, 3, 1993

Goldberg ID, Rosen EM. HGF/SF: Effects on motility and morphology of normal and tumor cells. Hepatocyte growth factor-scatter factor (HGF/SF) and the c-met receptor: Birkhäuserverlag Basel/Switzerland, pp 341-349, 1993

Grimstad IA. Direct evidence that cancer cell locomotion contributes importantly to invasion. Exp. Cell Research: 173, 515-523, 1987

Gupta N, Kanal L. Gradient based image motion estimation without computing gradients. Int. J of Computer Vision, 22(1), 81-101, 1980

Hader DP. Image Analysis in Biology. CRC Press 1992

Haemmerli G. Cell motility and cell shape. Eur J Cancer: 16, 1-2, 1980

Haemmerli G, Staehli P. In vitro motility of cells from human epidermoid carcinomas. A study of phase-contrast and reflection contrast cinematography. Int. J. Cancer: 27, 603-610, 1981

Hallett MB, Davies EV, Pettit EJ. Fluorescent methods for measuring and imaging the cytosolic free  $\text{Ca}^{2+}$  in neutrophils. Methods: A Companion to Methods in Enzymology 9, 591-606, 1996

Hallett MB, Davies ED, Campbell AK. Spatial and temporal analysis of  $\text{Ca}^{2+}$  signals in individual neutrophils using ratio imaging of fura2. Surveys in Subcellular Methodology 21, Cell Signalling: Experimental Strategies (Eds Reid, GMW Cook and JP Luzio) Royal Society Chemistry. pp 273-286, 1991

Haralick RM, Shanmugan K, Dinstein IH. Textural features for image classification. IEEE Trans Systems, Man and Cybernetics: SMC-3, 6, 610-621, 1973

Harding KG. Leg ulcers. J R Soc Med: 84(9), 515-516, 1991

Harris A, Behaviour of Cultured Cells on Substrata of Variable Adhesives, Exp. Cell Research, vol. 77, pp. 285-297, 1973

- Hart IR, Saini A. Biology of tumor metastasis. *Lancet*: 339, 1453-1457, 1992
- Heath JP. Epithelial cell migration in the intestine. *Cell Biology International*: 20, 139-146, 1996
- Herbin M, Bon F X, Jeanlouis F, Dubertret L, Strauch G. Assessment of Healing Kinetics Through True Color Image Processing. *IEEE Trans Medical Imaging*, 12, 39-43, 1993
- Herman B, Le Masters JJ. *Optical Microscopy: Emerging Methods and Applications*. Academic Press: London, 1992
- Hiscox S, Jiang WG. Association of HGF/SF receptor , c-met, with the cell surface adhesion molecule, E-cadherin, and catenins in human tumor cells. *Biochemical and Biophysical Res Com* 261: 406-411, 1999
- Hoch M, Litwinowicz PC. A semi-automatic system for edge tracking with snakes. *Visual Computer*: 12, 2, 75-83, 1996
- Hoffman R. The modulation contrast microscope: principles and performance. *J of Microscopy* 110: 205-222, 1977
- Hoffmann-Wellenhof R, Smolle J, Helige C. Qunatitive Assessment of melanoma single-cell motility in vitro. *Experimental Dermatology*: 3, 219-226 , 1994
- Hoch M, Litwinowicz. A semi-automatic system for edge tracking with snakes. *Visual Computer* 12: 75-83, 1996
- Hoppe A, Jiang WG, Wertheim D, Melhuish J, Williams R, Harding K. A computer system for analysis of movement of cancer cells. *Anticancer Research*, 17, Number 6A, pp. 4039-4040, 1997
- Hoppe A, Jiang WG, Wertheim D, Williams R, Harding K. A System for Computer Analysis of Cancer Cell Movement. *Anticancer Research*: 18, 2691-2694, 1998a
- Hoppe A, Wertheim DF, Melhuish JM, Williams RJ and Harding KG. Computer analysis of wound images. *Wound Repair and Regeneration*, 6, A488, 1998b
- Hoppe A, Wertheim DF, Melhuish JM, Williams RJ and Harding KG. Computer analysis of wound images. *Wound Repair and Regeneration* 6(5), pp A488, 1998c
- Hoppe A, Wertheim D, Jiang W.G, Williams R, Harding K. A computerised system for assessment of cancer cell movement. VIII Mediterranean conference on Medical and Biological Engineering and Computing. June 14-17, Cyprus. Published on CD. ISBN 9963-607-13-6, 1998d

- Hoppe A, Wertheim D, Jiang WG, Williams R and Harding K. Interactive image processing system for assessment of cell movement. Medical & Biological Engineering & Computing, 37(4), 419-423, 1999a
- Hoppe A, Wertheim DF, Jiang WG., Williams R and Harding K. A Computer System for Assessment of cancer cell movement. Proceedings of Medical Image Understanding and Analysis 99, Oxford University, July 19-20, 1999b
- Hoppe A, Korzynska A, Wertheim D. A computer system for the analysis of Neutrophil Movement. Medical & Biological Engineering & Computing, 37(2), 1000-1001, 1999c
- Hoppe A, Hallett MB, Dewitt S, Wertheim DF, Williams RJ. Adaptive Spline Method for Extracting Ca<sup>2+</sup> and Morphological Measurements from Motile Human Neutrophils. Proceedings of Medical Image Understanding and Analysis 2000, University College London, July 10-11, 2000a
- Hoppe A, Wertheim D, Melhuish J, Harding KG, Williams R. A Spline Method for Assessing Wound Images. Medical Signal and Information Processing Conference, University of Bristol, Sept. 2000b
- Hoppe A, Morris H, Melhuish J, Clark M, Harding KG, Williams RJ. Comparison of wound image analysis and clinicians' ranking of chronic wounds. 4th Meeting of the European Tissue Repair Society & Wound Healing Society, Brussels, May. 5-8, 2000c
- Hoppe A, Jiang WG, Wertheim D, Williams R, Harding K. Computerised analysis of HRT18 cells.. Proceedings of the VIII Int. Congress of the Metastasis Research Society, Imperial College of Science, Technology and Medicine, London, 24-27 Sept. 2000d
- Horn BKP, Schunk BG. Determining optical flow. Artificial Intelligence, 17, 185-204, 1981
- Huang TS. Modelling, analysis and visualisation of non-rigid object motion. Proc. of 10th ICPR, 361-364, 1990
- Hubel DH, Wiesel TN. Functional architecture of macaque monkey visual cortex. Proc. Royal Society London, B198, 1-59, 1977
- Jensen P, Kharazmi A. Computer assisted image analysis assay of human neutrophil chemotaxis in vitro. J of Immunological Methods: 144, 43-48, 1991
- Jiang WG, Hallett MB, Puntis MCA. Review Paper: Motility factors in cancer invasion and metastasis. Surg. Res. Comm: 16, 219-237, 1994a
- Jiang WG, Puntis MCA, Hallett MB. Molecular and cellular basis of cancer invasion and metastasis: implications of treatment. British Journal of Surgery: 81, 1576-1590, 1994b

- Jiang WG, Hiscox S, Singhrao SK, Singhrao SK, Nakamura T, Puntis MCA, Hallett MB. Inhibition of HGF/SF Induced Membrane Ruffling and Cell Motility by Transient. Elevation of Cytosolic Free  $Ca^{2+}$ . *Experimental Cell Research*: 220, 424-433, 1995
- Jiang WG, Hiscox S. Hepatocyte growth factor/scatter factor, a cytokine playing multiple and converse roles. *Histology and Histopathology*: 12, 537-555, 1997
- Jiang WG, Hiscox S, Cai J, Martin T, Matsomoto K, Nakamura T, Mansel RE. Antagonistic effects of NK4, an novel HGF variant, on the in vitro angiogenesis of human vascular endothelial cells. *Clinical Cancer Research*, 5, 3695-3703, 1999
- Julesz B. Textons, the element of texture perception and their interactions. *Nature*: 290, 91-97, 1981
- Kass M, Witkin A, Terzopolous D . Snakes: Active contour models . *Proceedings of the first International Conference on Computer Vision*: pp 259-268, 1987
- Keevil CW, Walker JT. Normanski DIC microscopy and image analysis of biofilms. *Binary Comput. Microbiol.*4: 93-95, 1992
- Killich T, Plath PJ, Wei X, Bultmann H, Rensing L, Vicker MG. The locomotion, shape and pseudopodial dynamics of unstimulated Dictyostelium cells are not random. *J of Cell Science*: 106, 4, 1005-1013, 1993
- Kittler J, Illingworth J, Föglein J. An automatic thresholding algorithm and its oerformance. *IEEE Proc. 7<sup>th</sup> Int. Conference on Pattern Recognition*, Montreal, pp. 287-289, 1984
- Korzynska A. "A Method of Segmentation of Neutrophil Images observed in a Cell Monitoring System" in *Proc. VII Mediterranean Conference on Biomedical Engineering and Computing*, Cyprus, 1998
- Krauss AH, Nieves AL, Spada CS, Woodward DF. Determination of leukotriene effects on human neutrohil chemotaxis in vitro by differential assessment of of cell motility and polarity. *Journal of Leukocyte Biology*: 55, 201-208, 1994
- Lee CC, Chung SY, Park RH. A comparative performance study of several global thresholding techniques for segmentation. *Comput. Vision, Graphics, Image Proc*: 52,2, 171-190, 1990
- Lee J, Ishihara A, Theriot JA, Jacobson K. Principles of locomotion for simple-shaped cells. *Nature*: 363, 167-171, 1993
- Lindblom A, Liljegren A. Tumor markers in malignancies. *BMJ*: 320, 424-427, 2000

- Marr D, Hildreth E. Theory of Edge Detection. Proc R Soc Lond, vol B207, pp 187-217, 1980
- Mekkes J R, Westerhof W. Image Processing in the Study of Wound Healing. Clinics in Dermatology, 13, 401-407, 1995
- Mikic I, Krucinski S, Thomas JD. Segmentation and tracking in echocardiographic sequences: Active contours guided by optical flow. IEEE Trans. Medical Imaging: 17, 2, 274-284, 1998
- Miller JV, Bren DE, Lorensen WE, O'Bara RM, Wozny MJ. Geometrically Deformable Models: A method for extracting closed geometric models from volume data. Computer Graphics, 25: 217-226, 1991
- Miyata Y, Nishida E, Sakai H. Growth Factor- and Phorbol Ester Induced Changes in Cell Morphology analyzed by Digital Image Processing. Exp. Cell Research: 175, 2, 286-297, 1988
- Nomura A, Miike H, Koga K. Field theory approach determining optical flow. Pattern Recogn. Lett. 12: 183-190, 1991
- Schnorrenberg F, Pattichis C, Kyriacou K, Schizas CN. Computer-aided detection of breast cancer nuclei. IEEE Trans Information Technology in Biomedicine 1: 128-140, 1997
- Okamoto K, Hassan A, Schmidt WD. New tracking algorithm for particle image velocimetry . Experiments in Fluids: 19, 342-347, 1995
- Papula L. Mathematik fuer Ingenieure 2. Vieweg Verlag Braunschweig/Wiesbaden, 1991
- Peterfreund N. Robust Tracking of position and velocity with Kalman snakes. IEEE Trans. Pattern Analysis and Machine Intelligence: 21,6, 564-569, 1999
- Peterfreund N. The velocity snake: Deformable contour for tracking in spatio-velocity space. Computer Vision and Image Understanding: 73,3, 356-356, 1999
- Pettit EJ, Hallett MB. Release of 'caged' cytosolic  $Ca^{2+}$  triggers rapid spreading of human neutrophils adherent via integrin engagement, J. Cell Sci . 111, 2209-2215, 1998
- Pons MN, Vivier H, Remy JF, Dodds JA. Morphological characterisation of yeast by image analysis. Biotechnol. Bioengng, 42: 1352-1359, 1993
- Pratt W, Faugeras OD, Gaglowisz A. Visual discrimination of stochastic texture fields. IEEE Trans Systems, Man and Cybernetics: SMC-8, 11, 796-804, 1978
- Prewitt JMS, eds. Lipkin BS, Rosenfeld. A Object Enhancement and Extraction. Picture Processing and Psychopictorics, Academic Press, 1970

- Robinson GS. Detecting and coding of edges using directional masks. University of Southern California, Image Processing Institute, Report no. 660, 1965
- Romanelli M. Objective Measurements of venous ulcers deposition and granulation with skin colour reflectance analyser. *J Geriatr Dermatol*, 5, 319-323, 1997
- Rosen E, Meromsky L, Setter E, Vinter DW. Smooth muscle-derived factor stimulates mobility of human tumor cells. *Invasion Metastasis*: 10, 49-64, 1990
- Rueckert D, Burger P, Forbat SM, Mohiaddin R D , Yang GZ. Automatic tracking of the aorta in cardiovascular MR images using deformable models. *IEEE Transactions on Medical Imaging*, Vol. 16, No. 5, 1997
- Sahoo PK, Soltani S, Wong AKC, Chan YC. A survey of thresholding techniques. *Comput. Vision, Graphics, Image Proc*: 4, 233-260, 1988
- Sangwine SJ. Colour in image processing. *Electronics & Communication Engineering Journal*, pp 211-219, Oct. 2000
- Schiffmann E . Motility as a principal requirement for metastasis. *Cancer Invest*, 8, 673-674, 1990
- Schindewolf T, Stolz W, Albert R, Abmayr W, Harms H. Classification of Melanocytic Lesions with Color and Texture Analysis using Digital Image Processing. *Analytical and Quantitative Cytology and Histology*, 15, 1-11, 1993
- Schreiner T, Degen E, Baschong W. Fibroblast migration and proliferation during in vitro wound healing. *Res Exp Med*: 193, 195-205, 1993
- Shenderov AD, Sheets MP. An Oscillatory Model of Cell Locomotion. *Biophysical Journal*: 72, 2382-2389, 1997
- Shenderov AD, Sheetz MP. Inversely Correlated Cycles in Speed and Turning in an Ameba: An Oscillatory Model of Cell Locomotion. *Biophysical Journal*: 72, 2382-2389, 1997
- Shufelt JA. Texture Analysis for Enhanced Color Image Qunatization. *Graphical Models and Image Processing*: 59,3, 149-163, 1997
- Siegert F, Weijer CJ, Nomura A, Miike H. A gradient method for the quantitative analysis of cell movement and tissue flow and its application to the analysis of multicellular Dictyostelium development. *J Cell Science* 107: 97-104, 1994
- Slavik J. Microspectrofluorometry: Measuring Ion Concentrations in Living Microbes. *Digital Image Analysis of Microbes* (eds. Wilkinson MHF, Schut F), John Wiley & Sons Ltd, 1998

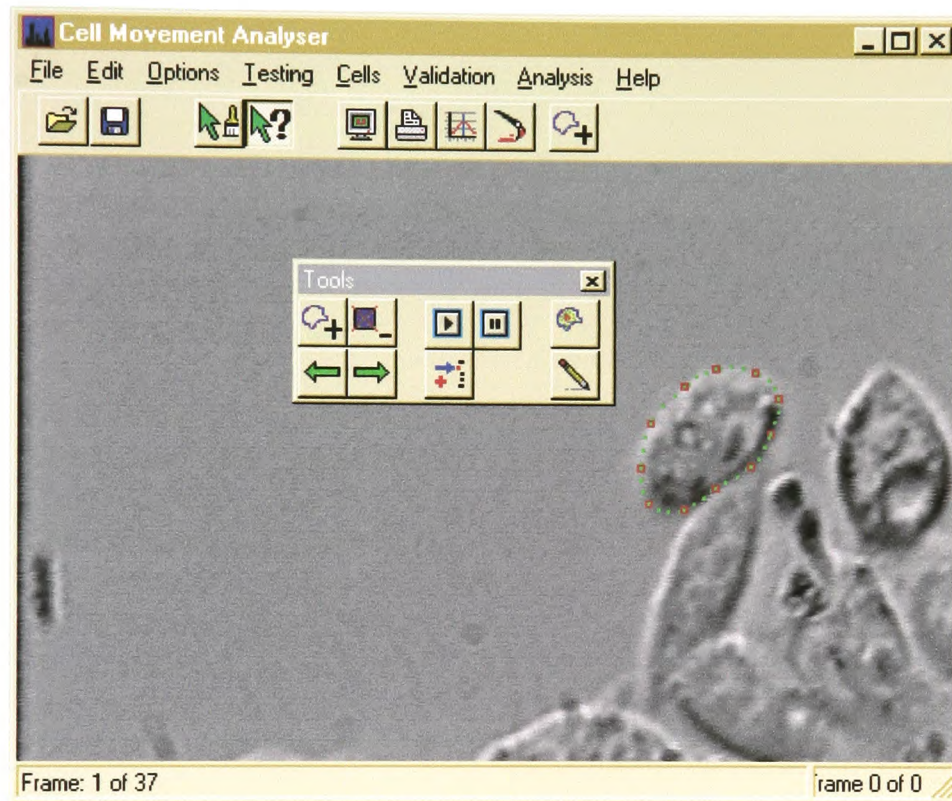
- Soll DR. The use of computers in understanding how animal cells crawl. *Int Rev Cytol*: 163, 43-104, 1995
- Stoker M, Gherardi E. Regulation of cell movement: The motogenic Cytokines, *Biochem Biophys Acta* 1072, 81-102, 1991
- Schreiner T, Edegen M, Baschong W. Fibroblast migration and proliferation during in vitro wound healing . *Res Exp Med*: 193, 195-205, 1993
- Tatsuka M, Jinno S, Owada M, Kakunaga T. A Digital Image Processing System for quantative Dynamic Morphology in Cultured Mammalian Cells. *Exp Cell Research*: 185, 342-352, 1989
- Terzopolous D, Szeliski R. Tracking with Kalman Snakes. *Active Vision*: pp 3-20, MIT Press, 1996
- Thompson WB, Barnard ST. Lower-level estimation and interpretation of visual motion. *Computer*, 14, 8, 20-28, 1981
- Thurston G, Jaggi B, Palcic B. Cell motility measured with an automated microscope system. *Exp Cell Research*: 165, 380-390, 1986
- Turner MR. Texture Discrimination by Gabor Functions. *Biological Cybernetics*: 55, 71-82, 1986
- Van Vliet, Boddeke FR, Sudar D, Young IT. Image Detectors for Digital Image Microscopy. *Digital Image Analysis of Microbes* (eds. Wilkinson MHF, Schut F). John Wiley & Sons Ltd, 1998
- Verschueren H, Houben B, De Braekeleer J, De Wit J, Roggen D, De Baetselier P. Methods for computer assisted analysis of lymphoid cell shape and motility, including Fourier analysis of cell outlines. *J of Immunological Methods*: 163, 1, 99-113, 1993
- Virchow R. Über bewegliche thierische Zellen. *Virchows Arch*: 28, 237-240, 1863
- Weber I, Albrecht R. Image Processing for combined bright-field and reflection interference contrast video microscopy. *Computer Methods and Programs in Biomedicine*: 53, 2, 113-118, 1997
- Wechler H. Texture Analysis. A Survey. *Signal Processing*: 2, 271-282, 1980
- Wilkinson MHF, Schut F. *Digital Image Analysis of Microbes*. Wiley Publishers, 1998. ISBN 0-471-97440-4
- Whitaker M. Fluorescence Imaging in Living Cells. *Cell Biology: A laboratory handbook* (ed. Celis JE), pp. 37-43, Academic Press, 1994

Zahm J-M, Kaplan M, Herald A-L, Doroit F, Pierrot D, Somelette P, Puchelle E. Cell Migration and Proliferation during in vitro Wound Repair of the Respiratory Epithelium. *Cell Motility Cytoskeleton*: 37: 33-43, 1997

Zicha D, Dunn GA. An Image Processing System for Cell Behaviour Studies in Subconfluent Cultures. *J of Microscopy*: 179, 1, 11-21, 1995

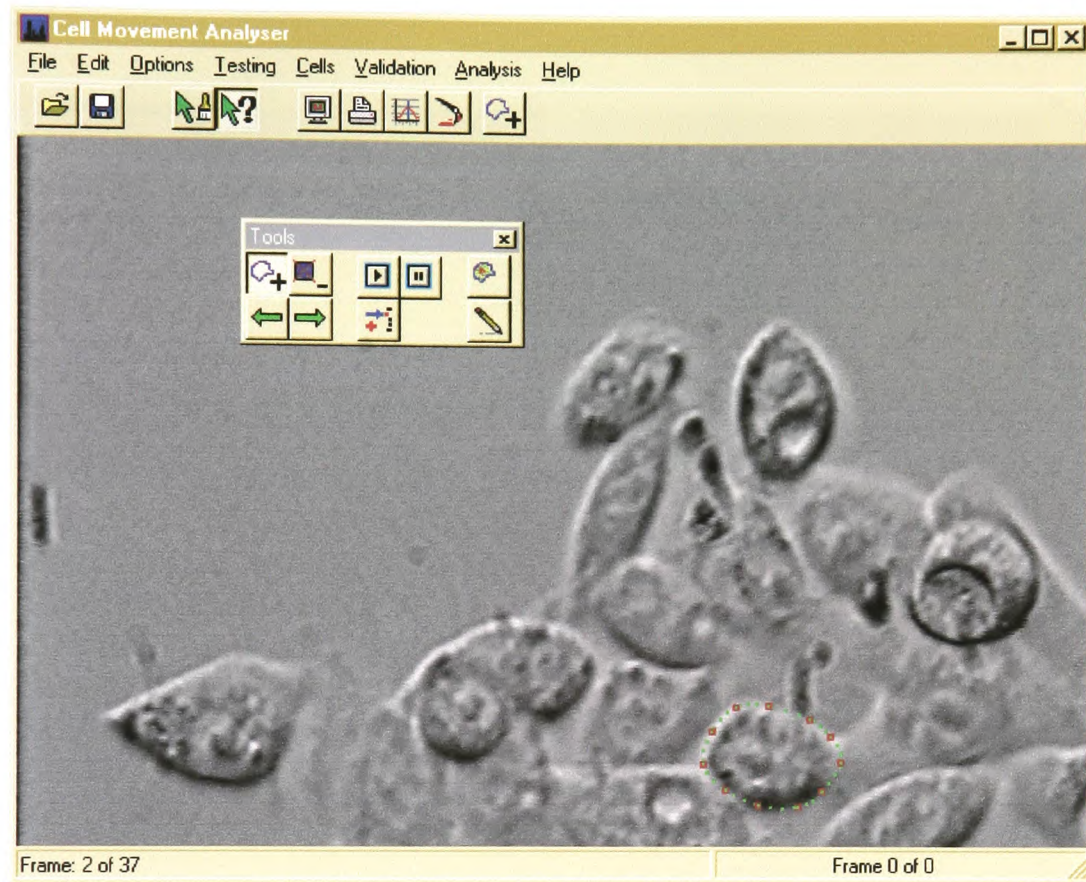
## Appendix B - Snapshots

### Snapshot Cell Movement Analyser I



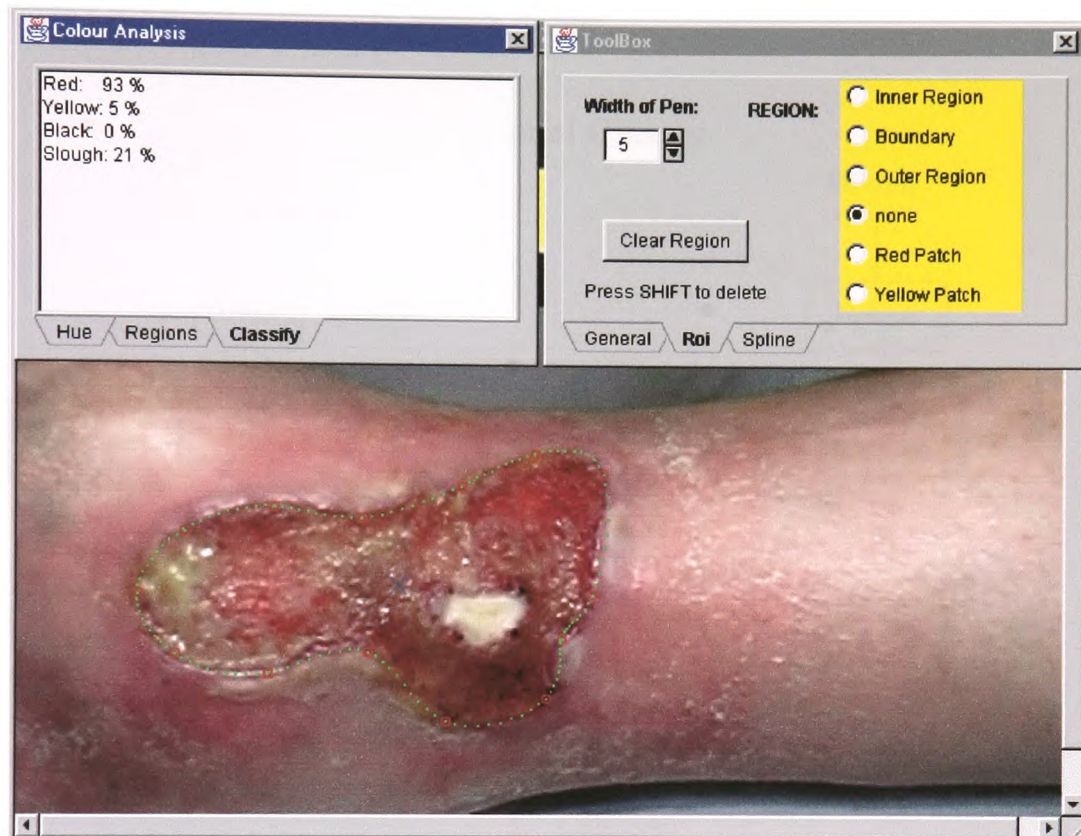
Example of the application for the spline boundary for tracking a semi-detached cell. Tools in the toolbox can be used to interactively change the position of control points (red) if the suggested position is found not to be sufficient.

## Snapshot Cell Movement Analyser II



Example of the application for the spline boundary for tracking a clustered cell.

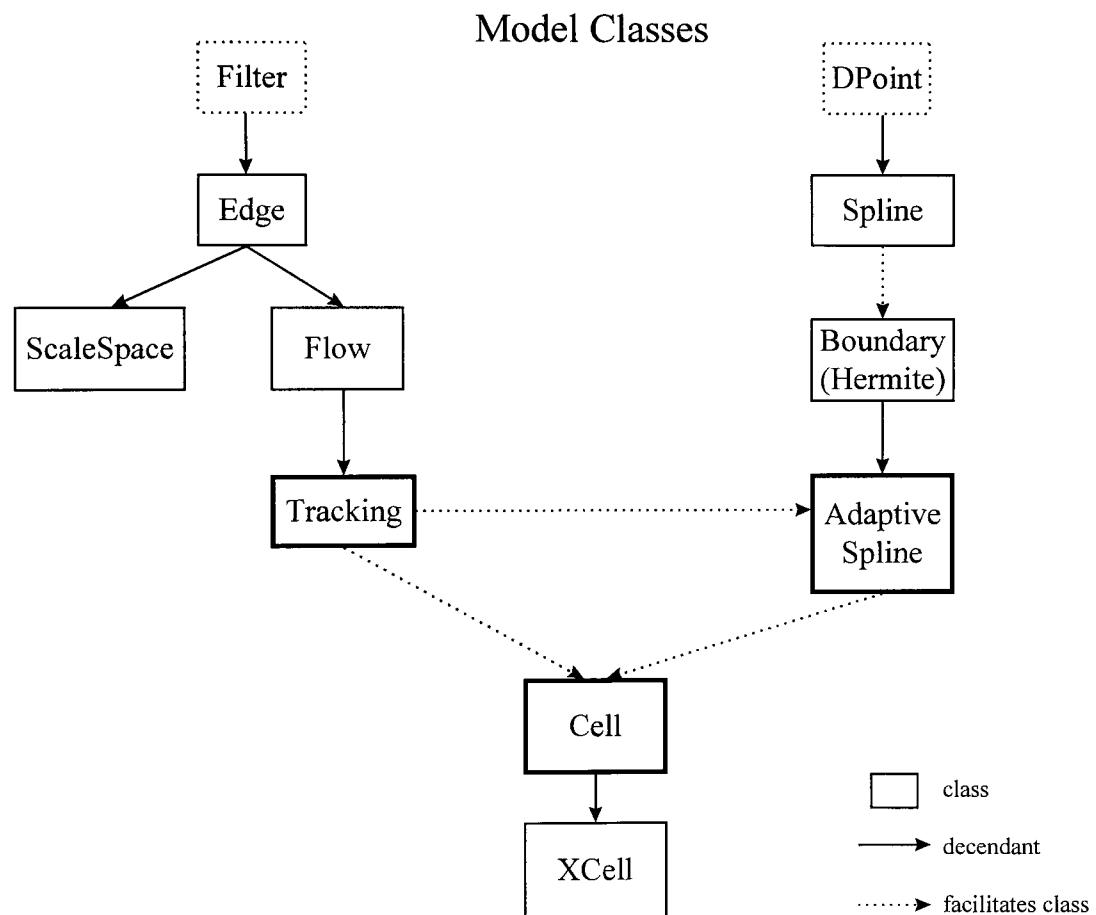
## Snapshot Wound Imaging Toolbox



Example showing the wound imaging toolbox. An image of a leg ulcer was delineated using the spline boundary (green) and salient control points (red).

## Appendix C - Software Implementation

### Class Diagram - Adaptive Spline Model



## ***Brief Class Description***

### **Filter**

Base filter class implementing contrast stretching, spatial filter masks, histogram equalisation, Gaussian smoothing.

### **Edge**

A collection of edge detection methods such as Sobel, Prewitt, Laplacian, Laplacian of Gaussian.

### **ScaleSpace**

Methods to reduce or increase the spatial resolution of images. Used for tracking at different scales.

### **Flow**

Movement estimation techniques are implemented in this class. The method used for movement estimation is area matching based on the sum of squared differences.

### **Tracking**

This class coordinates the tracking of cells using spatio-temporal information from the flow class and adaptive spline class.

### **Dpoint**

Base class describing a control point with position and confidence parameters.

### **Spline**

This class extends Dpoint to form a spline segment.

**Boundary**

Adds a cubic spline and C2 continuity to the Spline class, forming a Hermite spline. Calculation of area, centroid and perimeter length are added. Control points can be added and deleted.

**AdaptiveSpline**

This class makes the Hermite spline adaptable. A boundary profile can be generated from the normal vector. Image values along the profile can be used for relocation purposes. The relocation process using gradient is implemented in this class.

**Cell**

The cell is the centre piece of the Cell Movement Analyser software. It contains a list of adaptive spline boundaries for each frame. User interaction is coordinates from here as well as the re-sampling of the spline boundary. This class has the decision making process implemented which ultimately decides about the relocation of each control point.  $T_{\text{gradient}}$ ,  $T_{\text{flow}}$  and  $T_{\text{flow2}}$  determine the level of confidence required to move a control point.

**Xcell**

A graphical representation of the adaptive spline to draw it onto a Tcanvas object.

## ***Class Spline***

```
/*
 * The Spline class is derived from the DPoint class and
 * describes a single cell segment as a cubic spline interpolation
 * DPoint is extended with ax, bx, cx, dx and ay, by, cy, dy
 *
 *
 * Author: A Hoppe
 */

class Spline : public DPoint {

// --- Properties ---

protected:
double ax, bx, cx, dx;           // x - parameters of spline segment
double ay, by, cy, dy;           // y - parameters of spline segment
public:
double Area;                      // area of the spline segment
double Length;                   // length of the spline segment

public:
int Colour;                       // colour of control point
bool marked;                     // a marked segment cannot be deleted
DPoint Center;                   // centroid of the spline segment

// --- image features in near neighbourhood and confidence values ---
DPoint Flow;
DPoint Gradient;
DPoint Orth_Grad;
DPoint Flow_2;                   // flow at half scale

// --- Constructor ---
Spline() : DPoint()
{
x=y=0;
ax=ay=bx=by=cx=cy=dx=dy=1.0; marked=false;
}

// --- Methods ---
// set x-coefficients of the spline segment
void setXCoefficients( double a, double b, double c, double d) {
    ax = a; bx = b; cx = c; dx = d;
}

// set y-coefficients of the spline segment
void setYCoefficients( double a, double b, double c, double d) {
    ay = a; by = b; cy = c; dy = d;
}

// retrieve coordinate values
int X_s(double s) { return (int)(0.5+ax+bx*s+cx*s*s+dx*s*s*s); }
int Y_s(double s) { return (int)(0.5+ay+by*s+cy*s*s+dy*s*s*s); }

double angle(double s);
void recalc();                   // calculates area, length and centroid of this
segment
};
```

## ***Class Boundary***

```
/*
 * The Boundary class is a collection of spline boundary segments which
 * form a closed body. This is then used to render the boundary
```

```

* of a single cell.
* Author: A Hoppe
*/

```

```

class Boundary {
// ----- Properties -----
public:
    DPoint Center;           // Center of Gravity of area
    DPoint Nucleus;          // Position of the Nucleus
    int Area;                // Area of the enclosed field
    int Length;              // length of perimeter
    int Size;                // position in array of spline segments
(1..n)
    DPoint* spl[1000];       // max 1000 spline segments in boundary

// --- Constructor and Destructor ---
    Boundary() {
        Center.x=-7; Center.y=-7;
        Nucleus.x=-3; Nucleus.y=-3;
        for (int i=0; i < 1000; i++) spl[i]=NULL;
        Size=0;
    }

// ----- Methods -----

// add a new point
virtual void add(int x, int y);

// add a new point without sorting
virtual void justAdd(int x, int y);

// delete points within the radius of 3 pixel
virtual void del(int x, int y);

// move Center and points to new location x and y
virtual void moveTo( int x, int y);

// move single point to a new location
virtual void moveSingle( int x, int y);

// calculate area, length and centroid of the closed boundary
virtual void recalc();

// delete all points contained in this boundary
virtual void clear();

// clone this boundary
virtual Boundary* clone();

// save boundary to filestream
void saveToFile( FILE* out);

// load boundary from filestream
bool loadFromFile( FILE* in);

// sort points clockwise around the cell
void sort();

protected:

// calculating the length of the boundary
int length();
// dealing with the array of spline points
void swap(int a, int b);
void del(int pos);

};

```

## Implementation of sorting for minimal length in **Boundary** class

```
void Boundary::sort() {
    int minLength; // minimum length encountered
    if (Size < 4) return; // need more than 3 points

    // assess the length of all possibilities
    minLength = length();
    for (int m=Size-1; m >= 0; m--) {
        for (int n=Size-1; n > 0; n--) {
            if (length() < minLength) minLength=length();
            swap( n, n-1); // swap the position of points
        }
    }
    // find the minimum length again and stop sorting
    if (minLength == length()) return;
    for (int m=Size-1; m >= 0; m--) {
        for (int n=Size-1; n > 0; n--) {
            if (minLength == length()) return;
            swap( n, n-1);
        }
    }
}

void Boundary::swap(int a, int b)
{
    DPoint* s;
    s = spl[a]; spl[a]=spl[b];
    spl[b]=s;
}
```

## Class Adaptive Spline

```
class AdaptiveSpline : public Hermite
{
    // --- Properties ---
public:
    int P_area;
    int P_perimeter;
    int P_size;
    Bitmap* bmp; // reference Bitmap
    Bitmap* profile; // image containing the
    // profile information
    int xp[33]; // x position of vector
    int yp[33]; // y position of vector
    float v[33]; // single vector
    // values
    int p_x[500], p_y[500]; // array of x,y positions;
    int polar[500]; // polar coordinates

    // --- Constructor ---
}
```

```

AdaptiveSpline() : Hermite() { profile = NULL;}

// --- Methods ----

// clone this spline
virtual Boundary* clone();

// create a new orthogonal profile with number of vectors per segments
void createProfile( Bitmap* bmp, int vectors, float sigma);

// calculates the total profile and paint it on the bitmap
void paintOrthogonalVector(Bitmap* bmp, double ds, int colour);

// save orthogonal profile as bitmap, derv indicates first derivative
void saveProfile(char* filename);

// mark the highest gradient on profile
void markBoundary(Bitmap* bmp, int segm);

// --- Methods that work on a single profile element segm(s) ---
protected:
// calculates a single profile, coordinates stored in xp,yp
void calcOrthProfile( int segm, double s);

// calculates a single profile with image data at scale in v and xp, yp
void calcOrthProfile(Bitmap* bmp, int segm, float s);

// calculate the weighted profile at offset dx(centre+dx) and sigma
void weightProfile( int dx, float sigma);

// derive orthogonal profile
void deriveProfile();

// relocates the spline according to max values along +- search pixels of
spline segment
float relocateNormProfile( Bitmap* bmp, int segm, int &index, int search);

// relocate the spline according to sum along profile and high gradient
void relocateCombiProfile( Bitmap* bmp, int segm, int &index);

// calculate the difference along the normal profile (returns normalised 1
diff)
float diffNormProfile( Bitmap* bmp, int segm);

// calculate the sum along the normal profile (returns normalised sum)
float sumNormProfile( Bitmap* bmp, int segm);

// ----- segment relocation methods ----
public:

// relocate this segment
void relocateSegment( Bitmap* bmp, int segm);

protected:

// relocate at index and sigma
void relocateSegm( int &index, float sigma);

// relocate according to highest pixel value along profile
void relocateSegm(int &index, bool derive, bool weight);

// normalisation methods

public:

void normaliseFlow();

void normaliseFlow_2();

};

```

## Implementation of fitting to gradient boundary in **AdaptiveSpline** class

```
// returns confidence parameter

float AdaptiveSpline::relocateNormProfile( Bitmap* bmp, int segm, int
&index, int search)
{
    Spline *s_1 = (Spline*)spl[segm];
    float max=0,result;
    int i;

    calcOrthProfile( segm, 0); // calculate x,y positions of profile vector

    for (i=16-search; i <= 16+search; i++)
    {
        s_1->x = xp[i]; s_1->y = yp[i]; // set new control point position
        matrix(); // recalc spline coefficients
        result=sumNormProfile( bmp, segm);
        if (result > max) { max=result; index=i; }
    }
    s_1->x = xp[16]; s_1->y = yp[16]; // set control point to old position
    matrix(); // recalc spline coefficients
    return max;
}

float AdaptiveSpline::sumNormProfile( Bitmap* bmp, int segm)
{
    Spline *s_1, *s_2;
    float ds;
    float sum=0;
    if (segm > 0 && segm < Size)
    {
        s_1 = (Spline*)spl[segm-1]; s_2 = (Spline*)spl[segm];
    }
    else
    {
        s_1 = (Spline*)spl[Size-1]; s_2 = (Spline*)spl[0];
    }

    // sum of three pixels of left spline segment
    for (ds=0.8; ds <= 1.0; ds=ds+0.1)
    {
        sum = sum + bmp->pix[s_1->X_s(ds)][s_1->Y_s(ds)];
    }
    // sum of three pixels of right spline segment
    for (ds=0.1; ds < 0.4; ds=ds+0.1)
    {
        sum = sum + bmp->pix[s_2->X_s(ds)][s_2->Y_s(ds)];
    }
    return 1-(sum/6.0); // return lower the sum the higher the gradient, hence
1-sum
}
}
```

## **Class Tracking**

```
class Tracking : public Flow
{
public:
    // --- Properties ---
    Bitmap *spbmp1, *spbmp2; // scale space bitmaps
    ScaleSpace scaling;

    // --- Constructor ---
    Tracking() : Flow() { spbmp1 = new Bitmap(); spbmp2= new Bitmap();}

    ~Tracking() { delete spbmp1; delete spbmp2;}
}
```

```

// --- Member Functions ---

/*
We calculate the absolute gradient with a prewitt filter
and search for the highest gradient in a size x size area.
All the control points are relocated according to the highest
gradient in that area.
It copies the previous positions of the control points onto
the next frame and relocates them according to the highest gradient.
*/
void maxGradient(Bitmap* bmp, Cell* c, int size);

/* We calculate the gradient in direction of the normal vector
* at each control point.
* The point is relocated according to the highest gradient
* in a 5x1 area
*/
void maxProfileGradient(Bitmap* bmp, Cell* c, int type, int size);

/* We calculate the flow approximation in the area around
* each control point. The best fit area is chosen
* bmp1 = old frame, bmp2 = new frame
*/

void flowArea( Bitmap* bmp1, Bitmap* bmp2, int size, int search, Cell* c);

/* Scale space flow tracking
*
*/
void flowAreaScale( Bitmap* bmp1, Bitmap* bmp2, int size, int search, Cell*
c);

/*
* calculate flow field around the nucleus position
*
*/
void flowNucleus( Bitmap* bmp1, Bitmap* bmp2, int size, int search, Cell*
c);

void flowNucleus( Bitmap* bmp1, Bitmap* bmp2, Bitmap* bmp1_2, Bitmap*
bmp2_2, Cell* c);

void flowCytoplasm( Bitmap* bmp1, Bitmap* bmp2, int size, int search, Cell*
c);

};

```

## Implementation of area matching using **flowArea**

```

void Tracking::flowArea( Bitmap* bmp1, Bitmap* bmp2, int size, int search,
Cell* c)
{
    AdaptiveSpline* s;
    Spline* segm;      // spline segment
    int xp, yp;
    float C_flow;

    s = c->spl();      // get spline boundary from cell

    for (int i=0; i < s->Size; i++)
    {
        segm=(Spline*)s->spl[i];
        xp = (int)segm->x; yp = (int)segm->y;
        //C_flow=intCorr( bmp1, bmp2, size, search, xp, yp, xp, yp); // relocate
according to intensity area correlation
        C_flow=flowField( bmp1, bmp2, size, search, xp, yp);
        segm->Flow.x=xp; segm->Flow.y=yp; segm->Flow.alpha=C_flow;
    }
}

```

## Class Flow

```
class Flow : public Edge {
public:
// --- Properties ---

// --- Constructor ---
Flow() : Edge() { }

// --- Methods ---

// performs  $bmp1 = |bmp1 - bmp2|$ 
void absDiff( Bitmap* bmp1, Bitmap* bmp2);

// performs  $bmp1 = |bmp1 - bmp2| + |bmp3 - bmp2|$ 
void absDiff( Bitmap* bmp1, Bitmap* bmp2, Bitmap* bmp3);

/* relocates point pt(xpos,ypos) according to best correlation of
intensities
size e.g. 5 = 5x5 area
search e.g. 7 = 7x7 search area around search centre (s_x,s_y)
returns confidence (0..1) as float
*/
float intCorr( Bitmap* bmp1, Bitmap* bmp2, int size, int search, int s_x,
int s_y, int &xpos, int &ypos);

float flowField( Bitmap* bmp1, Bitmap* bmp2, int size, int search, int
&xpos, int &ypos);

/* relocate point pt (xpos, ypos) in area size*size (e.g 5x5)
according the the highest value occuring in that region
*/
void maxVal( Bitmap* bmp, int size, int &xpos, int &ypos);

};
```

## Implementation of flowField and intCorr

```
float Flow::intCorr( Bitmap* bmp1, Bitmap* bmp2, int size, int search, int
s_x, int s_y, int &xpos, int &ypos)
{
    int x1,y1, x2, y2, xp=xpos, yp=ypos;
    mat_1 = init(mat_1,search, search); // squared differences in search
    area

    int src_x=xp-size/2, src_y=yp-size/2;
    int ar_x, ar_y;
    float diff, maxima=0, averg=0, std=0;

    for (y2=0; y2 < search; y2++)
        for (x2=0; x2 < search; x2++)
        {
            diff=0;
            ar_x=x2+s_x-search/2-size/2;
            ar_y=y2+s_y-search/2-size/2;

            for (y1=0; y1 < size; y1++)
                for (x1=0; x1 < size; x1++)
                {
                    diff = diff + pow( bmp2->pix[ar_x+x1][ar_y+y1]-bmp1->
                    pix[src_x+x1][src_y+y1],2);
                }
            // assign abs diff to result matrix and normalise

            mat_1[x2][y2]= 1 - diff;

            averg = averg + mat_1[x2][y2];
        }
}
```

```

    averg = averg/(search*search);    // calculating the average difference

    // searching for maxima in result matrix and assign new
    // positions to xp,yp
    for (y2=0; y2 < search; y2++)
        for (x2=0; x2 < search; x2++)
        {
            std = std + pow(mat_1[x2][y2]-averg,2);

            if (mat_1[x2][y2] > maxima)
            {
                maxima=mat_1[x2][y2];
                xpos=xp-search/2+x2;
                ypos=yp-search/2+y2;
            }
        }
    std = sqrt( std/(size*size));
    if (maxima < 0) return 0;

    return maxima;
}

float Flow::flowField( Bitmap* bmp1, Bitmap* bmp2, int size, int search, int
&xpos, int &ypos)
{
    float pos_mat[11][11]; // position matrix (max 11 x 11)
    float confidence;
    int x,y,xp=xpos, yp=ypos;
    for (y=0; y < 11; y++)
        for (x=0; x < 11; x++) pos_mat[x][y]=0;

    for (y=-2; y <= 2; y++)          // 5x5 area of flow vectors
        for (x=-2; x <= 2; x++)
        {
            xpos=xp+x; ypos=yp+y;
            confidence=intCorr( bmp1, bmp2, size, search, xpos, ypos, xpos, ypos);
            pos_mat[5+xpos-xp-x][5+ypos-yp-y] = pos_mat[5+xpos-xp-x][5+ypos-yp-y]
+ confidence;

        }

    // calculate the overall direction of the flow field
    float sum=0.0001,xdx=0, ydy=0;
    for (y=0; y < 11; y++)
        for (x=0; x < 11; x++)
        {
            sum=sum+pos_mat[x][y];
            xdx=xdx+x*pos_mat[x][y];
            ydy=ydy+y*pos_mat[x][y];
        }
    xpos=(int)(0.5+xdx/sum); ypos=(int)(0.5+ydy/sum);
    xpos=xpos-xp-5; ypos=ypos-yp-5;

    return sum/25;
}

```

## ***Class Cell***

```

class Cell
{
    // ---- Properties ---
public:
    int Frame;                                // frame range: 1...n
    AdaptiveSpline* boundary[1000];          // max 1000 frames
}

```

```

FPoint cytoplasm[100];           // feature points within cell
int numFeatures;                 // number of features points in
cytoplasm

float T_gradient;                // gradient threshold
float T_flow;                    // flow threshold
float T_flow2;                   // flow threshold at half resolution

// --- Constructor ---
Cell()
{
    for (int i=0; i<1000; i++) boundary[i]=NULL;
    Frame = 0; // no frames present
    numFeatures=0; // no current feature points
    T_gradient=0.6; T_flow=0.6; T_flow2=0.6;
}

~Cell()
{
    for (int i=0; i < 1000; i++)
        if (boundary[i] != NULL) delete boundary[i];
}

// --- Methods ---

void add(int x, int y);

void move(int x, int y);

void copyPoints();

void del(int x, int y);

void setNucleus( int x, int y);

void addFeaturePoint( int x, int y);

DPoint* getNucleus();

int getArea() { return boundary[Frame]->Area; }

AdaptiveSpline* spl() { return boundary[Frame]; }

// --- Adaptive Spline Methods ---

void resample();

void refit();

void gradFit();

// --- Persistence Methods ---

// save boundary to filestream
void saveToFile( FILE* out);

// load boundary from filestream
bool loadFromFile( FILE* in);

// export parameter of motility for further analysis

```

```

bool exportData(char* filename);

// this method logs all data of the cell and writes into cell.log in temp
void logData();

// ---- Exporting Data ----
protected:

void exportArea(FILE* out);
void exportCellArea(FILE* out);
void exportPerimeter(FILE* out);
void exportPosition(FILE* out);
void exportDistance(FILE* out);
void exportNuclVelocity(FILE* out);
void exportCellVelocity(FILE* out);
void exportCellRoundness(FILE* out);
};

```

### implementation **gradFit** and **refit** in class cell

```

void Cell::gradFit()
{
    int i;
    AdaptiveSpline* s = spl();          // reference to spline boundary
    Spline* segm;                       // reference to single spline segment

    for (i=0; i < s->Size; i++)
    {
        segm=(Spline*)s->spl[i];
        if (segm->Flow.alpha > T_flow || segm->Flow_2.alpha > T_flow2)
            if (segm->Orth_Grad.alpha > T_gradient) { segm->x = segm->Orth_Grad.x;
segm->y = segm->Orth_Grad.y; }
        }
        s->sort(); s->matrix(); s->recalc();
    }

// relocate the spline boundary
void Cell::refit()
{
    int i;
    AdaptiveSpline* s = spl();          // reference to spline boundary
    Spline* segm;                       // reference to single spline segment

    for (i=0; i < s->Size; i++)
    {
        segm=(Spline*)s->spl[i];
        //segm->x = segm->Flow_2.x; segm->y = segm->Flow_2.y;
        //segm->x = segm->Flow.x; segm->y = segm->Flow.y;

        if ((segm->Flow.alpha > segm->Flow_2.alpha) && segm->Flow.alpha >
T_flow) { segm->x = segm->Flow.x; segm->y = segm->Flow.y; }
        else if (segm->Flow_2.alpha > T_flow2) { segm->x = segm->Flow_2.x; segm-
>y = segm->Flow_2.y;}
        }
        s->sort(); s->matrix(); s->recalc();
        gradFit(); // using gradient information to relocate control points
    }
}

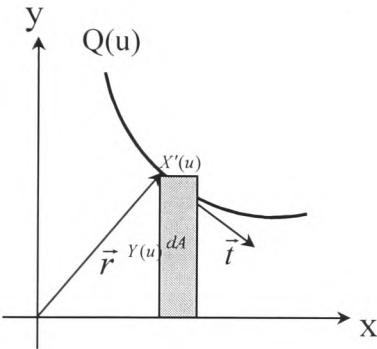
```

## Appendix D – Spline Calculations

The spline equations on the following pages were solved symbolically with the help of the software package Derive.

### Area

Calculation of Spline Area underneath a spline segment  $Q(u)$ :



$$\vec{r} = \begin{pmatrix} X(u) \\ Y(u) \end{pmatrix}$$

$$\vec{t} = \frac{\vec{r}(u + \Delta u) - \vec{r}}{\Delta u}$$

$$\vec{t} = \lim_{\Delta u \rightarrow 0} \frac{\vec{r}(u + \Delta u) - \vec{r}}{\Delta u} = \begin{pmatrix} X'(u) \\ Y'(u) \end{pmatrix}$$

$$A = \int_{(A)} Q(u) du$$

The area of each segment  $A_i$  with the linear parameter  $u \in [0..1]$  is calculated as

$$A_i = \int_0^1 Y_i(u) \frac{\partial X_i(u)}{\partial u} du$$

Since  $X(u)$  and  $Y(u)$  are known as a cubic spline segment, the area for each segment can be calculated symbolically as:

$$1. X(u) = a + b u + c u^2 + d u^3$$

$$2. \frac{\partial X(u)}{\partial u} = b + 2 c u + 3 d u^2$$

$$3. Y(u) = e + f u + g u^2 + h u^3$$

$$4. A_i = \int_0^1 Y(u) \frac{\partial X(u)}{\partial u} du = \int_0^1 (e + f u + g u^2 + h u^3) (b + 2 c u + 3 d u^2) du$$

Equation 4 has been solved symbolically with the *Derive* software package.

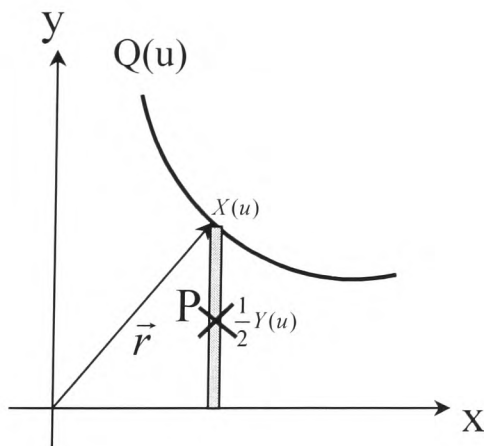
$$A_i = b \left[ e + \frac{f}{2} + \frac{g}{3} + \frac{h}{4} \right] + c \left[ e + \frac{2f}{3} + \frac{g}{2} + \frac{2h}{5} \right] + d \left[ e + \frac{3f}{4} + \frac{3g}{5} + \frac{h}{2} \right]$$

The total area is calculated as the sum of the area underneath n segments.

$$A = \sum_n A_i .$$

### Centroid

The centre of area  $P(x_c, y_c)$  is calculated as [Papula 1991]



The centroid  $P(x_c, y_c)$  is calculated as

$$x_c = \frac{1}{A} \int x dA$$

$$y_c = \frac{1}{A} \int y dA$$

The centroid is calculated as the sum of infinitesimal areas  $dA$  underneath the curvature  $Q(u)$  multiplied by their respective x and y position of each area  $dA$  and divided by the total area.

The area element  $dA$  is calculated as  $Y(u) * X'(u)$  while the x-position of each element  $dA$  is  $X(u)$ . This yields the following equation for calculation the x-coordinate of the centroid underneath each spline segment  $x_i$ :

$$x_i = \frac{1}{A_i} \int_0^1 Y_i(u) X_i(u) \frac{\partial X_i(u)}{\partial u} du$$

Again, the area element  $dA$  is calculated as  $Y(u) * X'(u)$  while the y-position of each element  $dA$  is  $\frac{1}{2} * Y(u)$ . This yields the following equation for calculation the y-coordinate of the centroid underneath each spline segment  $y_i$ :

$$y_i = \frac{1}{2 A_i} \int_0^1 Y_i^2(u) \frac{\partial X_i(u)}{\partial u} du$$

### Perimeter Length

The perimeter length of a single spline segment  $i$  can be calculated as

$$L_i = \int_{(C)} Q(u) du$$

The length of each segment is the vector sum of x and y component of the tangential

vector  $\vec{t} = \begin{pmatrix} X'(u) \\ Y'(u) \end{pmatrix}$  such as

$$L_i = \int_0^1 \sqrt{[X'_i(u)]^2 + [Y'_i(u)]^2} du .$$

However, this equation was not solved explicitly. A piecewise approximation using ten linear sub-segments per spline segment was used to calculate the length of each segment. The total length was then calculated as

$$L = \sum_n L_i .$$

## **Appendix E - Published Research**

Two full journal papers and four peer reviewed conference publications have been prepared as a result of the work described in this thesis.

## A System for Computer Analysis of Cancer Cell Movement

A. HOPPE<sup>1</sup>, W.G. JIANG<sup>2</sup>, D. WERTHEIM<sup>1</sup>, R. WILLIAMS<sup>1</sup> and K. HARDING<sup>2</sup>

<sup>1</sup>Department of Electronics and IT, University of Glamorgan, Mid Glamorgan, CF37 1DL;

<sup>2</sup>Department of Surgery, University of Wales College of Medicine, Cardiff, CF4 4XN, U.K.

**Abstract.** *Background:* Motility of cancer cells is a principal cellular parameter, essentially required in the invasion and formation of distant metastasis in human cancer. Measures to stimulate or inhibit motility of cancer cells may play an important part in the understanding of metastasis biology. The aim of this study was to develop a computer system to analyse and evaluate the movement of cells. *Method:* Software was developed which enabled cell boundary definition by specifying salient points around the cell. The position of the centre of area was calculated. Six human cancer cells treated with a motogen and cells without added motogen were analysed by the system. *Results:* We observed higher velocities and greater variation in area and velocity of the cells treated with HGF/SF motogen compared with control cells. *Conclusion:* The system enables rapid analysis of cell area, velocity and movement, and may thus be of value in further understanding cell motility.

The study of cancer cell motility is important in understanding metastasis [1-3]. The effect of stimulating or inhibiting motility of cancer cells may play an important part in the understanding of metastasis biology in cancer.

It has been suggested that the motogens, such as Hepatocyte Growth/Scatter Factor (HGF/SF), may be a trigger for the metastatic spread of cancer cells. When added to cancer cells *in vitro*, this factor stimulates both growth and motility, leading to a 'scattered' cell colony [4,5]. A number of microscopic methods have been reported, but these offered limited information on precise and quantitative measures.

Cell velocity provides a description of cell motility but is dependent on how cell position is defined. It is unclear, whether the cell position is best defined by the position of the nucleus or the centre of the cell area (centroid).

In recent years, some cell movement analysis methods have been described which record the movement of detached cells through automatic cell tracking [6-11]. However, the identification of cells within a clustered colony is difficult as

cells may be partly obscured by or interfere with neighbouring cells.

The aim of this study was to develop a computer system to analyse and evaluate movement of individual cancer cells within a cell colony. The system has been applied to analyse the movement of HT 15 human colon cancer cells.

### Materials and Methods

**Materials.** Human colon cancer cells HT15 (obtained from the European Collection for Animal Cell Culture, Salisbury, England) were used. Cells were cultured in DMEM medium supplemented with 10% foetal calf serum, penicillin, and streptomycin. The medium was HEPES buffered to provide a stable pH during long period recording.

Two sets of HT15 human colon cancer cells of the same cell line were analysed, one of them with added motogen. The motogen used was a recombinant human hepatocyte growth factor from DNA-transfected CHO cells [12].

Cells were prepared and cultivated on petri dishes (Nunc, Denmark) and kept in an incubator at a temperature of 37°C and 5% CO<sub>2</sub>. The cell culture was placed under a Leica DM IRB microscope (Leitz GmbH, Germany) with a heat control and an attached colour CCD camera. The dish was kept at a constant temperature of 37.2°C. A Leica HMC20 Hoffmann Condenser was used to enhance the structural features of the cells. A cell colony with up to 10 cells were chosen at random from the culture and monitored for three hours on a time-lapsed video system (Panasonic, Japan) connected to the camera. In a second series, 40 ng/ml motogen (HGF/SF) was added to a colony of 10 cells and also monitored for three hours.

**Hardware and software implementation.** In summary, images were first captured from the video tape at an equivalent of a 5 minute interval in real time. The position of cells could be defined by two methods; the centre of area (centroid) and the position of the nucleus. From the cell boundary the area of the cell can be measured and from its position the velocity and movement can be calculated. Thus changes in area, velocity and movement of single cells within a cell colony were analysed.

Frames were digitised as a series of true-colour images at a resolution of 768 by 576 pixels using a DT3 153 frame grabber board (Data Translation, MA, USA). To reduce the amount of disk space and to further speed up the image processing, images were converted into grey scale. Software was written using Borland C++ (Borland Int. Inc., CA, USA) in conjunction with the Data Translation frame grabber Software Development Kit (SDK) for Windows95 (Microsoft Corp., Seattle, USA).

The video tape was replayed and images were digitised at an equivalent of a 5 minute interval and stored in a series of grey scale bitmap files. Evaluation and processing of the cell images was performed on a personal computer. Analysis software was also designed in Borland C++ and incorporated image processing, calibration and evaluation functions to describe the movement of cells. The results of the analysis

*Correspondence to:* Andreas Hoppe, Department of Electronics and IT, University of Glamorgan, Mid Glamorgan, CF37 1DL, U.K. Tel: +44 1443 482530 FAX: +44 1443 482541.

**Key Words:** Cell, metastasis, computer analysis, cell velocity.

can be viewed within the software or exported to a spreadsheet or statistical software package for further evaluation.

**Cell description.** The shape of individual cells may be described by their membrane, representing the cell boundary, the area it occupies, and its nucleus. An indication of the position of a cell may be calculated from its centre of the area (centroid) and therefore depends on the shape of the boundary. Alternatively the cell position may be defined from the position of the nucleus.

The software allows the cell boundary to be defined by drawing around the cell with a mouse or by specifying salient points on the cell boundary, which is a more rapid method. The boundary is defined with a mathematical interpolation of discrete points (two-dimensional rendering) on the cell boundary. The boundary can be described by just a few fragments and can be adjusted by moving points placed on it. The system reconstructs the full boundary through a closed interpolating spline. Furthermore, the software incorporates image processing methods to enhance the images in order to facilitate easier detection of the cell boundary.

The cell membrane can be considered as a curvature formed by the enclosed cytoplasm, a liquid with a high viscosity. Such a curvature is unlikely to develop sharp discontinuities or corners. The nature of this type of boundary may be described as 'naturally' formed.

In our method the outline of the cell membrane is described by segments, which are marked by a few points placed on the boundary. The transition between each segment must be smooth according to our requirement for a 'natural' curvature. Hence the first and the second derivative at the end of each segment equal those at the beginning of the following.

One type of spline which is described by such attributes is a Natural Cubic Spline, a special form of a Hermite Interpolation [13]. Figure 1 shows a clustered cell describe by a Natural Cubic Spline. Once the shape of the boundary has been defined mathematically, the area and the centre of area (centroid) can be calculated from the segment coefficients.

**Image processing.** Image processing techniques have been implemented in the software so if necessary the appearance of the cell boundary can be highlighted. These include functions such as histogram equalisation and contrast enhancement which is of value in extending the dynamic range of grey-levels available. Additionally, a 5 x 5 Laplacian filter matrix can be applied to each frame to locate edges or highlight other high frequency components, such as boundary segments or the nucleus.

**Validation.** An image with three different detached cell shapes with a known area and centroid position was created. We applied our method of describing the cell boundary with a natural hermite cubic spline to the cells five times. We observed a maximum error in area and centroid calculation of 3%.

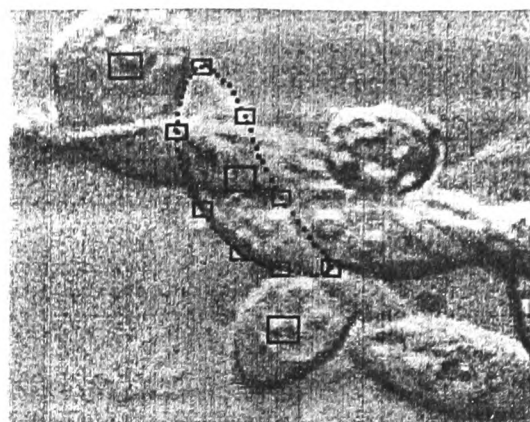


Figure 1. Cell defined with Natural Cubic Spline.

## Results

**Cell spreading.** Six cells of each cell colony were chosen to be analysed and their area, velocity and direction of movement was calculated. The control cells appeared to show less movement and smaller changes in area and velocity than cells treated with HGF/SF. Figure 2 shows an example of the paths, in area of 30 micrometers square, of a single control and a single HGF/SF stimulated cell within a cell colony.

**Cell area.** The median area of the six control cells within one cell cluster at the start of the recording was  $259 \mu\text{m}^2$ . The maximum area of these six cells was  $428 \mu\text{m}^2$  while the minimum was  $164 \mu\text{m}^2$ . There were only small variations in area of the control cells. In contrast, there were greater changes in area in the cells treated with HGF/SF. The median area of the six cells with added motogen has risen from  $289 \mu\text{m}^2$  to its maximum at  $417 \mu\text{m}^2$  during the first 35 minutes. The area of these cells appeared to change in a periodic fashion.

**Cell velocity.** The median velocity, calculated from the centroid of six control cells belonging to the same cluster was

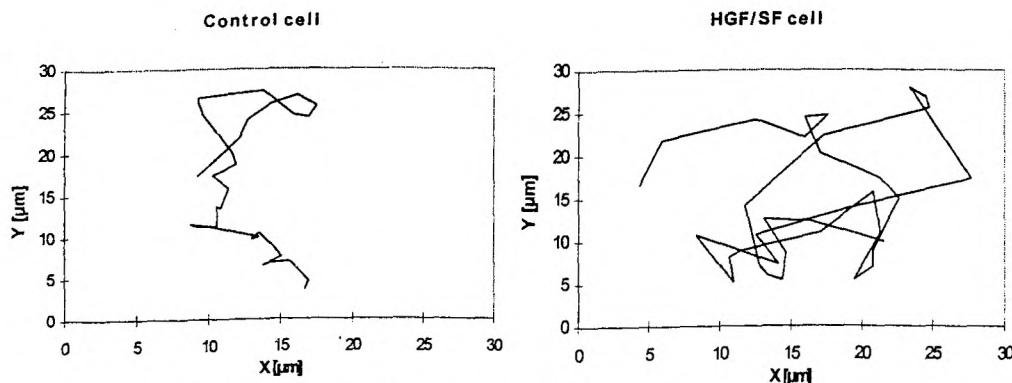


Figure 2. Example of movement paths of a single control and HGF/SF cell over 3 hours.

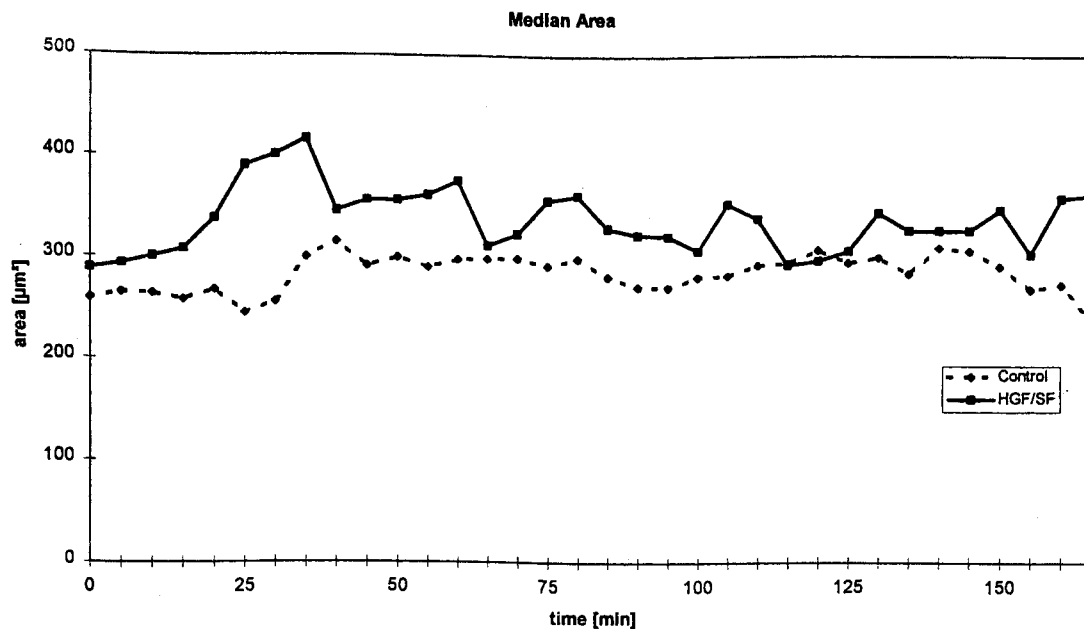


Figure 3. Median area of Control and HGF/SF cells.

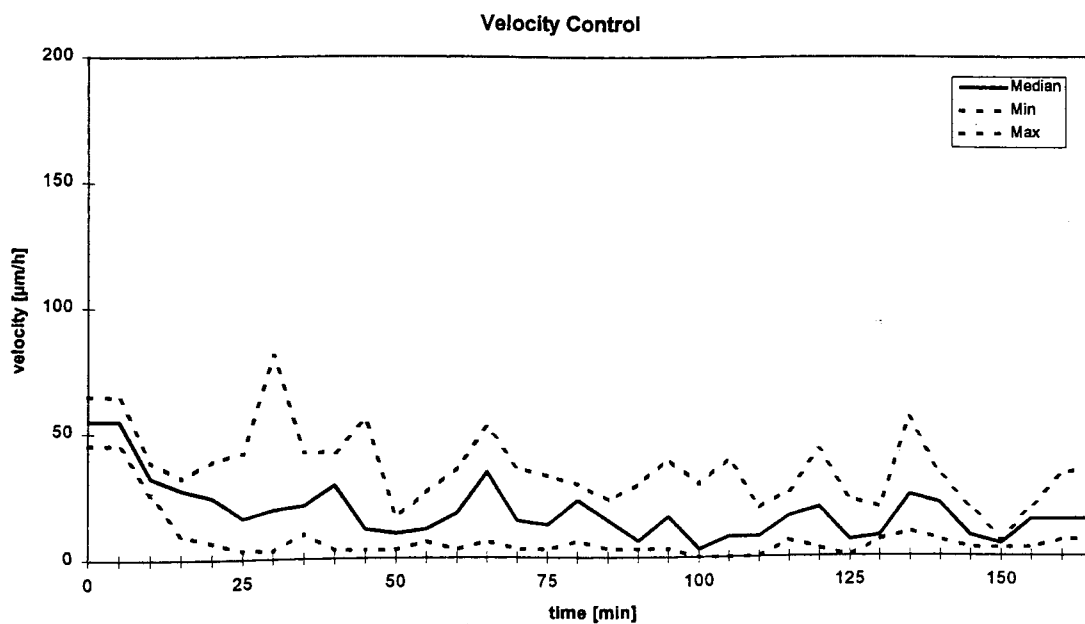


Figure 4. Velocity of six Control cells.

55  $\mu\text{m}/\text{h}$  at the start of the recording. It was observed that the velocity changed over time in both control and HGF/SF treated cells. In this investigation we observed the velocity of HGF/SF treated cells was approximately twice that of control cells. Moreover, there was also a greater variability observed in the HGF/SF cells. The range of the velocity was 7  $\mu\text{m}/\text{h}$  to 190  $\mu\text{m}/\text{h}$ , while the range of the control cells was 0  $\mu\text{m}/\text{h}$  to 81  $\mu\text{m}/\text{h}$ .

## Discussion

In this study we have developed a new computer based system that enables rapid analysis of cell movement and cell velocity. This system enables analysis of cell behaviour within a clustered colony. The system allows the position of cells to be described both by calculation of the cell centroid and by specifying the position of the nucleus.

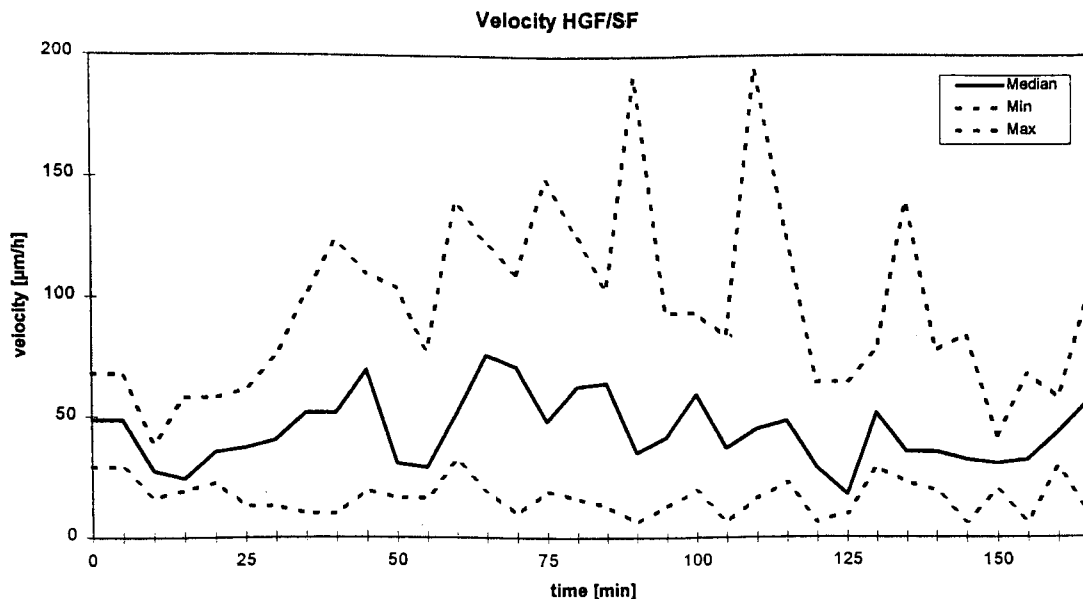


Figure 5. Velocity of six HGF/SF treated cells.

We have validated the system by analysing artificially generated cell shapes and found agreement within 3% of area. We have applied a new technique for rapidly defining the cell boundary and found it compares well with manual marking of the entire cell boundary. There may be greater errors with cells showing membrane ruffling because of approximation around the cell. Ruffling normally appears from 5 minutes [12] and reaches a maximum in 30 minutes. This is perhaps one factor that contributes to the increase of area in the first 30 minutes seen in this study.

We observed greater velocities in cells treated with motogen than control cells which is in accordance with previous studies [14]. However, we also observed that cell velocity varies in time and our results suggest that this variation is greater in cells treated with motogen. Cell area was found to be similar in cells with and without motogen, however, there was greater variation in area with time in those cells treated with motogen. Cell motility plays an important role in the establishment of cancer metastasis. It is also an important factor on chemotaxis and endothelium penetration. The system reported here may therefore provide a useful tool in these studies.

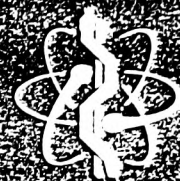
## References

- Jiang WG, Hallett MB, Puntis MCA: Review Paper: Motility factors in cancer invasion and metastasis. *Surg Res Comm* 16: 219-237, 1994.
- Schiffmann E: Motility as a principal requirement for metastasis. *Cancer Invest* 8: 673-674, 1990.
- Liotta LA, Rao CN, Wewer UM: Biochemical interactions of tumor cells with the basement membrane. *Ann Rev Biochem* 55: 1037-1057, 1986.
- Weidner KM, Behrens J, Vandekerckhove J, Birchmeier W: Scatter factor: Molecular characteristics and effect on the invasiveness of epithelial cells. *J Cell Biol* 111: 2097-2108, 1990.
- Rosen E, Meromsky L, Setter E, Vinter DW, Goldberg ID: Smooth muscle-derived factor stimulates mobility of human tumor cells. *Invasion Metastasis* 10: 49-64, 1990.
- O'Gorman L, Arthur C, Sanderson AC, Preston JR: A system for automated liver tissue image analysis: Methods and results. *IEEE Trans Biomedical Engineering* 32: 696-705, 1985.
- Azzara A, Chimenti M, Azzarelli L, Fantini E, Carulli G, Ambrogio F: An image processing workstation for automatic evaluation of human granulocyte motility. *J Immunological Methods* 148: 29-40, 1992.
- Azzara A, Carulli G, Rizzuti-Gallaci A, Minnucci S, Capochiani E, Ambrogio F: Motility of the rhG-CSF-induced neutrophils on patients undergoing chemotherapy: evidence for inhibition detected by image analysis. *Brit J Haematol* 92: 161-168, 1996.
- Zicha D, Dunn GA: An image processing system for cell behaviour studies in subconfluent cultures. *J Microscopy* 79: 11-21, 1995.
- Zahm J-M, Kaplan H, Herald A-L, Dorot F, Pierrot D, Somelette P, Puchelle E: Cell Migration and Proliferation during *in vitro* wound repair of the respiratory epithelium. *Cell Motility Cytoskeleton* 37: 33-43, 1997.
- Thurston G, Jaggi B, Palcic B: Cell Motility Measurements with an Automated Microscope System. *Exp Cell Research* 165: 380-390, 1986.
- Jiang WG, Hiscox S, Singhrao SK, Nakamura T, Puntis MCA, Hallett MB: Inhibition of HGF/SF - induced membrane ruffling and cell motility by transient elevation of cytosolic free  $Ca^{2+}$ . *Exp Cell Res* 220: 424-433, 1995.
- Bartels R, Beatty JC, Barsky BA: An Introduction to Splines for use in Computer Graphics and Geometric Modeling. Morgan Kaufmann Publishers, 1992.
- Bhargava MM, Li Y, Joseph A, Liang J, Rosen EM and Goldberg ID: HGF/SF: Effects on motility and morphology of normal and tumor cells. *In: Hepatocyte growth factor-scatter factor (HGF/SF) and the c-met receptor*. 341-349, 1993. Birkhäuser Verlag Basel/Switzerland. Eds: Goldberg ID and Rosen EM.

Received March 24, 1998

Accepted April 24, 1998

# Medical & Biological Engineering & Computing



Incorporating **CELLULAR ENGINEERING**

## Contents

Volume 37 No. 4 July 1999

### Imaging

- Fractal-based image texture analysis of trabecular bone architecture: C. Jiang, R. E. Pitt, J. E. A. Berram and D. J. Aneshansley ..... 413
- Interactive image processing system for assessment of cell movement: A. Hoppe, C. Wagner, W. G. Jiang, R. Williams and K. Harding ..... 419
- Dual-beam laser illuminator for fluorescence microscope for *in vivo* microcirculation studies: M. Shiotani, S. Ienicka and A. Kamiya ..... 424

### Bioimpedance

- Real-time extraction of tissue impedance model parameters for electrical impedance spectrometry: S. Kim, B. Ristic, R. A. Peura and R. M. Dunn ..... 423

### Dialysis

- Comparison of optical, electrical and centrifugation techniques for haematocrit monitoring of dialysed patients: M. Y. Jaffrin and C. Fournier ..... 433

### Biomechanics

- A three-dimensional definition for the flexion-extension and adduction-abduction angles: P. Li, Cheng and M. Pearcy ..... 440
- Registration and geometric modelling of the spine during scoliosis surgery: a comparison study of different preoperative reconstruction techniques and intraoperative tracking systems: J.-M. Mac-Thiong, C.-E. Aubin, J. Carssereau, J. A. de Guise, P. Brodeur and H. Lado ..... 445
- In vivo* measurements of skeletal muscle power output using new capacitive strain gauges: P. B. Cooper, G. J. Wilson, D. T. A. Harman, O. Kawaguchi, K.-F. Huang, A. Martinez-Doll, R. Carrington, E. Puchner, R. Crameri, C. Hiram and S. N. Hunyor ..... 451

### Respiratory measurement

- Improved accuracy and extended flow range for a Fleish pneumotachograph: N. O. T. Strömberg and M. J. Grönqvist ..... 456
- Effect of ambient respiratory noise on the measurement of lung sounds: H. Pasterkamp, G. R. Wodicka and S. S. Kraman ..... 461

### Sleep analysis

- Expert system classification of sleep/waking states in infants: C. A. Holzmann, C. A. Perez, C. M. Had, M. San Martin, F. Pizarro, J. P. Perez, M. Gamdo and R. Pierand ..... 466

### Cardiac electrophysiology

- Assessment of spatial resolution of cardiac pace mapping when using body surface potentials: R. Fran, B. B. Punske and G. Stronk ..... 477
- Phase response curve based model of the SA node: simulation by two-dimensional array of pacemaker cells with randomly distributed cycle lengths: S. Abramowicz-Swan and S. Akselrod ..... 482
- Modelling a parasympathetic rhythm in a heart-transplant patient: M. Costa, I. R. Pimentel, T. Santiago, M. J. Radooni, J. Melo and E. Ducla-Souza ..... 492

### Cardiovascular measurement

- Flow dependence and time constant of the change in nitric oxide concentration measured in the vascular medial: S. Moonizuki, M. Goto, Y. Ohda, Y. Ogasawara and R. Kiyawa ..... 497
- Evaluation of Karmunen-Luave expansion for feature selection in computer-assisted classification of aortic stenosis heart valve status: M. Yazdandpanahi, L. Alardi, L.-G. Durand and R. Guardo ..... 504
- Left ventricular pressure gradient: a computer model simulation: P. Verdonck, J. Vierendeels, K. Remslagh and E. Dijk ..... 511
- Development and preliminary clinical tests of an impedance sensing VDD recording pacemaker for diagnosis and research: D. R. Edgar, J. M. K. Harwood, D. J. Woodhouse, J. Baker and D. B. Shaw ..... 517

### Communication

- Magnetism for polarisation of cardiac tissue at a sealed boundary: B. J. Reinf ..... 520

### Technical note

- Instrumented staircase for ground reaction measurements: R. Planer, M. Raduetti, C. Frigo, J. Quinlan and G. Schmidt ..... 523

## Cellular Engineering

- Atomic force microscopic measurement of the mechanical properties of intact endothelial cells in fresh arteries: H. Miyazaki and K. Hayashi ..... 530

- A non-parametric method for the analysis of experimental tumour growth data: R. Chignola, D. Liberati, E. Orsola, C. Anselmi, R. Foroni, S. Sartoris, A. Brandolini, G. Tridante and G. Andriagnetto ..... 537

# Interactive image processing system for assessment of cell movement

A. Hoppe<sup>1</sup> D. Wertheim<sup>1</sup> W.G. Jiang<sup>2</sup> R. Williams<sup>1</sup> K. Harding<sup>2</sup>

<sup>1</sup>School of Electronics, University of Glamorgan, Pontypridd, CF37 1DL, UK

<sup>2</sup>Department of Surgery, University of Wales College of Medicine, Cardiff, CF4 4XN, UK

**Abstract**—The study of cancer cell motility is considered to be important in understanding cancer metastasis. The movement behaviour of cells within clustered cell colonies is of particular interest. Changes in cell movement, area and velocity can be an indicator of cell spreading. The aim of the study is to develop and apply a computerised interactive image processing system to quantify the movement of cells within cell clusters. A semi-automatic boundary description method based on two-dimensional rendering is devised. The system is later combined with image-processing methods that facilitate the relocation of the cell boundary over time; this forms a new approach to assessing cell movement. These methods are incorporated into a software system, enabling an interactive procedure to define and monitor the movement of single cells in cell clusters from digitised microscope images. Validation of the method shows a maximum error of 10% in defining the area through a cubic spline interpolation. The system is applied to analyse the movement and area of HT115 human colon cancer cells. The system provides tools for the analysis of movement, area and velocity of single cells in cancer cell colonies and may thus be of value in further understanding cancer cell motility.

**Keywords**—Cell, Cancer, Image processing, Cell movement, Interactive

Med. Biol. Eng. Comput., 1999, 37, 419–423

## 1 Introduction

IN RECENT years, several methods to track the movement of cells have been described (THURSTON *et al.*, 1986; ZICHA and DUNN, 1995; WU *et al.*, 1995; SHUTT *et al.*, 1998; SIEGERT *et al.*, 1994). These methods typically employed an automated image vision approach and were used to track the movement of single cells (THURSTON *et al.*, 1986; ZICHA and DUNN, 1995; WU *et al.*, 1995; SHUTT *et al.*, 1998). Thus, the movement of single, detached cells could be described by following the cell within an image. The position was either indicated by its centroid or by the position of its nucleus. In one system, the movement of the whole colony was examined by determining the optical flow of the cell colony (SIEGERT *et al.*, 1994; NOMURA and MIKE, 1991). However, no distinction was made between single cells within the cluster.

As cells often appear in clusters or cell colonies, there is particular interest in the movement behaviour of single cells in a clustered environment. However, it can be difficult for an automated image vision system to describe and therefore track individual cells correctly. This is due to the problem of overlapping cells and features becoming obscured in tightly clustered cells.

We have previously described the application of an interactive computer analysis system to assess the movement of cells in clusters (HOPPE *et al.*, 1998). The system was used to

investigate the effects of added motogen on the movement of cancer cells.

## 2 Aim

The aim of this study was to develop further an interactive, semi-automatic image-processing system, incorporating a cell tracking algorithm, to facilitate the monitoring of single cells in cell clusters.

## 3 Method

A cell is an object that can be described by its boundary (cell membrane), area (cytoplasm) and nucleus. Fig. 1 shows a cell with highlighted membrane, centroid (centre of area) and nucleus.

However, extracting the cell membrane automatically in a clustered environment can be difficult, because cells can overlap, as seen in Fig. 2. A traditional approach of defining the outline of a cell by means of pure image segmentation can be difficult to implement because of such boundary fragmentation.

### 3.1 Cell description

Our approach to defining a cell involves an interactive boundary description, with only a few salient points placed on the cell boundary. In a semi-automatic fashion, fragments of the boundary represented by spline segments between the points are specified at the beginning of the monitoring process. Image-processing functions for image enhancement are provided to aid

Correspondence should be addressed to Mr A Hoppe;  
email: [ahoppe1@glam.ac.uk](mailto:ahoppe1@glam.ac.uk)

First received 30 November 1998 and in final form 8 April 1999

© IFMBE: 1999

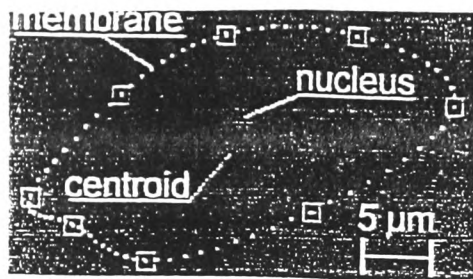


Fig. 1 Example showing features of a cancer cell

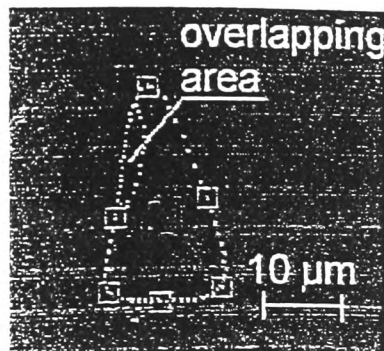


Fig. 2 Example showing highlighted cell in a cluster

the process. Once the cell has been described initially, the system looks for image features in the near neighbourhood of those points to track them in future frames.

The cell boundary is described by two-dimensional rendering of the cell membrane, combined with image-processing functions to reposition points automatically. If the repositioning is considered inappropriate, the user can interactively correct the position of a single point or all points. In addition, a template of the previous cell outline can be passed to the next frame and permits changes necessary to adjust the boundary.

### 3.2 Rendering

To describe a cell shape, a sequence of points are specified on the boundary that in some way describe how the curvature is formed. In the case of an interpolation, the curve is required to pass through the specified points shown in Fig. 3.

Mathematically, a spline segment can be described as follows:

$$Q_i(u) = (X_i(u), Y_i(u)) \quad 0 \leq u \leq 1 \quad (1)$$

Each point of a segment  $Q_i(u)$  is described by a function of the  $X_i(u)$  and  $Y_i(u)$  coordinates.

The nature of the cell boundary can be described as 'naturally' formed, and, hence, there are hardly any sharp edges or discontinuities within the shape itself. One type of spline that is appropriate for such curvature is the natural cubic spline, a special form of Hermite spline (BARTELS *et al.* 1992).

For example, the  $y$  co-ordinate of a single boundary segment is described through a cubic polynomial with the parameter  $u$ :

$$Y_i(u) = a_i + b_i u + c_i u^2 + d_i u^3 \quad 0 \leq u \leq 1 \quad (2)$$

The first derivative  $Y'_i(u)$  and the second derivative  $Y''_i(u)$  at the end of the  $i$ th segment equal those at the beginning of the following segment. It is important to note that we are dealing

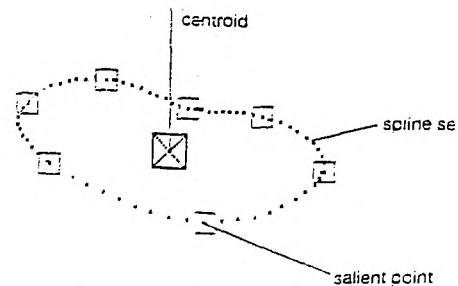


Fig. 3 Closed Hermite cubic spline curvature description

with a closed natural curvature, and, hence, the last is connected to the first segment.

By incorporating those constraints into our cubic segment equation, we are able to calculate symbolic spline coefficients.

Once the shape of the boundary has been defined mathematically, the area can be calculated as

$$A_i = \int Q_i(u) du$$

for each segment and

$$A = \sum A_i$$

as a total.

Similarly, the centroid,  $P_c(x_c, y_c)$  of that area is from

$$x_c = \frac{1}{A} \int_{(t,A)} x dA \quad y_c = \frac{1}{A} \int_{(t,A)} y dA$$

All boundary segments are described mathematically; the centre of area can be determined mathematically; cubic spline equation. It can be used to describe the cell in each frame and to calculate the area. Alternatively, the cell position can be specified by the centroid of the nucleus.

### 3.3 Image processing

The aim of the image processing is twofold: first, to enhance the visual appearance of cells to facilitate the initial defining the cell; secondly, to suggest the new points in the next frame.

**3.3.1 Image enhancement:** Digitised grey scale images from cells can express a poor range of grey-levels. Therefore imaging techniques to reduce noise and extend grey-level range were implemented.

Images were acquired at an equivalent of a 5 s interval. Frames were averaged which resulted in a 20 s frame. This was found to be adequate to reduce the unwanted noise. Furthermore, to enhance the global appearance of cells, contrast stretching and histogram equalisation were applied. A  $3 \times 3$  Laplacian filter matrix can be used to highlight the cells' boundary and ease the process.

**3.3.2 Point relocation:** The cell boundary is described by a two dimensional cubic spline that is determined by points placed on the cell membrane. The system looks for image features that can be associated with that location and might be relocated in the next frame. Points are usually placed on a fragmented piece of boundary. A two-dimensional derivative filter yields the high-frequency components

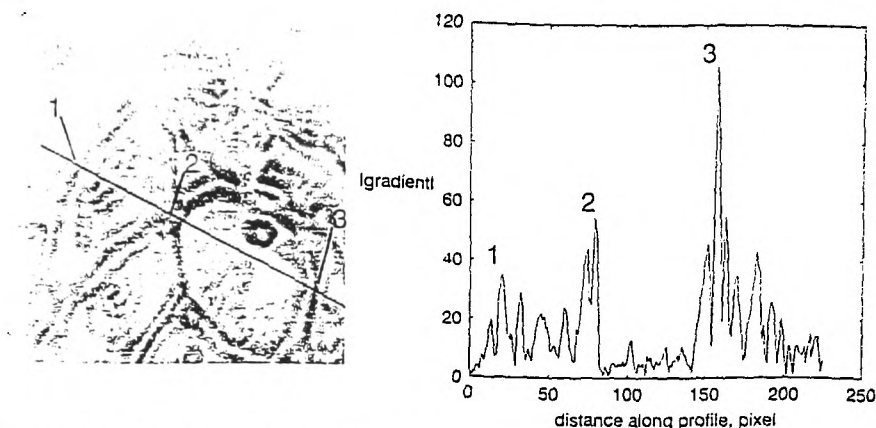


Fig. 4 Gradient image profile and corresponding profile graph

image, thus helping to identify boundaries. The points are 'logged' onto such image features, which are not likely to change between two frames. The points are relocated according to the highest absolute local gradient calculated with a two-dimensional  $3 \times 3$  Prewitt filter.

Fig. 4 shows the profile of a 250 pixel length line through the first derivative of a cell cluster image. The image shows the intensity of absolute gradient values, whereby dark regions express high gradient values.

The cell boundaries on this profile are numbered from one to three. The boundary of the cells in the profile can be identified by the highest gradient value. This clearly highlights the principle behind the point relocation method, whereby the system looks for a maximum gradient in the local  $5 \times 5$  area around salient points, which it tries to follow over time. The diagram in Fig. 5 explains the tracking process.

Salient points are placed on the cell boundary in the first frame. The system suggests the position of these points in the next frame. If the user is not satisfied with the relocation, tools are provided to adjust the boundary to ensure a close fit.

#### 4 Implementation

We developed the software package to enable the capturing and processing of microscopic cancer-cell images. Software was specially written for the DT3153 image-capture board\* to capture images from a video source at a selectable interval. Images are captured as true colour  $768 \times 568$  bitmaps and subsequently converted into 8-bit grey scale versions. Image-

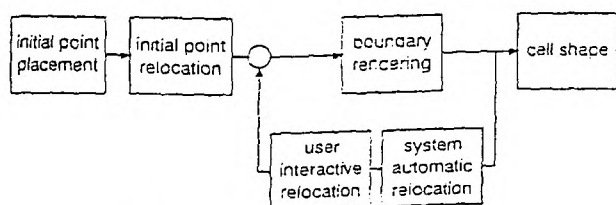


Fig. 5 Schematic diagram of interactive point-relocation method

\*Data Translation, Marlboro, USA

†Sun Microsystems USA

‡Inprise, USA

\*\*Microsoft, USA

††Leica DM IRB, Germany

‡‡Hoffman Greenvale, NY, USA

§Panasonic WV-CL350, Japan

processing algorithms were designed using the JAVA language† and tested on a Solaris Unix workstation† as well as on a standard personal computer.

The algorithms were ultimately ported to C++ and incorporated into analysis software designed in Borland C++ Builder‡ for Windows95\*\*.

The analysis software facilitates functions to describe cell movement and allows export of the analysed data.

#### 5 Application

HT115 human colon cancer cells without added mitogen were monitored on a real time video system for 30 min, as previously described (HOPPE *et al.*, 1998). An inverted fluorescent microscope††, fitted with an HMC20 condenser‡‡ and a digital camera§ connected to a real-time video system, was used to record the images. The condenser was used to enhance the appearance of the cell boundaries. Frames from the microscope video recording were captured every 5 s, and four such frames were averaged to reduce noise.

The system was applied to analyse the movement, velocity and area of HT115 cells over a period of 30 min, according to the centre of area. The area was calculated every 20 s. Five minute intervals were chosen for the calculation of velocity, as little or no movement occurred within this time based on visual analysis. Calibration was achieved with a special  $250 \mu\text{m}$  square marked on a slide.

The validation was performed in three steps:

- The accuracy of the semi-automatic spline-based description method for cell area and cell position was analysed using a test image shown in Fig. 9.
- The gradient-based point relocation method on the test image was analysed.
- the repeatability of the cell description techniques was investigated in images of real cells.

#### 6 Results

A cell colony with at least ten cells was chosen at random, and changes in the movement and area of four such cells were analysed. The velocity was calculated according to the centre of area. Fig. 6 shows an example of area and velocity of four HT115 cells.

The position and the velocity of the cells were calculated according to the centroid (centre of area). The position of the centroid can be viewed in a tracking diagram. Fig. 7 shows the movement of a single cell within a cell colony in an area  $400 \mu\text{m}^2$ . Changes in the cells' shape over time can also be compared. Fig. 8 shows an example of changes in cell boundary at 5 min intervals over a 10 min period.

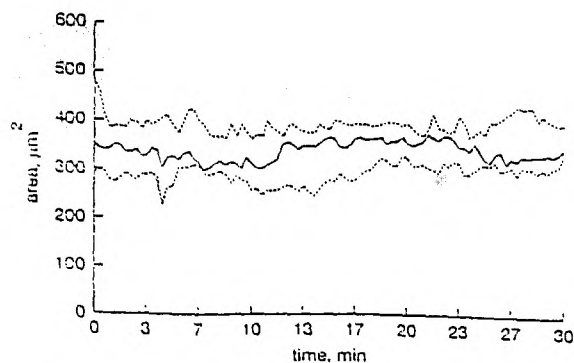


Fig. 6 Median area and velocity of four HT115 cells. (—) Median; (---) minimum/maximum

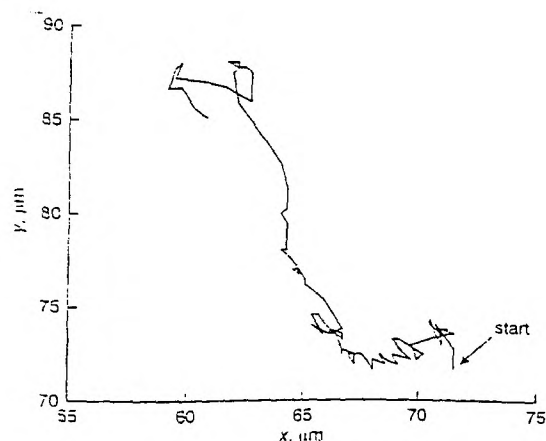
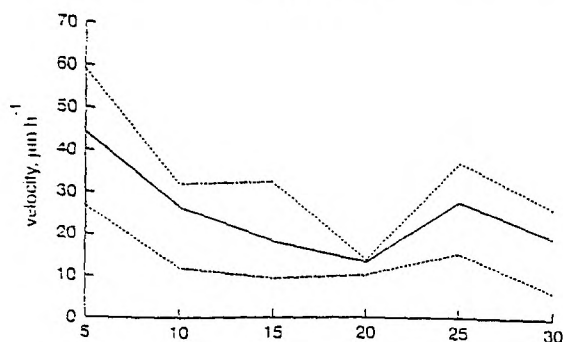


Fig. 7 Tracking diagram of single HT115 cell

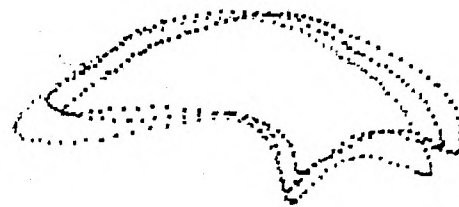


Fig. 8 Example of changes to cell shape over 10 min. (---) 0; (---) 5 min; (—) 10 min

## 6.1 Validation of cell description

An image of a single cell was cut out of a cluster and placed on a uniform white background. A  $3 \times 3$  smoothing filter was applied to ease the transition between cell boundary and background. The cell was defined ten times, with seven salient points placed on the cell boundary.

Fig. 9 expresses the calculated area on ten different occasions.

The actual area value with which it was compared was calculated by pixel-counting. The area was  $348 \mu\text{m}^2$  and represented by a horizontal line on the graph in Fig. 9. In ten tests, we observed that the actual area was slightly larger than the calculated one, with a maximum error of 10%. The mean area was  $322 \mu\text{m}^2$ , and the range was from  $313 \mu\text{m}^2$  to  $345 \mu\text{m}^2$ . This could be explained by membrane roughness resulting in limited definition of the cell boundary.

## 6.2 Point relocation validation

The cell in the artificial test image was moved at a rate of 1 pixel per 20 s. This results in a velocity of  $1.147 \mu\text{m}/\text{h}$ . The system should be able to find image features to 'log' and further follow those features according to the linear movement of the test cell.

In this test, the user did not interactively alter the suggested points, and the velocity was calculated every 20 s. As shown in the upper graph of Fig. 10, the area was initially defined correctly by placing seven salient points on the outside cell boundary. The criterion for the point-relocation method was the highest first derivative in the near neighbourhood. Points moved towards the middle of the cell membrane, resulting in a reduction overall. The cell was followed correctly for

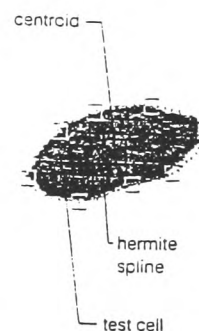
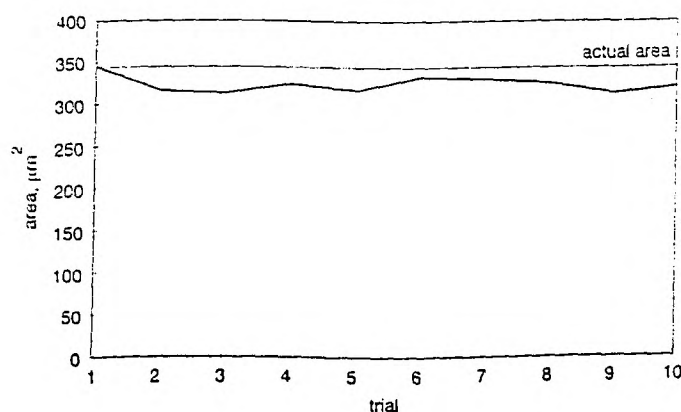


Fig. 9 Area of test cell and test cell image (trial 1) with spline. Centroid marked as a square.

on. This is represented by the constant velocity after three iterations of point relocation, as marked by a broken line in the graphs in Fig. 10.

### 6.3 Repeatability validation

In this part of the validation, the movement of a single cell within a cell cluster was assessed three times with the semi-automatic boundary-description method.

Fig. 11 shows the velocity of the same cell in three trials. The solid line expresses the median velocity of those three trials, with expected error bars. The expected error is calculated on the basis that there is an inherent error due to point displacement of one diagonal pixel ( $\sqrt{2}$  pixels). This results in an absolute error of  $5 \mu\text{m h}^{-1}$  measured at a 5 min interval.

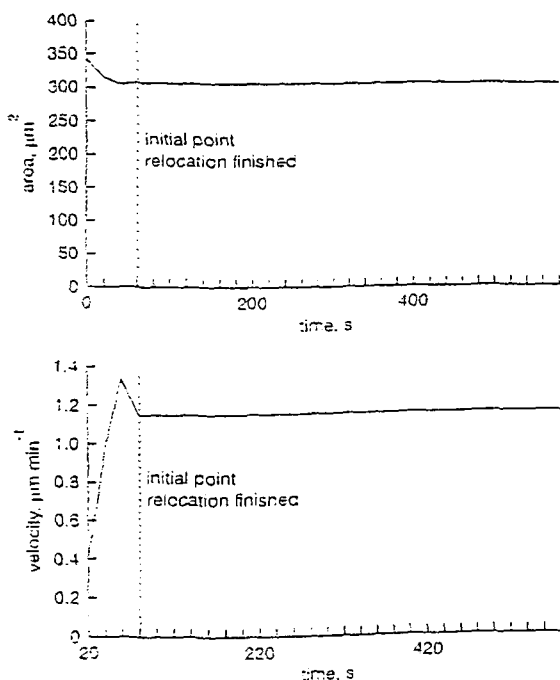


Fig. 10 Area and velocity of test cell under linear movement conditions

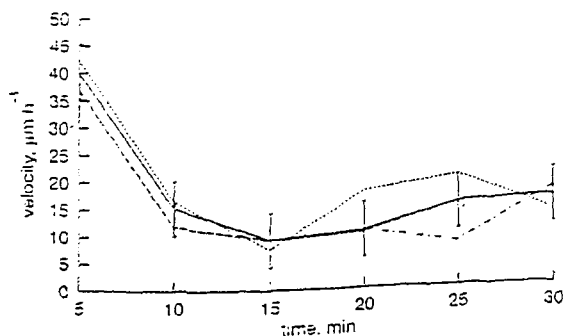


Fig. 11 Velocity and expected velocity error of a single cell analysed three times. (—) Trial 1; (---) trial 2; (····) trial 3; (—) median

## 7 Conclusions

In this study, we have developed a new computer system for rapid analysis of cell movement, area and cell velocity. Furthermore, this system enables analysis of cell behaviour within a clustered cell colony.

An advantage of this system is that it allows the definition of the cell position from the centre of area (centroid) and also by specifying the position of the nucleus. The cell velocity is calculated from the cell position and can be expressed according to the centroid or the position of the nucleus.

The operator can also choose to copy the outline of the cell boundary to successive frames and adjust as necessary. The system also includes enhancement methods that may help to identify the cell boundary. The validation experiments confirmed the performance of the system. A possible way of reducing error is to increase the magnification. However, the cell membrane may not appear as a clear border, and, hence, there is an inherent possible error; this may be particularly evident in membrane ruffling.

The semi-automatic point-relocation method proved to be of value to the rapid tracking of cells. As the system is interactive, the operator can redefine the spline boundary description of the cell, if the computer-generated boundary deviates from that observed by eye. The interactive system may also be applicable for the analysis of isolated cells. The system is being used to investigate the effects of motogen on cancer-cell movement. However, this system is not restricted to cancer cells alone; other types of cell, such as neutrophils and others that display defined boundaries, can also be analysed.

Cell motility is thought to play an important role in the establishment of cancer metastasis. Thus this system may be of value in the study of cancer metastasis.

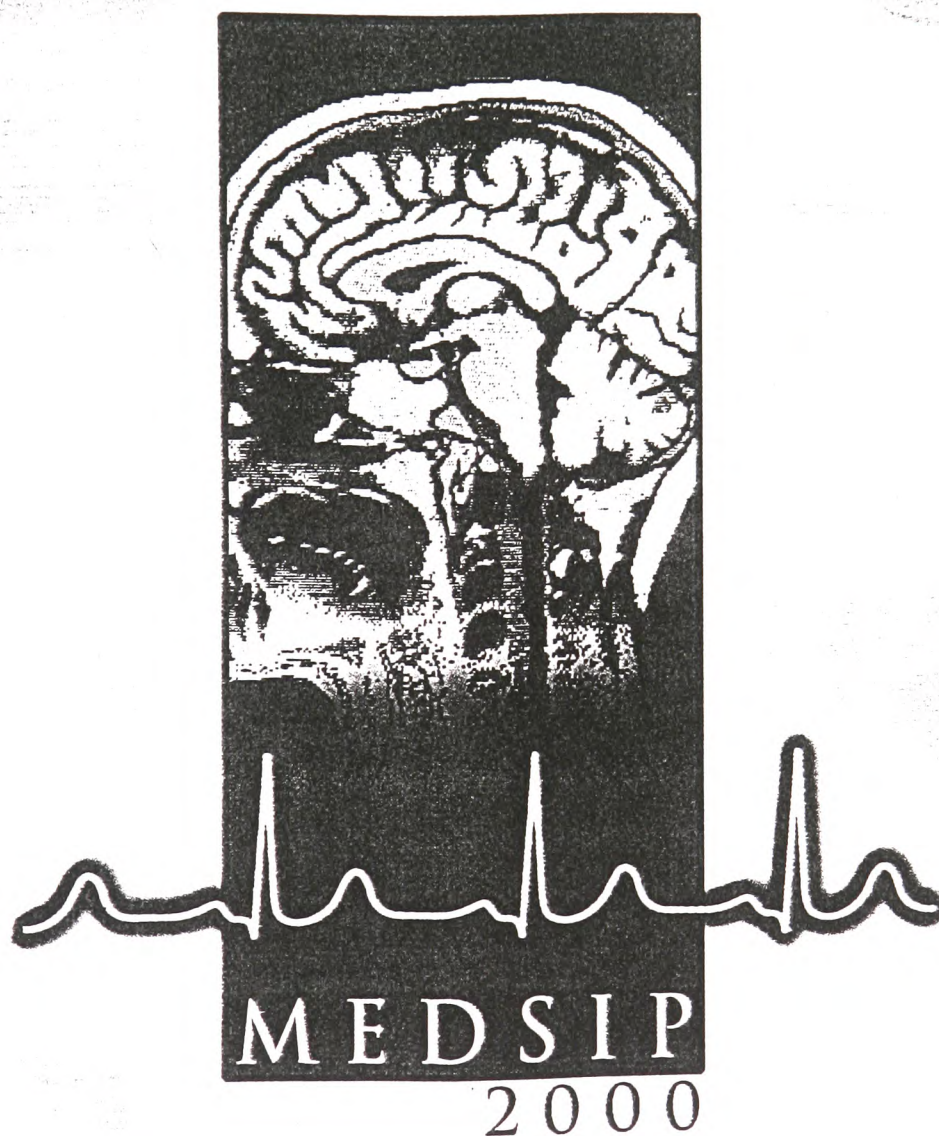
## References

- BARTELS, R., BEATTY, J.C., and BARSKY, B.A. (1992): 'An Introduction to splines for use in computer graphics and geometric modelling' (Morgan Kaufmann Publishers)
- HOPPE, A., JIANG, W.G., WERTHEIM, D., WILLIAMS, R., and HARDING, K. (1998): 'A system for computer analysis of cancer cell movement.' *Anticancer Res.*, **18**, pp. 2691–2694
- NOMURA, A., and MIKE, H. (1991): 'Field theory approach for determining optical flow.' *Pattern Recognit. Lett.*, **12**, pp. 183–190
- SHUTT, D., JENKINS, L., CAROLAN, E., STAPLETON, J., DANIELS, N., KENNEDY, R., SOLL, D. (1998): 'T cell chemoattractants: demonstration with a newly developed single cell chemotaxis chamber.' *J. Cell Sci.*, **111**, pp. 99–109
- SIEGERT, F., WEIER, C.J., NOMURA, A., and MIKE, H. (1994): 'A gradient method for the quantitative analysis of cell movement and tissue flow and its application to the analysis of multicellular Dictyostelium development.' *J. Cell Sci.*, **107**, 97–104
- THURSTON, G., JAGGI, B., and PALCIC, B. (1986): 'Cell motility measurements with an automated microscope system.' *Exp. Cell Res.*, **165**, 380–390
- WU, K., GUTHRIE, D., and LEVINE, M.D. (1995): 'Live cell image segmentation.' *IEEE Trans., BME-42*, pp. 1–12
- ZICHA, D., and DUNN, G.A. (1995): 'An image processing system for cell behaviour studies in subconfluent cultures.' *J. Microsc.*, **179**, pp. 11–23

## Authors' biographies

This research is part of a collaborative, multidisciplinary project between the Medical Electronics and Signal Processing Research Unit (MESPRU), School of Electronics, University of Glamorgan and the Department of Surgery, University of Wales College of Medicine.

# International Conference on Advances in Medical Signal and Information Processing



CONFERENCE PUBLICATION No 476

## A SPLINE BASED METHOD FOR ASSESSMENT OF WOUND IMAGES

A Hoppe<sup>1</sup>, D Wertheim<sup>2</sup>, J Melhuish<sup>3</sup>, K G Harding<sup>3</sup>, R J Williams<sup>1</sup>

<sup>1</sup>School of Electronics, University of Glamorgan, Pontypridd, CF37 1DL, UK

<sup>2</sup>School of Computer Science, Kingston University, KT1 2EE, Surrey, UK

<sup>3</sup>Wound Healing Research Unit, University of Wales College of Medicine, CF4 4XN, Cardiff, UK

ahoppel@glam.ac.uk, rjwillia@glam.ac.uk

D.Wertheim@kingston.ac.uk

wsrjmm@cardiff.ac.uk, wsrkgh@cardiff.ac.uk

Tel: 01443 482530, Fax: 01443 482530

Chronic wounds are often painful, debilitating and frequently present a major challenge to clinicians. For example, predicting the healing process may be difficult.

Software was written to examine colour and appearance in the vicinity of the wound boundary. The technique was based on a spline delineation of the wound boundary. The software was applied to analyse the hue, saturation and intensity of 10 wound images acquired with a digital video camera. The images included a colour scale for reference.

The system was used to investigate the differences of hue, saturation and intensity in three regions in the vicinity of the wound boundary.

Our results indicate that there was small variation in the hue of the red colour patch compared with the overall variation in hue of the 10 images. For the majority of wounds there was a clear trend in intensity and saturation in the boundary region.

Thus, this system may be of value in further understanding wound healing.

## INTRODUCTION

Objective measurement of the healing progress in wounds is considered to be of great

importance to the clinician. It may be of value in determining whether a treatment is appropriate or if modification is required. At present it is difficult to predict how well wounds heal. The physical size of wounds is used for the assessment of the progress of healing.

It has been suggested that analysis of wound colour may be of clinical value, Romanelli (1), Boardmann et al. (2), Mekkes et al. (3), Herbin M et al. (4). Furthermore, texture has been used as a descriptor of skin melanomas, Schindewolf T et al. (5) and leg ulcer appearance, Hoppe et al. (6).

Wounds responding positively to treatment get smaller over time, forming new tissue at the peripheral edge. However, non responding wounds or indeed, infected wounds, may stagnate or increase in size. The state of the tissue in the boundary region may hence be of value in describing new healing characteristics.

In this study, in order to achieve more objective and therefore more accurate measurements of wound appearance, digital image acquisition is used. This is combined with a spline based technique and image analysis to assess the profile of the wound boundary.

## AIM

The aim of this study was to develop a digital system for assessing colour and appearance in wound images. This combines a new spline technique and image analysis to assess changes in the profile of the wound boundary and its periphery.

## METHOD

Images of leg ulcers on 10 patients were obtained using a digital video camera (Panasonic NVDX100 B, Matsushita Electric Industrial Co. Ltd., Japan). This camera incorporates three separate CCD arrays, each one for the red, green and blue colour plane. This provides good colour reproduction and reduces interference between neighbouring pixels. The camera was operated in still picture mode and images were acquired in true-colour and subsequently downloaded digitally to a PC workstation.

A graduated scale with additional colour patches was held close to the wound in order to provide a means of colour reference. A 10W video light was mounted on the video camera and used to improve lighting conditions.

### Colour Representation

All ten images of leg ulcers were taken under clinical conditions, hence the lighting conditions could not be fully controlled. Images taken from the camera are described by its Red, Green and Blue component. In this colour model, however, the value of each component strongly depends on the light intensity.

Therefore, we used the HSI (Hue, Saturation, Intensity) colour model Gonzalez et al. (7). There, the intensity is separated from the other two components. Hue is the measure of wavelength of the main colour and represented by an angle  $[0^\circ..360^\circ]$ , saturation is related to the amount of white light included, while the intensity is a measure of brightness.

We compared the variation of hue, saturation and intensity values in red colour patches of ten wounds taken under clinical conditions. The red hue region reaches from  $330^\circ$  to  $30^\circ$ . We modified the HSI colour model by shifting the hue range to allow a continuous range of red hue values as seen in table 1.

TABLE 1 - Colour conversion

colour	hue range $[\circ]$	shifted hue $[\circ]$
red	330-30	120-180
yellow	30-90	180-240
green	90-150	240-300
turquoise	150-210	300-360
blue	210-270	0-60
violet	270-330	60-120

### Wound Boundary Description

The objective for the descriptor of the boundary was to provide a flexible and easy method to define and refine the approximate location of the boundary in a wound image.

To describe a wound shape, a sequence of control points is specified on the boundary which will in some way describe how the curvature is formed. In the case of an interpolation, the curve is required to pass through the specified points - hence the operator defines the shape of the delineated boundary by a few control points. The closed boundary is divided into spline segments using cubic polynomials.

Mathematically, the  $i$ th spline segment may be described as follows:

$$Q_i(u) = (x_i(u), y_i(u)) \quad 0 \leq u \leq 1 \quad (1)$$

Each point of a segment  $Q_i(u)$  is described by a function of the  $x_i(u)$  and  $y_i(u)$  co-ordinates.

$$x_i(u) = a_{ix} + b_{ix} u + c_{ix} u^2 + d_{ix} u^3 \quad (2)$$

To ensure a smooth transition between spline segments, we set the first derivative as well as the second derivative at the end of one segment equal to those at the beginning of the following segment.

$$\dot{x}_i(1) = \dot{x}_{i+1}(0) \quad \ddot{x}_i(1) = \ddot{x}_{i+1}(0) \quad (3)$$

This type of spline is known as a Hermite spline, Bartels et al. (8) with  $C^2$  continuity. Fig 1 shows an example wound image with a boundary delineated by a Hermite spline.



Fig 1: Wound image with delineated spline boundary

### Wound Profile

Once the boundary has been described mathematically, we can derive an orthogonal vector at any given position of the spline. The normal vector  $n(u)$  can be calculated as

$$n(u) = \left( \frac{-\dot{y}(u)}{\sqrt{\dot{x}(u)^2 + \dot{y}(u)^2}}, \frac{\dot{x}(u)}{\sqrt{\dot{x}(u)^2 + \dot{y}(u)^2}} \right) \quad (4)$$

from which the angle can be obtained. The profile, which is 31 pixels in width, is centred over the boundary location and divided into three regions: Outer boundary, boundary region and inner boundary as seen in fig 2. The width of the outer and the inner section is 10 pixels while the boundary section has a width of 11 pixels.

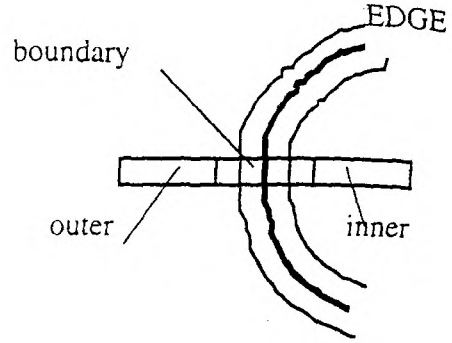


Fig 2: Wound profile regions

Each wound was described by eight spline segments and in this study, we took two profiles per segment. However, the number of profiles per spline segment can be set to a different number. We analysed the mean and standard deviation of hue, saturation and intensity values occurring in those three regions of 16 profiles per wound.

To investigate the changes within each profile the absolute values of the 1st derivatives along the profile were calculated.

Again, we investigated changes in the three regions of 16 profiles per wound. Fig. 3 shows a single wound with 16 profiles along the spline boundary. This image corresponds to wound 3 in table 3 to table 6.

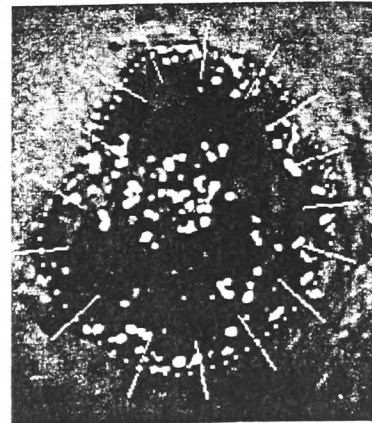


Fig 3: Wound image with profiles along the spline boundary

## Analysis

Our analyses were focused on two issues: How much variation is observed in hue, saturation and intensity in wound images taken under clinical conditions?

The second aspect looked into the profile of hue, saturation and intensity around the wound boundary.

## RESULTS

### Colour Assessment

We have analysed the range in hue values for a red colour patch held close to 10 wounds. We compared these values to the range of hue values occurring within each wound. Hue values were mapped (Hue  $\rightarrow$  Hue') according to Table 1. Fig. 4 shows the comparison of red hue ranges in colour patches and wound area.

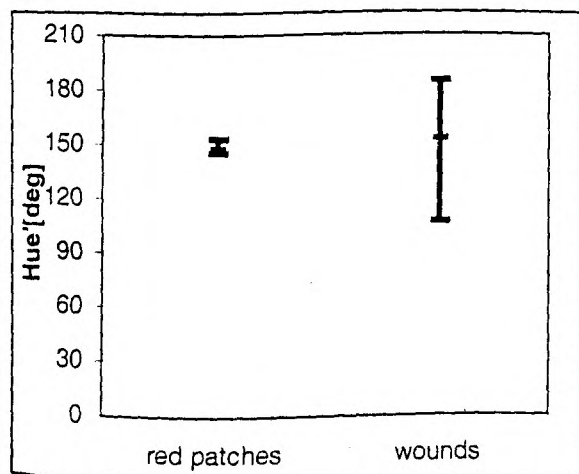


Fig 4: Comparison of range of red hue values in the 10 images of the red colour patch and 10 wounds

The colour patch was of uniform hue and we observed a six degree variation despite being taken under different lighting conditions. The total range of hue values observed over the 10 wounds extended over the whole range of red. Some even extended into the yellow range of

hue, which is in accordance with a previous study, Hoppe et al. (6).

TABLE 2 - Range of median values in 10 images of colour patch

	Median		% of range
	min	max	
Red Hue	144	150	10
Saturation	69	99	30
Intensity	168	240	28

In table 2, the variations in red hue, saturation and intensity in the 10 images of the red colour patch are shown. The range of scale for the red hue was 60 degrees, the range of saturation was 100% and the range of intensity was 255.

The Hue components showed the least variation with 10% over its range. Saturation and intensity expressed a much higher variation of up to 30% between images of the same colour patch.

### Boundary Profile

We analysed the mean and standard deviation of values occurring in the outer (o), boundary (b) and inner (i) region of the profile of 10 wound images. The analysis was performed on hue, saturation and intensity values.

TABLE 3 - Mean hue and standard deviation in 10 wound images

WOUND	HUE' [°] (mean)			HUE' [°] (stdev)		
	o	b	i	o	b	i
1	141	149	154	6	7	5
2	169	167	154	8	7	3
3	170	160	153	9	11	6
4	149	150	150	4	3	3
5	151	153	156	9	9	10
6	146	144	147	6	5	6
7	141	143	142	3	3	1
8	156	153	153	2	2	2
9	141	143	145	3	3	2
10	155	154	152	3	3	2

As seen in table 3, we observed that most wounds have little differences in mean hue between the three regions in the profile despite its different appearance. However, there was

no obvious trend by which the mean hue values increased or decreased from the outer towards the inner wound region.

TABLE 4 - Mean saturation and standard deviation in 10 wound images

WOUND	SAT (mean)			SAT(stdev)		
	o	b	l	o	b	l
1	21	31	38	9	13	11
2	57	54	49	15	10	5
3	19	32	44	5	12	13
4	49	65	75	12	17	14
5	41	52	58	9	16	17
6	34	51	59	15	20	21
7	39	52	58	9	10	6
8	<b>60</b>	<b>83</b>	<b>91</b>	<b>11</b>	<b>14</b>	<b>8</b>
9	40	62	88	15	23	13
10	47	53	61	8	10	6

As seen in table 4, there seems to be a common pattern between the three regions of the profile for the mean saturation. All except one appeared to increase from the outer to the inner region of the wound boundary. Three wounds are marked bold in tables 3 to 6, which were classified as being likely to be infected from visual inspection of images by an experienced clinician. The mean saturation of wound 2 decreased from the outer to inner region unlike the data from the other wound images. The highlighted wounds also seem to be more saturated on the outer boundary.

TABLE 5 - Mean Intensity and standard deviation in 10 wound images

WOUND	INT(mean)			INT(stdev)		
	o	b	l	o	b	l
1	160	143	144	35	37	26
2	153	170	184	36	27	19
3	125	99	105	26	29	41
4	182	147	125	46	49	43
5	156	141	137	32	36	36
6	158	140	135	30	32	39
7	129	111	110	22	26	16
8	<b>166</b>	<b>120</b>	<b>108</b>	<b>29</b>	<b>30</b>	<b>24</b>
9	220	191	161	25	36	25
10	121	98	86	25	28	20

As seen in table 5, the mean intensity values appear to decrease from the outer towards the inner boundary profile. Again, the profile of the likely infected wound 2 behaved differently. However, this behaviour was not observed in wound 8 and 10, which were also considered to be infected.

TABLE 6 - Median and range of absolute 1st derivatives along wound profile

WOUND	HUE[°] median			HUE[°] min			HUE[°] max		
	o	b	l	o	b	l	o	b	l
1	1.5	1	1	0	0	0	10	15	9
2	1	1	1	0	0	0	11	26	15
3	1	2	1	0	0	0	15	19	25
4	1	1	1	0	0	0	9	4	5
5	1	1	1	0	0	0	8	20	10
6	1	1	1	0	0	0	14	9	6
7	1	1	1	0	0	0	6	5	5
8	1	1	1	0	0	0	10	6	5
9	1	1	1	0	0	0	27	20	4
10	1	1	1	0	0	0	4	7	5

Table 6 shows the median, minimum and maximum of the absolute 1st derivatives of hue values. The low median values indicate small differences between neighbouring pixels in hue.

## CONCLUSIONS

The results suggest that recording wound images digitally on a 3 CCD camera is a feasible way of assessing wound appearance under clinical conditions.

Despite the influence of daylight and/or fluorescent light, there was a maximum variation of 6 degrees in the hue value of the red colour patch. However, there is more variation in saturation and intensity values in the images of the red colour patch.

Over the 10 wound images, the range of hue values within the wound areas covered the whole red hue region; in some images even into the yellow region. This may be due to slough in the wound bed.

The spline boundary description is a fast and flexible way to determine the approximate

location of the edge. We used the spline to obtain the orthogonal vector, which forms the basis for the image analysis profile.

In our analysis, we divided the orthogonal profile vector into three regions. In most images we observed an increase in saturation from the outer to the inner wound boundary and a decrease of intensity from the outer to the inner wound boundary. Interestingly, we observed small changes in hue between the three regions despite the different visual appearance.

Three of the ten wounds were considered to be infected by visual inspection from an experienced clinician. In one of these cases, the hue, saturation and intensity expressed a different trend.

This study suggests that it is important to include a colour scale for reference when taking wound images for further analysis. Furthermore we have developed and applied a spline based technique for assessment of hue, saturation and intensity in the vicinity of wound boundaries which can be used to investigate changes in wound appearance.

This system may therefore be of value in further understanding the healing process of wounds.

### Acknowledgement

We are grateful for help received from staff at the Wound Healing Research Unit at the University of Wales College of Medicine, Cardiff.

### REFERENCES

1. Romanelli M, 1997, "Objective Measurements of venous ulcers deposition and

granulation with skin colour reflectance analyser", *J Geriatr Dermatol*, **5**, 319-323

2. Boardmann M, Melhuish J, Palmer K, Harding K.G, 1994, "Hue Saturation and Intensity in the healing wound image", *Jl of Wound Care*, **3**, 314-319

3. Mekkes J R, Westerhof W, 1995, "Image Processing in the Study of Wound Healing", *Clinics in Dermatology*, **13**, 401-407

4. Herbin M, Bon F X, Jeanlouis F, Dubertret L, Strauch G, 1993, "Assessment of Healing Kinetics Through True Color Image Processing", *IEEE Trans Medical Imaging*, **12**, 1, 39-43

5. Schindewolf T, Stolz W, Albert R, Abmayr W, Harms H, 1993, "Classification of Melanocytic Lesions with Color and Texture Analysis using Digital Image Processing", *Analytical and Quantitative Cytology and Histology*, **15**, 1-11

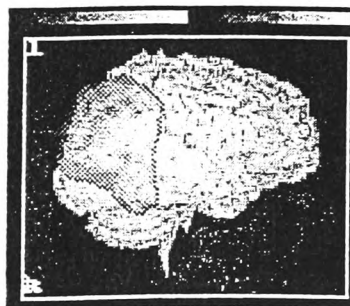
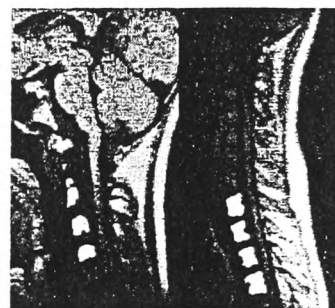
6. Hoppe A, Wertheim DF, Melhuish JM, Williams RJ and Harding KG, 1998, "Computer analysis of wound images", *Wound Repair and Regeneration*, **6(5)**, A488

7. Gonzalez R C, Woods R E, 1993, "Digital Image Processing", Addison-Wesley Publishing Company

8. Bartels R, Beatty JC, Barsky BA., 1992, "An Introduction to Splines for use in Computer Graphics & Geometric Modeling", Morgan Kaufmann Publishers ,

**Proceedings of**

# **Medical Image Understanding and Analysis MIUA2000**



**University College London**  
**Monday 10<sup>th</sup> - Tuesday 11<sup>th</sup> July 2000.**

# Adaptive Spline Method for Extracting $\text{Ca}^{2+}$ and Morphological Measurements from Motile Human Neutrophils

A. Hoppe<sup>a1</sup>, M.B. Hallett<sup>b</sup>, S. Dewitt<sup>b</sup>, D. Wertheim<sup>c</sup>, R. Williams<sup>a</sup>

<sup>a</sup>School of Electronics, University of Glamorgan, Pontypridd, U.K.

<sup>b</sup>Department of Surgery, University of Wales College of Medicine, Cardiff, U.K.

<sup>c</sup>School of Computer Science and Electronic Systems, Kingston University, Surrey, U.K.

**Abstract.** The study of cell motility is thought to be important in understanding the behaviour of cells. We have devised a semi-automatic boundary description method based on two-dimensional rendering. This is combined with a relocation method to track the movement of single neutrophils. We used the system to analyse the morphology of neutrophils and information of cytosolic free  $\text{Ca}^{2+}$  concentration and cell shape. The results of the validation indicated a maximum difference of 3% in area between our adaptive spline method and a linear interpolation of the cell boundary. Furthermore, we devised and applied a method to assess the calcium concentration in a dynamic region defined in relation to a localised cell shape change.

## 1 Introduction

Neutrophils are blood cells which are crucial for combating infection within the body. They achieve this by moving from the blood stream to a site of infection where they engulf (phagocytose) and kill the infecting micro-organism. These cells are thus both phagocytic and chemotactic, and are capable of rapid and specific changes in cell shape.

Despite the importance of this cellular activity, it has been surprisingly difficult to establish a link between an intracellular chemical change with a cell and the accompanying cell shape change. However, several lines of evidence suggest that changes in cytosolic free  $\text{Ca}^{2+}$  concentration may play a role in the response [1]. Using  $\text{Ca}^{2+}$  imaging techniques, it is possible to acquire images which contain information of both cytosolic free  $\text{Ca}^{2+}$  concentration and cell shape. Several image processing techniques have been proposed to assess morphological changes of cells and to quantify their movement [2,3]. However, the inability to extract  $\text{Ca}^{2+}$  data from a dynamic region defined in relationship to a localised cell shape change remains a major problem. In static cells, a region of interest is usually defined within which cytosolic free  $\text{Ca}^{2+}$  concentration is extracted. With neutrophils, this approach extracts data from regions of differing cell activity at different times as the cell moves relative to the region of interest. A particularly useful data extraction would be a computer assisted extraction of  $\text{Ca}^{2+}$  data from the forming and moving pseudopods as well as the whole cell body.

In this paper a spline-based semi-automatic method is presented which permits this objective to be met. The method relies upon the use of spline points, the positions of which are recalculated in successive images. Some of these points can also be used to define a dynamic region of interest from which the  $\text{Ca}^{2+}$  data is extracted.

## 2 Materials and Method

### Neutrophil Isolation

Neutrophils were isolated from heparinized blood of healthy volunteers as described previously [4]. Following dextran sedimentation, centrifugation through Ficoll-Paque (Pharmacia) and hypotonic lysis of red cells, neutrophils were washed and resuspended in Krebs buffer (120 mM NaCl, 4.8 mM KCl, 1.2 mM  $\text{KH}_2\text{PO}_4$ , 1.2 mM  $\text{MgSO}_4$ , 1.3 mM  $\text{CaCl}_2$ , 25 mM HEPES and 0.1% bovine serum albumin, adjusted to pH 7.4 with NaOH).

---

<sup>1</sup> Email: ahoppe1@glam.ac.uk

## Measurement and Imaging of cytosolic free $\text{Ca}^{2+}$ concentration

Neutrophils were loaded with fura-2 from its acetoxy-methyl ester as previously described [2]. This fluorescent indicator of cytosolic free  $\text{Ca}^{2+}$  concentration provides quantitative information of when the ratio of two excitation signals is calculated [5]. Excitation at 340nm and 380nm was achieved by using a rapid access monochromator changer (Delta-RAM) with a transfer time between wavelengths of 2 msec and emission images (>490nm) two wavelengths were acquired using an intensified IC-200 CCD camera (Photon Technology International, Surbiton, UK) coupled to an inverted Nikon microscope. Ratios of the images were calculated using ImageMaster (PTI). Acquisition of ratio images was performed after 16 frame averaging, and using only a thresholding algorithm (no masking applied) which produced a cell image of equal size to that viewed by phase contrast. This enabled both cytosolic free  $\text{Ca}^{2+}$  concentration and cell shape to be measured simultaneously and calculated from the same image data set. The cytosolic free  $\text{Ca}^{2+}$  concentration was calculated as the mean pixel value within cell area which excluded the actual cell edge as this was often contaminated with artefactual ratiometric values resulting from the low fura2 intensity in this region [6].

## Image Segmentation

We have further developed a previously described system which assessed the movement of clustered cancer cells [7]. This system incorporates a model based segmentation approach using a cubic spline interpolation to render the boundary of cells. A neutrophil is specified from the first frame by marking a few salient points (10-20 points) on the cell boundary while the computer automatically interpolates and fits a suitable closed boundary. In consecutive frames, the system refits these points to changes in the boundary. If necessary, single control points can be added, moved or deleted manually to ensure a close fit to the cell boundary. The software calculates the cell position from the centre of area (centroid), and in addition the area and the length of the perimeter.

The whole boundary is divided into segments and each segment is described by a cubic spline, a special form of a Hermite spline [8]. Each segment is determined by a start and finish point as well as four polynomial coefficients. The x coordinate of a single boundary segment  $Q_i(u)$  is described as a cubic polynomial with the parameter u:

$$Q_i(u) = (x_i(u), y_i(u)), \quad x_i(u) = a_i + b_i u + c_i u^2 + d_i u^3 \quad 0 \leq u \leq 1 \quad (1)$$

The first derivative as well as the second derivative at the end of each segment equal those at the beginning of the next segment. All boundary segments are described mathematically and thus the centre of area (centroid) and perimeter can be determined from the cubic spline equation. As a shape descriptor, we calculate the roundness as defined:

$$\text{roundness} = \frac{\text{perimeter}^2}{4\pi \cdot \text{area}} \quad (2)$$

Figure 1 demonstrates the fitting process of a cubic spline to a neutrophil boundary



a) original (bar: 5 $\mu\text{m}$ )    b) point placement    c) smoothing+fitting    d) result

**Figure 1.** Example of boundary fitting to a single, stained neutrophil (centroid X, control points ;)

The cubic spline can also be used as a first approximation for the initial cell shape. It then locates ten times more points on the boundary where the orthogonal vector intercepts the boundary. This way a more accurate description is achieved, but the boundary is not as smooth. A slightly jagged boundary may give inappropriately high readings of perimeter length, therefore we calculated the perimeter from the cubic spline only.

## Tracking

Tracking is initiated by placing a few salient control points close to the cell boundary. The boundary often appears jagged and a 3x3 median filter is applied locally to smooth the boundary and to reduce noise. The fitting of points onto the boundary is performed along the normal vector  $n(u)$  at each control point.

$$n(u) = \left( \frac{-y'(u)}{\sqrt{x'(u)^2 + y'(u)^2}}, \frac{x'(u)}{\sqrt{x'(u)^2 + y'(u)^2}} \right) \quad (3)$$

The edge is located within a  $\pm 10$  pixel profile orthogonal to each control point. The edge is located wherever two values, which are not the background, appear in the profile towards the cell. In consecutive frames, control points of the previous frame are copied onto the next one and adjusted with the same relocation method as described.

## Pseudopods

One of the objectives was to monitor calcium changes in expanding and retracting pseudopods. Since there are no landmarks within the cell image apart from the boundary, we devised a method by which we relate the definition of the pseudopod to the overall shape of the boundary. Whenever a pseudopod is forming, the user highlights once those control points that describe the expanding/retracting region. The pseudopod is tracked like the rest of the cell body but forms a sub-region of the spline boundary defined only by the selected number of control points as seen in the example in figure 2.



**Figure 2.** Example of a single neutrophil with highlighted pseudopod region before and after retraction (bar: 5 $\mu$ m)

## 3 Results

We have applied our method to track six neutrophils in two series (phag\_3 and phag\_5) with three cells each. The cells were delineated with the described spline equation from which the area, length of perimeter and roundness was calculated. We observed a median area of 62  $\mu$ m<sup>2</sup> (range: 41  $\mu$ m<sup>2</sup> - 169  $\mu$ m<sup>2</sup>) and a median perimeter length of 32 $\mu$ m (range: 27 $\mu$ m - 49 $\mu$ m).

The following graph shows the roundness of three cells per series. A roundness of 1.0 describes a circular shape, higher values express more complex shapes.

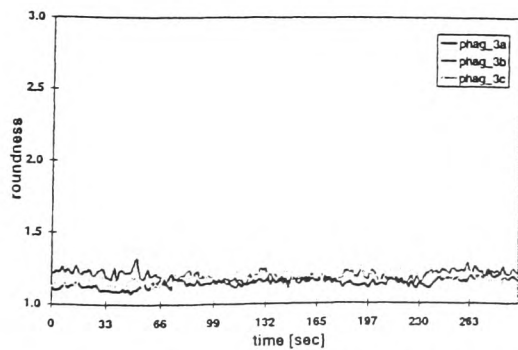


**Figure 4.** Roundness of three cells in phag\_3 series

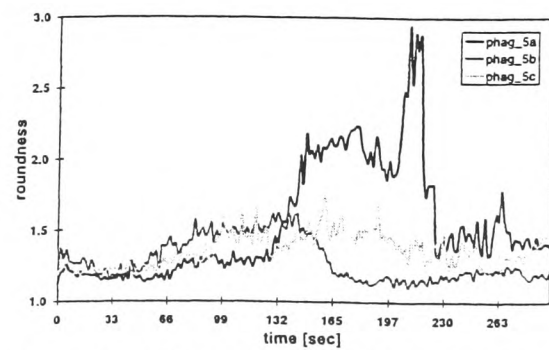


**Figure 5.** Roundness of three cells in phag\_5 series

By visual inspection, neutrophils in the phag\_5 series appeared to show greater phagocytosis and changes in cell shape than cells in the phag\_3 series; this is supported by our observation of greater variation in roundness in the phag\_5 series compared to the phag\_3 series. We have also calculated the  $\text{Ca}^{2+}$  concentration in the cell body. The following graph shows the calculated calcium concentration and roundness of a single neutrophil.

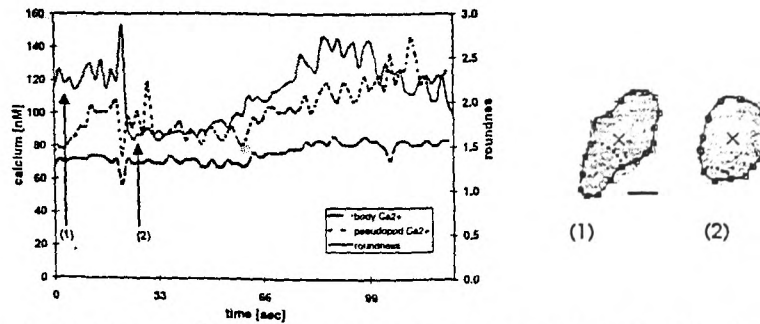


**Figure 6.** Example of Calcium  $\text{Ca}^{2+}$  concentration in the cell body (-) and a pseudopod (--) of the same cell. The roundness of the cell body is also plotted as a comparison to the  $\text{Ca}^{2+}$  concentration.

The two cell images on the right correspond to the position marked in the graph (bar:  $5\mu\text{m}$ ).

In this example we observed a greater calcium concentration in the region of the pseudopod compared to the overall concentration within the neutrophil. The graph suggests that there may be a relationship between the morphology of the neutrophil and the calcium concentration of the pseudopod.

## Validation

We have previously validated the adaptive spline method against artificial cell shaped objects [9] and observed a maximum error of 3% in area. We compared also the cubic spline boundary description with a description based on a linear interpolation using 50 points placed on the cell boundary. We delineated the same neutrophil image six times using 10 control points placed approximately equally spaced around the cell boundary. The relocation was performed after a median filter had been applied. We observed a maximum difference of 3% in area between linear and cubic interpolation. The maximum difference in perimeter length between the linear interpolation of 50 points and the 10 point cubic spline interpolation was 10%. However, the spline perimeter was smaller in all six cases, while the area calculated by the spline was three times less than and three times more than the linear interpolation.

## 4 Conclusion

In this study we developed and applied a semi-automatic method to track single neutrophils. The method is based on a cubic spline interpolation of the boundary combined with a relocation mechanism for the control points. Furthermore, this approach enables the definition and semi-automatic tracking of expanding or retracting pseudopods and the analysis of area, perimeter, roundness and calcium  $\text{Ca}^{2+}$  concentration. The semi-automatic nature of the technique enables manual intervention if, for example, two cells are attached. Thus, this system may help in investigating the role of calcium concentration in neutrophil motility.

## References

1. Pettit, E.J. & Hallett, M.B. "Release of 'caged' cytosolic  $\text{Ca}^{2+}$  triggers rapid spreading of human neutrophils adherent via integrin engagement", *J. Cell Sci.* 111, 2209-2215, 1998.
2. Thurston G, Jaggi B, Palcic B. Cell Motility measurements with an Automated Microscope System. *Exp. Cell Research* 165: 380-390, 1986
3. Zicha D, Dunn GA. An image processing system for cell behaviour studies in subconfluent cultures. *J Microscopy* 179: 11-21, 1995.
4. Davies, E.V. and M.B.Hallett. "A novel pathway for  $\text{Ca}^{2+}$  signalling in neutrophils by immune complexes", *Immunology* 85, 538-543, 1995.
5. Hallett, M.B., Davies, E.V and Pettit, E.J., " Fluorescent methods for measuring and imaging the cytosolic free  $\text{Ca}^{2+}$  in neutrophils" *Methods: A Companion to Methods in Enzymology* 9, 591-606, 1996.
6. Hallett, M.B., E.V.Davies, and A.K.Campbell, "Spatial and temporal analysis of  $\text{Ca}^{2+}$  signals in individual neutrophils using ratio imaging of fura2", *Surveys in Subcellular Methodology* 21, "Cell Signalling: Experimental Strategies" (Eds Reid, GMW Cook and JP Luzio) Royal Society Chemistry. pp 273-286, 1991.
7. Hoppe A, Wertheim D, Jiang WG, Williams R, Harding K. "An interactive image processing system for assessment of cell movement" *Medical & Biological Engineering & Computing*, 37, 4, 419-423, 1999
8. Bartels R, Beatty JC, Barsky BA. An Introduction to Splines for use in Computer Graphics & Geometric Modeling. Morgan Kaufmann Publishers, 1992.
9. Hoppe A, Jiang WG, Wertheim D, Williams R, Harding K. "A System for Computer Analysis of Cancer Cell Movement" *Anticancer Research*, 18, 2691-2694, 1998

# Medical & Biological Engineering & Computing



**Incorporating CELLULAR ENGINEERING**

Volume 37, Supplement 2, 1999

Proceedings of the  
European Medical & Biological  
Engineering Conference

*EMBEC '99*

**PART II**

November 4-7, 1999  
Vienna, Austria

Journal of the International Federation for Medical & Biological Engineering

## A COMPUTER SYSTEM FOR THE ANALYSIS OF NEUTROPHIL MOVEMENT

A Hoppe\*, A Korzynska\*\*, D Wertheim\*\*\*

\*School of Electronics, University of Glamorgan, Pontypridd, UK

\*\*Institute of Biocybernetic and Biomedical Engineering, Polish Academy of Sciences, Warszawa, Poland

\*\*\*School of Computer Science, Kingston University, Surrey, UK

ahoppe1@glam.ac.uk, akorz@ibib.waw.pl, D.Wertheim@kingston.ac.uk

**Abstract:** The study of neutrophil motility is thought to be important in the assessment of immunodeficiency disorders. Several automated methods of assessing the movement of cells in brightfield microscopy have been described. In some cases, a fully automatic approach might not be appropriate. The aims of this study were to develop and apply a computer system to assess the area and velocity of neutrophils with a semi-automatic spline interpolation method and to investigate texture based segmentation. We applied our system for the analysis of the movement of neutrophils. In one series of neutrophil images, we observed a median area for the neutrophils of  $118 \mu\text{m}^2$  [ range 90 to  $131 \mu\text{m}^2$  ].

Our semi-automatic spline method appears to be well suited for describing the shape of neutrophils. An automated boundary relocation function to support the process of boundary definition was investigated. As the system is interactive, the user may modify the computer generated boundary by moving control points as necessary. The system thus enables interactive definition of neutrophils and hence calculation of position, area, velocity and compactness. Our system may therefore be of value in investigating neutrophils.

### Introduction

Several automated methods for assessing the movement and chemotaxis of cells in brightfield microscopy have been described. Most methods are devised from an automatic cell detection mechanism that identifies the cell body in each frame [1,2]. Other cell movement analysis systems register similarities between consecutive frames and use optical flow analysis to relocate a region in consecutive frames [3]. In some cases, a fully automatic approach might not be appropriate to ensure correct cell boundary definition.

We therefore developed an interactive computer system based on a semi-automatic spline interpolation method to assess the movement of neutrophils. We further extended the system with a regional texture based relocation method.

### Materials and Methods

Two series of microscopic neutrophil images were digitised at a 2 second interval, one other series was digitised at 25 frames per second for 2 seconds. Each image contained a single or two separated neutrophils. Neutrophils were obtained from fresh finger blood coming from healthy, grown-up donors. Cells were isolated using the Harris method based on their adhesion to glass [4].

Images were acquired using a OPTIPHOT-2 (Nikon) microscope fitted with a LWD condenser connected to a 1/2" CCD camera (J COHU). The frame grabber used was the SVIST (WIKOM) and images were digitised as 8-bit  $512 \times 512$  gray level images and subsequently read into our analysis software. We used our system to investigate changes in movement path, velocity, area and compactness of three series of neutrophil images.

Instead of describing the cell boundary with a series of pixel locations, our approach is based on a mathematical description of the cell boundary. The shape of the boundary is described by a Hermite spline interpolation which can easily be modified to make a close fit. The boundary is divided into segments between salient control points placed on the boundary of the neutrophil. This approach allows an interactive relocation process [5] as only a few salient control points may be required to describe the shape of the neutrophil.

Figure 1 shows an example of a single neutrophil described by an interpolated hermite spline boundary with marked centroid and control points.



Figure 1: Example of a neutrophil described by Hermite spline (dashed line). Centroid marked by a cross, salient points are marked by open squares

The position of the cell is calculated as its centroid from the overall spline shape. The software also calculates the area, velocity and the compactness, defined as  $(\text{Perimeter})^2 / \text{Area}$ .

Initially, the neutrophil is described in the first frame by placing a few salient control points on the boundary. In consecutive frames, the outline of the previous frame can be copied as a template and adjusted as necessary.

We have also investigated a more automated segmentation method based on a regional texture descriptor. This approach is combined with a method to relocate the position of the control points. The texture descriptor is calculated as the mean value of the absolute differences of intensities for two dimensions in a  $5 \times 5$  region.

Control points are relocated according to the highest mean value in a  $5 \times 5$  region around the previous position. Points can be adjusted interactively if automatic relocation does not appear to be appropriate.

## Results

In two series of neutrophil images 28 frames were analysed. For the first series, we observed a median area for the neutrophils of  $118 \mu\text{m}^2$  [range 90 to  $131 \mu\text{m}^2$ ]. We observed a median compactness of 20 [range 16 to 24]. In a second series we observed a median area of  $82 \mu\text{m}^2$  [range 64 to  $90 \mu\text{m}^2$ ] and a median compactness of 34 [range 30 to 37].

We compared our spline based cell description with a manual description (drawing around) on six cell images. We observed a maximum difference in area of less than 7% between the manual description and the spline method.

## Discussion

Segmentation of neutrophils can be particularly complex when pods build during movement which may be difficult to distinguish from the surrounding halo. Halo is usually excluded but if it covers part of the cell it needs to

be included [6]. A feature of the spline method is that it can interpolate over parts of the cell boundary that are separated by halo and hence have similar intensity values.

The accuracy of the automatic point relocation method depends on cell features not changing dramatically between frames. We are investigating further the more automated boundary detection function to support the process of boundary definition

## Conclusion

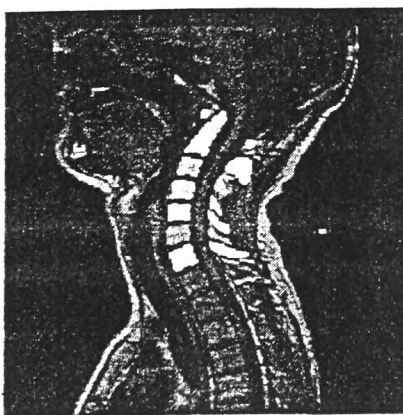
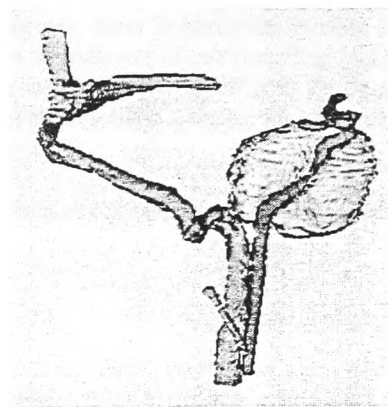
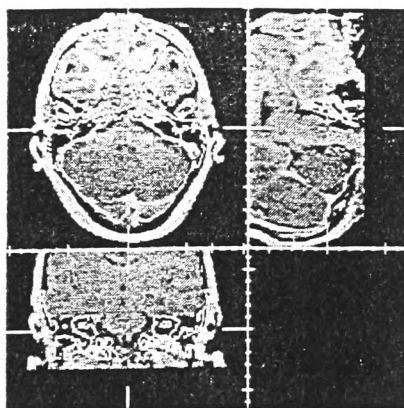
Our semi-automatic spline method appears to be well suited for describing the shape of neutrophils. As the system is interactive, the user may modify the computer generated boundary by moving points as necessary. The system thus enables interactive definition of neutrophils and hence calculation of position, area, velocity and compactness. Our system may therefore be of value in investigating neutrophils.

## REFERENCES

- [1] Azzara A, Carulli G, Rizzuti-Gallaci A, Minnucci S, Capochiani E, Ambrogi F. Motility of the rhG-CSF-induced neutrophils on patients undergoing chemotherapy: evidence for inhibition detected by image analysis. *Brit J Haematol*, vol. 92, pp. 161-168, 1996.
- [2] Zicha D, Dunn GA. An image processing system for cell behaviour studies in subconfluent cultures. *J Microscopy*, vol. 179, pp. 11-21, 1995.
- [3] Siegert F, Weijer CJ, Nomura A, Miike H. A gradient method for the quantitative analysis of cell movement and tissue flow and its application to the analysis of multicellular Dictyostelium development. *J Cell Sci*, vol. 107, pp. 97-104, 1994.
- [4] Harris A. "Behaviour of Cultured Cells on Substrata of Variable Adhesives" *Exp. Cell Research*, vol. 77, pp. 285-297, 1973.
- [5] Hoppe A, Wertheim D, Jiang WG, Williams R, Harding K. An interactive image processing system for assessment of cell movement. *Medical & Biological Engineering & Computing*. [In press]
- [6] Korzynska A. "A Method of Segmentation of Neutrophil Images observed in a Cell Monitoring System" in *Proc. VII Mediterranean Conference on Biomedical Engineering and Computing*, Cyprus, 1998.

Proceedings of

# Medical Image Understanding and Analysis 99



Examination Schools, Oxford.  
19-20<sup>th</sup> July 1999.

# A Computer System for Assessment of Cancer Cell Movement

A. Hoppe<sup>a</sup>, D. Wertheim<sup>b</sup>, W.G. Jiang<sup>c</sup>, R. Williams<sup>a</sup> and K. Harding<sup>c</sup>

<sup>a</sup>School of Electronics, University of Glamorgan, Pontypridd, U.K.

<sup>b</sup>School of Computing Science and Electronic Systems, Kingston University, Surrey, U.K.

<sup>c</sup>Department of Surgery, University of Wales College of Medicine, Cardiff, U.K.

**Abstract.** The study of cancer cell motility is considered to be important in improving understanding of cancer metastasis. Changes in cell movement behaviour may be an indicator of cell spreading. The movement of cells in clustered cell colonies is of particular interest.

We have previously described a semi-automatic boundary description method based on two-dimensional computerised rendering of the cell boundary. In this preliminary study, we have used our system to compare the position of cells calculated according to the centroid and according to the position of the nucleus. The system may be of value in further understanding cancer cell motility.

## 1 Introduction

In some previous studies, the movement of single, detached cells were described by separating the cell from its surrounding background [1-3]. As cells can appear in cell colonies, there is particular interest in the movement behaviour of clustered cells as changes in cell movement may be an indicator of cell spreading [4,5]. Due to the fact that tightly clustered cells may overlap or features may not be visible, it may be difficult for an automated image vision system to track individual cells correctly. We have previously described a system for computer analysis of cell movement and applied this system for the analysis of cell velocity [6,7].

The aim of this study was to apply our previously described system to compare the position of the centroid with the position of the nucleus in cancer cells.

## 2 Method

Cancer cell images were captured as true colour 768 by 568 bitmaps and subsequently converted into 8-bit grey scale images. Analysis software was designed in the Java 1.1.6 Language (Sun Microsystems, U.S.A) under Linux 5.3 (Suse GmbH, Germany). The software facilitates image processing functions to describe cell movement and allows export of the analysed data.

Two sets of HT115 human colon cancer cells, one set with and one set without added HGF/SF motogen, were monitored for at least 90 minutes at a constant temperature. The motogen was added to stimulate the spreading of cells. A time-lapsed video recording system with a colour CCD camera connected to a microscope (Leica, Leitz, Germany) was used to record the cell colony. The microscope was fitted with a Hofman condenser (HMC20) to enhance the visibility of the cell boundaries. Images were digitised at an equivalent of a five-minute interval in real time and subsequently read into the analysis software.

The system incorporates a semi-automatic approach, whereby cells are specified in the first frame by marking a few salient points on the cell boundary while the computer automatically interpolates and fits a suitable closed boundary. In consecutive frames, the system tries to relocate these points. If necessary, single points can be added, moved or deleted to ensure a close fit to the cell boundary. This software allows the definition of the cell position from the centre of area (centroid) and also by specifying the position of the nucleus.

In this study, we have used our system to compare the position of the centre of area with the position of the nucleus.

---

Email: AHOPPE1@GLAM.AC.UK

## 2.1 Rendering

To describe a cell shape, a series of points are specified on the boundary which will describe how the curvature can be formed. In the case of an interpolation, the curve is required to pass through the specified points. The whole boundary is divided into segments and each segment is described by a cubic spline. A suitable type of spline which is appropriate to describe natural curvatures is the natural cubic spline, a special form of a Hermite spline [8].

The y coordinate of a single boundary segment is described as a cubic polynomial with the parameter  $u$ :

$$Y_i(u) = a_i + b_i u + c_i u^2 + d_i u^3 \quad \text{with } 0 \leq u \leq 1 \quad (1)$$

The first derivative  $Y_i'(u)$  as well as the second derivative  $Y_i''(u)$  at the end of each segment equal those at the beginning of the following segment. By incorporating those constraints into the cubic polynomial segment equation all the spline coefficients of each segment can be calculated.

All boundary segments are described mathematically and thus the centre of area (centroid) can be determined from the cubic spline equation. It can thus be used to describe the position of the cell in each frame and hence to calculate the velocity. Figure 1 shows a single HT115 human colon cancer cell with a cubic spline boundary description.

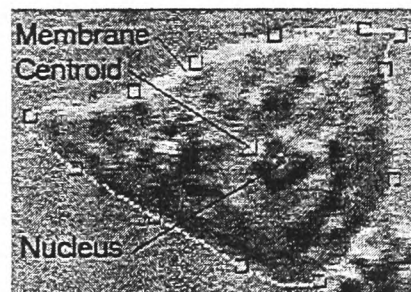


Figure 1. Example of a HT115 cell with highlighted cubic spline boundary description

## 2.2 Cell Boundary Location

Our approach is based on a two-dimensional rendering of the cell boundary with just a few salient points specified on the cell boundary. In a semi-automatic fashion, fragments of the boundary represented by a spline segment are specified manually in the first frame. Image enhancement functions are provided to facilitate this process. Subsequently, the points are logged onto positions with the highest absolute gradient in a 5x5 neighbourhood. The gradient is calculated with a two-dimensional 3x3 Prewitt filter.

This method has been designed so that the user can check and control the boundary relocation by moving single points if necessary.

Alternatively, a template of the previous cell outline can be passed to the next frame and the system permits changes necessary to adjust to the correct boundary. The position of the nucleus can be marked manually in the cell body.

### 3 Results

HT115 human colon cancer cells were monitored on a time-lapsed video system for at least 90 minutes. In this preliminary study, a cell colony with at least six cells was chosen at random and the movement of 3 such cells was analysed. The position of the cell according to the centroid and the position of the nucleus were compared in cells without added motogen (control cells) and cells with added motogen (HGF/SF).

The Euclidean distance between centroid and nucleus position of those cells without added motogen showed less variation over the monitoring period than cells with added HGF/SF motogen as can be seen in figure 3. Figure 2 shows the range in Euclidean distance of three control cells and three cells with added HGF/SF motogen.

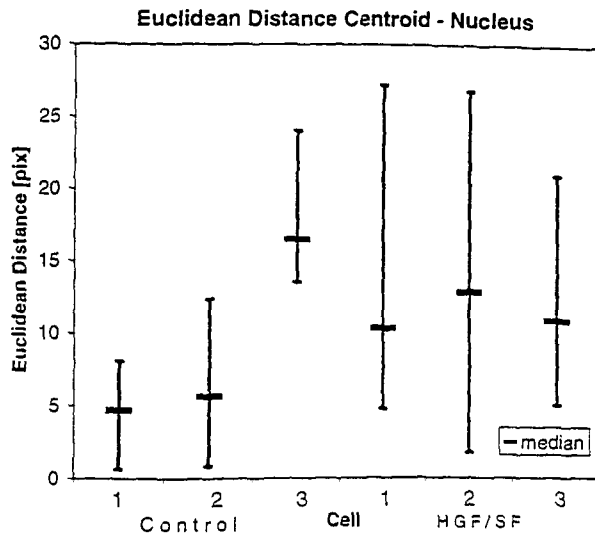


**Figure 2.** Range in Euclidean distance of three Control and HGF/SF cells

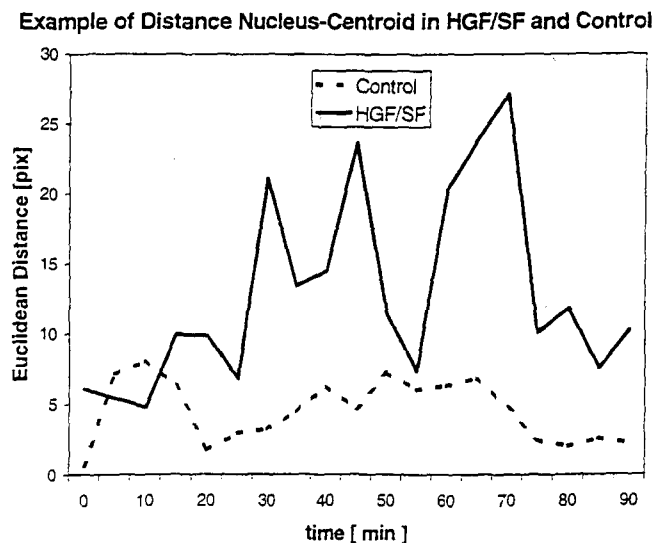


**Figure 3:** Example of a single HGF/SF and Control cell showing changes in Euclidean distance over a 90 minute period

In this preliminary study, we observed a higher range in Euclidean distance between nucleus position and centroid in cells with added motogen as compared to cell with no added motogen.

### 4 Conclusion

In this study we applied a newly developed computer system for rapid analysis of cell movement and cell velocity to investigate movement of cancer cells. Furthermore, this system permits the analysis of cell position according to the centroid of the cell and the position of the nucleus.

In this preliminary study, we observed greater variation in Euclidean distance (Nucleus-Centroid) of those cells with added motogen compared to control cells.

This system enables the analysis of area, velocity and relative distance between nucleus and centroid and hence may be of value in better understanding the movement behaviour of clustered cancer cells.

## References

1. Thurston G, Jaggi B, Palcic B. Cell Motility measurements with an Automated Microscope System. *Exp. Cell Reserach* 165: 380-390, 1986
2. O'Gorman L, Arthur C, Sanderson AC, Preston JR. A system for automated liver tissue image analysis: Methods and results. *IEEE Trans Biomedical Engineering* 32: 696-705, 1985
3. Zicha D, Dunn GA. An image processing system for cell behaviour studies in subconfluent cultures. *J Microscopy* 179: 11-21, 1995
4. Jiang WG, Hallett MB, Puntis MCA. Review Paper: Motility factors in cancer invasion and metastasis. *Surg. Res. Comm* 16: 219-237, 1994.
5. Schiffmann E. Motility as a principal requirement for metastasis. *Cancer Invest.* 8: 673-674, 1990
6. Hoppe A, Jiang W G, Wertheim D, Williams R, Harding K. A system for computer analysis of cancer cell movement. *Anticancer Research* 18: 2691-2694, 1998
7. Hoppe A, Wertheim D, Jiang WG, Williams R, Harding K. An interactive image processing system for assessment of cell movement. *Medical & Biological Engineering & Computing*. [accepted for publication]
8. Bartels R, Beatty JC, Barsky BA. *An Introduction to Splines for use in Computer Graphics & Geometric Modeling*. Morgan Kaufmann Publishers ,1992